PhD. Thesis

Ocean Monitoring Using L-Band Microwave Radiometry and GNSS-R

Enric Valencia i Domènech

Advised by Dr. Adriano Camps

June 15, 2012

Passive Remote Sensing Laboratory

Departament de Teoria del Senyal i Comunicacions

Universitat Politècnica de Catalunya

Preface

The knowledge of sea surface salinity (SSS) is a key issue to understand and monitor the Earth's water cycle. Accurate and systematic measurement of SSS was not possible until the ESA's Soil Moisture and Ocean Salinity (SMOS) mission was launched in 2009. The SMOS mission uses L-band microwave radiometry to infer SSS from measurements of the ocean's emissivity. However, the ocean surface emissivity is not only dependent on SSS, but also on sea surface temperature (SST), incidence angle, polarization, and sea surface roughness (i.e. sea-state). While the dependence on most of these parameters is well-known, and can be properly accounted for, the accurate estimation and correction of the sea surface roughness contribution remains a challenge.

The Passive Advanced Unit (PAU) project was born in 2003 with the main objective of studying how to correct ocean L-band brightness temperature for the sea-state effect by using an emerging technology such as reflectometry of opportunity GNSS signals (GNSS-R). GNSS-R is based on measuring the forward scattered GNSS signals so as to infer geophysical properties of the scattering surface. Particularly, the PAU project proposed to use direct observables from the reflected signal's Delay-Doppler Map (DDM) to parameterize sea surface roughness, and link those observables to the brightness temperature variations induced by sea-state, without using scattering/emissivity models. In this line, prior work was performed by J.F. Marchan-Hernandez in his PhD. Thesis (UPC, Barcelona, 2009). In that work, a first version of the PAU GNSS-R receiver was developed, and first experimental results were obtained that supported the hypothesis that direct GNSS-R observables can be used to describe sea-state.

This PhD. Thesis follows on that research, and steps into the use of GNSS-R observables for estimation of the sea-state contribution to the ocean L-band brightness temperature. The work presented here was undertaken between 2008 and 2012, and comprises contributions to three main fields: GNSS-R

hardware development, experimental results, and theoretical studies. Firstly, the PAU GNSS-R instrument was re-designed and re-implemented for improved sensitivity and stability. Secondly, results from ground-based and airborne experiments were obtained, that prove the hypothesis that GNSS-R observables can be used to successfully correct L-band brightness temperature for the sea-state effect, resulting in an improvement in the SSS retrieval accuracy. Finally, theoretical studies to foresee the performance of the PAU concept in a future spaceborne mission were conducted, along with the development of a new technique to obtain ocean surface scattering coefficient images from measured DDMs.

Contents

CONTENTS

III   Towards Spaceborne
Sea State Monitoring Using GNSS-R Techniques   181

CONTENTS

List of Figures

LIST OF FIGURES

10

15

19

LIST OF FIGURES

List of Tables

List of Acronyms

ADC Analog to Digital Converter

ALBATROSS Advanced L-BAnd emissiviTy and Reflectivity Observations of the Sea Surface

C/A GPS Coarse Acquisition code

CLS Constrained Least Squares

DD Delay-Doppler

DDM Delay-Doppler Map

DDS Direct Digital Synthesis

ECMWF European Centre for Medium-range Weather Forecasts

ESA European Space Agency

FOV Field Of View

FPGA Field Programmable Gate Array

FSM Finite States Machine

GNSS Global Navigation Satellite System

GNSS-R GNSS Signals Reflectometry

GO Geometric Optics

GPS Global Positioning System

GRAJO GPS and Radiometric Joint Observations

griPAU GPS Reflectometer Instrument for PAU

LIST OF ACRONYMS

GODAE Global Ocean Data Assimilation Experiment

IF Intermediate Frequency

INTA Instituto Nacional de Tecnica Aerospacial

IR Infrared Radiometer

P GPS Precise code

LEO Low Earth Orbit

LHCP Left Hand Circular Polarization

MIRAS Microwave Imaging Radiometer by Aperture Synthesis

MSS Mean Square Slopes

NOAA National Oceanographic and Atmospheric Administration

PAU Passive Advanced Unit

PIT-PoC PARIS Interferometric Technique Proof of Concept

P^{2}EPS PAU/PARIS End-to-end Performance Simulator

PRN Pseudo Random Noise

PSF Point Spread Function

PSU Practical Salinity Unit

RF Radio Frequency

RHCP Right Hand Circular Polarization

RMSE Root Mean Squared Error

SAR Synthetic Aperture Radar

SMOS Soil Moisture and Ocean Salinity

SNR Signal to Noise Ratio

SRF Scattering Reference Frame

SS-BSAR Space-Surface Bistatic SAR

SSS Sea Surface Salinity

SST Sea Surface Temperature

SV Space Vehicle

SWH Significant Wave Height

TIR Thermal Infrared Radiometer

TPR Total Power Radiometer

UK-DMC United Kingdom Disaster Monitoring Constellation

UTC Coordinated Universal Time

VHDL VHSIC Hardware Description Language

WAF Woodward Ambiguity Function

WD Wind Direction

WF Waveform

WISE WInd and Salinity Experiment

WS Wind Speed

XCW Cross Correlation Waveform

1

Introduction

1.1 Sea surface salinity within the Earth processes

Water plays a key role in all the geological and biological processes that take place in our planet. Cycling endlessly between oceans, atmosphere and land, it triggers and supports life, shapes the Earth and drives the weather and the climate (Fig. 1.1). Recalling that oceans account for more than 96% of the water on Earth, it is important to study the mechanisms that govern the ocean-to-atmosphere interface.

The sea surface salinity (SSS) is an oceanographic parameter that depends on the balance between precipitation and fresh water river discharge, ice melting, atmospheric evaporation, and mixing and circulation of the ocean surface water with deep water below. It is usually expressed using the practical salinity unit (PSU) of the practical Salinity Scale of 1978 (PSS-78).

In the open ocean the SSS ranges between 32 psu and 38 psu, with an average value of 35 psu. It is maximum in sub-tropical latitudes, where evaporation is more important than precipitation. Conversely, the salinity drops below the average around the Equator, where there is more precipitation, and in polar regions, due to ice melting and snowfall. Salinity and temperature are the two variables that control the density of the ocean water, which increases with increasing salinity and decreasing temperature.
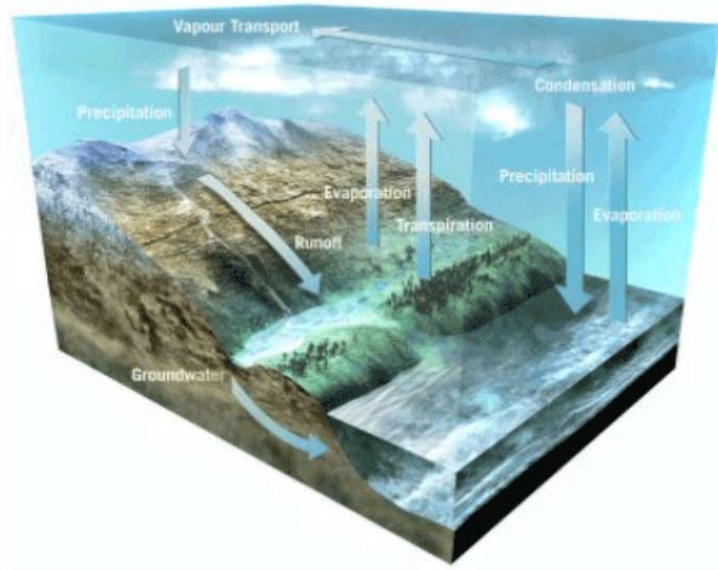
Figure 1.1: The Earth's water cycle [1].

Density itself is a very important oceanographic parameter, since ocean currents are generated by horizontal differences in density, and also its vertical profile determines the effect that surface winds, heating, and cooling have on subsurface waters. Salinity, through density, also determines the depth of convection at high latitudes. During the formation of sea ice, composed mainly of fresh water, dense cold salty water masses remain in the surface. At some point the water column losses its balance and denser water sinks. This vertical circulation is one of the engines of the global oceanic circulation known as the thermohaline circulation (Fig. 1.2). This sort of oceanic conveyor belt is a key component of the Earth's heat engine, and therefore strongly influences the weather and the climate. Therefore, SSS is directly linked to the climate.

Salinity also determines the behavior of the ocean-air interface where gas and heat exchange take place. The increased precipitation of tropical latitudes can locally create pockets of fresh water where the upper layer is more stable, thus reducing the gas transfer. SSS also influences the vapor
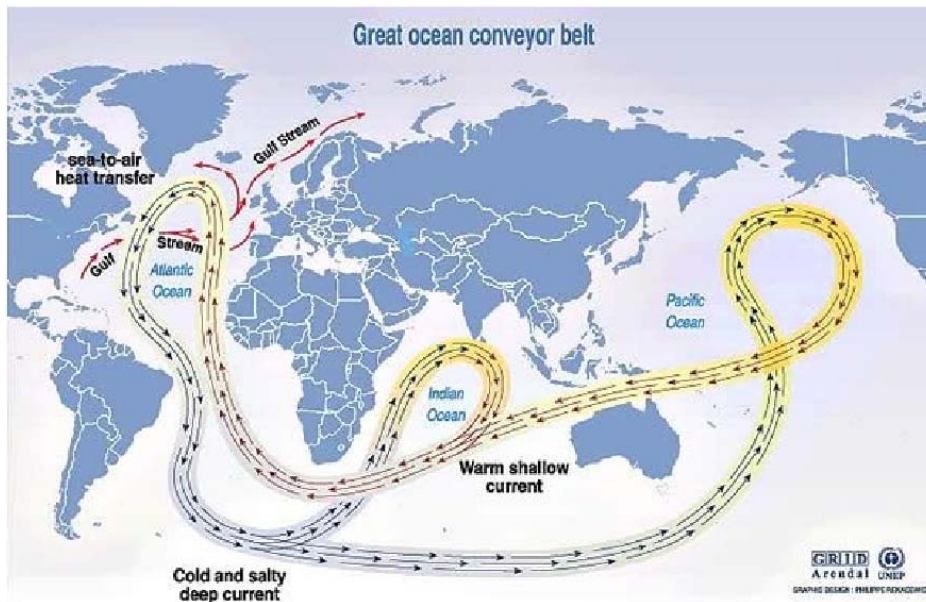
Figure 1.2: Thermohaline circulation acts as a global conveyor belt that redistributes heat throughout the whole planet [2].

pressure of sea water, thus controlling the evaporation rates.

Nowadays, Sea Surface Temperature (SST) along with other oceanographic parameters such as Wind Speed (WS) or sea surface topography are monitored on a regular basis from spaceborne sensors. However, SSS retrieval from space has not been possible until the SMOS mission [1]. Therefore, while ocean circulation models already incorporate satellite SST, WS and altimetry, they were lacking accurate SSS data. To overcome this limitation usually temperature-salinity correlations are used, based on the density conservation principle over a certain water volume [3]. However, the validity of this principle is seriously questioned at the surface, where heat and gas exchange between sea and air takes place [4]. This results in modeling errors that hinder the modeling of surface currents. The severity of this lack of data is clearly understood considering that SSS has never measured for 42% of the ocean surface, and that it has been measured less than four times over the past 125 years for 88% of the ocean surface [5] (Fig. 1.3).
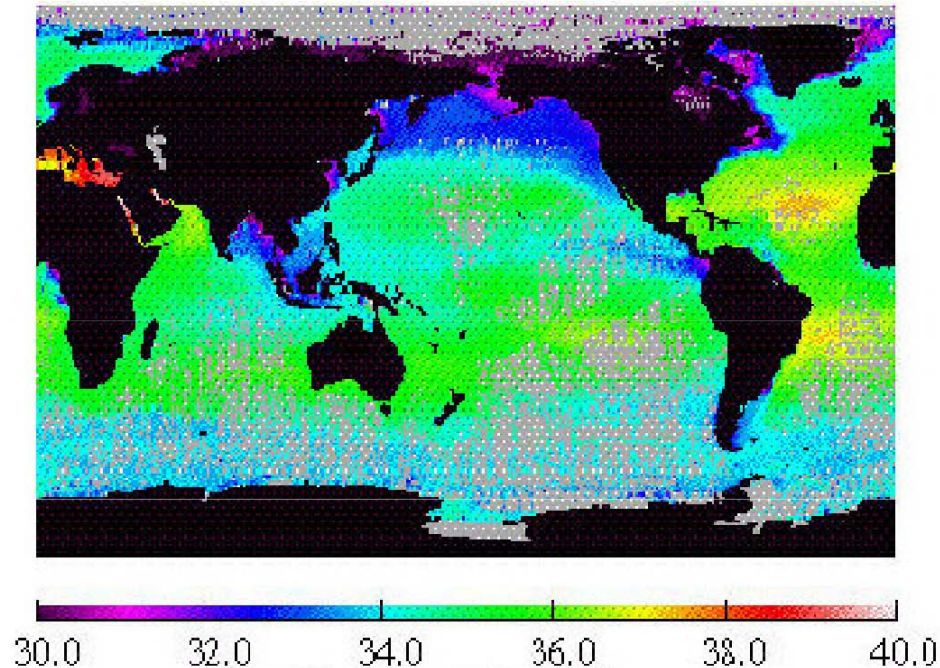
Figure 1.3: Existing SSS measurements (scale in PSU). Gray areas represent absence of data [5].

1.2 Measuring sea surface salinity from space: the SMOS mission

Despite the key role SSS plays in the water cycle, no global and systematic measurements were available until the launch of the ESA's SMOS mission in November 2nd, 2009. The Soil Moisture and Ocean Salinity mission is measuring SSS, among other geophysical parameters, for the first time systematically from space [6] (see Fig. 1.4). Its goal is to provide global and frequent soil moisture and sea surface salinity maps. Both variables are crucial in weather, climate, and extreme-event forecasting, and they are being provided on spatial and temporal scales compatible with applications in climatology, meteorology, and large scale hydrology.

Figure 1.4: Global SSS map retrieved by the SMOS Barcelona Expert Center from SMOS data (www.smos-bec.icm.csic.es).

SMOS was selected by the European Space Agency (ESA) as an Earth Explorer Opportunity mission within the frame of the ESA Living Planet Program. The Earth Explorer missions are designed to address critical and specific issues that have been raised by the scientific community whilst demonstrating breakthrough technology in the observing techniques. Earth Explorer missions are, in turn, split in two categories: the so-called "core" missions and the "opportunity" missions. Unlike the core missions, opportunity missions are smaller and more focused on a specific issue, and aim at demonstrating the feasibility of emerging technologies.

This mission was selected for feasibility study in May 1999 by ESA's Program Board for Earth Observation. Since then, a successful Phase A feasibility study (2000-2001) and a Phase B (2002) for further definition and critical breadboarding were completed (the Phase B payload design was

completed in October 2003). Approval for full implementation was given in November 2003 and Phase C/D started in mid-2004. The Critical Design Review of the payload took place in November 2005. Finally, SMOS was launched in November the 2nd, 2009 from the Plesetsk cosmodrome (Russia) in a Rockot launcher. After a successful deployment and Commissioning Phase, now it is fully operational.

SMOS carries the first-ever, polar-orbiting, space-borne, 2-D interferometric radiometer. SMOS has a Sun-synchronous polar dawn-dusk circular orbit. The orbit altitude is 763 km, the inclination is 98,4° with 06:00 h local solar time at ascending node, and the latitude coverage is at least ±80°. The minimum foreseen lifetime is 3 years, in order to cover at least two seasonal cycles. Temporal resolution is 3 days revisit time at Equator. Spatial resolution spans from 32 km at its best up to 100 km in the field of view (FOV) swath edge (Fig. 1.5).

Considering the spatial resolution constraints, the overall goal for SSS retrieval from SMOS data is to meet the Global Ocean Data Assimilation Experiment (GODAE) optimized requirement for open ocean SSS. The pilot experiment GODAE aimed at demonstrating the feasibility of real-time global ocean modeling and data assimilation systems, both in terms of their implementation and their utility. Following the recommendations of the Ocean Observing System Development Panel, the proposed GODAE accuracy requirement for satellite SSS is specified as 0.1 psu for a ten-day and 2° x 2° resolution for global ocean circulation studies.

The most suitable technique for SSS remote sensing is microwave radiometry at L-band (see Chapter 2) [7]. For this reason, the chosen SMOS payload is MIRAS (Microwave Imaging Radiometer by Aperture Synthesis), an L-band, two-dimensional, synthetic aperture radiometer with multi-angular and dual/fully-polarimetric imaging capabilities, able to measure the brightness temperature of the Earth within a wide field of view and without any mechanical antenna sweeping. It has a Y-shaped deployable structure, con-
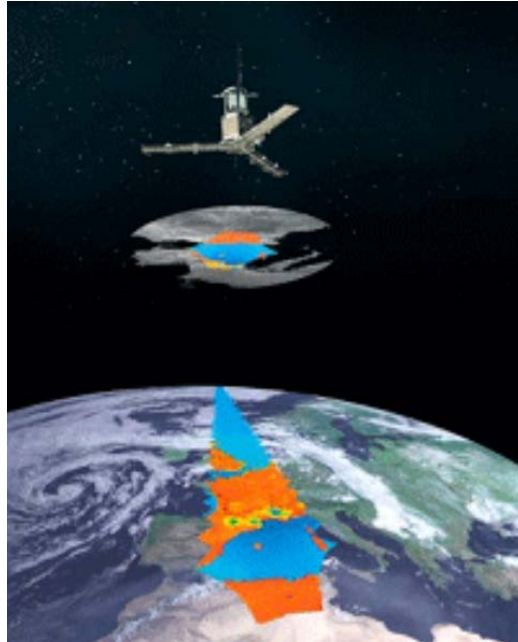
Figure 1.5: SMOS observation geometry. The field of view has a hexagon-like shape of 1000 km approximately [1].

sisting of 3 coplanar arms, 120° apart each other. The total arm length is about 4.5 m with an angular resolution of approximately 2°. The range of incidence angles is variable (spanning from 0° to almost 65°) within the FOV, and depends on the distance between the pixel and the sub-satellite track. To achieve an even greater angular excursion and fully exploit its viewing capability the array is tilted 32° with respect to nadir.

One of the main drawbacks of L-band radiometry is the small sensitivity of the brightness temperature (T_B) to the SSS (see Chapter 2). Therefore other parameters may easily mask the SSS signature, if not properly accounted for. The sea surface roughness is probably the parameter with the largest impact on the retrieved SSS [8] as, so far, it is not possible to be accurately modeled and corrected for as it is the sea surface temperature (SST) effect, for instance. Different approaches have been proposed to deal with the sea surface roughness effect. For instance, in the SMOS mission an effective

wind speed is retrieved along with the other variables that minimize the mismatch between the observables and the direct model [9]. In Aquarius (a joint NASA/CONAE planned mission to measure SSS), an L-band scatterometer is used to retrieve the L-band sea surface radar cross section (σ^0), which is used in the SSS retrieval algorithms [10] to perform the sea state correction. Nonetheless, the sea surface roughness correction is still a limiting factor in terms of SSS retrieval quality. Thus, further studies are required, as well as new techniques may be developed to improve this required correction.

1.3 The PAU concept

A potentially feasible approach to derive collocated sea state measurements is to use a Global Navigation Satellite System Reflectometer (GNSS-R) secondary payload. GNSS-R was first envisioned in 1993 for ocean mesoscale altimetry [11] using GPS reflected signals, and it has been used to retrieve other oceanographic variables [12, 13, 14, 15, 16, 17, 18, 19].

The main advantage of this approach is that, being a passive instrument, the extra cost in terms of power and mass budgets is not significant. Nevertheless, the fact of being a bistatic system, causes a "forward" scattering phenomena that resembles to the physical emission processes that determine the surface's brightness temperature. This leads to the hypothesis that the GNSS-R synergy with a radiometric system will be stronger that the one with a traditional scatterometer measuring the back-scattered power.

The Passive Advanced Unit (PAU) project aimed at demonstrating the synergy of combining radiometric and reflectometric observations to perform this correction. It was proposed in 2003 to the European Science Foundation (ESF) within the frame of the European Young Investigator (EURYI) Awards program, and granted in 2004 [20].

The PAU sensor consists of a suite of three different sensors envisioned for jointly ocean remote sensing: an L-band radiometer with digital beam-

forming (either real or synthetic aperture) and polarization synthesis, a GPS reflectometer (sharing the RF front-end with the radiometer), and an infrared radiometer to measure the sea surface temperature.

The main technological goal of the PAU concept was to prove the feasibility of using the same hardware front-end for the radiometer and the reflectometer. To do so a new radiometer topology was envisioned [21] (Fig. 1.6): The antenna output is connected to a Wilkinson power splitter, thus dividing the signal in two in-phase signals (S_{A1} and $S_{A2} = S_{A1}$). Additionally, the $100 \ \Omega$ resistance of the Wilkinson splitter adds two noise signals that are $180°$ apart (S_{n1} and $S_{n2} = -S_{n1}$). Thus, the incoming signal is not chopped, as required to track the GNSS signal.

The main scientific goal of this project is to explore whether a direct GNSS-R observable (see Chapter 2) can be linked to the T_B variations associated to the sea state without the use of any sea surface spectrum and emission/scattering models, thus avoiding their inaccuracies and discrepancies. Collocated sea brightness temperatures and GNSS-R measurements can result in a significant improvement of the retrieved SSS as preliminary explored in [19].
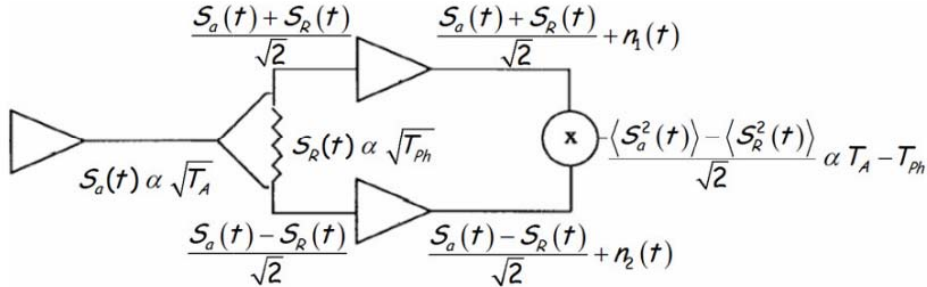
Figure 1.6: Conceptual topology of an elementary PAU receiver.

1.4 This PhD. Thesis

This PhD. Thesis arises within the framework of the PAU project with two main and diverse motivations:

- Design and implementation of the GNSS-R signal processor of the PAU instrument.

- Performance of experimental and theoretical studies to support the hypothesis of the beneficial synergy among GNSS-R and radiometric systems for SSS measuring.

According to that, this dissertation is divided into three parts:

- Part I: GNSS-R hardware development.

- Part II: Experimental results.

- Part III: Towards spaceborne sea state monitoring using GNSS-R.

In Part I, the design and implementation of the GPS Reflectometer Instrument for PAU is presented. Details of the final signal processor implementation and the design trade-offs are explained, along with the instrument performance.

Part II is devoted to present the results derived from different ground-based and airborne experiments that have involved the deployment of both GNSS-R and radiometric instruments for measuring the ocean surface. The experimental setups and the data-processing strategies are described, and the main results are discussed. Moreover, a study performed during a stay as invited researcher at the National Oceanic and Atmospheric Administration (NOAA, Boulder, USA) to retrieve wind direction from airborne GNSS-R measurements, is also presented in this part.

Finally, Part III presents the theoretical studies in a GNSS-R spaceborne scenario. In this line, a simulation study is presented to assess the performance of using direct GNSS-R observables for sea state monitoring from space. Moreover, a new technique to perform spaceborne imaging of the ocean surface from GNSS-R measurements is presented, and a possible application for oil slick detection is explored.

2

Theoretical background

2.1 Microwave radiometry

Microwave radiometry is the most suitable technique for sea surface salinity remote sensing [7]. The key concepts of this measurement technique are summarized in this section (mostly from [22]).

2.1.1 Thermal emission

All matter at an absolute temperature above 0 K emits electromagnetic radiation throughout the whole electromagnetic spectrum. This emission is caused by electron transitions from higher to lower energy bands. Since the transition probability depends upon the density and the kinetic energy of the particles, an increase of the absolute temperature results in an increase of the energy radiated by the object being.

The concept of blackbody defines an idealized object that absorbs all the incident electromagnetic radiation at all frequencies, from all directions and polarizations, and becomes a perfect emitter. When the thermodynamic balance is reached, it radiates isotropically all the incident energy. Planck's radiation law explains the spectral distribution of the unpolarized blackbody radiation:

$$B_f = \frac{2hf^3}{c} \frac{1}{e^{(hf/kT)} - 1} \quad \left[\frac{\text{W}}{\text{m}^2 \cdot \text{ sr } \cdot \text{ Hz}}\right], \quad (2.1)$$

where $h = 6.63 \cdot 10^{-34}$ J·s is the Planck's constant, c is the speed of light in m/s, $k = 1.38 \cdot 10^{-23}$ J/K is the Boltzmanns constant, f is the radiation frequency in Hz, and T is the absolute physical temperature in K.

At microwave frequencies (roughly from 1 to 30 GHz, with wavelengths between 20 and 1 cm) it is possible to approximate Eqn. 2.1 by a 1st degree Taylor polynomial, since $hf/KT \ll 1$, thus obtaining the Rayleigh-Jeans approximation:

$$B_f \cong \frac{2kT}{\lambda^2}, \quad (2.2)$$

where $\lambda = c/f$ is the electromagnetic wavelength. Equation 2.2 shows that the spectral brightness temperature and the physical temperature do have a linear dependence. Assuming an ideal antenna and receiver surrounded by a blackbody at a constant physical temperature T, and considering the bandwidth (B) of the receiver narrow enough so that the spectral brightness density can be considered flat throughout the whole frequency range, it can be demonstrated that the power collected by the antenna is given by:

$$P_{bb} = kTB. \quad (2.3)$$

However, most natural objects are not black bodies, since they do not absorb all the radiation that reaches them, but reflect a part of it. Therefore, the absorbed radiation that is re-emitted afterwards is smaller than that of a blackbody: they are called "gray" bodies. The power emitted by a gray body is also proportional to the physical temperature, and the proportionality constant is called emissivity (e). Since the relationship among power and temperature is then linear, the concept of brightness temperature is defined omitting the kB terms, which are constant for a given system:

$$T_B = e \cdot T. \tag{2.4}$$

The emissivity is dependent on the dielectric constant, the roughness of the object, the observation angles (θ, ϕ), and the polarization of the electromagnetic wave. Its value ranges from zero (perfect reflectors such as ideal metals) to one (blackbodies).

The detection of variations in the brightness temperature emitted by objects is the core of passive remote sensing techniques. The radiation emitted by the Earth can be collected to infer geophysical parameters of the surface under observation. Whereas the so-called active instruments rely on a transmitter to send energy towards the surface and measuring the properties of the reflected signal, passive sensors rely on the natural Earth's emission.

2.1.2 Contributions to the brightness temperature measured by a radiometer

The radiation reaching an antenna pointing towards the Earths surface from the space is composed of the power emitted by the surface $(T_B = T)$, the power emitted by the atmosphere in the upwards direction (T_{up}), and the power from the atmosphere and from outside the Earth which is reflected on the Earth's surface (T_{sc}). Assuming a scattering-free atmosphere, the so-called apparent temperature T_{ap} can be expressed as (Fig. 2.1):

$$T_{ap}(\theta, \phi) = T_{up} + \frac{1}{L_a}(T_B + T_{sc}), \tag{2.5}$$

where L_a is the atmospheric attenuation. From Eqn. 2.5 it can be seen that for high values of L_a, the terms T_B and T_{sc} are heavily attenuated, and the apparent temperature is approximately the upwelling one. At low microwave frequency bands, the Earth's surface can be remotely sensed since the atmospheric attenuation is low.

The term T_{sc} is composed by both the atmospheric (T_a) and the ex-
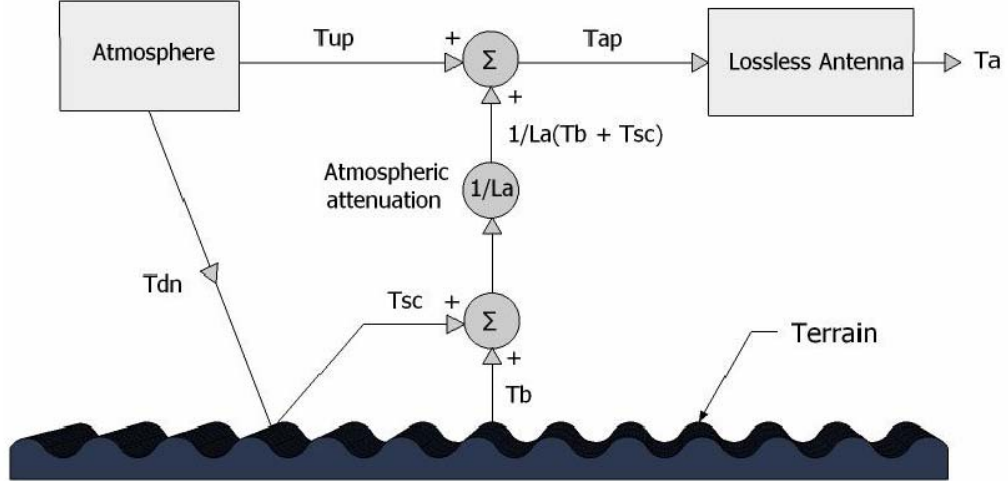
Figure 2.1: Components of the apparent temperature T_{ap} [22].

traterrestrial components (T_{ext}). This T_{ext} contains contributions from the isotropic cosmic background, the galactic radiation, and the Sun:

$$T_{ext} = T_{cos} + T_{gal} + T_{sun}. \tag{2.6}$$

Additionally, the polarization of the radiation may change as it passes through the ionosphere. This effect is known as Faraday rotation. Therefore, in order to use the measured T_{ap} to perform SSS retrievals, first it is necessary to account for all the terms in Eqn. 2.5 that are not related with the sea surface itself.

2.1.3 Brightness temperature of the ocean surface

The emissivity of seawater at microwave frequencies can be calculated, for example, using the Klein and Swift model [23] for given Sea Surface Temperature (SST) and SSS values. As stated in [24], the sensitivity of the emissivity to SSS increases as the frequency decreases from 1.5 to 0.4 GHz, for typical oceanic SST values. On the other hand, the sensitivity to errors in SST

increases over that range. Thus, a frequency between 0.8 and 1.5 GHz is optimal. The emissivity for vertically polarized radiation is significantly more sensitive to salinity variations than for horizontal polarization. The protected frequency band at 1.413 GHz (1.400-1.427 GHz) is the lowest one available for passive observations, and satisfies the constraints to perform successful SSS retrievals with the highest possible sensitivity from space [25], with almost negligible atmospheric effects. Recalling Eqn. 2.4, the sea brightness temperature is related to the emissivity as:

$$T_B(\theta, p) = e \cdot SST. \tag{2.7}$$

Due to the high losses of the sea water, the sea surface can be considered a semi-infinite body. Then, the emissivity of a flat sea surface can be expressed as the complementary of the Fresnel power reflection coefficient:

$$e(\theta, p) = 1 - R(\theta, p), \tag{2.8}$$

where $R(\theta, p)$ is the Fresnel power reflection coefficient at p polarization (h: horizontal or perpendicular to the plane of incidence; or v: vertical or parallel to the plane of incidence), that depends on the incidence angle θ and on the complex dielectric constant (or dielectric permittivity) of the sea water ϵ_r :

$$
\begin{aligned}
R_h &= \left| \frac{cos\theta - \sqrt{\epsilon_r sin^2\theta}}{cos\theta + \sqrt{\epsilon_r sin^2\theta}} \right|^2, \\
R_v &= \left| \frac{\epsilon_r cos\theta - \sqrt{\epsilon_r sin^2\theta}}{\epsilon_r cos\theta + \sqrt{\epsilon_r sin^2\theta}} \right|^2.
\end{aligned}
\tag{2.9}
$$

However, considering the GPS signal, it is useful to obtain the expressions associated to circular polarizations.The polarization matrix can be expressed as (sub-indexes R and L stand for the right hand and left hand circular polarization states):

$$\begin{bmatrix} R_{RR} & R_{LR} \\ R_{RL} & R_{LL} \end{bmatrix} = \frac{1}{2} \begin{bmatrix} R_h + R_v & R_h - R_v \\ R_h - R_v & R_h + R_v \end{bmatrix}. \qquad (2.10)$$

Even though L-band offers the optimum retrieval conditions, the dynamic range of the T_B variations due to SSS changes is pretty small. Therefore, SSS retrieval by means of microwave radiometry requires a high sensitivity and accuracy. Figure 2.2 shows the brightness temperature dependence on the SST for several SSS values, considering a flat surface and nadir incidence angle. It is remarkable that the sensitivity to SSS decreases as the SST also decreases, so that the salinity retrieval in cold water areas becomes even more demanding. The sensitivity of the brightness temperature T_B at L-band to SSS has been widely studied. For instance, at nadir, the sensitivity is 0.5 K/psu for a sea surface temperature of 20°C, decreasing down to 0.25 K/psu for an SST of 0°C. On average, this sensitivity varies between 0.2 and 0.8 K/psu depending on the SST, the incidence angle, and polarizations [26].

So far, the sea surface has been considered flat when deriving the T_B dependence on SSS and SST. However, changes in the sea surface roughness can result in a variation of the brightness temperature (ΔT_B) of several K for very a rough sea surface [24], having a larger contribution to the overall T_B than the SSS itself.

In fact, the sea surface roughness is the major contributor to the deviations of the brightness temperature with respect to the flat sea model [8]. Taking into account these considerations, the polarization-dependent brightness temperature can be expressed as:

$$T_{B,p}(\theta) = T_{B\_flat,p}(\theta) + \Delta T_{B\_rough,p}(\theta, \vec{v}), \qquad (2.11)$$

where $\vec{v}$ is a generic vector that describes the sea surface roughness. Sea state is usually described by using the wind speed at 10 m above the surface (U_{10}) or the significant wave height (SWH). In the WISE field experiments [27], measurements of the $\Delta T_{B,p}(\theta, \vec{v})$ term were performed for different incidence

44
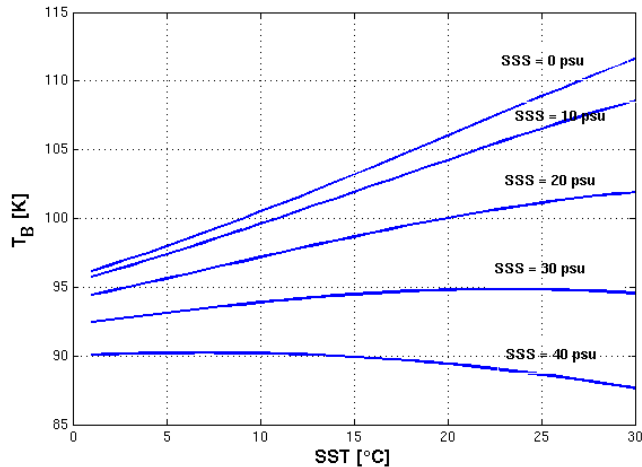
Figure 2.2: Ocean brightness temperature as a function of SST and SSS for a flat sea surface [23]. Average salinity in open ocean is around 35 psu.

angles and sea state conditions. From these measurements, the sensitivity of the brightness temperature increment to sea state variations was derived, both using the wind speed and the SWH (see Fig. 2.3). In the data processing of the SMOS mission, a combined model [28] derived from WISE that uses both wind speed and SWH was originally used. Today, more refined models have been derived from the SMOS measurements themselves.

However, the main issue of this empirical approach is that sea state auxiliary data is required to compute the appropriate brightness temperature correction. The availability of this sea state auxiliary data from other remote sensors or models is provided with typical spatial and time resolutions of 25 km and 6 h respectively. To overcome this limitation, one of the PAU concept's hypothesis is that measurements of the scattered GPS signal collocated with the radiometric measurements may improve the quality of the final SSS retrievals. This is one of the main points of this PhD Thesis, and it will be studied both from an experimental and a theoretical perspective.
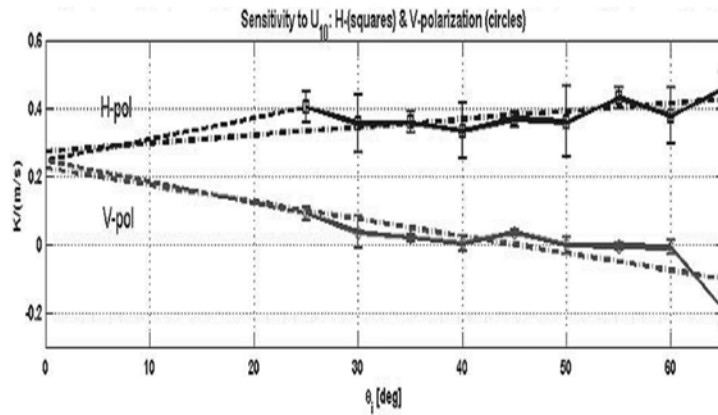
(a)
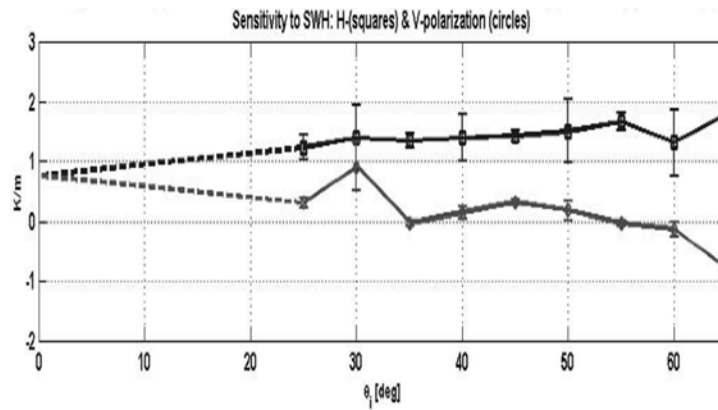
(b)

Figure 2.3: Sensitivities of the ΔT_B term as a function of the sea state described by: a) wind speed [K/(m/s)], and b) significant wave height [K/m] [27].

2.2 Scatterometry using GNSS signals of opportunity

Global Navigation Satellite Systems (GNSS) are satellite constellations that cover the entire Earth transmitting navigation signals to provide time and position information to users located on or near the Earth's surface. Such systems are used nowadays in a wide range of everyday situations, such as fleet management, search and rescue, wildlife tracking, vehicle guidance or leisure interactive maps, among many others. So far the American GPS is the only fully operational GNSS. The Russian GLONASS system is partially deployed, whereas the European GALILEO is scheduled to be completely operational in 2014. There are other GNSS systems planned , such as the Chinese COMPASS and the Indian IRNSS that are to be operative in the future. Altogether, more than 75 GNSS satellites will be available when all the currently planned systems will be deployed. The spectral allocation of the major GNSS signals is shown Fig. 2.4. This wide availability of signals has made them become a valuable opportunity source for Earth remote sensing.
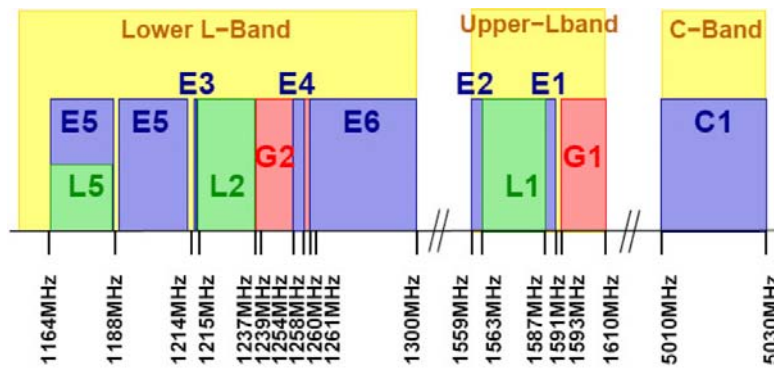
Figure 2.4: Radio Navigation Satellite Service band distribution after the World Radio Conference, Istambul, 8 May-2 June 2000, which discussed the allocation of the GALILEO signal spectrum. E and C bands (blue) are assigned to GALILEO, L bands (green) are for GPS, and G bands (red) are reserved for the GLONASS signals [29].

Since it was proposed in 1993 for mesoscale ocean altimetry [11], reflectometry using GNSS signals (GNSS-R) has been considered for other remote sensing applications. Among them, ocean scatterometry has probably become one of the most solid GNSS-R applications. It is true that other systems exist that already perform those measurements, such as microwave scatterometers or radar altimeters. For the particular application of sea state determination, the GNSS-R approach boasts a low mass and power constraints, since there is no transmitter, and a small antenna can be used. Also, the bistatic scattering geometry ensures a strong signal return in the specular direction, as opposed to the weak return for monostatic off-nadir configurations. Moreover, this technology is very suitable to be deployed as a secondary payload in a radiometric mission, since being a passive instrument, it does not interfere with the radiometric measurements. Thus, as proposed in the PAU concept [20], a GNSS-R scatterometer would be the ideal companion of an L-band radiometer in order to acquire collocated sea state information to perform the needed brightness temperature corrections. Actually, a space qualified version of the PAU instrument has been designed and manufactured by ADTelecom to be flown as a secondary payload in INTA's MicroSat-1 [30].

This section describes briefly the GPS signal that will be used throughout this work, and summarizes the principles of GNSS-R ocean scatterometry.

2.2.1   The GPS signal

The American Global Positioning System (GPS) was designed to provide 3D positioning anytime anywhere on Earth. To fulfill that goal at least four satellites have to be observed simultaneously at a given place and moment. In order to ensure the service even when one satellite fails it is necessary to consider a minimum of five visible satellites. These considerations result in a constellation of at least 24 satellites distributed in six orbital planes spaced 60° through the Equator with an inclination of 55°. The (at least four)

satellites in the same orbital plane are not equally spaced, but distributed so that the effects of a single satellite failure are minimized. Their orbital period is of 12 sidereal hours, which implies that the ground track repeats daily with a time shift of four minutes. The near circular orbits (eccentricity smaller than 0.02) have a medium height of 20163 km above the Earth's surface, which results in a mean satellite speed of 3.87 km/s approximately. The actual satellite visibility depends on the latitude, but there is always a minimum of 5 satellites in view, and for more than 80% of the time this minimum number is of 7.

The GPS signal structure was designed to allow multiple transmitters to use the same frequency band, and to have a certain tolerance to multi-path and jamming (a serious issue for military applications). It was also conceived to have a low power spectral density to avoid mutual interference with other microwave systems, and to allow estimating the ionospheric delay for accurate range determination. These features are achieved by means of spread spectrum techniques. In short, this implies to spread the bandwidth of the navigation signal (bi-phase modulation with a symbol rate of 50 Hz) by mixing it with a pseudo-random rectangular pulse train that has a much higher frequency than the data. The higher the spreading frequency, the larger the power spectral density decrease is for a given total radiated power. The spreading sequences used are known as pseudo-random noise (PRN), since they have autocorrelation and cross-correlation properties similar to those of Gaussian noise, but with the advantage that they can be accurately generated and regenerated, since they are in essence deterministic. Each GPS satellite has its own PRN code that not only allows to discriminate between transmitters, but also grants the required jamming and multi-path resilience and provides range estimations to determine the user position by triangulation.

In this work, the GPS L1 signal is used since it contains a public code that is relatively easy to work with. There are two main codes present at

this band: the public C/A, and the P codes.

The coarse acquisition (C/A) codes are used for the open-access civil service. They have a period of 1 ms to allow quick signal acquisition, with a length of 1023 chips. This implies a chip rate of 1.023 MHz, and a bandwidth 2.046 MHz. The C/A codes have high autocorrelation peaks to clearly identify an acquired satellite (Fig. 2.5) and low cross-correlation peaks so that the satellites do not interfere between them. In order to discriminate a weak signal surrounded by strong ones it is necessary for the autocorrelation peak of the weak signal to be higher than the cross-correlation peaks of the stronger signals. In the ideal case of using random sequences the codes would be orthogonal and the cross-correlations zero. The PRN codes used are almost orthogonal, and the cross-correlation values are as low as - 65/1023 (12.5% of the time), -1/1023 (75% of the time), or 63/1023 (12.5% of the time).

The precise code (P) is used for the restricted military signal. It has a chipping rate 10 times faster than the C/A code (10.23 MHz) that results in a ten-fold increase of the pseudo-range observable accuracy. The code period is 1 week, so that the direct acquisition of the code (i.e. the estimation of the code offset) is pretty cumbersome. Therefore, to acquire this P code special data fields of the navigation frames (Z-count and Time of Week TOW) are used.
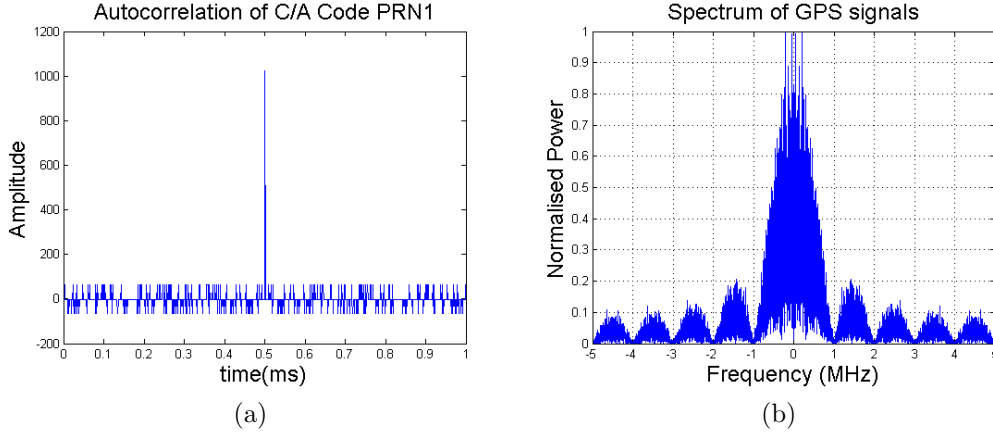
Figure 2.5: a) Autocorrelation, and b) spectrum of the GPS C/A code.

The C/A and P codes are modulated in-phase and quadrature onto the L1 carrier:

$$s_{L1}(t) = \sqrt{P_{C/A}}N(t)a(t)cos\left(2\pi(f_{L1})\right) + \sqrt{P_P}N(t)P(t)sin\left(2\pi(f_{L1})\right), \quad (2.12)$$

where $a(t)$ is the C/A code, $N(t)$ is the navigation message (50 Hz bi-phase code), $P(t)$ is the precise GPS code, $P_{C/A}$ is the transmitted power of the in-phase component, P_P is the power of the quadrature component, and $f_{L1} = 1575.42$ MHz.

2.2.2 Principles of GNSS-R over the ocean

GNSS-R is able to retrieve geophysical parameters through the scattering process where the signal interacts with the surface. Several models exist that describe this electromagnetic process over the ocean surface. In spite of its limitations, the most accepted and widely used is the Geometric Optics approximation to the Kirchoff Method [14]. This is due to the fat that it is a statistical approach that drastically reduces the computation cost of its

implementation, while providing quite accurate results around the forward scattering direction.

Applying a linear relationship between the incident and the scattered field through the Fresnel coefficients, the integral equations of the electromagnetic field on the surface simplify to the integration of the incident field over the surface. This accounts only for the induced currents on the surface, allowing to solve the integral equation through the Green's theorem, considering only the tangential fields. This approximation is valid provided that both the correlation length of the sea surface, and its average radius of curvature are significantly larger than the wavelength of the incident field. This method properly models the quasi-specular scattering, but it is not sensitive to the field polarization. The geometric optics (GO) or stationary phase approximation applies when the surface roughness (standard deviation of the surface height) is large compared to the wavelength. The surface is decomposed in a set of elementary facets that reflect the signal specularly and independently from the others. The resulting field is the incoherent sum from all the properly-oriented mirrors.

Adopting the GO approximation to the KM, Zavorotny and Voronovich [14] define a model for the acquired GPS signal after scattering on the ocean surface. There, the received signal can be modeled as an integral over the surface (reference system centered on the specular reflection point):

$$u(\vec{r}, t) = \int D(\vec{r})a\left[t - \frac{R_0 + R}{c}\right]g(\vec{r}, t)d\vec{r}, \tag{2.13}$$

where R_0 and R are the distances from a given surface's point to the transmitter and receiver respectively, $D(\vec{r})$ is the antenna pattern value projected onto the $\vec{r}$ surface's point, and

$$g(\vec{r}, t) = -\mathscr{R}\frac{e^{-2\pi j f_{L1} t}}{4\pi j R_0 R}e^{jK(R_0 + R)}\frac{q^2}{q_z}, \tag{2.14}$$

where $\mathscr{R}$ is the polarization sensitive field reflection coefficient (Eqns. 2.9

and 2.10), q_z is the vertical component of the scattering vector $\vec{q} = (q_\perp, q_z)$. More details of the received signal modeling are presented in [14].

Once the received signal is described, the next step is to model the acquisition process. Since $u(t)$ is a really weak signal whose power is well below the noise power, the autocorrelation properties of the C/A code (Fig. 2.5) may be applied to let the signal arise. This is done by correlation of the received signal with a local replica of the C/A code as it will be further seen (Eqn. 2.17). This cross-correlation is known as the waveform (in the delay domain τ) or delay-Doppler Map (DDM) when the Doppler shift domain is also considered. It is modeled as:

$$Y(\Delta\tau, \Delta f_D) = T_c \int D(\vec{r})\chi(\Delta\tau, \Delta f_D)g(\vec{r}, t_0)d^2\vec{r}, \tag{2.15}$$

where $(\Delta\tau, \Delta f_D)$ are the delay and Doppler difference with respect to the specular reflection point, T_c is the coherent integration time, and $\chi(\Delta\tau, \Delta f_D) \approx \Lambda(\Delta\tau)S(\Delta f_D)$ is the autocorrelation function of the C/A code (known as the Woodward Ambiguity Function or WAF in the SAR field), which is usually approximated by the product of a triangle and a sinc function in the delay and Doppler domains respectively. However, due to SNR maximization purposes, the DDM is normally integrated incoherently. Thus, the average power of the DDM can be statistically expressed as a function of the probability density function of the surface's slopes (P):

$$\overline{|Y(\Delta\tau, \Delta f_D)|^2} =$$
$$T_c^2 \int \int \frac{|\mathscr{R}|^2}{4\pi R_0(\vec{r})R(\vec{r})} D(\vec{r})\Lambda^2(\Delta\tau)S^2(\Delta f_D)\frac{q^4(\vec{r})}{q_z^4(\vec{r})}P\left(-\frac{\vec{q_\perp}}{\vec{q_z}}\right)d^2\vec{r}. \tag{2.16}$$

These Eqns. 2.15 and 2.16 are usually referred to as the Zavorotny-Voronovich model of the waveform/DDM [14].

At the time of actual acquisition, the complex DDM is computed through

the correlation of the received scattered signal with a local replica of the GPS code at several delay lags (τ) and Doppler shifts (f_D) around the central Doppler frequency:

$$Y(\tau, f_D) = \int_0^{T_c} s(t)a(t+\tau)e^{-j2\pi(f_{L1}+f_D)t}dt, \qquad (2.17)$$

where $s(t)$ is the received signal, $a(t)$ is the local replica of the GPS C/A code, (τ, f_D) are the delay and Doppler coordinates, f_{L1} is the frequency of the GPS L1 signal, and T_c is the coherent integration time (i.e. correlations are added in a complex way). However, in most applications, the so-called power-DDM is used, which is obtained by averaging series of N power DDMs during an incoherent integration time equal to $N \cdot T_c$:

$$\overline{|Y(\tau, f_D)|^2} = \frac{1}{N}\sum_{n=1}^{N}|Y(\tau, f_D)|^2. \qquad (2.18)$$

To retrieve the geophysical parameters of the scattering surface from the measured GNSS-R data, there are two main approaches:

- Fitting a model which is adjusted by the desired parameters to the measurements (traditional approach).

- Deriving some observable from the measurements that can be directly linked to the desired surface property (proposed by the PAU concept).

The concept of using an observable from the GNSS-R measurements to directly describe the sea state allows reducing the intense computation requirements that are needed when performing Monte-Carlo simulations to fit the measurements. However, experimental studies are mandatory to determine the empirical relationships among the desired geophysical parameter/s, and some property of the measured data.

The DDM is a 2-D function that can be regarded as the distribution of the scattered power over the glistening zone (i.e. surface zone that contributes

to the received scattered power), which is at the same time related to the mean square slopes (that parameterizes the brightness temperature changes according to [31]). Since it takes into account all the power contributions from the complete glistening zone, it contains more information (i.e. azimuthal dependence) than just the peak value, or the time domain waveform or cut of the DDM at f_D=0. For a specular surface (i.e. very calm sea) the DDM will be very similar to that obtained when acquiring the direct signal, except for a scaling factor due to the Fresnel reflection coefficient of the surface, and to propagation. However, the rougher the surface the more spread the DDM is. Indeed, a quantitative measurement of that DDM spreading should be thought as a direct descriptor of sea state.

The direct GNSS-R observable proposed in the framework of the PAU project is the volume of the normalized (maximum equal to one) Delay-Doppler Map (DDM) limited to a threshold above the noise level [19] (V_{DDM}). Thus, the integral of the DDM, after normalizing its peak value and setting a threshold to reduce the impact of noise (Fig. 2.6), can be related to the sea surface roughness (surface's mean square slope) [18].

In this PhD. Thesis, this approach will be explored in depth in order to assess its feasibility to seamlessly retrieve sea state using GNSS-R and, one step further, use it to perform the appropriate radiometric corrections to improve the quality of the final sea surface salinity product.
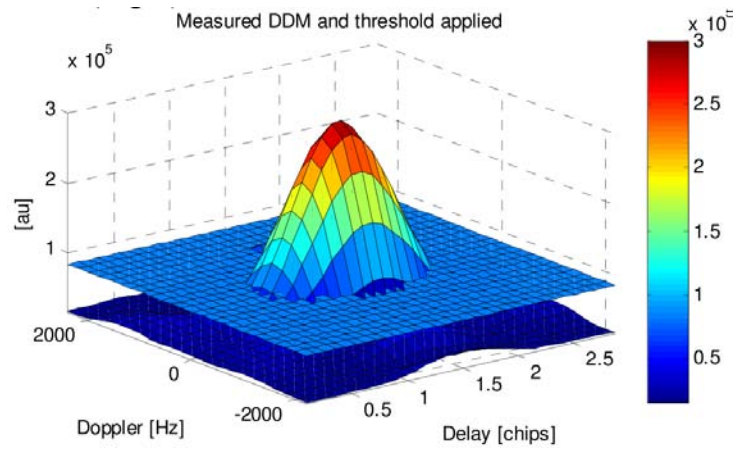
Figure 2.6: A measured (in a ground-based experiment) 1 s incoherently integrated DDM before normalization with a 20% threshold applied to compute its volume. Note that noise is well below this threshold.

Part I

GNSS-R Hardware Development

3

griPAU: The GPS Reflectometer
Instrument for PAU

3.1 Introduction

The evolution of GNSS-R techniques, has brought the need for new instruments that can conveniently process the received scattered GNSS signals in order to apply and test the new remote sensing approaches.

The simplest approach to the problem might be the direct digitalization of the received signals and the storage of the resulting data stream for off-line processing [32]. The main drawbacks of this technique are that: 1) the system's required data storage capacity is very high, and 2) the processing time is also high. Taking these two factors into account, it can be foreseen that a system such as this one, will prevent performing real-time acquisition.

In order to take the largest benefit of the available measuring time, it is necessary to develop an instrument that implements the signal acquisition and tracking, along with the required correlations to compute the DDMs in real time allowing further integration to reduce the data throughput. It has to be noticed that, to perform coherent integration for time periods longer than just 1 ms (GPS C/A code repetition period), the receiver must compute the DDMs in perfect real-time, so as not to introduce phase discontinuities

that would affect the final measurements.

In this context, the GPS Reflectometer Instrument for PAU (griPAU) has been completely developed as one of the main goals for the presented PhD. Thesis. griPAU is the appropriate GNSS-R receiver and signal processor for the PAU project. It is an instrument that computes one complex 24 x 32 points DDM in real-time every millisecond, and implements user-defined coherent and incoherent integration times.

The griPAU instrument has been developed from a previous operational version [33]. This former version has been redesigned applying state-of-the-art digital design techniques so as to improve and enhance the instrument's performance by achieving a strict synchronism and taking the largest benefit of the available hardware resources in the Field Programmable Gate Array (FPGA). The main elements of the system that have been replaced or modified are listed in Table 3.1 along with the resulting system improvements.

In this chapter the griPAU instrument is presented, focusing in the two main aspects of the development:

- Section 3.2 explains the instrument's principle of operation, and describes its architecture focusing on each sub-system.

- Section 3.3 presents the main trade-offs that have been considered along the development process in order to achieve the optimal instrument performance considering the available resources (mainly in the digital hardware part).

Table 3.1: Main system modifications and their resulting improvements/ enhancements

Former instrument version	griPAU	Improvement / enhancement
Software control unit	Dedicated hardware finite states machine (FSM) control unit	
Input data buffer based on two RAM memories sharing a bus	Input data buffer based on a dual-port RAM memory using a single bus	Strict synchronism level achieved and improved stability and sensitivity.
-	Single and ultra-stable clock reference	
Linear polarization antenna for the direct signal path	Right hand circular polarization (RHCP) antenna for the signal path	
Delay estimation algorithm only used I component of the direct signal	Delay estimation algorithm enhanced to use both in-phase (I) and quadrature (Q) components of the direct signal	Improved robustness in front of multi-path and signal fading.
-	Revised synchronism of the delay estimation algorithm	Reduced delay estimation time from 16 ms to 5 ms.
-	Revised and optimized resource usage	DDM size increased from 16x16 to 24x32 points.
Fix antenna for the reflected signal path	Automatic tracking of the specular point over the scattering surface	Scatterometric measurements not affected by the antenna radiation pattern modulation.

3.2 Instrument description

3.2.1 Principle of operation

The purpose of the griPAU instrument is to compute the DDMs in real time (Eqn. 3.1). To compute then, the scattered signal received has to be correlated with a local replica of the GPS C/A code for several values of the delay (τ) and Doppler offsets (f_D):

$$DDM(\tau, f_D) = \int_0^{T_c} s(t)a(t+\tau)e^{-j2\pi(f_{L1}-f_D)t}dt, \qquad (3.1)$$

where $s(t)$ is the received signal, $a(t)$ is the local replica of the GPS C/A code, (τ, f_D) are the delay and Doppler coordinates, and T_c is the integration time. If no noise is assumed, the received direct signal $s(t)$ has the form:

$$s(t) \approx \sqrt{P_{C/A}}N(t)a(t)cos\left(2\pi(f_{L1}+f_D')\right) \\ + \sqrt{P_P}N(t)P(t)sin\left(2\pi(f_{L1}+f_D')\right), \qquad (3.2)$$

where $N(t)$ is the navigation message, $P(t)$ is the precise GPS code, $P_{C/A}$ is the transmitted power of the in-phase component, P_P is the power of the quadrature component, and f_D' is the Doppler shift induced by the relative motion of the transmitter and the receiver. While in generic GPS receivers the navigation message is decoded, in the griPAU's implementation it is not, so changes in the navigation bit cause π-rad phase jumps that will dramatically reduce the resulting SNR [34]. This effect limits the maximum coherent integration time to 20 ms which is the period of the navigation bit if no further corrections are applied (see Section 4.5).

As it can be seen in Eqn. 3.2, the received signal undergoes a Doppler shift as it propagates from the transmitter to the scattering surface and then to the receiver. To correctly track the reflected signal the system has to be able to

detect and correct this Doppler shift. As griPAU has been designed to work in ground based applications at low heights, the Doppler shift induced in the reflected signal is the same as the induced in the direct one, and depends only on the transmitter motion. For an airborne or spaceborne receiver, the actual Doppler shift could be computed from geometric considerations using the navigation solution derived by the up-looking GPS receiver (Eqn. 3.3).

$$f_{D,xy} = \frac{\vec{V_t} \cdot \hat{n_i} - \vec{V_r} \cdot \hat{n_s}}{\lambda}, \tag{3.3}$$

where $f_{D,xy}$ is the Doppler frequency shift related to the specular reflection point, $\vec{V_t}$ is the transmitter velocity vector, $\vec{V_r}$ is the receiver velocity vector, $\hat{n_i}$ is the incidence direction unitary vector, $\hat{n_i}$ is the scattering direction unitary vector, and λ is the electromagnetic wavelength (see Chapter 2 for the geometry definition). Taking into account the maximum relative radial velocity among a ground fixed point and an orbiting GPS space vehicle, the minimum range of Doppler frequencies that the receiver has to be able to compensate for is -5 kHz $< f_D <$ 5 kHz [35].

griPAU's signal processor is embedded in a Xilinx Virtex 4 FPGA device using the VHDL hardware description language. The computed DDM size is limited by the available hardware resources. This implies that the Doppler shift of the received signal, as well as the time delay of its code have to be a-priori known so as to center the computing window around the DDM peak. The total number of correlators that can be implemented with the available resources not only determines the final DDM size, but also its resolution, as it will be discussed in detail in Section 3.2.3.

The implemented architecture has a total of three signal paths: one chain for the reflected signal, and two for the direct signal to estimate the Doppler shift and the time delay. For simplicity, a commercial Trimble GPS receiver is used to obtain the Doppler shift of the direct signal, as well as other geometry parameters such as the elevation an azimuth of the satellite to be tracked. However, the estimated time delay from the commercial GPS is not

good enough, and it is not updated frequently enough to keep track of the reflected signal. The time delay is then estimated from the direct signal by means of a circular correlation algorithm implemented in the signal processor:

$$R_{s_D,a} = IFFT\left(FFT(s_D) \cdot FFT^*(a)\right) \tag{3.4}$$

where s_D is the direct signal down-converted to baseband and with the Doppler shift corrected, and a is a local replica of the GPS C/A code. Using a circular cross-correlation based algorithm has the main advantage that it works in a continuous single acquisition state so no extra time is needed prior to start tracking the signal's delay. This allows the estimator to get locked very fast and quickly recovers if it gets unlocked. Other approaches, such as the early-prompt-late correlation algorithm [35] require an acquisition state prior to tracking which can last unacceptably long times for the presented application. Nevertheless, these other approaches demand more hardware resources to implement the required control logic.

Once the time delay and Doppler shift of the direct signal are known, these parameters are used to center the DDM window. Then, according to the DDM size and resolution, the (τ, f_D) coordinates are specified in samples and Hz respectively. The coordinates of each DDM bin are used to generate a set of signals which are the local replicas of the baseband C/A code with the corresponding time delays and Doppler shifts. These signals are then correlated with the down-converted reflected signal so as to obtain the resulting DDM.

3.2.2   Antenna and RF front-end

The selection of the down-looking antenna is a trade-off between directivity and beamwidth. On one hand the directivity must be high enough so as to increase the SNR, and on the other hand the beam must be wide enough so as to observe the whole glistening zone (i.e. area from where there are

significant contributions of the scattered power) without introducing much distortion due to windowing. During the design phase, the extent of the glistening zone for a height of 400 m, and a moderate wind speed of 10 m/s was estimated to be on the order of 200 m. This result leads to a beamwidth around 20°. The antenna had to be left hand circularly polarized (LHCP) as it is the main polarization of the right hand circular polarized (RHCP) signal after scattering on the surface.

The antenna used in the implementation of griPAU is an array of 7 microstrip patches. This antenna has a measured beamwidth of 22°, a main beam efficiency of 90.5%, and a gain of 16.2 dB (Fig. 3.1).

To avoid the modulation of the measurements by the antenna radiation pattern as the GPS satellite moves, the down-looking antenna is mounted on an automatic positioning system that performs a dynamic tracking of the specular reflection point over the observation surface. This effect is observed in Fig. 3.2 where the antenna was still and the measured DDM peak for different satellite passages is represented as a function of the elevation angle. Moreover, in Fig. 3.2 the antenna has been pointed towards the specular reflection point when the satellite elevation was 26°, and kept fixed during the capture. It is seen how the DDM peak, which is proportional to received power, decreases to half its maximum value (i.e. -3 dB) as elevation goes down from 26° to 15° which corresponds to a movement of half the beamwidth from the antenna boresight.

Once the direct and reflected signals have been collected, they are amplified, filtered, down-converted, and sampled. The receiver used in griPAU is a modification of the one developed in the frame of the PAU project [36]. This receiver has two chains with 120 dB gain, 2.2 MHz bandwidth, the output signal is centered at an intermediate frequency of 4.309 MHz, and the sampling frequency is 5.745 MHz.
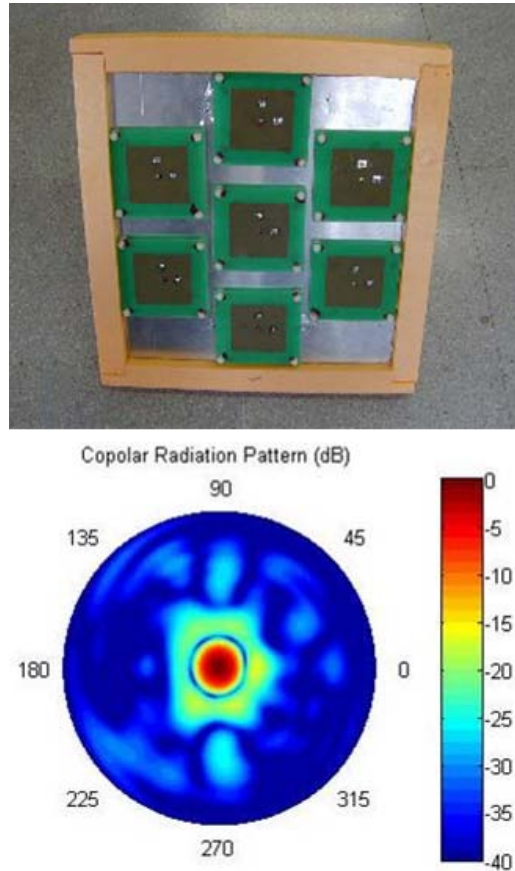
Figure 3.1: (Top) Down-looking antenna used to measure the reflected signal and (bottom) its measured radiation pattern.

3.2.3 Signal processor

The griPAU instrument signal processor (Fig. 3.3) has been designed and implemented using the digital hardware resources of a Xilinx Virtex 4 FPGA. The design has been carried out to achieve two main objectives:

1. To take the maximum benefit of the available hardware resources.

2. To keep a strict control of all the timing and synchronism rules so as to implement a system as stable as possible.
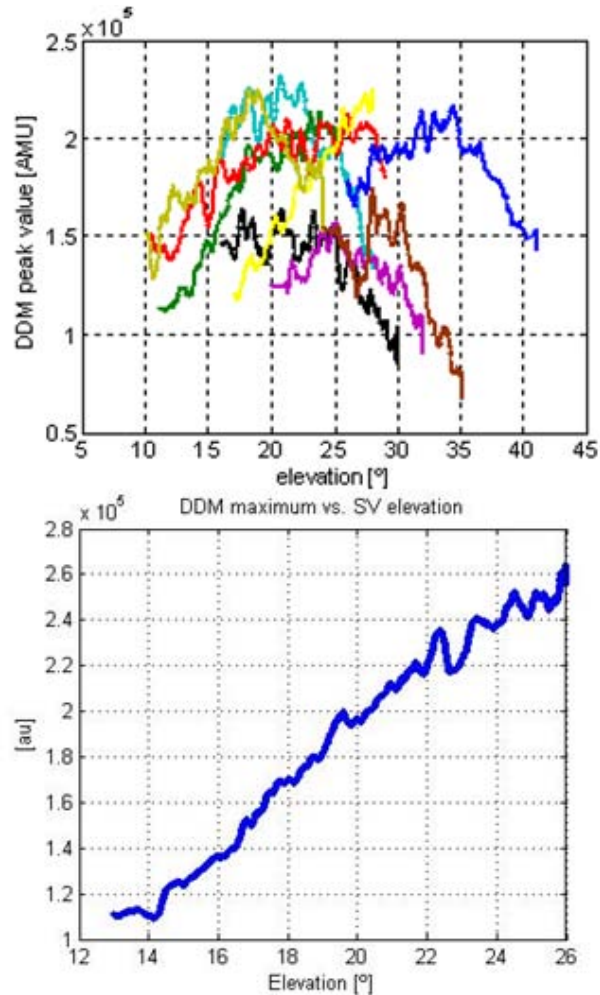
Figure 3.2: (Top) Antenna pattern modulation for different satellites vs. elevation angle, (bottom) DDM peak is modulated by the antenna radiation pattern when the antenna is kept in a fixed position. Quick oscillations are due to multi-path in the cliff, Speckle noise, and geophysical variability of the observables.

A high level block diagram of the signal processor implemented for the griPAU instrument is shown in Fig. 3.4, and a picture of its actual implementation is shown in Fig. 3.5. The griPAU signal processor has three signal paths: two for the direct signal and one for the reflected. One of the direct signal chains is connected to the Trimble GPS receiver to obtain the signal's

Figure 3.3: griPAU signal processor.

Doppler frequency offset. The second direct signal chain is used by the signal processor embedded in the FPGA to estimate the signal's delay after the RF front-end, sampling, and demodulation. Once the delay and Doppler offsets are known, the DDM generator core uses the demodulated, and sampled reflected signal to compute the Delay-Doppler Map. Since the FPGA clock frequency is much higher than the sampling frequency, hardware reuse techniques can be used to dramatically reduce the hardware resources needed, or alternatively, to increase the size of the computed DDM with the same hardware resources.

The up- and down-looking signal paths to be processed are conditioned and sampled at 8 bits with a sampling frequency of 5.745 MHz. Since the IF is 4.309 MHz, bandpass sampling can be used, and the signal is centered at a digital frequency of 0.25. At this digital frequency the tones needed to I/Q demodulate the input signals can be expressed using only two bits, and the digital I/Q demodulation can be performed very efficiently by using simple logical functions instead of multi-bit multipliers [37].

Once the signals have been I/Q demodulated, a digital low-pass filtering stage has been implemented to eliminate undesired high frequency components. This filter has also been designed to use the lowest possible amount

of resources. To achieve that, an IIR filter topology with only power of two coefficients has been designed so that multiplications and divisions are transformed into left-shift and right-shift operations avoiding again the use of resource-consuming multipliers and dividers [37]. At this point the main processing starts. To take advantage of hardware reuse techniques, the data acquired during a basic integration time (1 ms) is stored, so it can be read several times. The main blocks that allow this technique to be successfully dealt with, are the control unit and the data buffer (Fig. 3.4).

The hardware control unit is based on a finite states machine (FSM) built to replace the software control used in previous versions to have a tight control of the timing of the hardware reuse technique. One fourth of the complete DDM is computed at a time, and using the same hardware, the four DDM quadrants are serially computed during four time slots. All this process takes place in 1 ms which is the duration of the C/A code and the basic coherent integration time. Replacing the software control unit by a FSM has improved the synchronization of the four quadrants allowing to significantly increase the size of the DDMs (from 16 x 16 to 24 x 32 bins in the Virtex4 implementation) leading to a more stable system. Figure 3.6 shows two DDM captions: in the first one a synchronism problem has occurred,
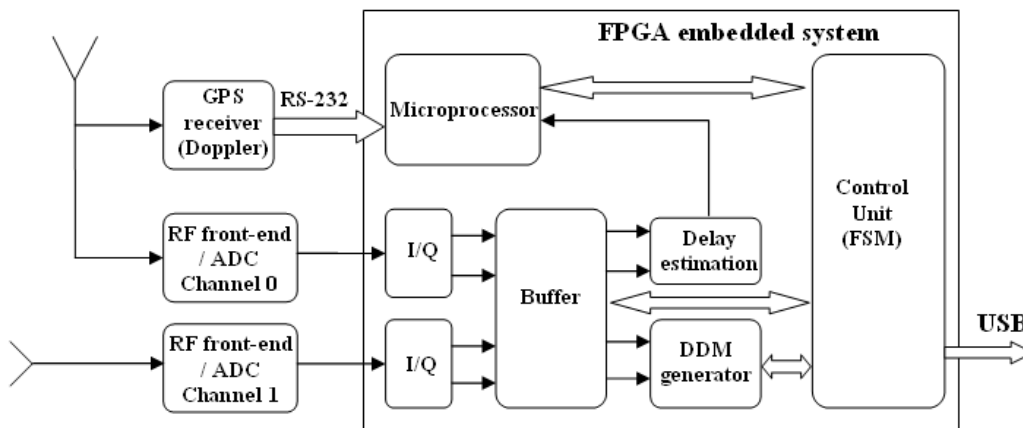
Figure 3.4: Block diagram of the griPAU signal processor.

Figure 3.5: Inside view of the griPAU signal processor.

while in the second one, computed with the described architecture, all the DDM parts are always perfectly aligned due to the high reliability of the hardware synchronism of the control unit.

Also a new data buffer has been implemented to avoid memory swapping and minimize timing problems. This new buffer is based on a dual-port RAM memory which has a depth twice the size of the IQ data sampled in 1 ms. With this implementation, the memory is divided in two zones, so when one half is written by the writing port, the data stored in the other half is read by the reading port and processed. Each millisecond the two halves exchange their roles without any physical memory swapping and data is properly updated.

The delay estimation algorithm has also been optimized leading to a reduction of the refresh time from 16 to 5 ms, allowing griPAU to track signals even in high dynamics scenarios. The delay estimator core is basically the one implemented in previous versions [33], using a FFT approach (Eqn. 3.4). Due to the zero-padding needed to adapt the number of samples (5745 samples) of the data to the next power of two (8192 samples), two correlation peaks appear. The griPAU implementation has improved this core performance
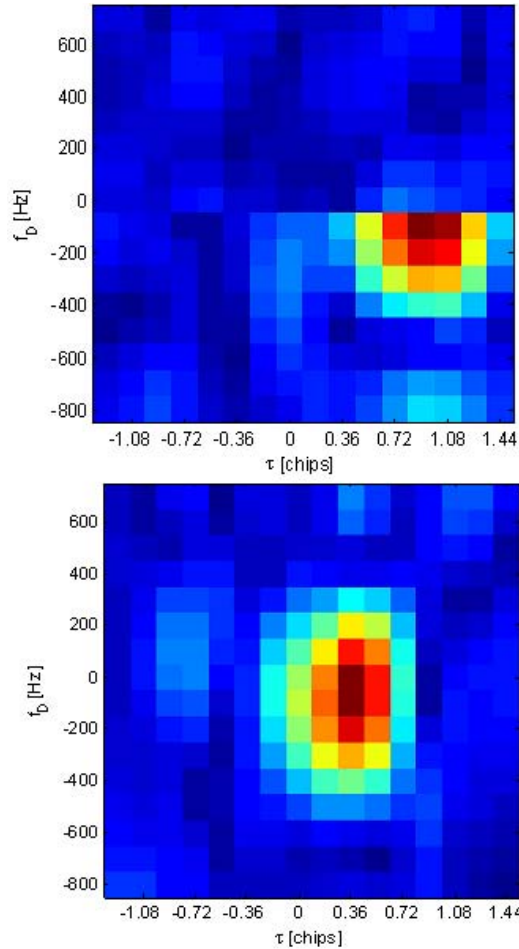
Figure 3.6: Sample 1 ms DDMs: (top) synchronism problem occurred during the acquisition translates in misalignment of the four quadrants (hardware reuse), and (bottom) synchronism problem solved.

avoiding peak detection errors by applying a threshold to check whether the returned delay is a valid one or if it corresponds to the secondary peak of the cross-correlation. If so, the known distance between peaks (in samples) is subtracted to get the correct delay value.

Figure 3.4 shows that the signal processor implements also a microprocessor. In the implementation of griPAU this microprocessor has been relegated just to interface the Trimble GPS, and to perform floating-point operations

that would consume too many resources if implemented in hardware. Notice that all the timing and synchronism responsibilities have been transferred to the FSM control unit, for improved robustness in front of the uncontrolled timing inherent to operative systems.

The last block of the griPAU signal processor is the DDM generator core which has remained essentially the same as in previous versions of the instrument [33]. This block generates each of the four DDM parts at a time (implementing the required correlation operations) and is controlled by the control unit so as to reuse the hardware.

3.2.4 Clocking scheme

When designing griPAU, the stress was put on preserving the phase coherence among all the systems clocks to prevent undesired decorrelation effects. The clocking policy has been redefined using an oven-controlled 10 MHz stabilized reference (Fig. 3.7), and the FPGA-built processor has been modified to work with the 103.41 MHz clock (instead of the original 100 MHz one), which is a direct multiple of the sampling frequency.

The final clocking scheme divides the single 10 MHz stable reference in two branches: one branch is used as the RF front-end reference for the phase-locked loops, and the other one is doubled in order to be the reference
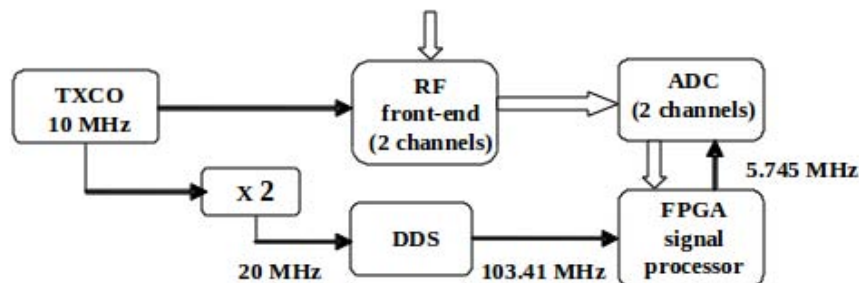
Figure 3.7: griPAU clocking scheme.

of a Direct Digital Synthesis (DDS) device that generates a very accurate 103.41 MHz clock reference for both sampling and processing in the FPGA. The accurate sampling frequency and perfect synchronism avoid artificial delay drifts caused by different chip lengths among the sampled signal and the local replica of the C/A code generated in the processing step, resulting in a very high stability.

3.2.5 Data output

Every 1 ms, griPAU computes one complex DDM of 24 x 32 bins. Each bin is a complex number with its real and imaginary parts quantified with 32 bits, which leads to a total data output rate of 6.14 Mbps. This throughput is delivered to an external PC via an USB interface.

Using a graphical interface executed in the external PC, the user can control the instrument configuration (satellite to be tracked, capture length, etc.) and the computed data can be stored in raw format or further averaged by means of selectable coherent/incoherent integration times.

3.3 Instrument performance and trade-offs

3.3.1 Delay estimation

A study has been undertaken to improve the final estimation error rate (i.e. increasing the signals SNR) related to the direct signal path used for delay estimation. Sample results of the three approaches tested are shown in Fig. 3.8. The first delay estimator uses only the in-phase signal (I). The second one uses both the in-phase and quadrature (Q) components of the direct signal to improve its robustness in front of noise, multi-path, as well as preventing signal fading due to phase rotation. This has the drawback of increasing the hardware resources (multipliers) needed if only the in-phase component is used. The third and more efficient approach works with both

I/Q components and uses a wide-beam RHCP antenna instead of a single linear polarization one to improve the robustness of the signal in front of undesired reflections and multi-path.

To validate the improvements implemented in the delay estimation algorithm, real GPS direct signal captions have been performed. Real signal has been used to test the system when all the effects, such as undesired reflections and multi-path, are present. Figure 3.8 shows the delay estimation performance as a function of the algorithm implemented.

The performance is nearly perfect for the last configuration. It is seen that, if the error rate is defined as the number of errors per number of measurements, it is reduced from 6.7% when only the I component of the signal is processed, down to 1.7% when both I/Q components are processed, using all the signal's available power, and down to a nearly negligible value of 0.03% when multi-path is avoided by using a RHCP antenna.

The fast linear evolution (two complete code lengths in 1 min) of the delay is due to the inaccuracy of the sampling frequency which causes a difference between the chip lengths of the received signal and the local replica. This artificial delay evolution is overcome when the new clocking scheme is applied since the clock reference given by the DDS allows the signal processor to generate a very accurate sampling frequency. With the ultimate griPAU implementation, only the true delay evolution is observed as in Fig. 3.9.

3.3.2 Delay-Doppler Map size and resolution

Although using a very accurate sampling frequency and avoiding potential artificial delay drifts, the residual difference between the actual sampling frequency and the theoretical one considered at processing, still causes some measurements variance due to the variable DDM discrete sampling points (i.e. the delay estimation is not able to distinguish subsample variations).

This effect is deterministic, and the relationship of the final DDM amplitude variation with the resolution is monotonically decreasing, so the vari-
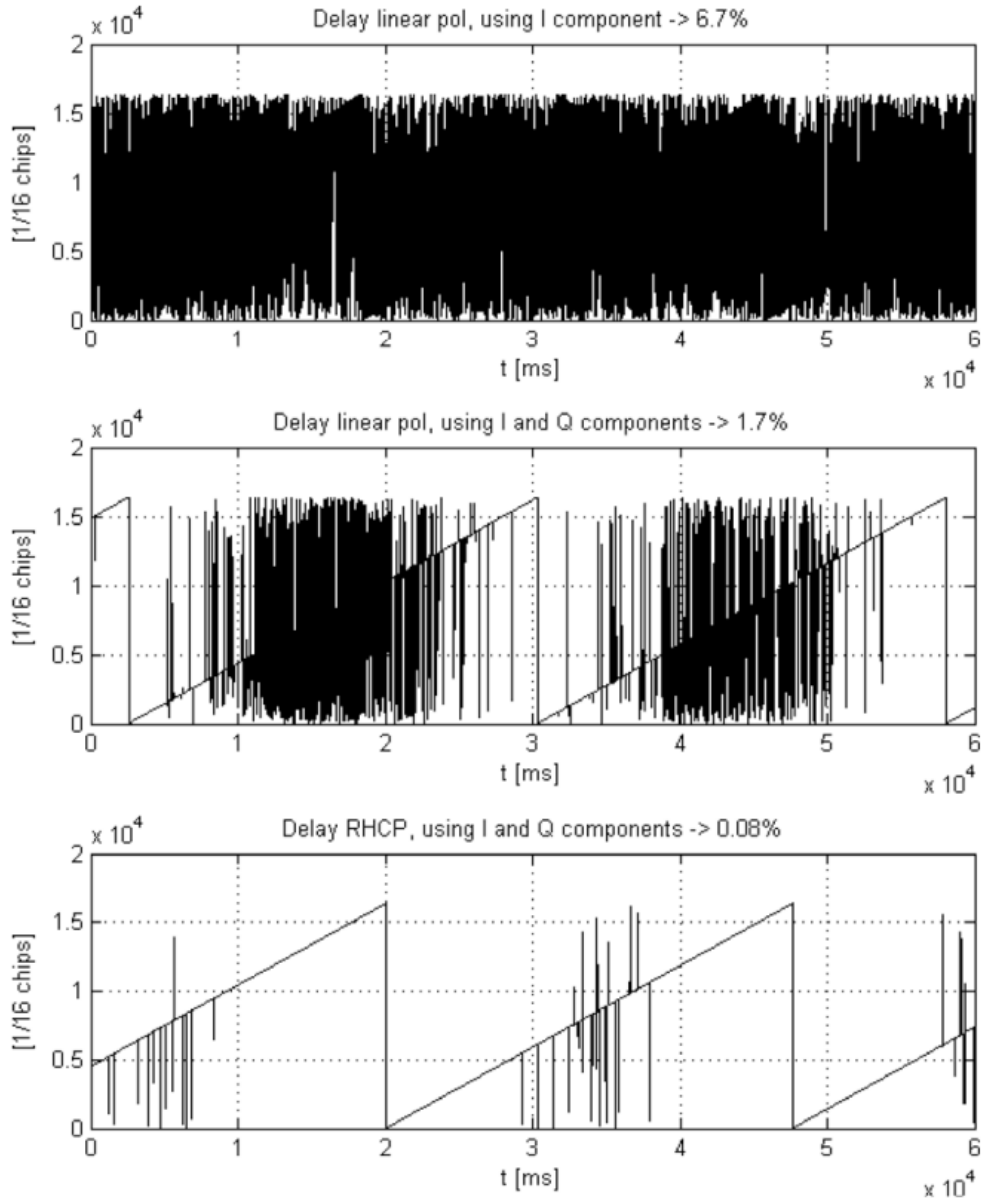
Figure 3.8: Delay estimation performance for different estimator algorithms, (top) using only the in-phase (I) component (6.7% error rate), (center) using in-phase and quadrature components (1.7% error rate) and, (bottom) using I and Q components and a RHCP antenna to receive the direct signal (0.03% error rate).
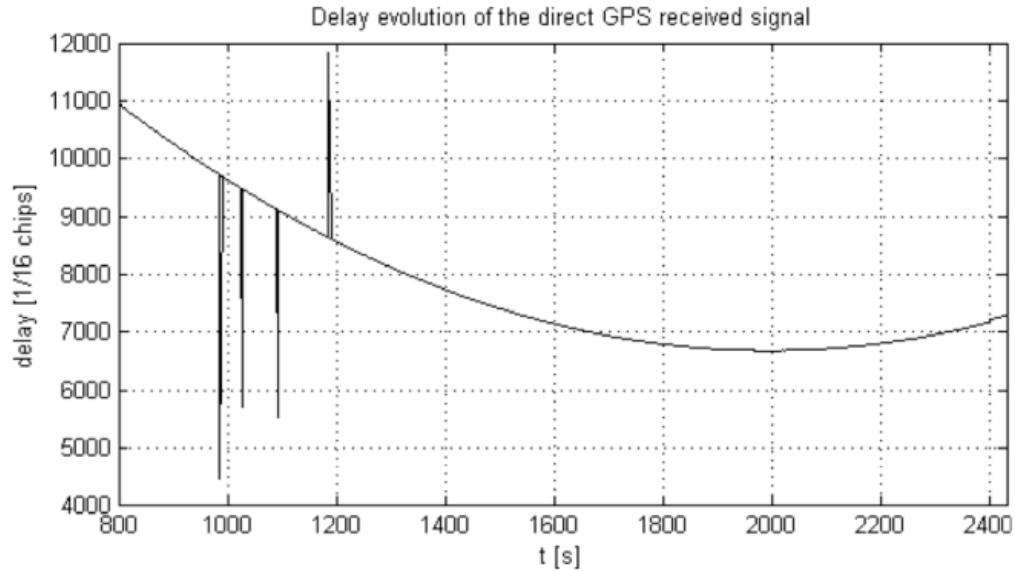
Figure 3.9: Delay evolution measured using the new clocking scheme. Error rate is nearly negligible.

ance can be reduced by reducing the DDM cell size in the delay dimension. Also, if the DDMs are not to be truncated, the total DDMs size has to be increased. In the design and implementation of griPAU, the system has been re-arranged in order to take advantage of all available FPGA resources, so the total DDM size has been increased from 16 x 16 points up to 24 x 32 points allowing to compute the DDMs with a delay resolution as low as 0.5 samples (0.09 chips) (Fig. 3.10), so the measurements' variance due to shifts in the DDM peak's position in delay, in amplitude as well as in normalized DDM volume is significantly reduced. The relationship among these variances and the delay resolution has been studied.

Using a GPS synthetic signal three series of DDMs have been computed configuring the instrument with three different delay resolution values (2, 1, and 0.5 samples corresponding to, 0.36, 0.18, and 0.09 chips, respectively) while keeping the Doppler resolution constant (200 Hz) (Fig. 11). The effect of variable DDM sampling points is clearly observed, both in the normalized
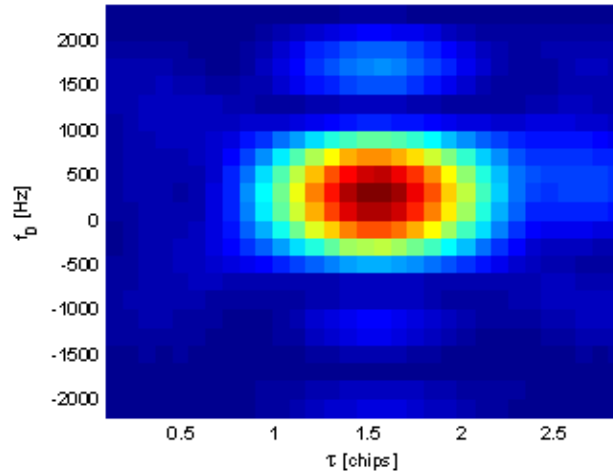
Figure 3.10: Sample 24 x 32 points, 0.09 chips resolution, 1-ms DDM measured over the ocean surface from a 382 m height.

volume and the maximum value when a coarse resolution of 2 samples is used. These values present an evolution between two extreme values which correspond to the DDM sampled at the true maximum and 2 samples away from it. This effect is reduced when 1 sample resolution is used and it can be nearly neglected when the DDM is computed with 0.5 samples resolution. With this fine resolution, the measurement's variance is only due to the system's noise. As it can be appreciated in Fig. 3.11, the normalized DDM volume and the maximum module present (in a stronger way when using poor resolutions) a kind of triangular modulation originated by the linear evolution of the time delay between the true DDM peak and its adjacent sample.

3.3.3 Instrument sensitivity and stability

When operating in the normal mode, 1 s incoherently integrated DDMs are measured. Setting the DDM resolution to 200 Hz in Doppler and 0.5 samples (0.09 chips) in delay, the measurements (Fig. 3.12) have a very small standard deviation (0.9% of the DDM peak value and 0.03% of the normalized
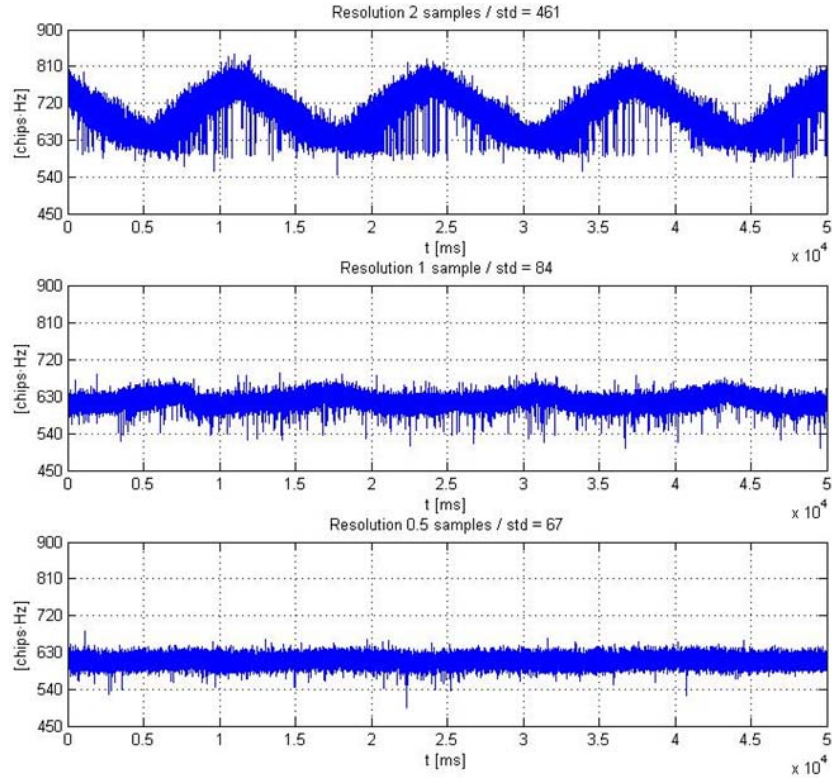
Figure 3.11: DDM normalized volume vs. DDM resolution measured using a synthetic GPS signal to avoid multi-path and other error sources: (top) $\Delta\tau = 2$ samples (0.36 chips), (center) $\Delta\tau = 1$ sample (0.18 chips) and, (bottom) $\Delta\tau = 0.5$ samples (0.09 chips).

DDM volume maximum value equal to one, units [chips · Hz]). This error determines the reflectometer's sensitivity (i.e. the minimum DDM peak or the minimum normalized DDM volume variations that can be detected or measured by the instrument).

In order to evaluate the systems performance concerning the correlation time of the coherently integrated measurements a synthetic GPS direct signal has been used. As this signal is simply a GPS C/A code up-converted to RF, its correlation with the local replica should be constant. However, system inaccuracies and noise cause some residual decorrelation of the measured
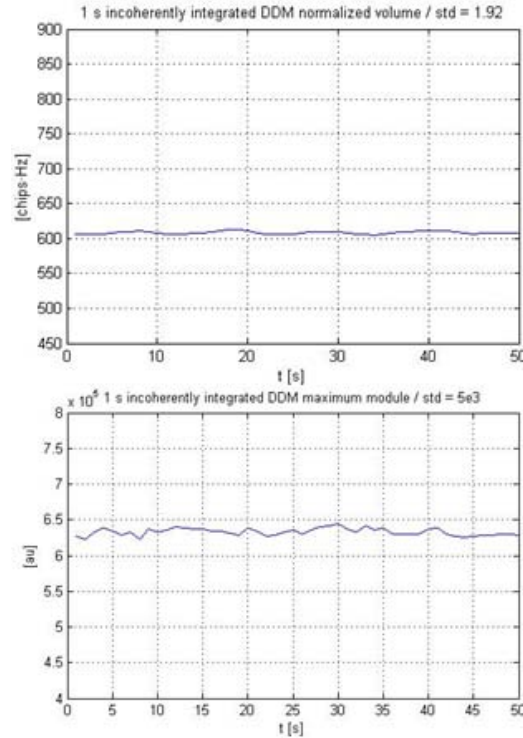
Figure 3.12: DDM 1-s incoherently integrated (top) volume (relative error = 0.03%) and, (bottom) peak module (relative error = 0.9%).

DDMs when coherent integration is performed. To evaluate this parameter (i.e. DDM decorrelation time due to the instrument), the evolution of the DDMs maximum is studied. Results are shown in Fig. 3.13. For instance, if the time that the measurements decorrelate to a 90% of the maximum is considered, the instrument can perform coherent integration up to 100 ms (Fig. 3.13). Taking into account that at L-band the sea correlation time is estimated to be of the order of tens of milliseconds at most [38], the griPAU can be used to the study of physical phenomena of the sea surface that require coherent integration or phase information. This is a significant improvement result of the large effort carried out in the systems synchronism, sampling frequency accuracy, and improved clocking scheme.
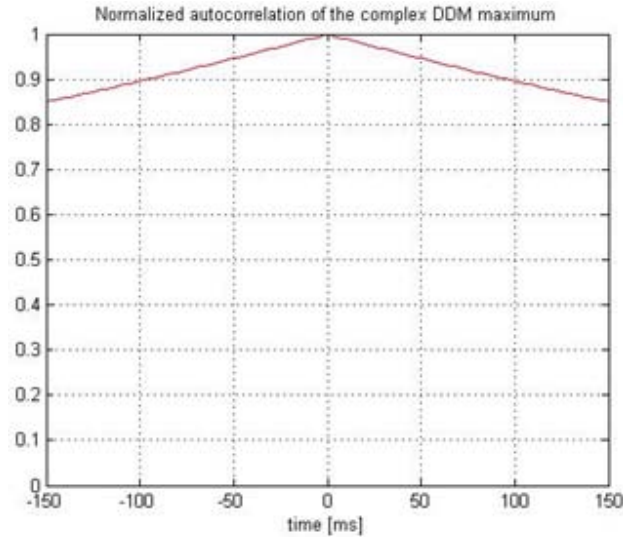
Figure 3.13: Normalized autocorrelation of the complex DDM maximum.

3.4 Conclusions

Emerging new GNSS-R remote sensing techniques have led to the need of
implementing adequate and robust receivers. In this chapter the design and
implementation of the GPS Reflectometer Instrument for PAU (griPAU) has
been presented, as well as some relevant measurements showing its perfor-
mance.

The griPAU computes high resolution complex Delay-Doppler Maps in
real-time. The computed DDMs are 24 x 32 points with configurable delay
and Doppler resolution as well as selectable coherent (minimum = 1 ms,
maximum = 100 ms for correlation loss $\Delta\rho < 10\%$) and incoherent (minimum
of one coherent integration period and not limited maximum, typically ≤ 1 s)
integration time. Its design has focused on achieving an extremely stable and
sensitive instrument making the best use of the available digital hardware
resources of a FPGA, and taking an exquisite care of synchronism and phase
coherence. In particular, the stability of the instrument allows to coherently

80

integrate up to more than 100 ms, which is longer than the ocean correlation time at L-band, thus enabling the system to perform deeper studies about the ocean. Moreover, the achieved instruments sensitivity (DDM peak relative error = 0.9% and DDM volume relative error = 0.03% @ T_i = 1 s) will improve the quality of the results for geophysical parameters retrieval.

This implementation has resulted in a fully operational real-time complex DDM GNSS-R instrument that has already been used in field experiments over sea and land, with very promising results.

Part II

Experimental Results

4

ALBATROSS 2009: The Advanced L-BAnd emissiviTy and Reflectivity Observations of the Sea Surface field experiment

4.1 Introduction

The Advanced L-Band emissivity and Reflectivity Observations of the Sea Surface (ALBATROSS) field experiments were conducted in 2008 [18] and 2009 [39], to test the assumptions that:

1. It is possible to use direct GNSS-R observables as a sea-state descriptor.

2. GNSS-R observables can be directly used to correct the measured ocean L-band brightness temperature, without neither numerical emission/scattering models, nor ocean surface spectra models.

The aim was to acquire an extensive dataset of GNSS reflections collocated in time and space with radiometric brightness temperature data under

the largest range of sea-roughness conditions. This implied using ground-based instruments for long-term observation periods that, in both 2008 and 2009, involved one month long experiments.

The main result out of the ALBATROSS 2008 experiments was the assessment of the first hypothesis. However, both radiometric and GNSS-R datasets could not be well-linked mainly due to miss-collocation of the measurements in time and space.

A further step was done with the ALBATROSS 2009 experiment, where the experimental setup and deployed instruments were carefully improved to target the assessment of the second hypothesis. Moreover, the use of that time's recently developed griPAU signal processor (see Chapter 3) allowed to collect a complementary GNSS-R dataset that consisted of 1-ms complex DDMs in order to test new techniques using coherent measurements.

Furthermore, the acquired data also served to improve our understanding of the performance and behavior of GNSS-R techniques by testing new approaches. Thus, the ALBATROSS experiments were an opportunity to consolidate and enhance our knowledge on the ocean scattered GNSS-R signals, and on their processing techniques.

This chapter describes the ALBATROSS 2009 field experiment and presents its main results following this scheme:

- Section 4.2 presents the experimental setup including the instrumentation used and the available ground truth data for the ALBATROSS 2009 experiment

- Section 4.3 describes the different GNSS-R observables studied as direct sea state descriptors and shows their interrelation, as well as their relationship with the available wind speed ground-truth.

- Section 4.4 shows the relationships found between the measured brightness temperature variations caused by the sea state and GNSS-R derived observables.

- Section 4.5 presents the study performed on the sea correlation time from the acquired coherent GNSS-R data.

4.2 The ALBATROSS field experiment

4.2.1 Measurement site

The ALBATROSS field experiments were carried out at *El Mirador del Balcon* in the island of *Gran Canaria* (Canary Islands, Spain) (Fig. 4.1). This site is a scenic viewpoint located at the North-West coast of the island at a height of approximately 382 m above the sea surface. It is important for the measurement setup to be at such height in order to be able to cover the largest range of delays for the reflected signal and clearly separate the direct and the reflected signals. The experiments were performed during the months of June 2008 and 2009. The area is driven by the Trade Winds (Fig. 4.2), which are strong and moist, and induce a significant variability in the sea state. This place is also very adequate for the experiment as, because of the volcanic origin of the island, the ocean bathymetry increases very quickly away from the shore, and the sea waves reflected in the shore line bounce towards the West, leaving the wave-front clear from perturbations, so quasi-open sea conditions are found relatively close to the coast. From the measurement site it is possible to observe the sea surface from a height of 382 m and a window of 90° from West to North in azimuth, and from 0° to 45° in elevation.

4.2.2 Instruments overview

4.2.2.1 GPS Reflectometer Instrument for PAU (griPAU)

The griPAU instrument (see Chapter 3) is a real-time GPS reflectometer developed from a first version of the PAU projects reflectometer used in ALBATROSS 2008 [18]. The implementation of griPAU has improved the systems stability and the DDM resolution and size. The instrument acquires and processes the GPS C/A code at the L1 frequency (1575.42 MHz) and

(a)

(b)

Figure 4.1: a) Map of the Gran Canaria Island with the experiment site marked with an arrow; and, b) View of its North-West coast where the Mirador del Balcon is located.

computes in real time 32 x 24 points DDM with a resolution of 0.09 chips in delay and 200 Hz in Doppler. griPAUs antenna is an hexagonal 7-patch array with a -3 dB beamwidth of 22°. Two acquisition modes were defined for the experiments: continuous acquisition of single 1-ms complex DDMs, and 1-s incoherently averaged 1000 x 1 ms complex DDMs.
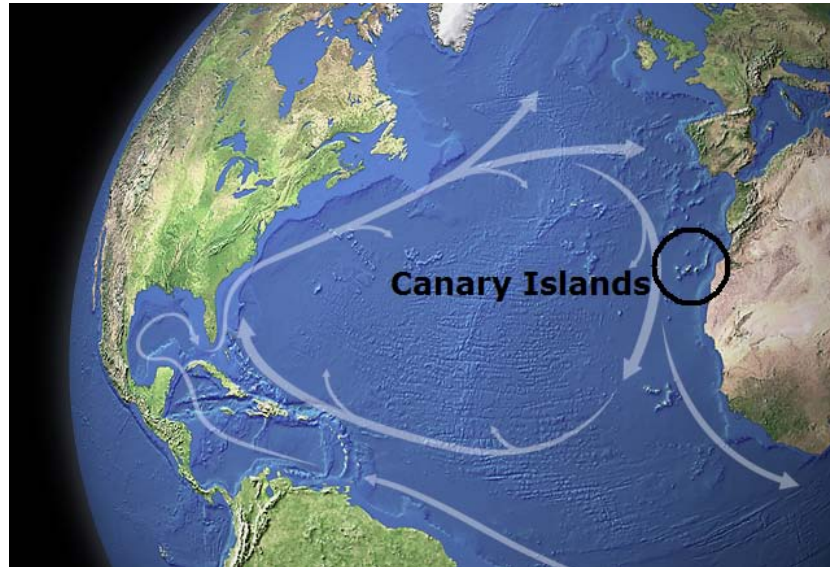
Figure 4.2: Trade Winds flow over the Canary Islands.

4.2.2.2   L-band Total Power Radiometer

A dual-polarization L-band total power radiometer (TPR) was designed and implemented to acquire radiometric data exactly collocated with the GNSS-R data for the ALBATROSS 2009 field experiment. This radiometer has a center frequency of 1.413 GHz and a bandwidth of 50 MHz. The basic integration time is 1 s (to match the 1 s incoherently averaged DDMs) and the input is sequentially switched between an internal hot load, vertical polarization (V-pol), and horizontal polarization (H-pol) antennas. The sky is used as a cold load to calibrate the measurements and the achieved (measured) radiometric sensitivity (at 1 s integration time) is 0.15 K (Fig. 4.3). The instrument has a good thermal stability (≤ 0.34 K/°C), but in order to compensate for gain and offset drifts a frequent hot and cold load calibration was performed every 5 minutes, during which the thermal drift is below 0.2°C.

4.2.3 Measurement setup and ground truth data

The main purpose of the ALBATROSS 2009 experiment was to collect an extensive dataset of collocated radiometric and GNSS-R data. To do so, the antennas of both instruments, griPAU and the TPR had identical designs (except for the central frequency and polarization), and were mounted in an automated positioning system on a mast tip that tracked the instantaneous position of the specular reflection point of the GPS signal over the sea surface. With this setup, GNSS-R data was not affected (modulated) by the antenna radiation pattern (i.e. the specular reflection always reaches the antenna by its boresight) and both the radiometric and GNSS-R data were perfectly collocated in time and space as both footprints were exactly coincident. The antenna patterns of both instruments are identical with a half-power beamwidth of 22°, which results in an approximately 600 m x 200 m footprint when projected onto the observation surface considering an elevation of 30°. In Fig. 4.4 the tower with the positioning system holding the antennas can be observed.
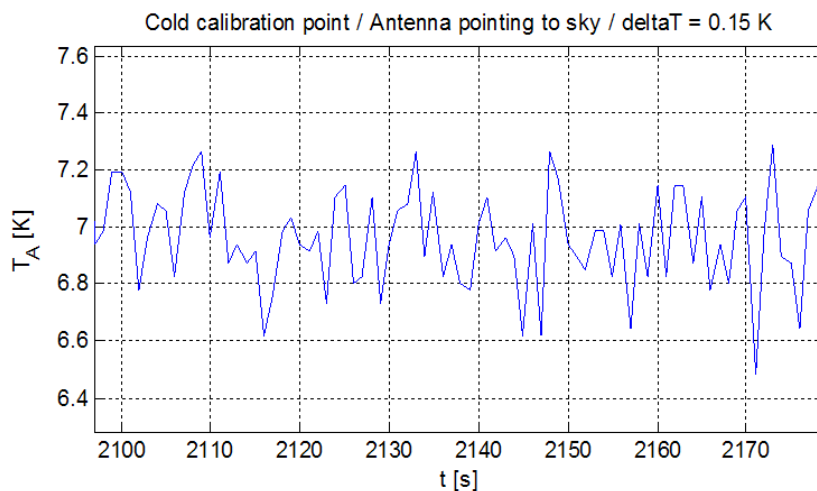
Figure 4.3: Detail of the calibrated antenna temperature when pointing to the sky. A radiometric resolution of $\Delta T = 0.15$ K is achieved with 1 s integration time.

In order to gather the appropriate ground-truth dataset, two buoys (Fig. 4.5) were moored in front of the experiment site 500 m away from the shore during both 2008 and 2009 experiments. The first one, developed by the Universidad de Las Palmas de Gran Canaria (ULPGC), carried a SeaBird SBE-37 thermo-salinometer and provided surface temperature and salinity measurements once per hour. The second buoy was a Triaxys mini intended to measure the directional wave spectrum to derive sea state information. Due to technical problems, the Triaxys buoy did not work during the whole 2009 experiment presented here, and an alternative ground-truth dataset was used for the sea state information, from a Spanish Harbor Authority buoy, moored 15 km North of the experiment site in front of the Agaete village, providing a single wind speed (WS) measurement averaged along 20 minutes each hour. As it is seen in Fig. 4.6, there was a high variability in terms of WS during the 20 effective days of experiment. The lack of exactly collocated sea state information was one of the main problems at the time of processing the re-
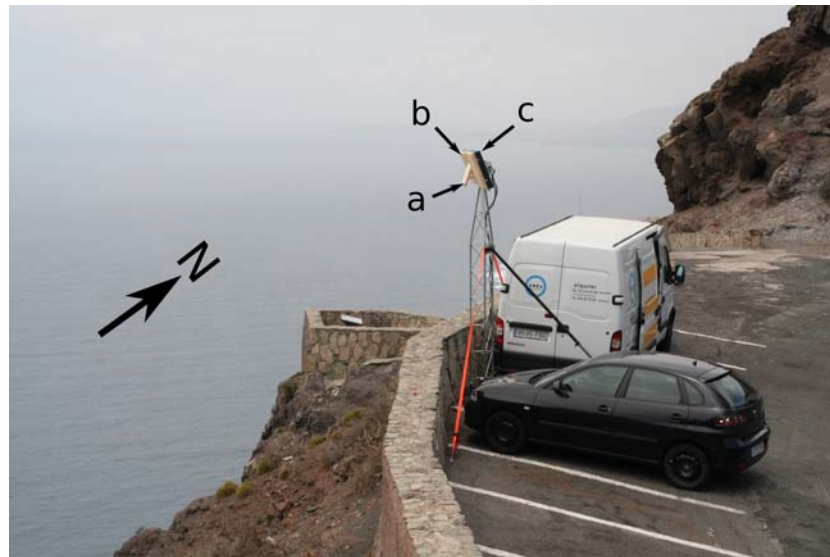
Figure 4.4: Measurement setup at the experiment site. a) griPAU's direct signal antenna, b) griPAU's reflected signal antenna, and c) L-band radiometer.

flectometer and radiometer's measurements, and when relating them to sea state, but this did not affect the derivation of direct relationships between them, which were perfectly collocated in time and space.

4.3 GNSS-R sea state direct descriptors

The possibility to derive a direct descriptor of the sea state using GNSS-R would avoid the use of any particular ocean surface spectrum and emission/scattering models. The first step of this work has been to use the AL-BATROSS data to study the relationship of different GNSS-R observables

(a)

(b)

Figure 4.5: a) Directional wave spectrum Triaxys buoy; and b) recovering the ULPGC salinity buoy at the end of the experiment.
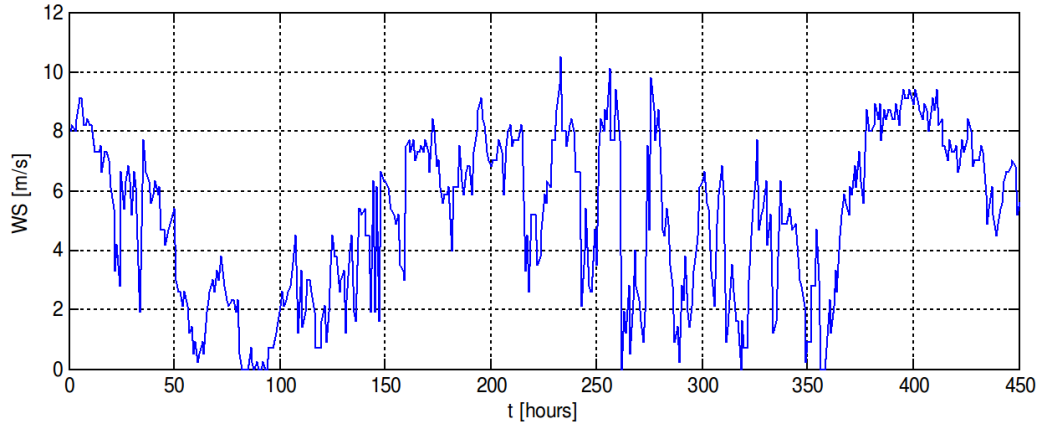
Figure 4.6: Wind speed record from the Spanish Harbor Authority buoy during the time of the experiment (from June 9th to July 2nd in 2009).

with the sea state/roughness. These observables are based on quantifying the DDM or waveform changes (related to the spread of the scattered power) caused by different sea surface roughness. Three observables have been studied: the volume of the normalized DDM, the scatterometric delay and the length of the waveform's tail.

The first descriptor considered is the normalized volume of the DDM [19] (V_{DDM}) derived by integrating the modulus of the DDM 2-D function (see Section I and eqn. 2.18)) after normalizing its peak value to 1, and setting a unique threshold above the noise level for all data to minimize the impact of the noise (Fig. 2.6). In this study the threshold has been experimentally set to 0.2. The volume of the normalized DDM is a robust observable proposed within the framework of the PAU project. It was observed to be linked to the sea state when processing the ALBATROSS 2008 dataset that included collocated ground-truth data from the Triaxys buoy [18]. The second parameter under study is the scatterometric delay [40] (ρ_{scatt}) defined as the time difference between the waveforms peak and the specular reflection delay which is the maximum of the waveform's first derivative [41] (Fig. 4.7). This parameter is related to the power spreading of the waveform due to the sea

surfaces roughness. The third observable used in this study is the length of
the waveforms tail (τ_{tail}) defined as the time that it takes to decay from its
maximum value to that value divided by e. The tail of the waveform contains information on the scattering surface [15], and the waveform's power
spreading.

As the three observables considered are supposed to be linked to the same
physical phenomena (i.e. power spreading of the scattered signal due to the
ocean's surface roughness), they have been cross-plotted to test this assumption. In Fig. 4.8 the three resulting plots are shown. As it can be seen, V_{DDM}
and τ_{tail} show a high correlation level with a computed Pearson correlation
coefficient $r = 0.74$. On the other hand, ρ_{scatt} seems not to be well correlated
with any of the other two observables. To follow with the study, the three
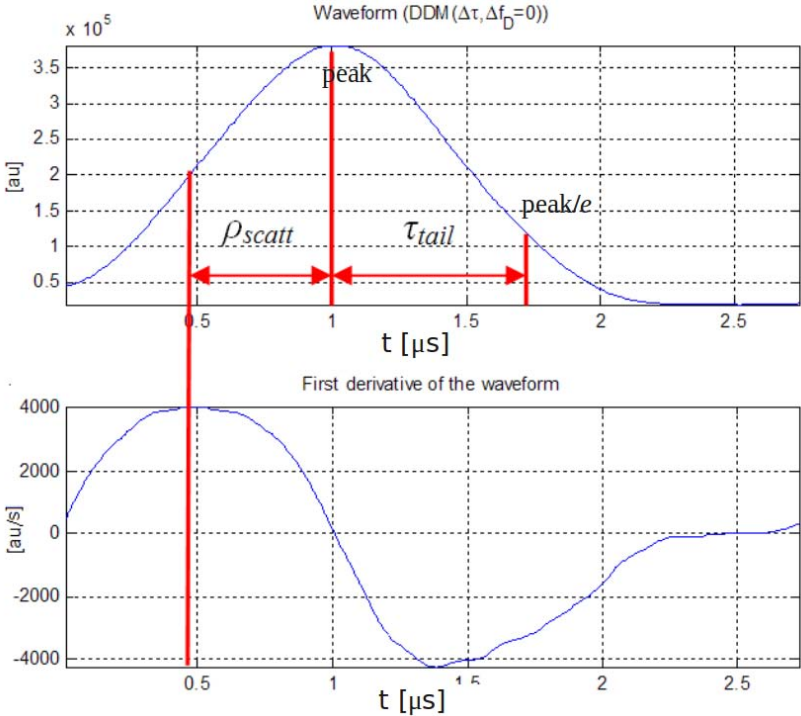
Figure 4.7: A measured 1 s incoherently integrated waveform (expressed in arbitrary units [au]) and its first derivative with the definition of ρ_{scatt} and τ_{tail}.

95

parameters have been plotted against their corresponding WS measurements in Fig. 4.9. It has to be noted that the high dispersion of the plots in Fig. 4.9 is due to: 1) the different time scales of the measurements (griPAU takes a measurement each second, while the WS is an average measurement over 20 minutes every hour); and 2) the fact that the WS data is not spatially well collocated with respect to the griPAU GNSS-R measurements. It can be observed though, that in Fig. 4.9a and Fig. 4.9b, V_{DDM} and τ_{tail} have a certain level of correlation with the WS measurements ($r = 0.47$ and $r = 0.35$, respectively). However, ρ_{scatt} appears not to be correlated at all with WS, which may be due to the fact that the leading edge of the waveform is not very sensitive to sea state for low height observations (i.e. most of the power concentrates in a few delay lags), and that the derivative is intrinsically a noisy operator.

These results indicate that V_{DDM} is the GNSS-R observable that best describes the sea state, probably because it provides information related to the whole glistening zone. However, this observable has the drawback that it requires the highest computational cost as the full DDM has to be computed instead of just a waveform ($DDM(\tau, f_D = 0)$). On the other hand, τ_{tail} is computationally the simplest one of the three considered, while it also presents an acceptable correlation with WS measurements.

(a)

(b)

(c)
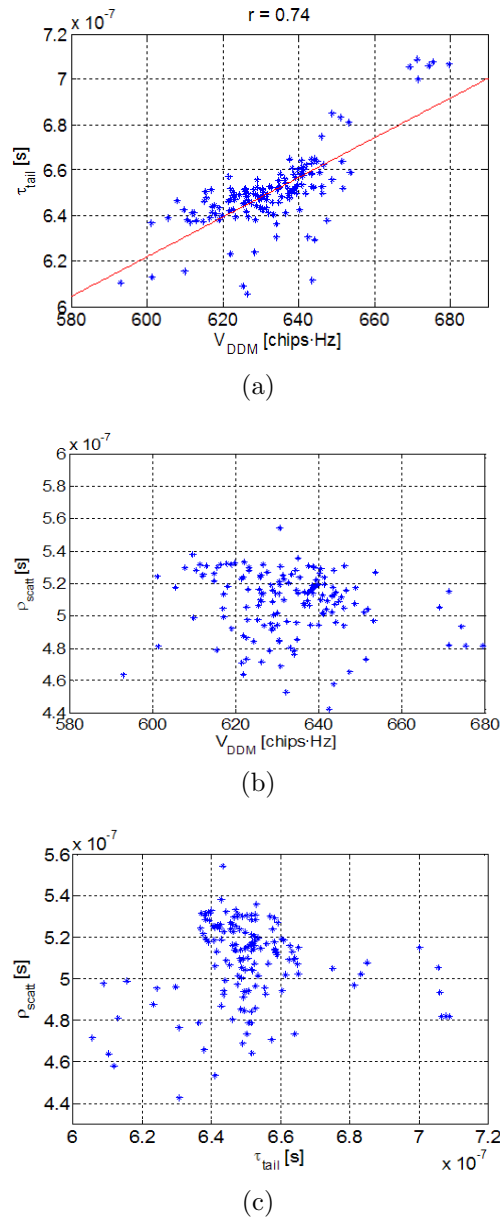
Figure 4.8: Relationship among the three considered GNSS-R observables: a) Length of the waveform's tail vs. normalized DDM volume, b) scatterometric delay vs. normalized DDM volume, and c) scatterometric delay vs. length of the waveform's tail.
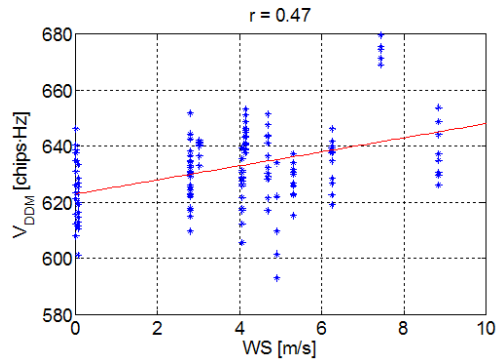
(a)
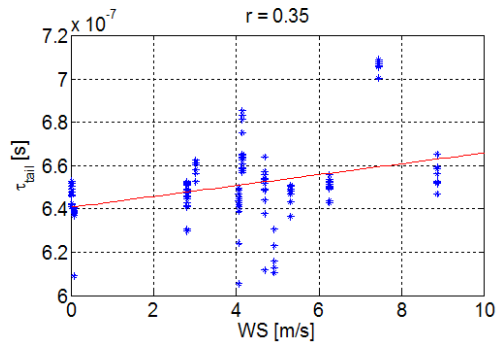
(b)
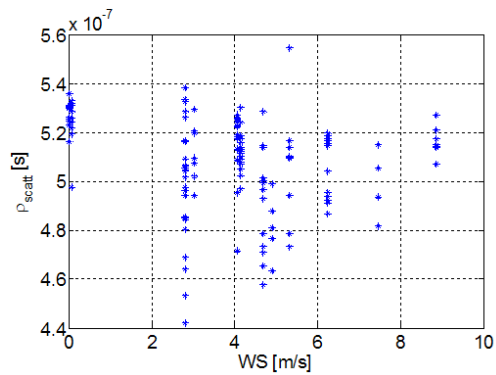
(c)

Figure 4.9: Relationship among the three considered GNSS-R observables and the
ground truth WS data: a) Normalized DDM volume vs. WS, b) Length of the
waveform's tail vs. WS and, c) Scatterometric delay vs. WS.

4.4 GNSS-R observables relationship with the brightness temperature variations

Once it has been seen that it is possible to directly relate some GNSS-R observables to the sea surface roughness avoiding the use of scattering models, the next step towards the correction of the SSS retrievals for the sea state effect is to link the GNSS-R observable variations to the brightness temperature variations caused by the sea state. The goal is to perform this step also directly, thus avoiding the use of sea surface spectrum and scattering/emission models. In Fig. 4.10 a typical capture of radiometric measurements is shown along with the predicted values by the small slope approximation (SSA) model [42] using the Elfouhaily et al. Spectrum multiplied by two as in [27], considering the mean 2 m/s WS measured by the Spanish Harbor Authority buoy during that particular radiometric capture, and the Klein an Swift permittivity model for sea water [23]. It is seen that the measured radiometric data is in good agreement with this model even for incidence angles up to ≈70°. Discrepancies observed for incidence angles below 55° are due to the radiation from the cliff picked up by the antenna's secondary lobes. Even though the absolute value is affected, the instantaneous changes are not.

To undertake this part of the study, a differential multi-angular analysis has been carried out. It is known that brightness temperature sensitivity to sea state is dependent on the incidence angle [27], so radiometric data has been binned by incidence angle in 5° steps. The not-so-steep slope of the cliff introduced uncontrolled offsets to the radiometric measurements that could not be totally calibrated. However, instantaneous brightness temperature variations could still be related to the sea state within periods of constant temperature and salinity. These $\Delta T_B(t)$ variations are computed by subtracting from the measurements their mean value for each incidence angle and each caption. Then, all the computed $\Delta T_B(t)$ are linked to the time-collocated GNSS-R observables variations ($\Delta V_{DDM}(t)$ and $\Delta \tau_{tail}(t)$), and the

slope of the scatter plot of these data has been computed in incidence angle bins of 5° to derive the sensitivity of $\Delta T_B(t)$. As an example, Fig. 4.11 shows the scatter plot of $\Delta T_B(t)$ vs. $\Delta V_{DDM}(t)$ at H-pol corresponding to the incidence angle bin from 55° to 60°. This process has been applied to all the data angular bins and polarizations to derive the sensitivity as a function of the incidence angle. The obtained curves are presented in Fig. 4.12 with respect to the normalized DDM volume change and in Fig. 4.13 with respect to the length of the waveforms tail change.

It is worth comparing these results to the WISE measurements [27] (Fig. 2.3). Figures 4.12 and 4.13 show that the brightness temperature variations induced by the sea state effect can be directly linked to GNSS-R observables such as the V_{DDM} or the τ_{tail}. These sensitivity curves, $\Delta T_B/\Delta\tau_{tail}$ and $\Delta T_B/\Delta V_{DDM}$, present a similar behavior to that observed when the WS is used as sea state descriptor (Fig. 2.3): at H-pol the sensitivity is positive and increases with increasing incidence angle, while at V-pol sensitivity presents
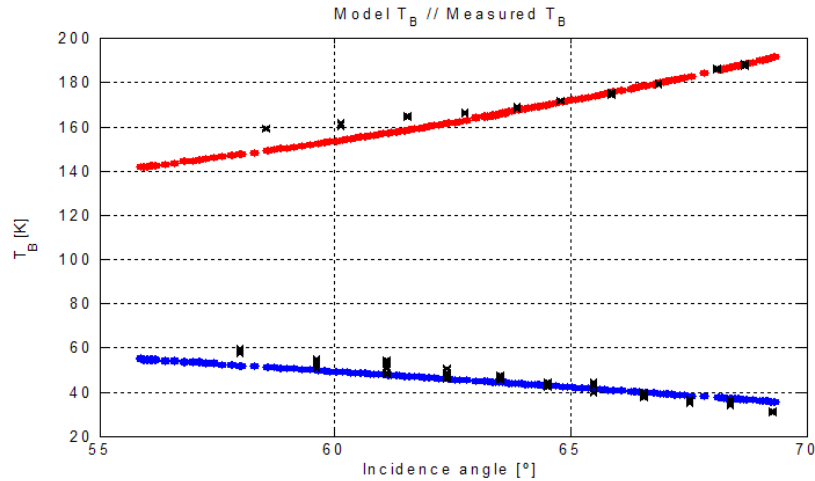
Figure 4.10: Measured (black crosses) and predicted brightness temperature for V-pol (red) and H-pol (blue) from the SSA model [42] using the Elfouhaily et al. Spectrum multiplied by two as in [27], considering the mean 2m/s WS measured by the buoy during the radiometric capture.
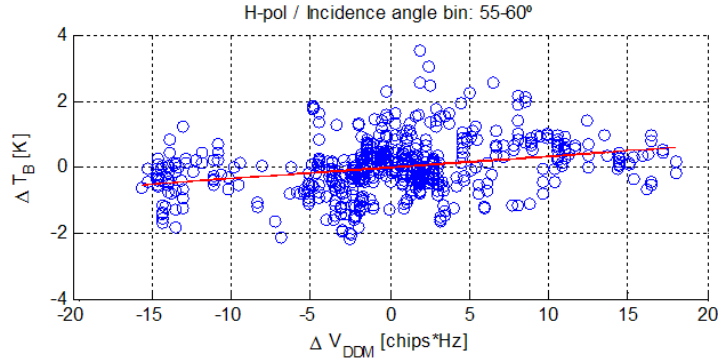
Figure 4.11: Linear fit (r=0.29) of the 1s data corresponding to the 55-60° incidence angles bin for H-pol.

a null around 55° incidence angle and decreases. Nevertheless, while the sensitivity trends are quite similar when considering V_{DDM} or τ_{tail}, when using this last observable the dispersion is larger as the confidence intervals (i.e. error bars) are larger. This is due to the fact that V_{DDM} is a more robust observable since it contains integrated information over the whole glistening zone, while τ_{tail} only takes into account the portion of the glistening zone that has a null Doppler shift. However, the trade-off among performance and computational cost of each GNSS-R observable has to be considered.

These resulting sensitivity curves show the feasibility of linking radiometric and GNSS-R data for brightness temperature correction for the sea state effect. Still, the ground-based measurement setup is not the optimum scenario in terms of GNSS-R measurements sensitivity to sea surface roughness. This fact is thought to be the main source of dispersion of the obtained sensitivity curves. Moreover, phenomena such as detected RFI at H-pol and multi-path in the cliff (which is also more important for H-pol), cause the final derived curves to have an unexpected behavior as the trend change that seems to occur at H-pol around 65-70° incidence angles. To derive an actually usable relationship among radiometric and GNSS-R measurements for real observation geometries (i.e. air/space-borne) data collected for these cases will need to be further analyzed. In this line, the measurements of the

airborne CoSMOS experiment are studied in Chapter 5 of this PhD. Thesis.
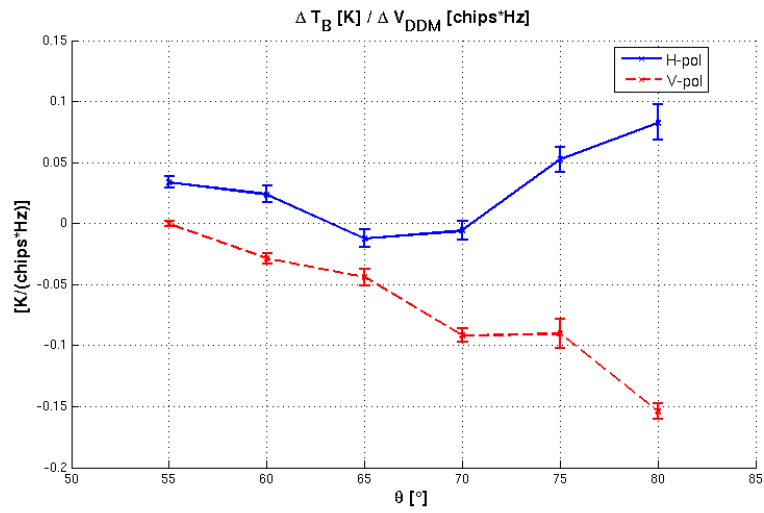
Figure 4.12: Retrieved sensitivity of the measured brightness temperature to sea surface roughness described by V_{DDM} for V-pol and H-pol.
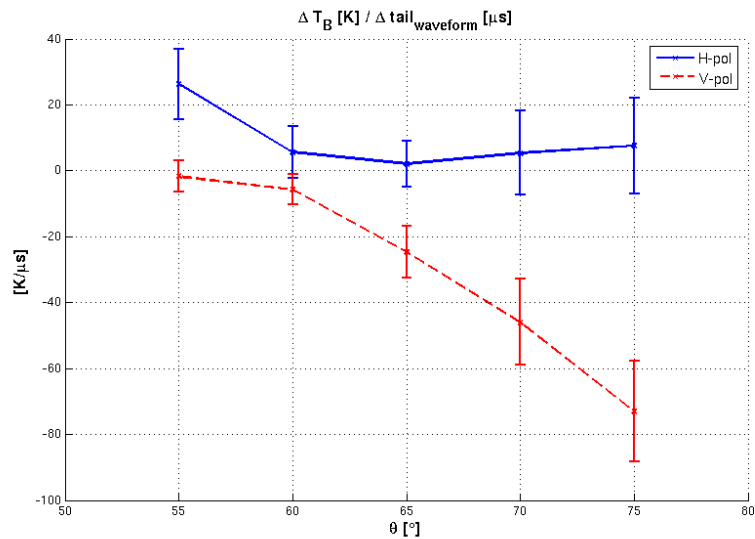
Figure 4.13: Retrieved sensitivity of the measured brightness temperature to sea surface roughness described by τ_{tail} for V-pol and H-pol.

4.5 Experimental determination of the sea correlation time

4.5.1 Methodology

The main purpose of the ALBATROSS 2009 experiment was to explore the feasibility of using radiometric/GNSS-R sensor synergies for sea state corrections. Furthermore, 1 minute-long series of 1 ms complex DDMs (coherent data) were collected to study the limits of GNSS-R techniques to process ocean measured data. More particularly, the maximum usable coherent integration time (T_c as defined in Section I) was envisioned as a key parameter to be accounted for. In ground-based and mid-height airborne observations, the overall SNR of the received scattered GNSS signals can be improved by means of coherent integration as the power scattered by the surface under observation is not spatially filtered by the Doppler bandwidth resulting from the coherent integration process (Doppler filtering effect [14, 17]). The maximum usable T_c depends on the sea correlation time (i.e. the time that the surface can be considered to be frozen so all the scattering contributions phases are assumed to be constant), which is a function of the sea state. It is the sea correlation time that limits this integration time and thus, the achievable SNR improvement.

To perform the study of the sea correlation time (detailed in [34]), the coherence time of the complex 1-ms measured DDM peak after accounting for the geometric variations has been used as an indicator of the scattering surface correlation time. This correlation time (τ_s) has been defined as the time that the modulus of the normalized autocorrelation function of the DDM's complex peak takes to decay down to $1/e$. The autocorrelation function of the DDM has been computed after correcting for the navigation bit polarity inversion effect which is clearly seen as phase jumps in Fig. 4.14. Otherwise, the navigation bit changes in the GPS message introduce pseudo-random

π rad phase jumps that cause the received signal to lose coherence quickly,
so the desired information is masked as the autocorrelation function rapidly
decays in 20 ms (Fig. 4.15a), which is the navigation bit period. In Fig. 4.15b
the same autocorrelation functions are shown after correcting for these phase
jumps due to the changes of the navigation message bit. As it can be seen, the
time they take to decay is inversely proportional to the WS so the retrieved
sea correlation time τ_s is a function of the sea state, as expected.

4.5.2 Results

The dataset used in this study comprises the one minute acquisitions of
complex basic DDMs that were taken in a stable time period relating to WS.
The ground-truth data available from a buoy moored in the open sea 18
km in front of the experiment site consists of one 20 minutes averaged WS
measurement per hour, so only stable periods have been selected so as to
consider the WS measurement confident enough to be a valid sample of this
study. A WS measurement has been considered to be from a stable period of
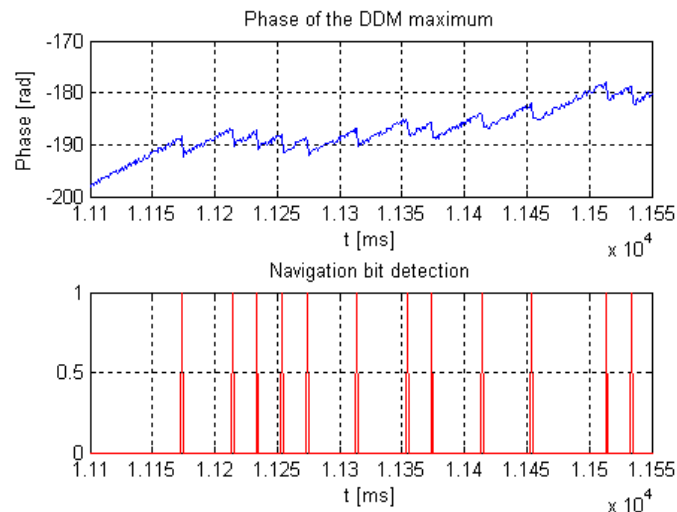
Figure 4.14: Phase jumps in the peak of the DDM caused by the navigation bit
polarity inversion.
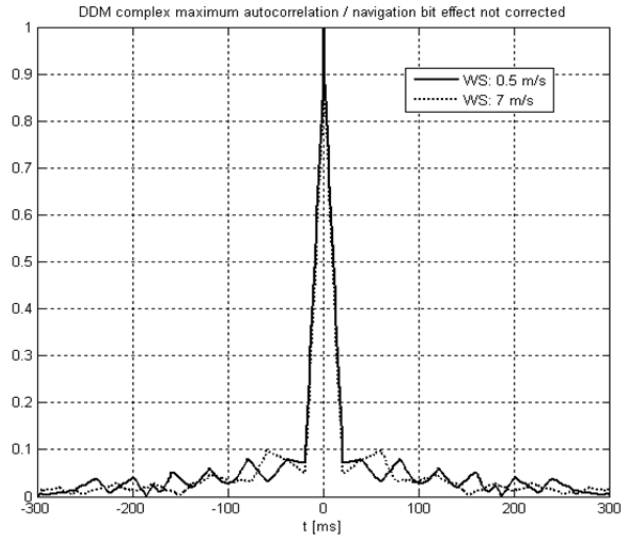
(a)
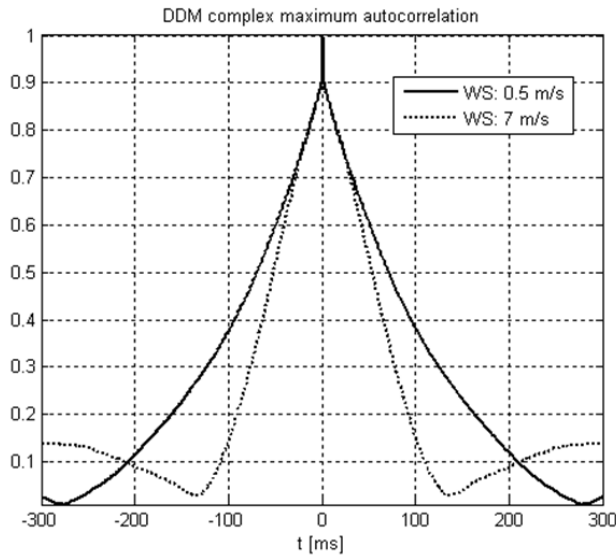
(b)

Figure 4.15: Autocorrelation of the complex DDM peak: a) navigation bit polarity inversion not corrected for: sea correlation time information is masked; and b) after correcting for the navigation bit effect, sea correlation time becomes evident as the autocorrelation function gets narrower for larger wind speeds.

time when the measurements from one hour before and after were the same WS value ± 1 m/s.

In Fig. 4.16 the retrieved sea correlation times are shown as a function of their corresponding WS measurements. In a qualitative way, a relationship among them is observed since the measured correlation time decreases as WS increases (i.e. sea surface gets rougher). To quantitatively evaluate this result, a model that parameterizes the sea correlation time as a direct function of the WS has been used [43]:

$$\tau_s = 3\frac{\lambda}{WS}erf^{-1/2}\left(2.7\frac{\rho}{WS^2}\right), \qquad (4.1)$$

where λ is the electromagnetic wavelength (0.19 m at $f_{L1} = 1575.42$ GHz), and ρ the resolution of the observed pixel. In the case of this study, the observed pixel has been considered to be the footprint of the antenna projected over the sea surface as a first approximation (although in very calm seas, the glistening zone sizes reduces to the first Fresnel reflection zone). Taking into account that the elevation angle range of the considered measurements is 14° to 30°, and that the observation height for the ALBATROSS 2009 measurement setup is 382 m, an antenna footprint size range from 340 to 686 m is obtained (antenna beamwidth of 22°). For these pixel size values, and for moderate wind speeds below 12 m/s, as the values observed in this study are, the model in Eqn. 4.1 for the sea correlation time can be simplified to 4.2 due to the saturation of the *erf* function. This model has been plotted along with the measurements in Fig. 4.16.

$$\tau_s \approx 3\frac{\lambda}{WS}. \qquad (4.2)$$

For WS above 4 m/s, the model predicts well the observed τ_s ($RMSE = 22.5$ ms). However, at the lower WS the model tends to fail and overestimates the sea correlation time, since this model fails below 2 m/s, and it is only considering the wind speed, which is not a complete sea-state descriptor,
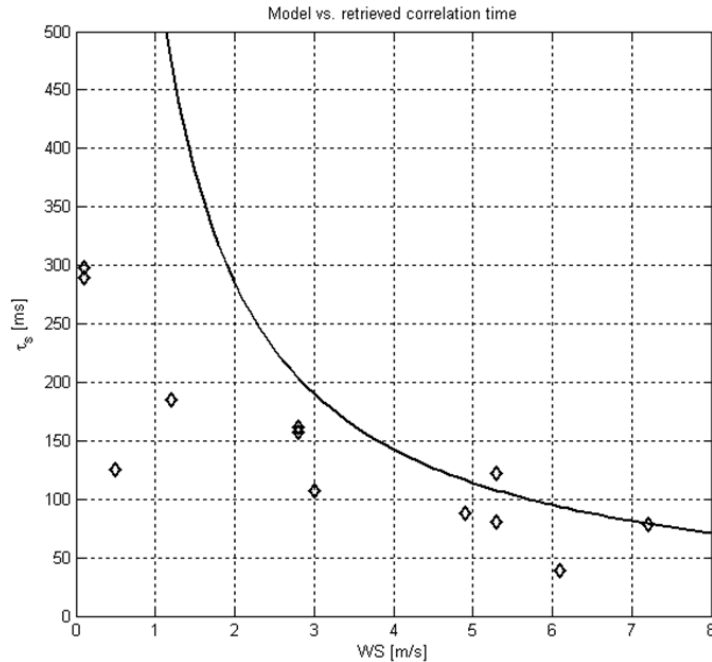
Figure 4.16: Retrieved sea correlation time (diamonds) and modeled correlation time (solid line) versus wind speed.

specially in this frequency range [27] In the limiting case of a 0 m/s WS, the model would predict an infinite correlation time, which is obviously not the case as sea roughness also depends on other parameters than just the wind speed (swell, etc.). Other causes of disagreement are due to the effect of noise and instrument inaccuracies on the acquired data, and to the reliability of the averaged ground-truth WS data available with respect to the actual WS value at the time of acquisition. It is relevant to note that the observed sea correlation time values are consistent with that observed in SAR applications which are of the order of a few tens of milliseconds [44, 38]. Finally, the retrieved correlation time has also been plotted as a function of another sea-state descriptor such as the average of the volume of the normalized DDM (V_{DDM}) over a 0.2 threshold [19, 18] computed for each acquisition (Fig. 4.17).

Although they are computed from the same DDM captions, there are
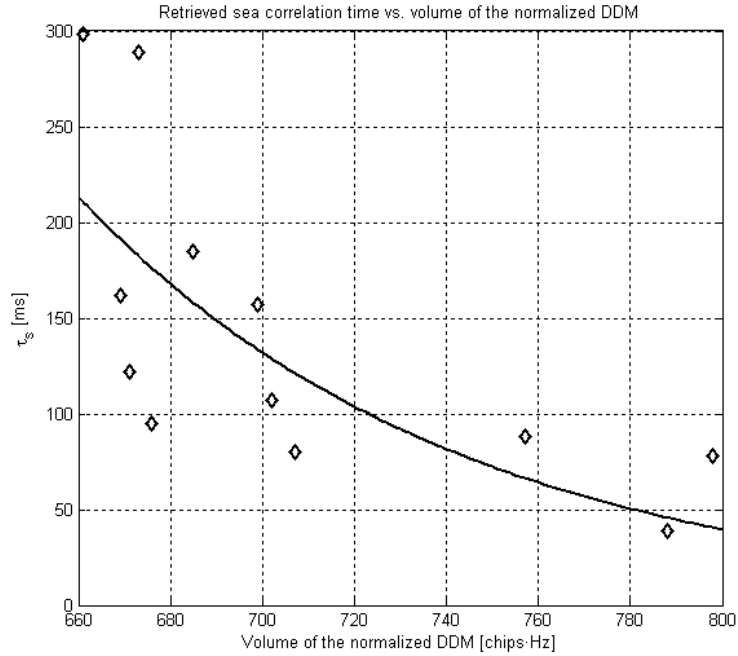
Figure 4.17: Retrieved correlation time (diamonds) versus the volume of the normalized DDM. The solid line corresponds to an exponential model fitted to the data.

three main reasons that allow to consider the retrieved τ_s and V_{DDM} as independent data sources usable to assess the presented correlation time retrieval technique:

1. The physical origin of the observations: τ_s, is computed from the contribution to the scattered field of the first Fresnel reflection zone, while V_{DDM} takes into account the contributions of the complete glistening zone, thus including coherent and incoherent scattering.

2. The different nature of the data used to compute them: V_{DDM} is computed from the module of the DDM and it does not practically decorrelate within the time scale of τ_s (less than 1% in 100 ms) that is computed using the DDMs peak complex value which phase contains

the information about the coherence of the scatterers.

3. The time scale of both observables is also different: τ_s is an instantaneous measurement that uses the 1 ms DDM series, while V_{DDM} is an average value of the overall 60 s series.

There is a clear relationship among both observables (Fig. 4.17) and the reliability of that descriptor is greater than just the WS because the normalized DDM volume contains information concerning exactly the glistening zone, and it is perfectly collocated in time with the retrieved sea correlation time since both parameters are computed using the same GNSS-R data capture. The measured sea correlation time can be fitted to an exponential model 4.3 so as to derive an empirical function that relates the sea correlation time to the normalized DDM volume, V_{DDM} (solid line in Fig. 4.17):

$$\tau_s = 587 \cdot e^{-0.012 V_{DDM}}.\tag{4.3}$$

4.6 Conclusions

In this study, the ALBATROSS 2009 field experiment and its main results have been presented. The two main goals of this experiment were: 1) to prove the feasibility of directly linking the brightness temperature variations caused by the sea state effect to GNSS-R observables avoiding the inaccuracy and discrepancies of emission/scattering modeling; and 2) to contribute to the in-depth study of the GNSS-R processing by determining the sea correlation time that limits the maximum usable coherent integration time.

Related to the first goal, three different GNSS-R direct observables have been studied: the volume of the normalized DDM (V_{DDM}), the length of the waveforms tail (τ_{tail}), and the scatterometric delay (ρ_{scatt}). The first two appear to be related to the sea surface roughness and show a high consistency among them. Moreover, these two observables have been successfully linked to the instantaneous brightness temperature variations induced by the sea state. Thus, the door to a better retrieval of the SSS product is opened. Unluckily, the problems found related to the measured brightness temperature absolute calibration due to the uncontrolled offsets introduced by the cliff have prevented the SSS retrieval itself. This issue has been addressed in Chapter 5 using radiometric and GNSS-R data from an airborne experiment.

With respect to the second goal, the collected coherent GNSS-R data has been used to retrieve the sea correlation time by means of studying the decorrelation of the DDM peak. The obtained results are consistent with the sea correlation time modeling and establish the maximum usable coherent integration time to a few tens of milliseconds when processing ocean measured data from ground (no Doppler filtering effect).

As a summary, it can be concluded that the ALBATROSS field experiments have provided successful results that encourage the pursuit of studies of GNSS-R techniques for remote sensing applications and the development of radiometric/reflectometric synergetic sensors.

5

The CoSMOS field experiment

5.1 Introduction

To further study the relationship of the variations induced by sea state on the T_B and the GNSS-R measurements, the data gathered during ESA's CoSMOS-OS 2007 air-borne experiment ([45]) is used in this study. In that experiment, different instruments were deployed on-board the Helsinki University of Technology (TKK) Skyvan aircraft to assess the feasibility of SSS retrievals using L-band microwave radiometry: the HUT-2D ([46]) and EMI-RAD ([47]) L-band radiometers, the GOLD-RTR GPS reflectometer ([48]), and others such as an infrared radiometer for SST measurements. The HUT-2D data were used in [49] for SSS retrievals and in [50] to test different approaches to correct for the sea state effect in T_B. One of the approaches in [50] is based on parameterizing the measured T_B changes with the sea surface mean square slopes (MSS) derived from the GOLD-RTR data. In this work, an improved approach is followed to reduce the SSS retrieval errors from the EMIRAD measurements, but directly using the GOLD-RTR data without the use of emission/scattering models in line with the concepts developed in the PAU project, and the ALBATROSS experiments.

Due to the limited flight time, only measurements corresponding to a reduced sea state variability could be gathered. Moreover, unlike the ALBA-

TROSS experiment (see Chapter 4), the measurements are not multi-angular since the radiometer's antenna beams where pointing to nadir and 40° aft only. These facts prevented from using the available experimental data to derive generalizable results such as angular dependence of the T_B variations sensitivity with the measurement incidence angle. However, the availability of well calibrated radiometric measurements allowed this study to go one step further attempting to assess the impact of the proposed correction on the final salinity product.

This chapter is devoted to the CoSMOS 2007 experiment data processing and derived results, and it is organized as follows:

- Section 5.2 presents the experiment details and describes the different datasets used: the radiometric measurements, the GNSS-R data and the available ground-truth.

- Section 5.3 explores the correction of the measured T_B for the sea state effect, by using the area under the waveform as a collocated GNSS-R observable which is intended to describe the sea surface roughness.

- Section 5.4 is devoted to assess the impact of the proposed T_B correction on the final SSS retrievals.

- Section 5.5 compares the obtained results to the ones from other T_B correction approaches such as the ones developed from the WISE experiments, that uses an empirical model to compute the required correction from wind speed data.

5.2 Available radiometric, GNSS-R and ground-truth data

The ESA-sponsored CoSMOS-2007 field experiment ([45]) consisted of two flights performed over the Gulf of Finland. The aim of these flights was to test the ability of different instruments to measure SSS gradients, so the flight tracks were planned to pass above an estuary area and open sea (Fig. 5.1). This track is referred to as the "test line" and it presents a SSS gradient from nearly 0 psu inside the estuary to approximately 4 psu in the open sea area. While the aircraft passed several times over the test line (around 20 passes), a vessel was collecting in-situ SSS, SST and sea state measurements along it. To avoid the Sun glint effect in the measurements, flights were performed in the evening, from 19:00h to 21:00h approximately.

The aircraft flew different instruments. In this study the datasets of three of them were used: the EMIRAD L-band radiometer ([47]), the GOLD-RTR GPS reflectometer ([48]), and a standard thermal infrared radiometer (TIR).

5.2.1 Radiometric data

The EMIRAD dataset contains calibrated polarimetric L-band measurements of the observed scenario. The raw data files provide the brightness temperature values for basic integration periods of 8 ms which have been further integrated up to 1 s to be time-collocated with the GNSS-R measurements from the GOLD-RTR instrument. With this 1 s integration time, the radiometric sensitivity is specified to be $\Delta T = 0.1$ K and the thermal stability is within ± 0.1 K. The EMIRAD's antenna is a horn with a 30° half-power beam width, and side-lobes below -17 dB with respect to the antenna's boresight gain. The data files also contain information regarding the aircraft position and attitude.

To minimize the impact of the aircraft attitude on the radiometric data, in
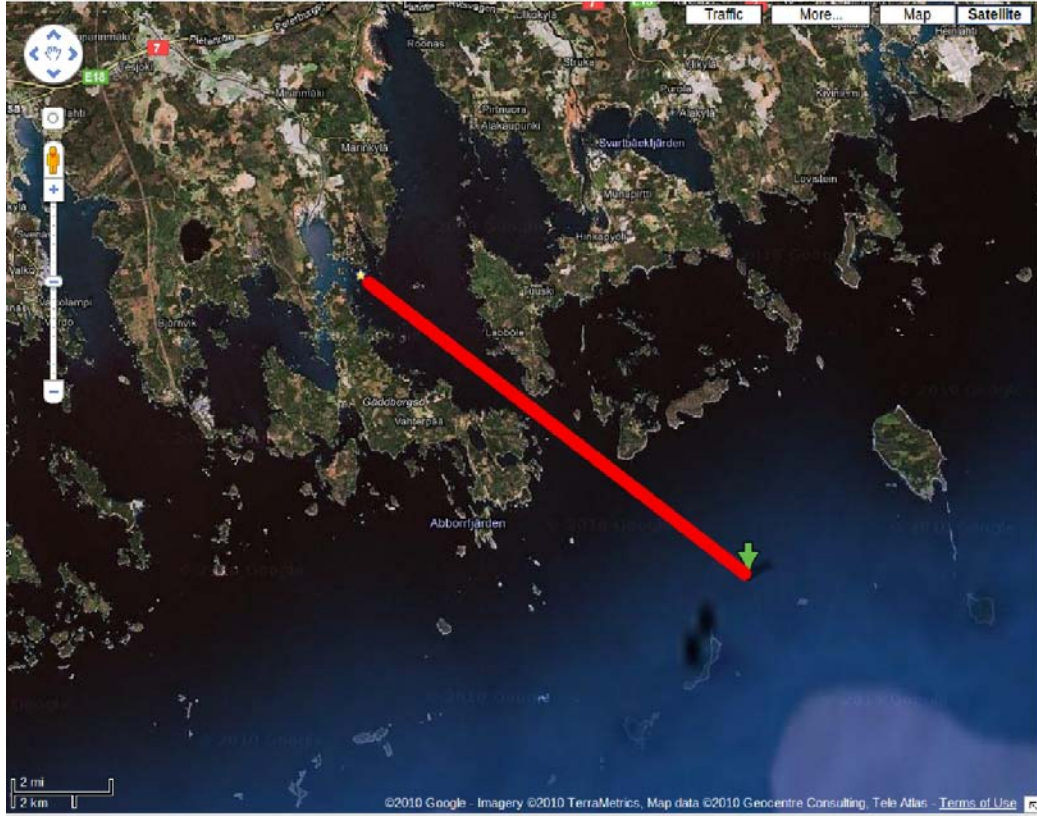
Figure 5.1: Test line: track of the flights performed during the CoSMOS-2007 experiment at the Gulf of Finland.

this work only the nadir-looking measurements have been processed from the two antennas on-board the aircraft (nominal incidence angles of 0° and 40°). Moreover, the chosen radiometric observable was the first Stokes parameter divided by two ($I/2$) as it presents a very low sensitivity to attitude variations for low incidence angles. This parameter is defined as the mean of the horizontally and vertically polarized brightness temperatures (see Eqn. 5.1).

$$\frac{I}{2} = \frac{T_H + T_V}{2} \tag{5.1}$$

5.2.2 GNSS-R data

The main product of the GOLD-RTR instrument are the so-called waveforms (see Eqn. 5.2) which are computed by correlating the received signal $(s(t))$ with a local replica of the GPS L1 $(f_{L1} =1575.42$ MHz) coarse acquisition (C/A) pseudo-random noise (PRN) code $(a(t))$, after compensating for the Doppler frequency shift (f_D) during a coherent integration time (T_c), as defined in [14]. This coherent integration process takes into account the phase of the complex correlation.

$$Y(\tau) = \int_0^{T_c} s(t)a(t+\tau)e^{-j2\pi(f_{L1}+f_D)t}dt \qquad (5.2)$$

However, the coherent integration time is limited by the coherence time of the scattered signal which depends on the scattering surface and the observation scenario's dynamics. For an airborne experiment as the one presented here, this time has shown to be of the order of a few milliseconds ([51]). The coherently integrated waveforms $(Y(\tau))$ can be further integrated incoherently during an incoherent integration time $T_i = N \cdot T_c$ in order to improve the resulting signal-to-noise ratio (SNR):

$$\overline{|Y(\tau)|^2} = \frac{1}{N}\sum_N |Y(\tau)|^2 \qquad (5.3)$$

For this experiment, waveforms were acquired in different ways (i.e. different PRNs and Doppler shifts) according to a established measuring cycle. This work uses the incoherently integrated 1 s waveforms computed for the highest elevation satellite present at each time, as the reflection is closer to nadir and, thus, the specular reflection point is closer to the radiometer antenna footprint. The considered reflections present a local incidence angle uniformly distributed between 5° and 40°.

In the absence of the complete DDMs, to study the sea surface roughness a parameter analogous to V_{DDM} (see [19]) was defined for the waveform in

this work. It is the area of the normalized waveform (A_{WF}) computed by integrating the area below the measured waveform in the delay domain. As for the case of the V_{DDM}, an empirically-determined threshold of 0.2 was used to minimize the impact of noise. The rationale of using this observable to parameterize the ocean surface roughness is that, for a very calm sea, the scattered signal will only be contributed from a small region close to the specular point while, for rougher surfaces, it will be contributed from larger surface regions which present larger physical delays. Thus, the power of the scattered signal will spread along the delay domain as the surface gets rougher. After normalization of the waveforms' peak value, the area below them is then a function of the surface roughness. As the waveforms are normalized, the unity of A_{WF} is the same as for the delay domain. In this work, the C/A code chip length (0.97 microseconds) is used.

To better show the concept of "waveform spreading" described by the A_{WF} parameter, the area of the ideal non-spread waveform was computed from the direct signal and subtracted from the area of the measured waveforms (i.e. the waveform cannot be thinner than the autocorrelation function of the C/A code, thus the area of this function acts as an offset). Although for direct signal its value should be theoretically equal to the area of the squared triangle (shape of the ideal autocorrelation function of the C/A code in the delay domain), it is actually a little bit larger due to the limited bandwidth of the system. This value is 0.63 chips and was subtracted from the A_{WF} for the reflected signal, to define a new parameter ΔA_{WF}. For a very calm sea, ΔA_{WF} should tend to 0, while it should increase for rougher seas.

Although waveforms from different PRNs and elevations were used, a high consistency among the derived A_{WF} was observed (i.e. A_{WF} proved to be independent of the different PRNs and elevation), as it was observed for the V_{DDM} in previous experiments such as the ones presented in [18] and [52].

116

5.2.3 Ground-truth data

The ground-truth dataset that was used in this work is formed by the SSS measurements taken by the vessel along the test line (Fig. 5.2), and the SST collocated measurements taken by the on-board TIR averaged up to 1 s. To obtain the SSS ground-truth measurements, TKK personnel took water samples (in bottles) that were analyzed later in an specialized laboratory. The SST measurements from the vessel were not used as they were not collocated in time with the radiometric data and did not reflect the water cooling effect along the evening, which leads to errors when trying to model the sea brightness temperature or to perform SSS retrievals. Due to the thermal cycle along the day, the parameter whose variations affect the most the measured brightness temperature is the SST. For the presented experiment, it ranged from 23.5°C to 20°C considering the different measurement spatial region and time. This variability was the reason to use the on-board instantaneous TIR SST measurements, and not the vessel ones. However, the SSS spatial distribution changed less than 0.5 psu in 24 h ([49]), so it can be considered constant during the 2.5 hour flights.
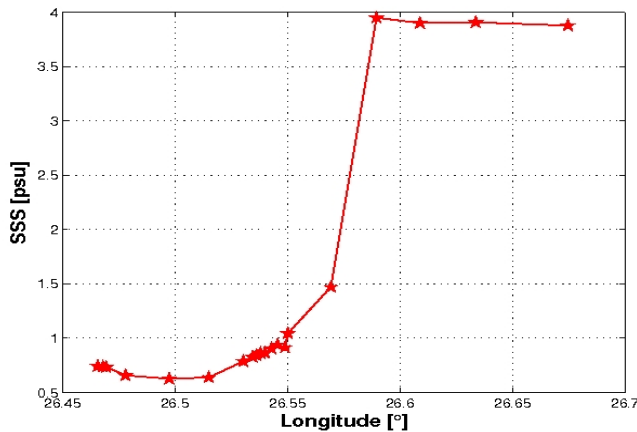
Figure 5.2: Sea surface salinity measurements taken by the vessel along the test line for the August 13th flights. Stars correspond to the actual sampled points.

There is not any available well collocated (neither in time, nor in space) sea state ground truth data. However, the vessel measurements (obtained by processing the data of two GPS-equipped buoys pulled by the vessel) showed a relatively calm sea during the flights ($mss < 0.025$; $SWH < 30$ cm). Moreover, the closest wind speed (WS) measurements in time and space (measurements at 18:00h UTC with a resolution of 0.25°), provided by QuickScat and ECMWF, were also low and very similar for both flights (QuickScat around 3.5 m/s and ECMWF around 2.5 m/s).

5.3 Brightness temperature correction using GNSS-R data

As seen in Eqn. 5.4, the ocean measured brightness temperature (after correction for the external contributions such as galactic, cosmic and atmospheric) can be divided to first order into two contributions: $T_{B,flat}$, the flat sea term, and ΔT_B, the increment introduced by the sea surface roughness.

$$T_B = T_{B,flat} + \Delta T_B \tag{5.4}$$

The flat sea contribution is computed from the Fresnel reflection coefficient Γ (Eqn. 5.5) using, for example, the sea water dielectric constant model of [23], since the emissivity can be assumed to be the complimentary value of the reflectivity:

$$T_{B,flat}^p = SST \left(1 - \Gamma^p \left(\theta, \epsilon\right)\right) \tag{5.5}$$

where p is the desired polarization, θ is the incidence angle, and ϵ is the dielectric constant of the sea water, which is a function of SSS and SST. Using the available ground truth data, the flat sea contribution was computed for each measurement taking into account the collocated SST and SSS measurements. Figure 5.3 shows the resulting flat sea contribution modeled for

the first Stokes parameter $I/2$, for the first flight. It can be observed how
$I/2$ changes according to SST, SSS and surface roughness variations as the
aircraft performed the different passes over the test line.

At this point, since the SSS and SST effects were modeled, the contribution of the sea state to the total brightness temperature could be estimated
by subtracting the modeled flat sea term from the actual measurements. The
spatial distribution of the final estimated ΔT_B is presented in Fig. 5.4, where
the different aircraft passes have been plotted in different colors. It can be
seen that ΔT_B presents a dispersion larger than the radiometric resolution of
the instrument and that it is a function of time. This ΔT_B is actually related
to the instantaneous sea state, except for the errors introduced by the model
used to compute $T_{B,flat}$, and the ground-truth errors.

In Fig. 5.4 some spatial features appear as spikes in the computed ΔT_B.
These phenomena occur in the region where the aircraft track passed closest
to land (transition from estuary to open waters) and, according to their
magnitude of a few kelvin, were thought to be caused by land contribution
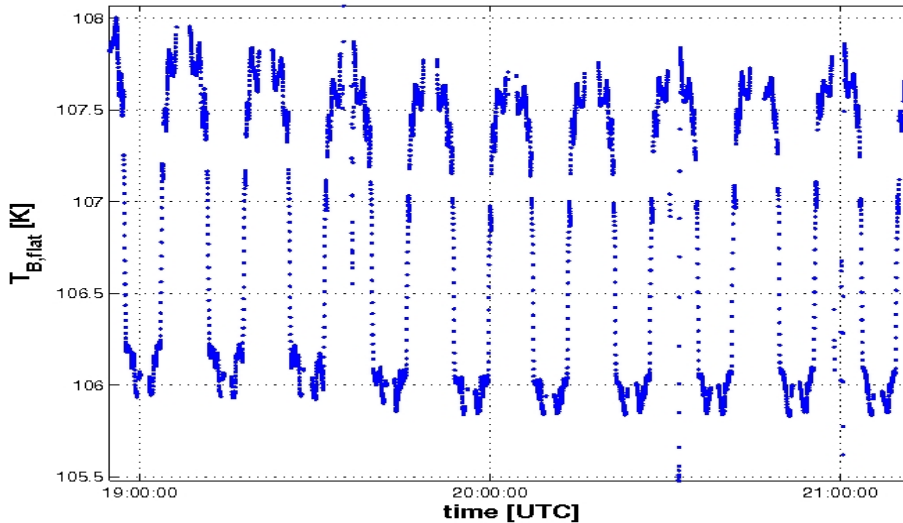
Figure 5.3: Simulated flat sea contribution to the measured first Stokes parameter.

to the overall measured brightness temperature which was collected through the antenna secondary lobes (roughly, a 300K brightness temperature of the land, attenuated 17 dB results in a 6 K contribution).

Moreover, this transition area is also the one that presented the largest SSS gradient. Due to the sparse SSS ground truth sampling, the final error among the interpolated ground-truth and the actual SSS may be larger, resulting also in a larger error in the modeling of the flat-sea contribution to the total brightness temperature. These errors (land contribution and ground-truth error) can mask the roughness effects and bias the final results, thus this region was discarded for processing.

In order to directly perform the sea-state correction, the derived ΔT_B needed to be parameterized as a function of a sea state descriptor. As mentioned above, the sea state descriptor chosen in this work is the area of the
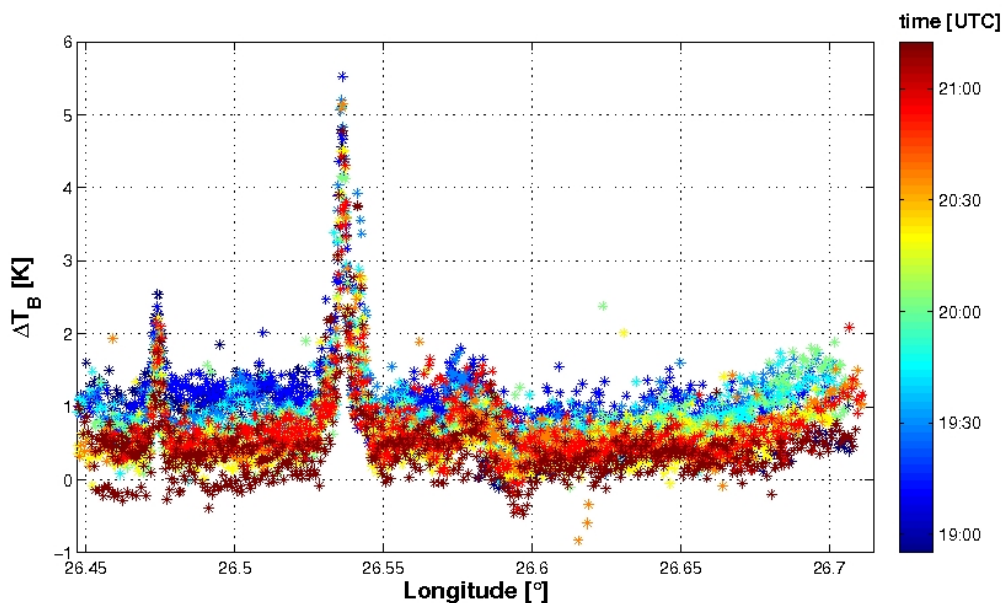
Figure 5.4: Spatial distribution of the brightness temperature increment computed from the first Stokes parameter measurements and the simulated flat sea contribution. Color scale represent the measurement time (i.e. different aircraft passes).

normalized waveforms which is obtained from the quasi-collocated GNSS-R measurements, and is conceptually similar to the volume under the normalized DDM ([19]). The time evolution of ΔT_B is plotted in Fig. 5.5 along with the time evolution of A_{WF}.

It is observed that both are highly correlated in time: both measurements present oscillations which are perfectly in-phase, as well as a slight decrease in their mean. This oscillation is attributed to the roughness variation observed as the plane flew over the two different roughness areas (estuary and open sea). This fact further supports the hypothesis that both are related to sea state.

Collocated measurements of ΔT_B are plotted as a function of the corresponding ΔA_{WF} in Fig. 5.6 along with the resulting regression line. These measurements present a Pearson correlation coefficient of $r = 0.41$. The polynomial coefficients of the performed geometric regression (see [53]) were used
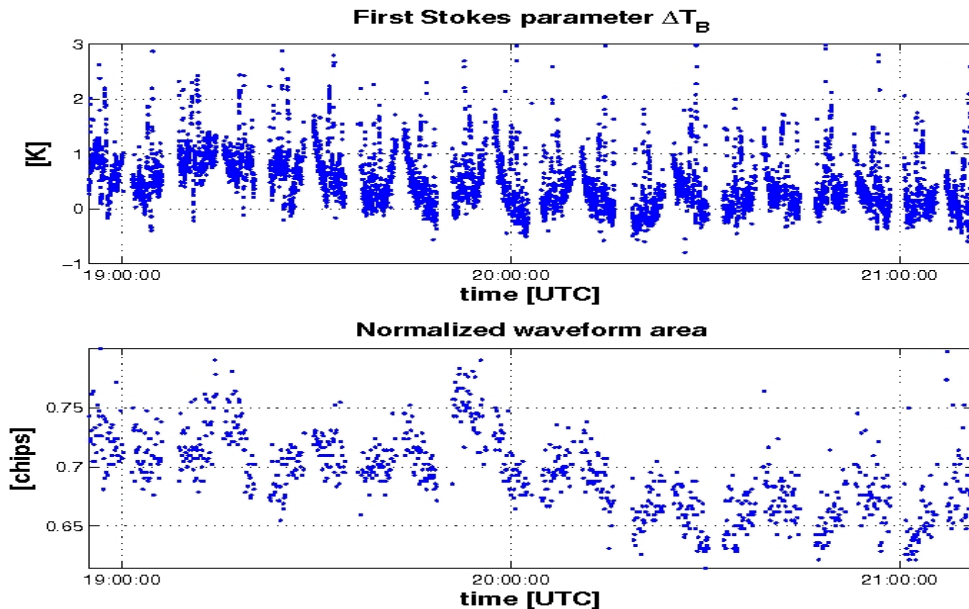
Figure 5.5: Time evolution of the computed brightness temperature increment, ΔT_B, and the normalized waveform area.

to compute an estimation of the actual ΔT_B from the A_{WF}. By subtracting this estimation from the T_B measurements, the sea state contribution was then corrected, better approaching to the desired $T_{B,flat}$ term.

In Fig. 5.7 the computed ΔT_B correction for all the aircraft passes is plotted as a function of the measurement longitude and with different colors depending on the measurement time. It can be seen that the correction needed is lower in the estuary waters part of the test line, than in the open sea areas. The required ΔT_B correction also decreases with time as the sea got calmer at the end of the day.

To assess the performance of the proposed sea surface roughness correction, it was applied to the first flight data. The resulting corrected first Stokes parameter is shown in Fig. 5.8 along with the raw radiometric measurements and the modeled flat sea contribution. The RMSE with respect to
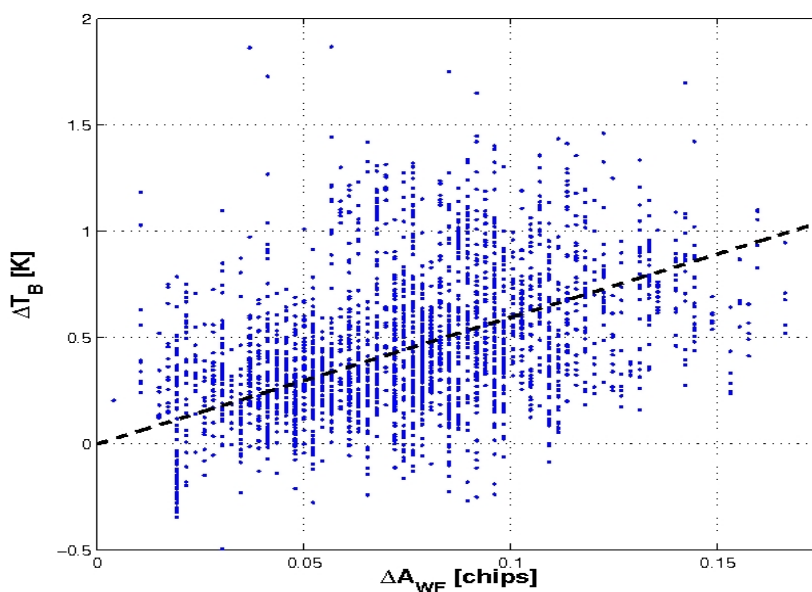
Figure 5.6: Measured ΔT_B plotted as a function of the spreading of the collocated waveform measurement described by ΔA_{WF}. Dotted line corresponds to the resulting geometric regression.
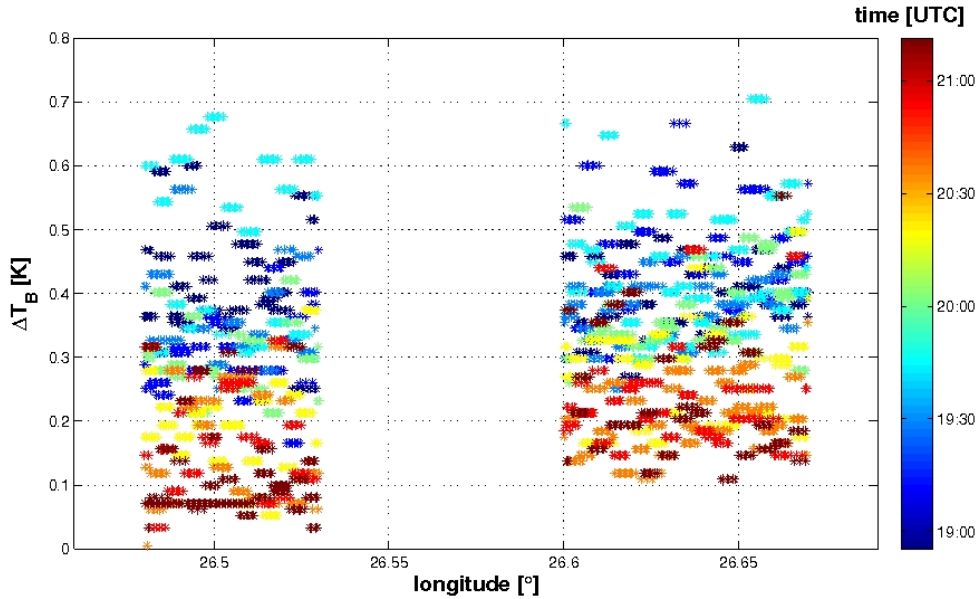
Figure 5.7: Computed ΔT_B correction from the waveforms' area as a function of the measurement longitude. Colors show the ΔT_B evolution in time.

the modeled first Stokes parameter $T_{B,flat}$ is reduced from 0.70 K to 0.30 K by applying the proposed correction. Spatial averaging can be performed to reduce the final brightness temperature error. In Fig. 5.9 the result of spatially averaging the raw and the corrected $I/2$ measurements with a cell size of 0.002° (approximately 100 m at the flight latitude) are shown. In this case, the sea state effect correction reduces the RMSE from 0.63 K to 0.12 K.

Although the correction needed for this dataset is not large (in the order of 0.5 K) due to the relatively low sea surface roughness conditions present during the flight ($mss < 0.025$; $SWH < 30$ cm), larger ΔT_B will be introduced by rougher sea conditions. However, the final error after correction is expected to be similar to the one achieved in this example as this error is mainly due to the dispersion of the radiometric measurements around the corresponding regression line (see Fig. 5.6), which is not dependent on the sea state.

5.4 Sea surface salinity retrieval

After applying the sea state correction to the measured $I/2$, its benefits to the final SSS product can be assessed. To do so, the inversion of the flat sea model (Eqn. 5.5) was used as a first approximation to the problem. Retrievals were performed for both raw and corrected radiometric measurements, and the derived SSS products are shown in Fig. 5.10. As a reference for the error introduced by the retrieval algorithm, also the SSS retrieved from the flat sea model itself and the ground-truth measurements have been plotted in Fig. 5.10. As it can be seen, the corrected values for the $I/2$ better match the in-situ SSS measurements. It has to be noticed that the highest $I/2$ values, that should correspond to non-real negative SSS, saturate down to 0.2 psu (the lowest salinity value that the used method can output). This fact will lead to an over-estimation of the SSS retrieval mean for the lowest
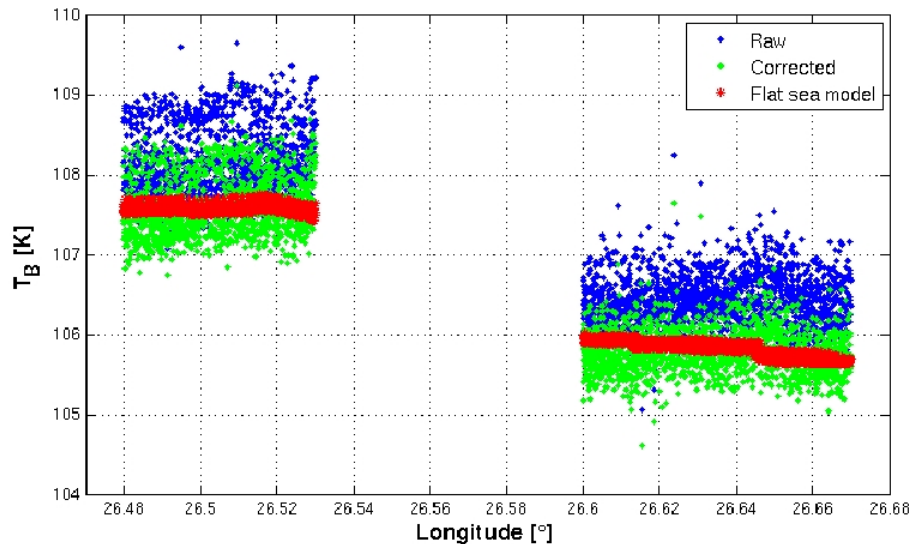
Figure 5.8: Comparison among the raw (blue) and sea state corrected (green) first Stokes parameter divided by two. The flat sea model computed from the ground truth is plotted in red.
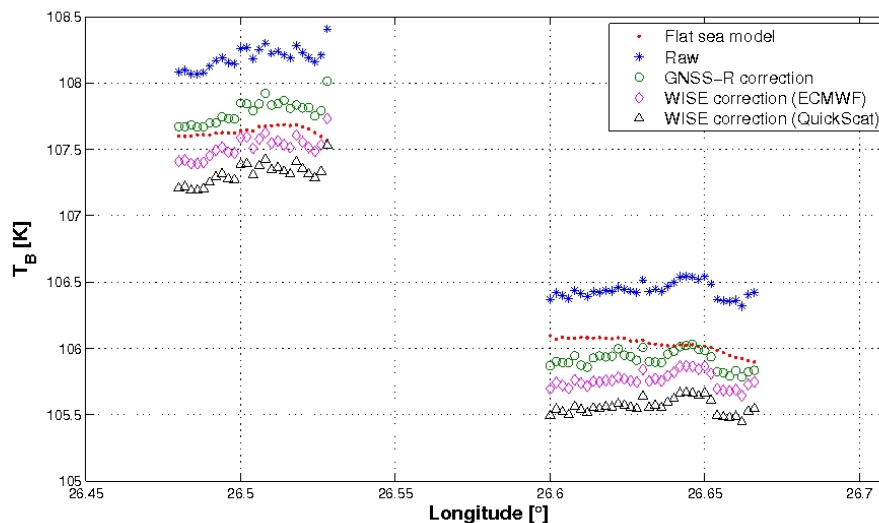
Figure 5.9: Comparison among the raw (blue) and sea state corrected (green) first Stokes parameter divided by two. The flat sea model computed from the ground truth is plotted in red.

salinity regions.

To further assess the benefits of the proposed correction, the SSS retrievals were also spatially averaged in longitude cells of $0.002°$ (approximately 100 m at the flight latitude). The averaged SSS retrievals are shown in Fig. 5.11, along with the values retrieved from the model itself and the ground-truth data. As it can be observed, in the highest salinity part of the test line, the retrieval from the corrected $I/2$ matches the in-situ measurements significantly better than the SSS retrieved from the raw radiometric measurements (RMSE of 0.51 psu and 2.8 psu respectively). However, for the lowest salinity region, the retrieval mean appears to be overestimated due to the aforementioned saturation effect. This is why the retrievals from the uncorrected $I/2$ measurements seem to match the ground-truth data better. For this reason, the quality of the retrieval was not assessed in this region as the introduced bias resulted in misleading conclusions.
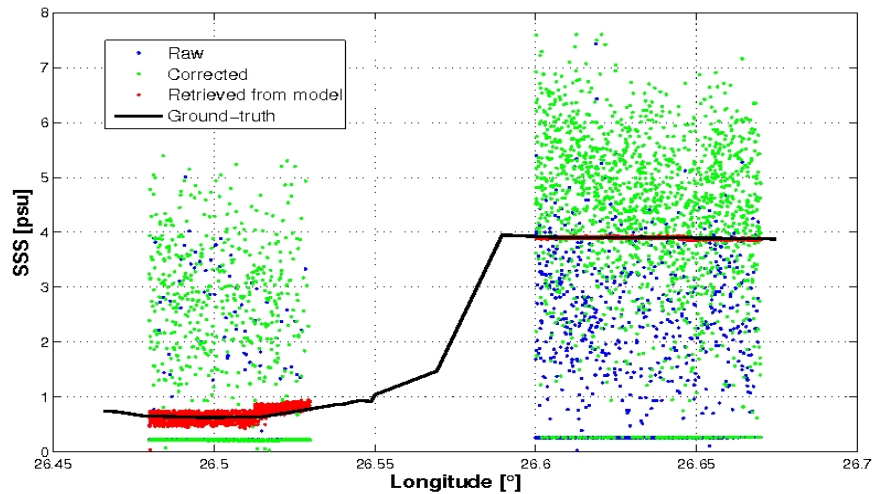
Figure 5.10: Comparison among the raw (blue) and sea state corrected (green) SSS products. The SSS product retrieved directly from the flat sea model (red) and the ground-truth SSS (black) are plotted as a reference.
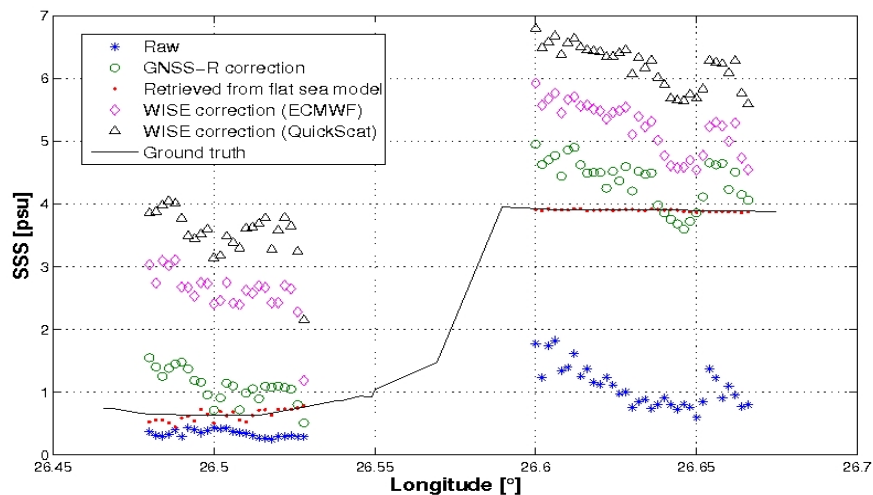
Figure 5.11: Comparison among the spatially averaged raw (blue) and sea state corrected (green) SSS products. The SSS product retrieved directly from the flat sea model (red) and the ground-truth SSS (black) are plotted as a reference.

5.5 Comparison with the WISE correction approach

In order to have a more complete picture of the brightness temperature correction process, the sea surface roughness correction problem was also approached by using the currently existing WISE model for the ΔT_B correction. In particular, the ΔT_B correction was computed from the QuickScat and the ECMWF WS measurements using the $I/2$ sensitivity to WS derived in the WISE experiment [27]. This sensitivity is about 0.25 K/(m/s) at nadir. However, a single WS measurement was available for the flight time along the test line. For both QuickScat and ECMWF WS measurements, ΔT_B appears overestimated (Fig. 5.9). The $I/2$ RMSE with respect to the flat sea model for the different correction approaches are shown in Table. 5.1.

Table 5.1: First Stokes parameter divided by two and SSS RMSE for the different correction approaches (spatially averaged to 100 m cells)

	$I/2$ [K]	SSS [psu]
Raw measurements	0.63	2.80
GNSS-R correction	0.12	0.51
WISE correction (ECMWF)	0.23	1.14
WISE correction (QuickScat)	0.42	2.33

SSS was also retrieved after applying the WISE correction for the two available WS data. For both WS data, the retrived SSS is higher than when using the collocated GNSS-R data to perform the sea state correction. The derived RMSE is 2.33 psu when using QuickScat and 1.14 psu when using ECMWF, also computed only for the highest salinity part of the test line to avoid the model inversion saturation that affects the lowest salinity region. The SSS RMSE for the different correction approaches are summarized in Table. 5.1.

Even though the WISE corrections do improve the final results with respect to the raw data (reduction of the error at the brightness temperature and SSS levels), these results show the benefits of using collocated GNSS-R

data to parameterize the sea surface roughness contribution to the measured brightness temperatures.

5.6 Conclusions

Previous ground-based studies linked the sea state and the brightness temperature variations caused by the sea state effect. In this work the CoSMOS-OS 2007 experiment data were used to extend those studies to the airborne case and to analyze the feasibility of improving the retrieval of SSS by jointly using collocated L-band radiometry and GNSS-R measurements. The GOLD-RTR measured waveforms were used directly, through their area after normalization of the peak amplitude, to compute the required instantaneous brightness temperature correction.

The first step of this process was to study the relationship among the ΔT_B induced by the sea state effect and the area of the normalized waveforms. This was done by subtracting the modeled $T_{B,flat}$ from the radiometric measurements to compute an estimation of ΔT_B. The first Stokes parameter divided by two ($I/2$) has been used as it is nearly independent of the aircraft attitude for low incidence angles. The time evolution of both ΔT_B and A_{WF} shows an instantaneous correspondence. When plotted one versus the other, both parameters present a Pearson correlation coefficient of $r = 0.41$, which is low most probably because of the noise present in the radiometric measurements. The A_{WF} was then used to compute the instantaneous brightness correction needed. After applying this correction, the error with respect to the $T_{B,flat}$ model was significantly reduced (RMSE from 0.63 K (raw measurements) down to 0.12 K when T_B was spatially averaged in approximately 100 m cells along the test line). This correction appeared to be robust in spite of the noise level of the used GNSS-R observable.

Once the corrected T_B were derived, the Fresnel-based brightness temperature model was inverted for SSS retrieval. A final improvement in the RMSE from 2.8 psu (raw measurements) down to 0.51 psu was achieved when applying the proposed correction prior to the SSS retrieval process, even though a simple retrieval method based on model inversion was used.

These results should improve when using more refined retrieval algorithms and further time and space averaging as it is done within the SMOS processor.

Moreover, the current WISE model for the ΔT_B as a function of the WS was also applied to the dataset. It was concluded that the final brightness temperature errors were further reduced by using time and space collocated GNSS-R data to parameterize the sea surface roughness, rather than when considering a single low-resolution WS measurement.

6

Wind direction retrieval from airborne measurements

6.1 Introduction

Previous experimental work in this PhD. Thesis (Chapters 4 and 5) was focused on the use of GNSS-R DDMs to retrieve information about the sea surface roughness. The approach chosen was to use descriptors directly derived from the measured DDMs, and to relate them to the desired geophysical parameter through empirical relationships. These descriptors were based on the measurement of the DDM spreading caused by surface's roughness.

However, the DDM not only contains information on the surface's roughness in a scalar way, but it also captures the directionality of the observation geometry. Thus, the direction of the wind driving the surfaces waves may also be inferred from this kind of GNSS-R data. Previous work has been performed by some authors in this direction [54, 55, 56, 57]. All these works are based on fitting the measured waveforms/DDMs with a model tuned by the surface's roughness (mainly directional mean square slopes), and wind direction.

The nature of the problem creates a double ambiguity at the time of wind direction retrieval. Firstly, the ocean spectrum symmetry makes indis-

tinguishable the waves' traveling direction thus creating a 180° ambiguity in the retrievals. Secondly, the bistatic mapping process creates another ambiguity, since the weights of each of the two surface's points contributing to a delay-Doppler bin cannot be derived from a single measurement. Literature states that at least measurements for two transmitting satellites must be used in order to solve for the latter [54, 57]. The 180° ambiguity caused by the ocean's spectrum symmetry cannot be solved, though.

In line with this PhD. Thesis, it was envisioned that the waves' traveling direction would be reflected in some feature of the measured DDMs shape, so it could be possible to retrieve it by means of some direct descriptor of that feature. The main advantage of achieving it is that the retrieval computation time and cost would be significantly reduced with respect to the model fitting approach, as it is when describing the oceans surface roughness by V_{DDM} or A_{WF}. To explore this approach, the work presented here was performed at the National Oceanographic and Atmospheric Administration (Boulder, USA) under supervision of Dr. Zavorotny. Measurements collected from the NOAAs Gulfstream IV aircraft were initially inspected, and it was observed that DDMs presented an asymmetry that was mainly caused by wind direction and receivers flying direction. A metric of this asymmetry was proposed, and successfully used for wind direction retrieval. This retrieval was performed by inverting an analytical model derived from simulation.

This Chapter presents the results of this work and it is organized as follows:

- Section 6.2 shows the asymmetry observed in the data, and introduces the simulation tools used.

- Section 6.3 presents a simulation study from which an asymmetry metric is derived and modeled by an analytical expression.

- Section 6.4 validates the derived model with real measured data.

- Section 6.5 presents the results obtained by inverting the model for wind direction retrieval from the airborne measured data.

6.2 Observation of measured data and validation of the P^{2}EPS simulator

From the January 24th, 2010 flight of the NOAA's Gulfstream-IV jet aircraft, different datasets were identified that presented the same wind speed, but different wind directions. For those datasets, the power distribution on the DDM appeared to be skewed along the Doppler axis. According to that, the hypothesis that the wind direction might be causing that asymmetry on the DDM was stated.

In Fig. 6.1 and Fig. 6.2, two measured DDM are shown along with their corresponding simulations. These measured DDMs were obtained by incoherently averaging 20 s of 1 ms DDM, following the integration strategy adopted by [58]. As it can be seen, both measurements are skewed along the Doppler domain. That asymmetry is basically observed in the low power region of the DDM from -5 dB with respect to the peak, and below. This behavior is also present in the simulated DDM, so the model used was actually able to describe these skewness properties. Notice that all the observation geometry parameters (elevation angle and receiver flying direction) were set to the ones corresponding to the measured data, in order to obtain the simulated DDM.

The simulation tool used was the PAU/PARIS End-to-end Performance Simulator (P^{2}EPS, [59]). This tool allows to compute DDM for a given observation geometry, and a given ocean surface described by the wind speed and direction. The model for the DDM is the Zavorotny and Voronovich one, and the PDF of the surface slopes is approximated by Gram-Charlier series parameterized by the directional mean square slopes of the surface (MSS). These directional MSS are obtained from the wind speed and direction. To do so, three different approaches were tested without observing significant differences in the resulting DDMs: a) integrating Elfouhaily spectrum using the cut-off wavenumber proposed in [60]; b) integrating Elfouhaily spectrum using the cut-off wavenumber proposed in [61]; and c) by the Cox and Munk

(a)

(b)
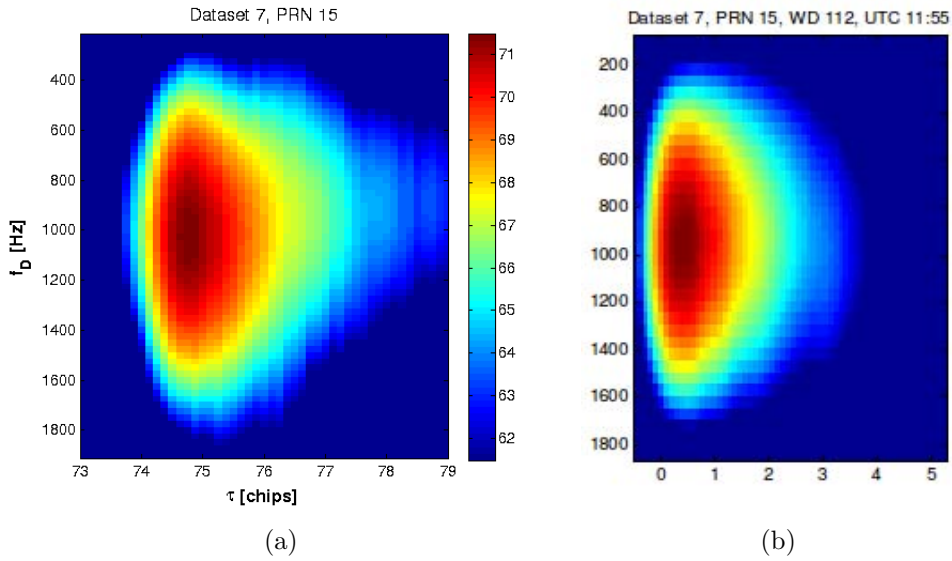
Figure 6.1: Dataset from UTC 11:55, PRN 15, $WS = 10$ m/s, $\phi = 112°$ (wrt N): a) Measured, and b) simulated DDMs.

(a)

(b)
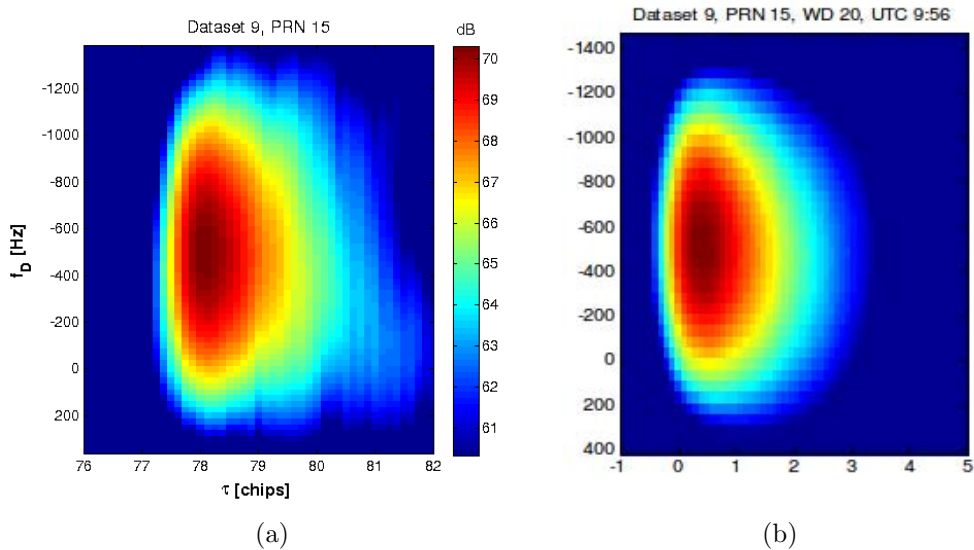
Figure 6.2: Dataset for UTC 9:56, PRN 15, $WS = 10$ m/s, $\phi = 20°$ (wrt N): a) Measured, and b) simulated DDMs.

relationships after applying the empirical modification proposed in [62].

The main benefit of using this simulator is its computational speed as it implements the improved DDM simulation algorithms proposed in [63]. Whereas the "classical" double integration over the surface needs around 10 minutes computation time, the improved algorithm only takes 0.5 s using the same PC, and for the airborne considered scenario. This computation acceleration allows to perform a comprehensive set of simulations to study the impact of different parameters on the simulated DDMs.

6.3 Modeling the DDM asymmetry

Once it was assessed that the P²EPS tool was able to reproduce the DDM skewness, a comprehensive simulation study was performed by sweeping through all the scenario's parameters, namely: elevation angle (γ), receiver's flying direction (α_{RX}), wind speed (WS) and wind direction (ϕ). The flight's height and speed were set to 12 km and 280 m/s respectively, since these were the mean values for the actual flight. The transmitter's flying direction was not considered as it was observed not to affect the measurements. This is due to the fact that the iso-delay and iso-Doppler lines layout within the glistening zone is mainly determined by the receivers speed and velocity, as it is much closer to the observed surface. The parameters used in the simulation are presented in Table 6.1.

From the simulation dataset obtained, it was observed that the DDM

Table 6.1: Considered values for the observation geometry and surface parameters.

	Range	Step
Receiver flying direction (α_{RX})	[0,360]°	22.5°
Elevation angle (θ_i)	[40,90]°	10°
Wind Speed (WS)	[4,20] m/s	2 m/s
Wind Direction (ϕ)	[0,360]°	22.5°

asymmetry was actually caused partially by wind direction, but other scenario parameters were also impacting the DDM shape. To describe this asymmetry and study its dependence on the observation geometry, a first new metric was envisioned. This metric was based on computing the vector from the DDM peak to the center of mass of the DDM skirt (CM_{skirt}), being defined as the DDM region whose power is within -5 dB and -8 dB with respect to the peak. Once the vector from peak to CM_{skirt} was computed, the DDM skewness was described by its argument defined as:

$$\varphi_{skew} = tan^{-1} \left(\frac{CM_{skirt,\tau} - peak_\tau}{CM_{skirt,f_D} - peak_{f_D}} \frac{\Delta\tau}{\Delta f_D} \right), \tag{6.1}$$

where $\Delta\tau$ and Δf_D are the delay and Doppler resolutions of the DDM. Figure 6.3 shows a graphical representation of the φ_{skew} asymmetry metric.
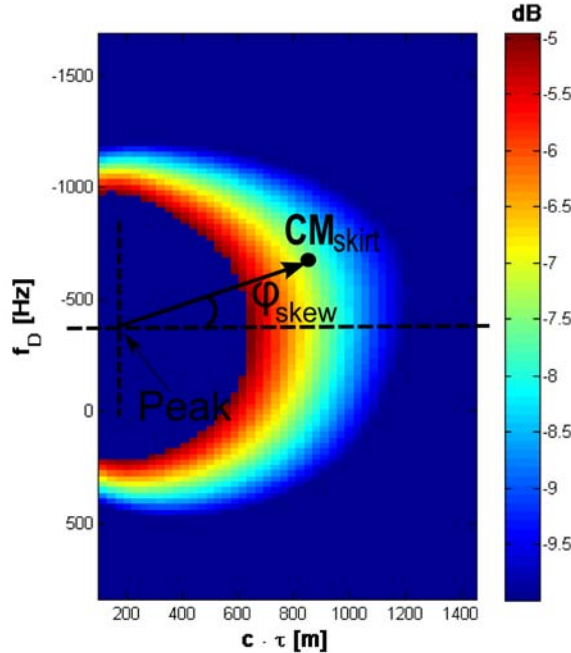
Figure 6.3: Definition of the DDM skirt's center of mass CM_{skirt}, and the skewness angle, φ_{skew}.
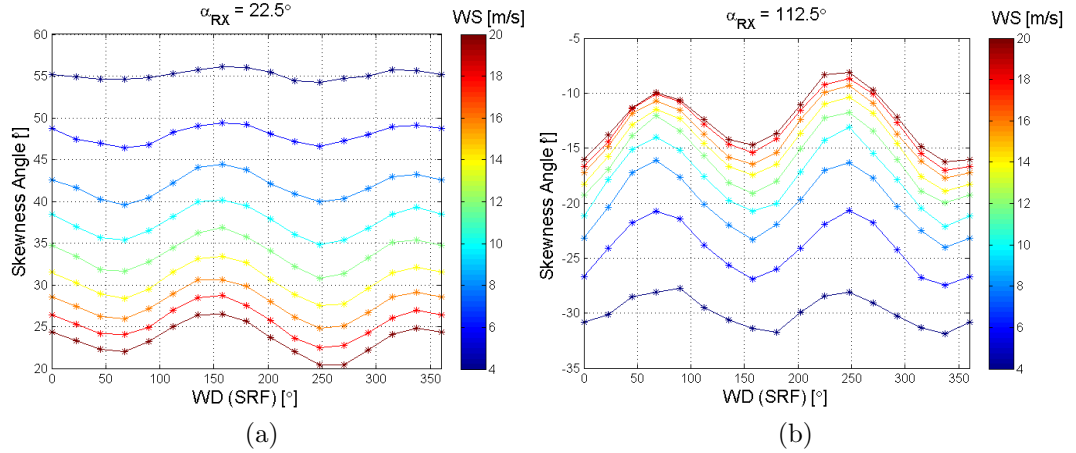
Figure 6.4: φ_{skew} as a function of wind direction and wind speed, for two different α_{RX} values.

Figure 6.4 shows the behavior of the skewness angle as a function of wind direction and wind speed for two different receiver's flying directions. Each figure corresponds to a specific α_{RX}, and the elevation angle is set to $\gamma = 70°$. All direction angles are referred to the scattering plane (scattering reference frame, SRF).

As it is observed, the skewness angle, φ_{skew}, as defined so far, is sensitive to wind direction, but it is very much sensitive to WS and receivers flight direction. These dependences are in line with the work in Zuffada et al. 2003, where the impact on the waveform of WS, ϕ and α_{RX} is presented.

In order to reduce the number of intervening parameters, φ_{skew} was redefined. The main idea was to try to make it independent of the DDM spreading caused by either the WS or the elevation angle. Indeed, this spreading can be described to some extent by the center of mass (CM) of the DDM region with a power greater than -4.3 dB (e^{-1}, when expressed in a linear way), as it was proposed by [58]. The new φ_{skew} was defined by taking CM as a reference to build the vector, instead of the DDM's peak. Then, the new definition became (a graphical representation of this new definition is shown
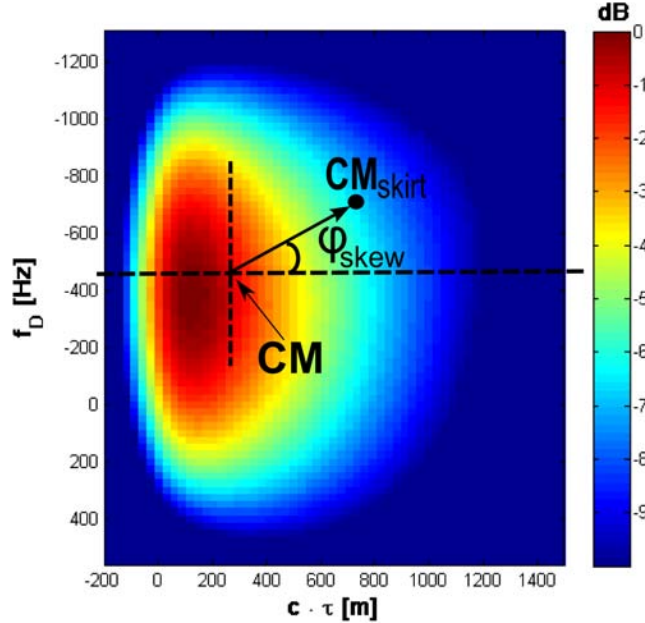
Figure 6.5: New definition of the skewness angle, φ_{skew}.

in Fig. 6.5):

$$\varphi_{skew} = tan^{-1}\left(\frac{CM_{skirt,\tau} - CM_{\tau}}{CM_{skirt,f_D} - CM_{f_D}}\frac{\Delta\tau}{\Delta f_D}\right). \tag{6.2}$$

Figure 6.6 shows the behavior of the new skewness angle as a function of wind direction and wind speed for two different receivers flying directions. Each figure corresponds to a specific α_{RX}, and the elevation angle is set to $\gamma = 70°$. All direction angles are referred to the scattering plane (SRF).

It can be seen that the new definition for φ_{skew} makes it nearly independent of the WS, as desired. For the most WS all the curves are stacked together, except for the corresponding to the lowest WS values of 4 and 6 m/s. This is due to the fact that when the sea is calm the reflection tends to be specular, and the DDM becomes less sensitive to wind direction variations. Moreover, the effect of the local incidence angle could also be considered as negligible, since its effect leads also a DDM spreading, and the

new definition of the skewness angle is practically independent of this effect.

From plots in Fig. 6.6, it can be concluded that wind direction, being retrieved from a single GNSS-R measurement, presents a double ambiguity since there exist four different wind directions with the same corresponding φ_{skew} (for each flight direction). To assemble all the values of the skewness angle as a function of wind direction and receivers flying direction, a surface plot is presented in Fig. 6.7 ($WS = 16$ m/s, and $\gamma = 70°$), along with its best analytical fit.

The expression used to fit the skewness angle distribution as a function of WD and α_{RX} is:

$$\varphi_{skew} = -\left(a \cdot cos(2\alpha_{RX} - 40) + b\right) \cdot sin(2\phi + c\alpha_{RX} + d)$$
$$+ e \cdot sin(2\alpha_{RX} - 20) + f, \tag{6.3}$$

where the six intervening parameters have been optimized in order to minimize the resulting residuals. Table 6.2 summarizes the values obtained for
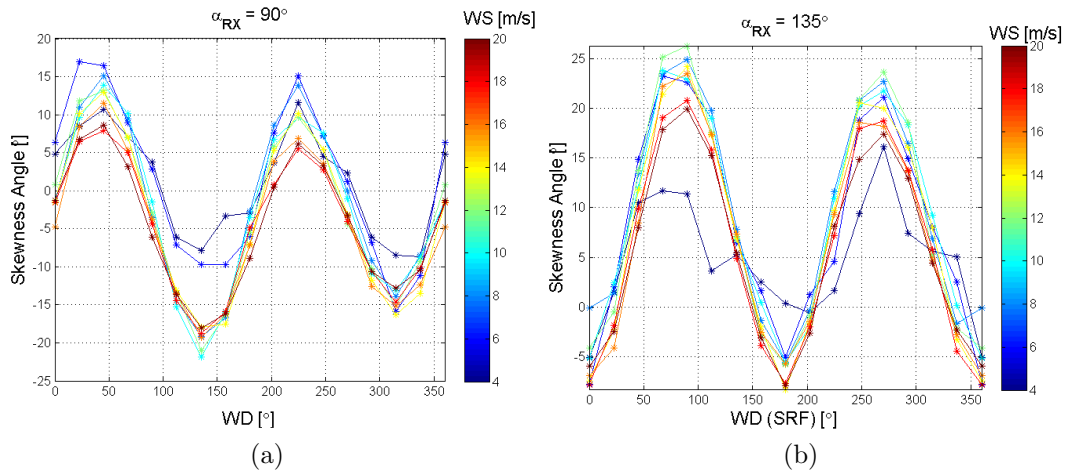
Figure 6.6: φ_{skew} as a function of wind direction and wind speed, for two different α_{RX} values.

these parameters.

Table 6.2: Optimized fit parameters.

a	b	c	d	e	f
-0.88	12.85	-1.88	-11.36	-7.82	-0.98

It can be seen in Fig. 6.7 that, using Eqn. 6.3 with the parameters in Table 6.2, a good approximation to the φ_{skew} surface is obtained. Actually, the fit's determination coefficient is $R^2 = 0.93$, and its residuals present an error RMS of 1.72°. The surface distribution of the error is shown in Fig. 6.8. Note that only the values of α_{RX} between 0° and 180° are shown. This is because the function is periodic, so the values from 180° to 360° repeat themselves.
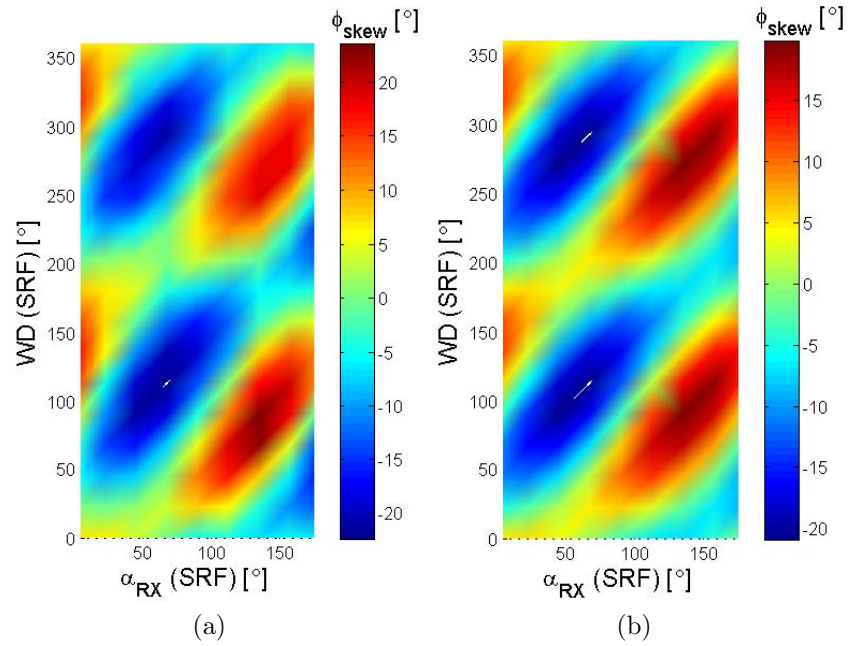
Figure 6.7: a) φ_{skew} as a function of wind direction and wind speed, and b) corresponding fit using Eqn. 6.3.
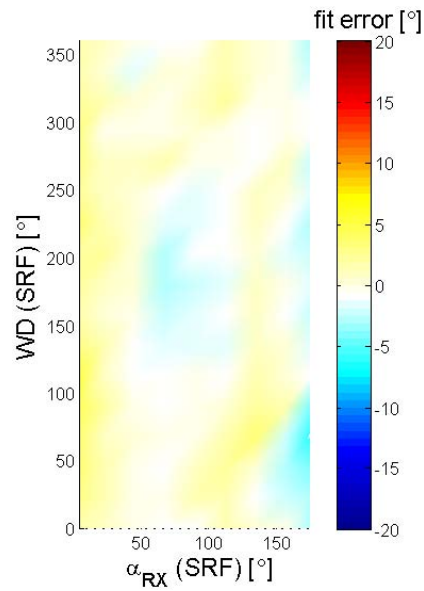
Figure 6.8: Error of the fit computed to model φ_{skew}.

6.4 Validation of the skewness angle model using real data

By studying the asymmetry of the DDM as a function of the observation geometry and the surface's wind speed and direction, a new metric was derived (skewness angle, φ_{skew}). This metric was used to establish a model that relates the DDM asymmetry to the wind direction and the receiver's flying direction.

To assess the validity of that model, real data was used. To do so, the available measurements of the January, 24th flight [58] were used, by computing the DDM's φ_{skew} angle. The ground truth for wind direction and the receivers flying direction were referenced to the SRF, so as to be consistent with the model. The measured φ_{skew} along with the measurements' parameters are presented in Table 6.3.

The ϕ and α_{RX} values from Table 6.3 (when referenced to SRF) were input to the φ_{skew} model (Eqn. 6.3) with the aim to compare the models outputs to the measurements. This is shown in Fig. 6.9 where the measured

Table 6.3: φ_{skew} measured from the January, 24th data along with the measurements' parameters.

Dataset	PRN	WS	WD (wrt N)	SV El/Az	RX dir (wrt N)	WD (SRF)	RX dir (SRF)	φ_{skew}
1	9	15.0	7.5°	55°/250°	91°	117.5°	159°	-4.4°
4	9	16.5	70.9°	60°/325°	80°	105.9°	245°	-20.8°
5	9	22.2	52.2°	60°/310°	97°	102.2°	213°	-4.3°
6	9	6.2	78.5°	66°/355°	86°	83.5°	269°	1.0°
6	15	6.2	78.5°	52°/155°	86°	283.5°	69°	-31.7°
6	27	6.2	78.5°	68°/15°	86°	63.5°	289°	20.9°
7	9	10.4	112.5°	63°/335°	84°	137.5°	251°	-17.7°
7	15	10.4	112.5°	60°/138°	84°	334.5°	54°	-10.0°
9	15	10.0	20.0°	68°/15°	88°	5°	287°	3.5°
10	15	17.5	26.0°	70°/48°	88°	338°	320°	25.4°

skewness angle is plotted versus the modeled one. The measured values tend to group around the 1:1 line except for a couple of outliers. The RMSE of the measurements versus the model is 13.3° (6.5° if the two outliers are not considered).

These are encouraging results, since the resulting error accounts for the addition of: the measurements' noise, the simulator DDM model errors and approximations, the surface fit errors made to derive the φ_{skew} model, and the errors of the SV and receiver position/velocities data. It has also to be noted that all measurements have been included regardless of their different elevations (52° to 78.5°) and WS (6.2 to 22.2 m/s), reinforcing the hypothesis of the φ_{skew} independence with respect to those parameters (related to DDM spreading).
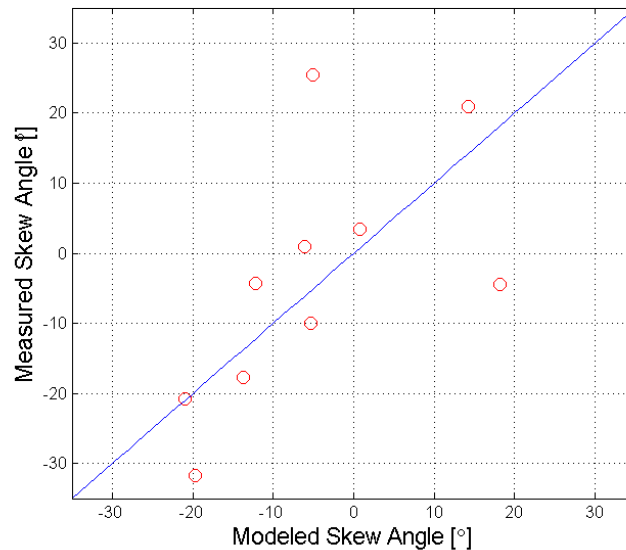
Figure 6.9: Measured versus modeled φ_{skew} (1:1 line is plotted in blue).

6.5 Wind direction retrieval

Once the skewness angle model has been validated, it has been used for wind direction retrieval through its inversion. However, retrievals from a single DDM measurement do present 4 possible solutions. This is due to the ambiguity of the measurement geometry (i.e. 2 xy points correspond to the same delay-Doppler cell), and to the ambiguity of the ocean spectrum itself (180° ambiguity that cannot be resolved). To solve for the first ambiguity, multiple DDM measurements of the same ocean surface are needed.

To invert the model for the wind direction retrieval, the measured φ_{skew} and the recorded α_{RX} have been used (expressed in SRF, see Table 6.3). The inversion of Eqn. 6.3 turned out to have 4 solutions that corresponded to the aforementioned ambiguities of the observation geometry and the ocean spectrum. These solutions are plotted in Fig. 6.10 for each of the 10 available measurements, at the time of the drop-sondes ground-truth measurements. Each one of the four solutions was plotted with a different color and symbol. It is observed that for all cases, except for two outliers (same outlying measurements as in Fig. 6.9), there is always one of the solutions that lays very close to the 1:1 line. The error of those solutions with respect to the ground-truth wind direction measurements has a $RMSE = 31°$ (10.4°, if the two outliers are not taken into account).

Table 6.3 shows that there are two datasets (datasets 6 and 7) with more than one DDM measurement. Those datasets are used to assess the ability to use more than one DDM measurement of the same ocean surface to resolve for the observation geometry ambiguity. To do so, it is needed to transform the solutions obtained for each of the single measurements, in order to be referenced to North (since SRF is not a common reference system). The relationship among both reference systems is the particular SV azimuth angle at the measurement time. By doing this, two of the four solutions did coincide, solving for one of the ambiguities, as it can be observed in Fig. 6.11. The

solutions from the three available measurements of dataset 6 are shown in Fig. 6.11a, and the ones from the two available measurements of dataset 7 are shown in Fig. 6.11b.

At this point, the entire flight dataset was thoroughly analyzed to assess the consistency of the WD retrievals. It was found that most of the measurements (50% approx.) were too noisy to derive a meaningful φ_{skew}. Actually, the noisier part of the flight is the one where the wind speed is higher (above 15 m/s) because of the lower SNR. Since the asymmetry metric is based on the lower power region of the DDM, it is more affected by noise impact. This fact could be overcome in future experiments by using higher directivity antennas, by using higher power signals such as the L5 one
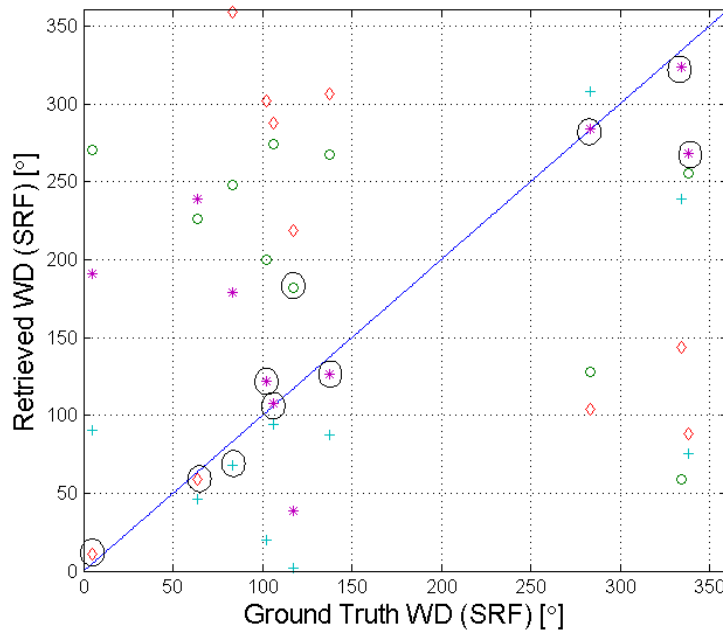
Figure 6.10: Retrieved wind direction. Note that there exist 4 possible solutions for each measurement. Each one of the 4 solutions is plotted with a different color and symbol. Circles mark the most likely one of those four. 1:1 line is plotted in blue.

(3 dB more powerful), or flying at lower altitudes.

Despite that, a time window where measurements from two satellites are present, both with acceptable SNR (SV 9 and 15) was found in the data. This time period spans from 11:55 to 12:15 UTC, which was the interval between datasets 7 an 6 (see Fig. 11). The measured DDM available every 5 minutes were used to perform the presented wind direction retrieval method, by computing the φ_{skew} angle and inverting the theoretical model in Eqn. 6.3. The obtained solutions are shown in Fig. 6.12 for the two different available SV, and after referencing to North through the SV azimuth compensation.

The use of two simultaneous DDM measurements allowed solving for one of the ambiguities since two of their solutions do consistently coincide. It is shown in Fig. 6.12 by the circles: the solid ones are marking the most likely solutions according to the known WD ground truth available from datasets 6
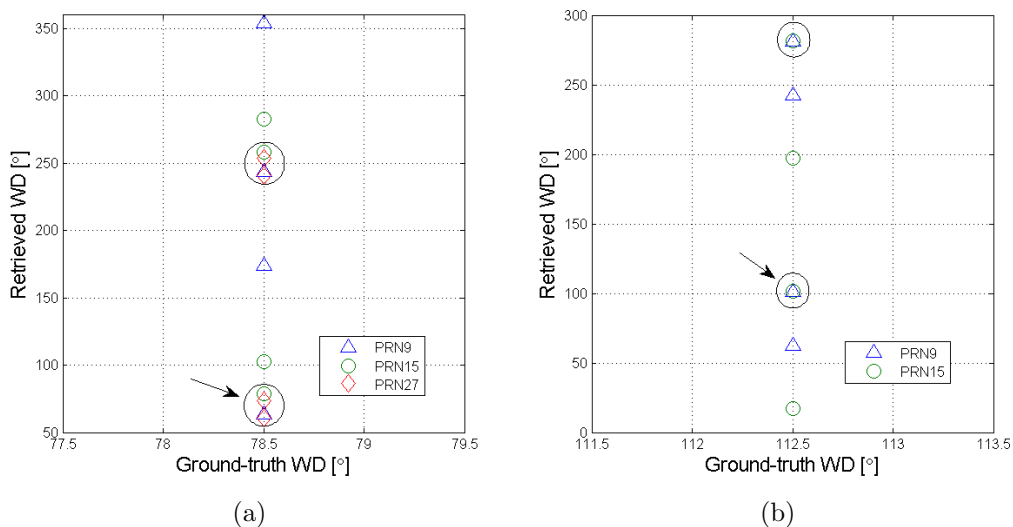
Figure 6.11: Solutions from all DDM measurements of: a) dataset 6, and b) dataset 7. Circles mark the coincident solutions. Arrow points to the closest to the ground-truth data.

and 7 (corresponding to 12:15 and 11:55 respectively); the dashed ones do mark the 180° ambiguous solution caused by the ocean spectrum symmetry.

The obtained ϕ retrievals are consistent along time during the period when measurements are characterized by a sufficient SNR. The time evolution of the solutions is totally attributable to the natural distribution of the wind vectors along the aircraft track. In conclusion, the retrieved ϕ from Fig. 6.12 was combined with the WS retrieved along the flight in [58]. The resulting wind vectors are plotted in Fig. 6.13. The vectors' length is proportional to the retrieved WS (range from 4 to 11 m/s) and their direction corresponds to the retrieved wind direction.
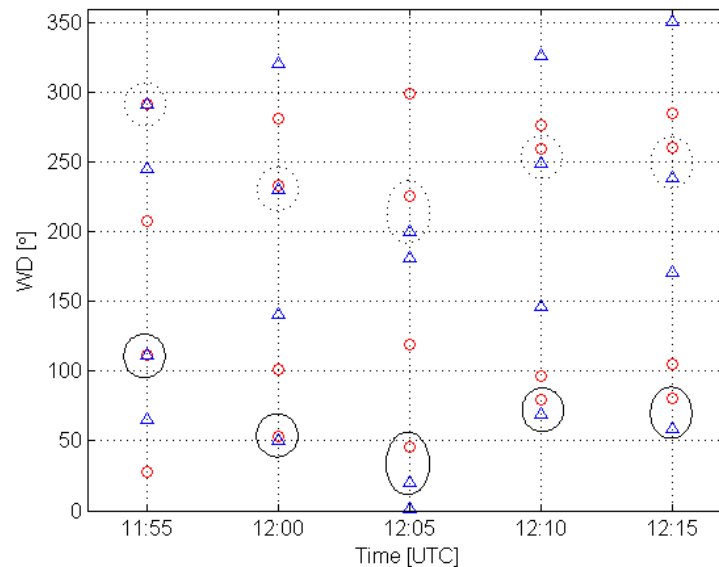
Figure 6.12: Retrieved wind direction from SV 9 (blue triangles) and SV 15 (red dots) measurements between 11:55 and 12:15 UTC. Circles mark the coincident solutions.
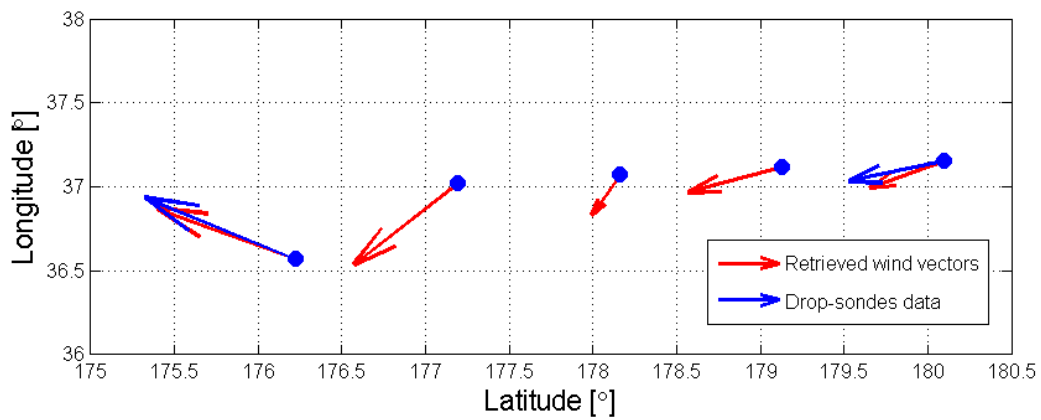
Figure 6.13: GNSS-R derived wind vectors. Vectors' length is proportional to WS retrievals from [58] (range from 4 to 11 m/s). Vectors' direction corresponds to wind direction retrieved by using the presented method.

6.6 Conclusions

The DDM can be regarded as the scattering coefficient distribution over the scattering surface, in the delay-Doppler domain. Thus, it contains information regarding the scattering surface properties. In this PhD. Thesis, information about the ocean surface roughness driven by the wind was retrieved by measuring the spread of the DDM using different descriptors. The observation of airborne data collected by NOAA revealed a DDM asymmetry that appeared to be related to the observation directionality, namely wind direction and receiver's flying direction.

To further explore this observation, intensive DDM simulations were performed, systematically sweeping through the observation geometry and surface parameters (receiver's flying direction, SV elevation, wind speed, and wind direction), considering the actual flight's mean speed and height. Simulations confirmed that the DDM skewness is due to the directionality of the problem (i.e. receiver's flying direction and wind direction). To measure the power map skewness in the delay-Doppler domain, a new metric was envisioned. This metric, named as skewness angle (φ_{skew}) was properly defined not to be sensitive to the parameters that cause a DDM spreading (wind speed and SV elevation angle), but remains sensitive to wind direction, and receiver's flying direction.

However, unlike the DDM spreading metrics used for surface roughness/WS retrieval, the skewness angle could not be directly linked to wind direction through an empirical relationship. It is because there are too many intervening parameters, and the relationships among them and the skewness angle have shown to be nonlinear. Moreover, there was not a sufficient amount of measured data (i.e. a limited sampling of the scenario parameters) to empirically derive a function for φ_{skew}. Instead, the skewness angle derived from simulations was accurately modeled by an analytical expression as a function of wind direction and receiver's flying direction. This model was successfully

validated using real data, by comparing the measured DDM asymmetry with the modeled one while using the ground-truth from drop-sondes for wind direction, and the aircraft's flying direction recorded by the navigation GPS receiver.

Once an appropriate skewness metric was defined and modeled, the measured skewness angles were used for wind direction retrieval by inverting the model. For a single DDM measurement, the model gives four possible solutions due to the double ambiguity of the problem. However, one of the solutions was always close to the ground-truth wind direction ($RMSE = 10.4°$). To solve for one of the two ambiguities, simultaneous DDM mesaurements for different SV were used. After referencing the solutions of the different measurement to the same reference system (North), two of the solutions do coincide. However, a 180° ambiguity still remains and cannot be solved since it is inherent to the ocean waves' spectrum. Even though, this ambiguity can be eliminated by calibrating the retrieved wind direction with available ground truth. Finally, the wind direction and wind speed retrievals were assembled into wind vectors for a part of the flight's track.

The main limitation of the proposed technique was given by the measurements' limited SNR. Since the power skewness caused by wind direction is observed in the lower power region of the DDM (from -4 dB to -8 dB w.r.t. DDM peak), wind direction retrievals are more sensitive to noise than wind speed retrievals (based on the higher power region of the DDM). Actually, it was found that for the particular flight conditions wind direction retrieval was not possible for wind speeds over 15 m/s, due to the insufficient SNR. To overcome this limitation, higher directivity antennas, more powerful signals, or lower flying altitudes should be used in further experiments.

7

The PARIS Interferometric Technique - Proof of Concept experiment

7.1 Introduction

The most common approach that has been used at the time of processing GNSS-R signals is that of correlating the received scattered signal with a locally generated "clean" replica of the known GPS C/A code. In this approach, the direct signal is only used to help the receiver in signal acquisition/tracking operations. However, GNSS satellites also transmit a set of signals that are not publicly accessible (e.g. the P and M codes within the GPS L1 band) which could also be used for remote sensing applications, that would provide the GNSS-R system with larger bandwidths and signal power. These signals' bandwidth/power increase should improve the system's performance (i.e. altimetric precision in the altimeter case).

To make use of the full set of GNSS signals within a determined band, the PARIS concept [11] has gone back to its origins, to change the "standard" GNSS-R processing scheme to one that directly correlates the received reflected signal with the direct one. By doing this, all the common signals collected by the antennas do contribute to the cross-correlation waveform, without having to precisely know the structure of each of the present sig-

nals. This new concept has evolved to an in-orbit demonstrating mission named PARIS-IoD [64]. Nevertheless, the implementation of this GNSS-R approach requires some modifications with respect to the "standard" ones. For instance, high directivity antennas are required in order to achieve a good cross-correlation waveform (XCW) SNR.

To start exploring the feasibility of the concept behind the PARIS-IoD, a set of proof-of-concept experiments sponsored by ESA are being undertaken. The first one of these was known as the PARIS Interferometric Technique - Proof of Concept (PIT-PoC), and took place in the Netherlands at the Zeeland Bridge. The experiment was led by the IEEC-ICE team (Barcelona), and the UPC (Barcelona) and TU Delft (Delft, The Netherlands) collaborated in it. It was a ground-based experiment based on deploying a mast over the sea with the two receiving antennas at its tip (see Fig. 7.1).
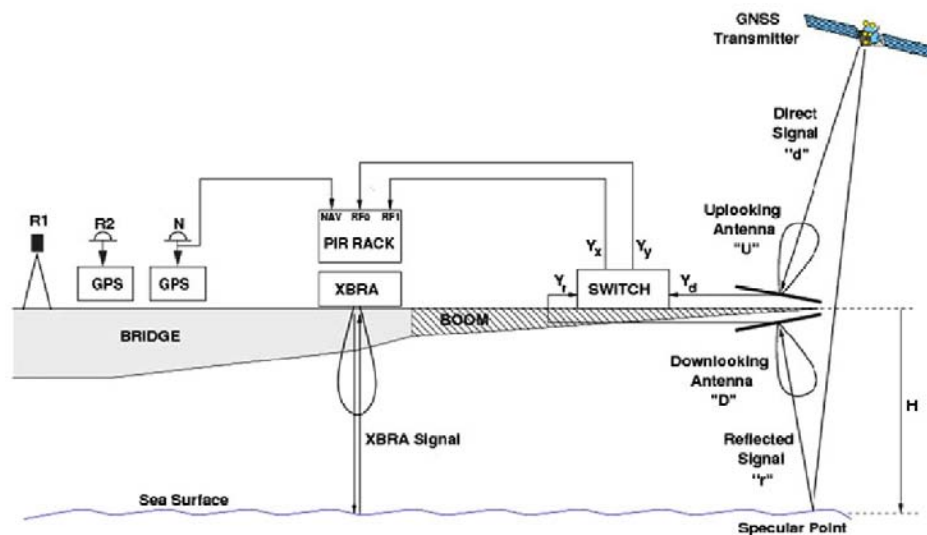
Figure 7.1: PIT-PoC experiment setup (figure from [65]).
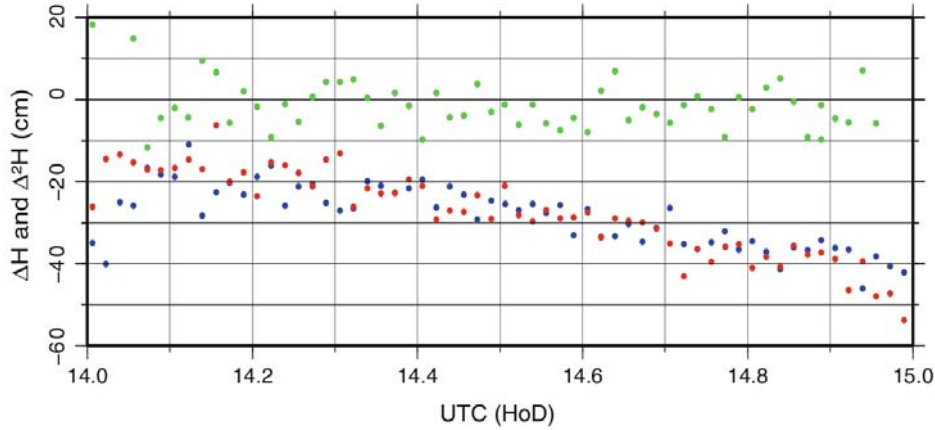
Figure 7.2: Variation of the single-difference $\Delta H(t)$ for both measurement days. Blue dots indicate day 1, and red refer to day 2. The values of the double-difference $\Delta^2 H(t)$ are represented with green dots (figure from [65]).

The PIT-PoC experiment lasted two days on July $7^t h$ and $8^t h$, 2010. The processing of the acquired data served to prove centimetric resolution for altimetry applications [65] using the GPS L1 band. This result can be observed in Fig. 7.2 where the final centimetric resolution is assumed to be the standard deviation of $\Delta^2 H(t)$ (for more information about the interpretation of this result, please refer to [65]).

In the framework of this PhD. Thesis, active support was given to the PIT-PoC experiment preparation and execution. In particular, the antennas along with their mechanical holding system, the RF front-end, and the calibration subsystem were designed and implemented. Moreover, an L-band radiometer was also deployed during the experiment, and the measurements of the GOLD-RTR (secondary GNSS-R receiver used in the experiment) were processed in order to try to link their variations to the ΔT_B observed by the radiometer for sea state effect correction purposes, in line with the objectives of this PhD. Thesis, as it was done in Chapter 4. Unfortunately, conclusive results could not be derived mainly due to two factors: a high level of contamination was present in the radiometric measurements due to

the urban environment, and very low roughness ($SWH < 20$ cm) conditions were encountered during the experiment.

This Chapter is organized as follows:

- Section 7.2 describes the hardware designed and implemented during the preparation of the PIT-PoC experiment, and

- Section 7.3 analyzes the radiometric and GOLD-RTR measurements to perform a sea surface roughness study.

7.2 Hardware development

7.2.1 Antennas

The performance of the proposed PARIS Interferometric Technique is highly dependent on the antennas that are used to collect the up (UP) and down (DW) signals. These are required to have a high directivity, low secondary lobes level and high back-to-front ratio in order not to get a contribution from undesired signals to the XCW. These requirements were specified for the PIT-PoC experiment to be $D = 16$ dB, secondary lobes below -20 dB with respect to the main lobe, and a back-to-front ratio lower than -35 dB.

To achieve the desired specifications, after a series of simulations, the selected antenna architecture (Fig. 7.3) was an hexagonal ground plane where 7 ceramic LHCP/RHCP patch antennas were mounted. These patch antennas were hexagonally positioned with an inter-element spacing of 0.7λ. The signal outputs of these patches were cabled to a microstrip non-resistive power combiner using semi-rigid coaxial cables. The combiner sums all the signals with appropriate weights (0 dB the central element and -7 dB the rest) so as to achieve the desired aperture taper.

The array combiners (Fig. 7.4) have been designed and implemented over
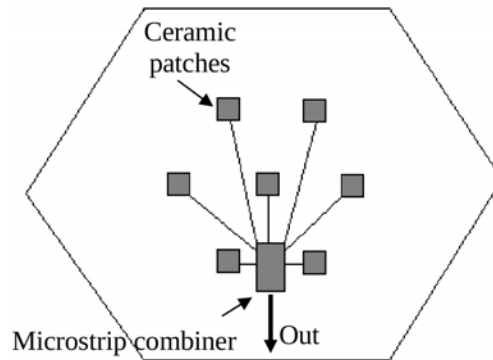
Figure 7.3: Antenna block diagram.
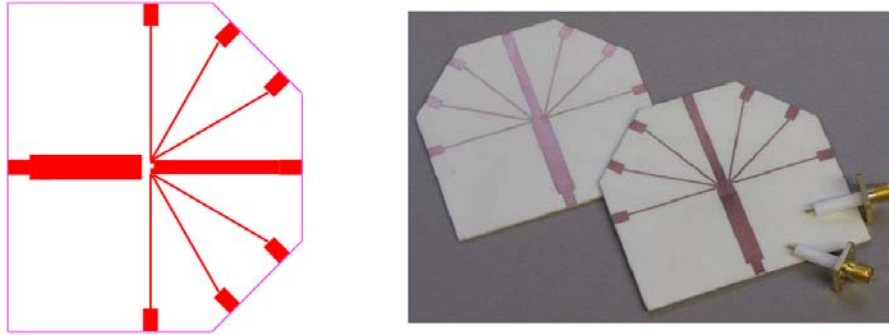
Figure 7.4: Design and implementation of the microstrip combiners.

a Roger 4003 substrate ($\epsilon_r = 3.53$). They have been mounted within aluminum boxes and SMA female connectors have been mounted at the ports.

Two hexagonal ground planes of aluminum-foam layers material have been cut to build both antennas (Fig. 7.5a). These ground planes have been properly crafted to hold the 7 ceramic patches (Fig. 7.5b, LHCP for the down-looking antenna and RHCP for the up-looking) and their respective SMA female connectors (Fig. 7.5c). The feeding network (Fig. 7.5d) is mounted within the back cavity that has been done in the foam. It consists of semi-rigid coaxial cables that route the elementary antennas' signals into the microstrip combiners. A front and back view of the finished antenna is seen in Fig. 7.5e and Fig. 7.5f. A female N-type connector has been mounted at the antennas' output port.

Once both antennas have been finished, a holding system has been mounted so as to measure their antenna patterns at the UPC anechoic chamber as seen in Fig. 7.5f. The resulting measurements are presented in Fig. 7.6 and Fig. 7.7. As it can be seen, the main goal of achieving a back-front ratio of -35 dB has been achieved and the secondary lobes are below -25 dB. The main drawback of this implementation concerns to the cross-polar level within the main beam which is as high as -8 dB. This fact is not foreseen to have a great impact as, due to the experimental setup, cross-polarized signals are not expected to reach the antennas by their main beam direction. The main

features of the antennas are summarized in Table 7.1.

The antenna beam was required to be steered 20° away from the boresight. The first approach was to implement an electrical steering adjusting the patch-combiner cables lengths so as to introduce the corresponding phase. In order to assess this approach, the resulting array factor was simulated and it was seen that the side-lobes level increased from -30 dB (antenna beam pointing to boresight) to an unacceptable -13 dB level (20° steering).

To overcome this effect and fulfill the antenna specifications, mechanical steering was then implemented. It uses a hinge-based system to mount the ground planes on the experiment mast. Steering is adjustable within a range of 5° to 75° by displacing an aluminum clasp along the mast. Details of the actual implementation are presented in Fig. 7.8.

Table 7.1: Main electrical/mechanical features of the implemented antenna

Gain	9.1 dB
Directivity	15 dB
Beam width (-3dB)	32°
Back-front ratio	< -35dB
S_{11} (within L1)	< -20dB
Size (diameter of the hexagonal ground plane)	80 cm
Weight (approx.)	1.8 kg
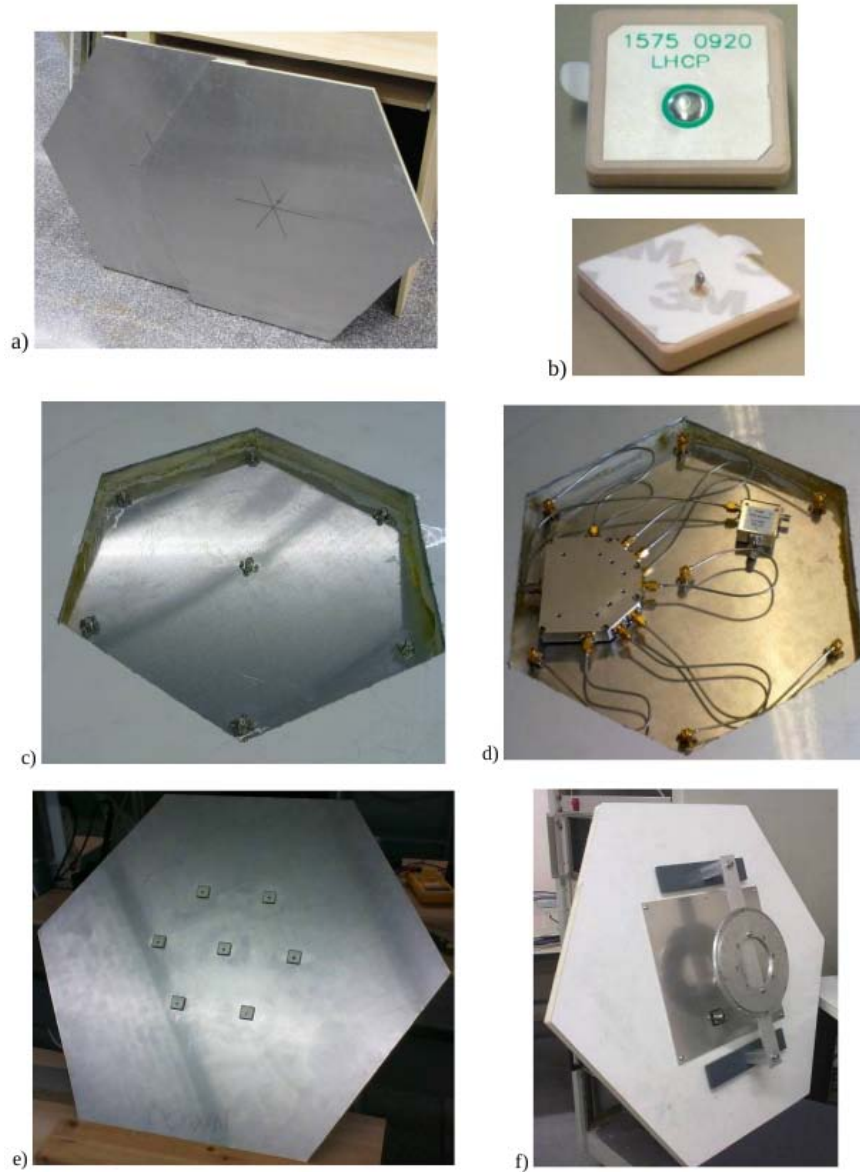
Figure 7.5: Implementation process of the up and down antennas: a) aluminum-foam ground planes; b) single ceramic patch; c) detail of the connectors used to route the output port of each patch; d) view of the feeding network; e) front view of the finished antenna; and f) back view of the antenna with the holding system mounted for its measurement at the anechoic chamber.
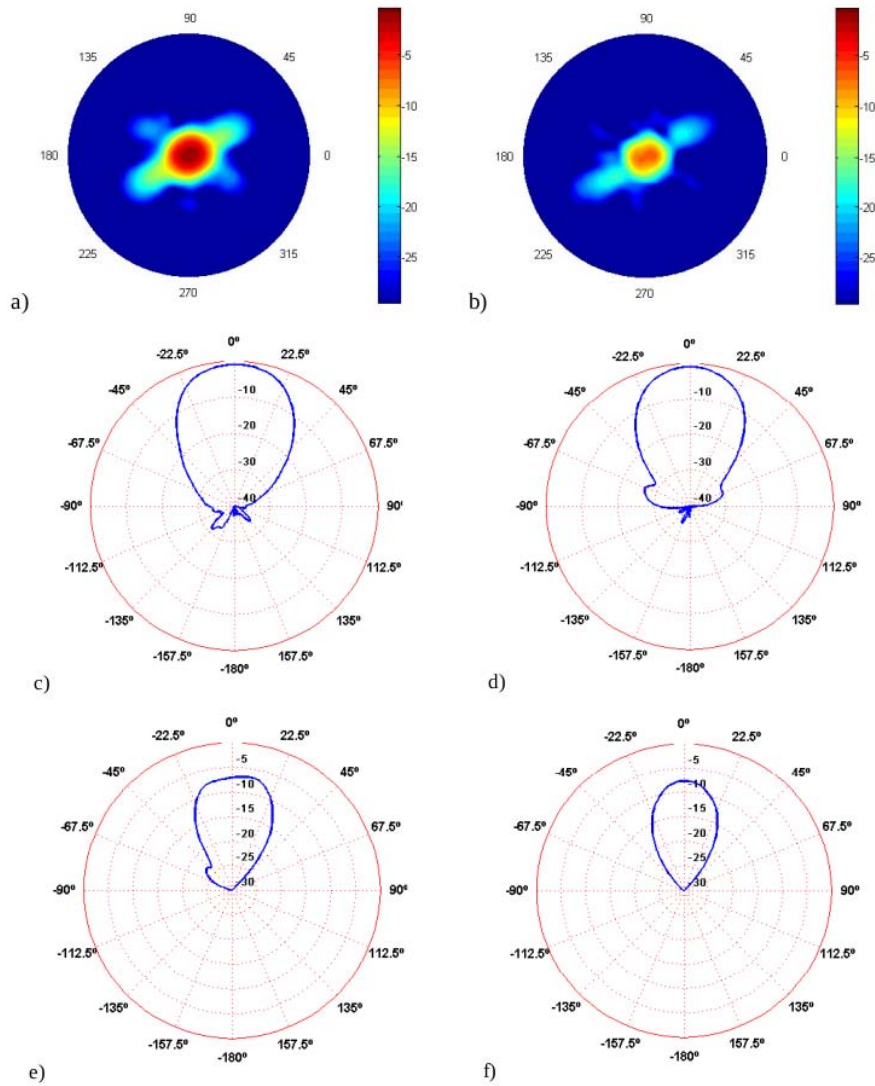
Figure 7.6: RHCP Up-looking antenna performance @1575.42 MHz: a) co-polar radiation pattern; b) cross-polar radiation pattern; c) cut of the co-polar pattern at $\phi = 0°$; d) cut of the co-polar pattern at $\phi = 90°$; e) cut of the cross-polar pattern at $\phi = 0°$; and f) cut of the cross-polar pattern at $\phi = 90°$.
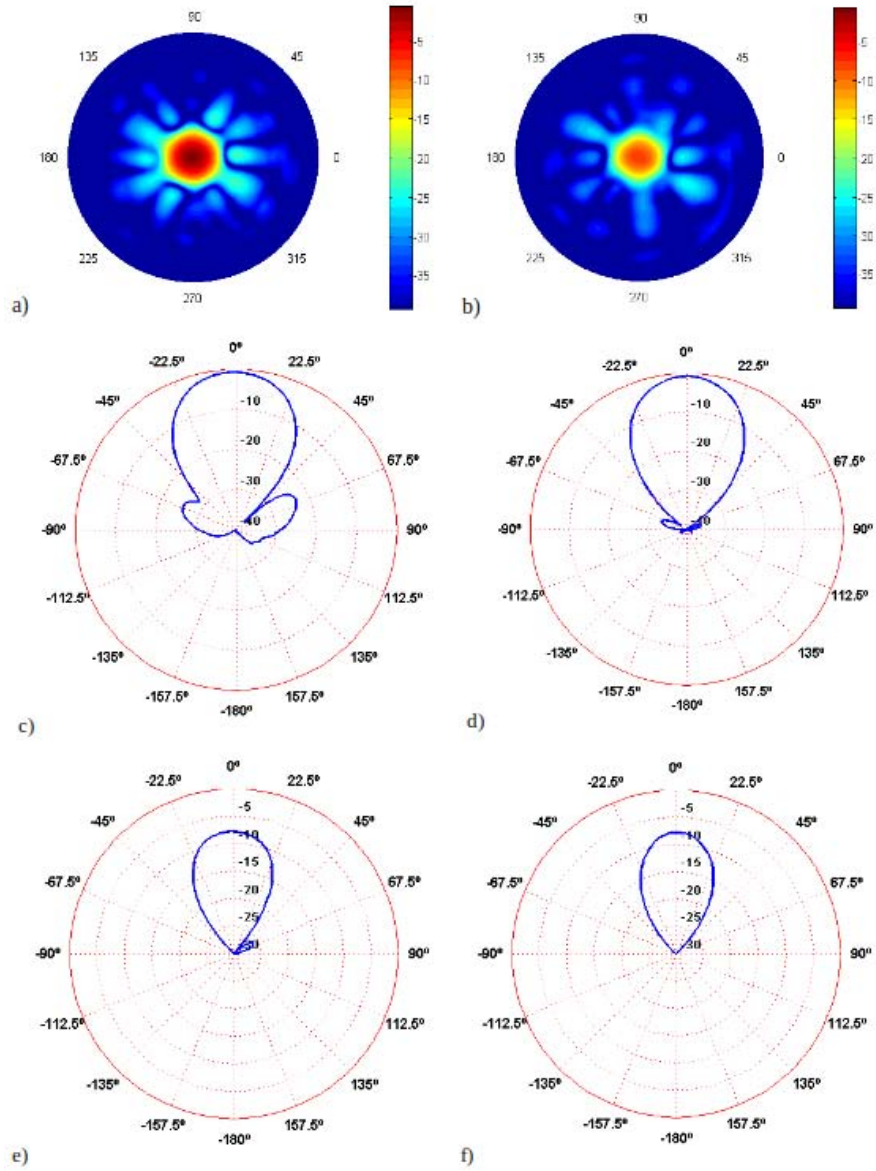
Figure 7.7: LHCP Up-looking antenna performance @1575.42 MHz: a) co-polar radiation pattern; b) cross-polar radiation pattern; c) cut of the co-polar pattern at $\phi = 0°$; d) cut of the co-polar pattern at $\phi = 90°$; e) cut of the cross-polar pattern at $\phi = 0°$; and f) cut of the cross-polar pattern at $\phi = 90°$.
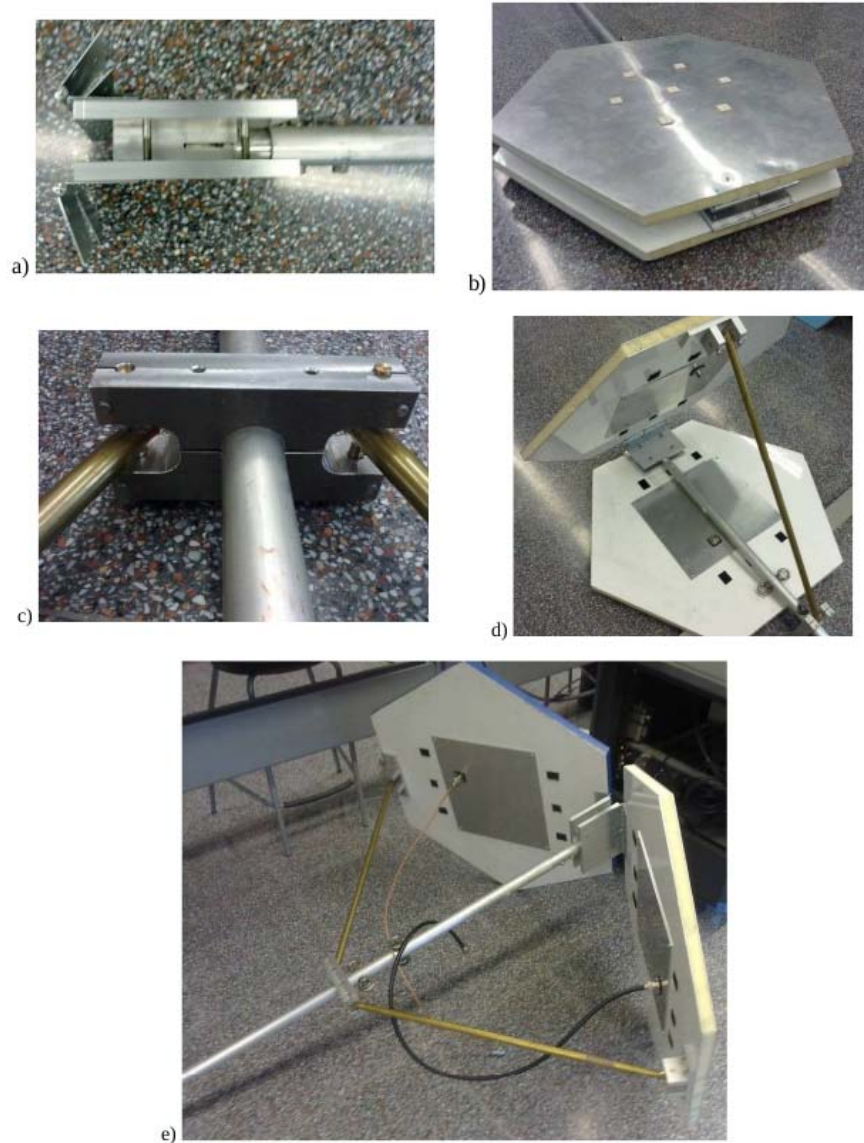
Figure 7.8: Mechanical beam steering implementation: a) detail of the front hinges mounted in the mast; b) antennas attached to the mast by the hinges system; c) detail of the aluminum clasp used to adjust the steering angle; d) back view of the steering system; and e) full steering system assembled.

7.2.2   RF front-end and calibration subsystem

One of the main aims of the PIT-PoC experiment was to demonstrate the proposed calibration techniques that involve swapping the up-looking (UP) and down-looking (DW) receiving paths, as well as injecting signals to both channels. To do so, a dedicated hardware was designed and implemented that could be physically integrable behind the antennas. This hardware, known as "Calibration Box", consists of three main stages: the swapping matrix that allows to swap the UP and DW signal paths to each of the two RF-front-ends, a low noise amplification stage, and a band-pass filtering of the signals. Apart from that, this subsystem also allows to inject common calibration signals to both front-ends such as a hot-load, a cold load or an external input. For more versatility, these signals can be attenuated by 3 dB, if required. For a better understanding, a block diagram of the "calibration box" is shown in Fig. 7.9.

To achieve the desired figures of merit, a modular philosophy (see Fig. 7.10) was follow implementing each systems stage within separate connectorized boxes containing the Critical Design Review (CDR) approved components. By this strategy, a high level of isolation was achieved and the system was easier to debug.

Each of the two signal chains was divided into three modules: the first one contains a 4-port switch that allows selecting the desired input (antenna, signal injection or matched load), and a 2-port switch that routes the signal to the proper second stage in order to perform the path swapping; the second stage contains a 2-port switch that selects the appropriate input from the first stage, an LNA and a band-pass filter; and the third stage contains an amplifier to achieve the required extra gain.

In addition to this, two additional modules were implemented: the signal injection module that generates calibration signals (hot and cold loads, etc.) and splits them into the receiving chains by means of a Wilkinson power splitter; and the power and switches control module.
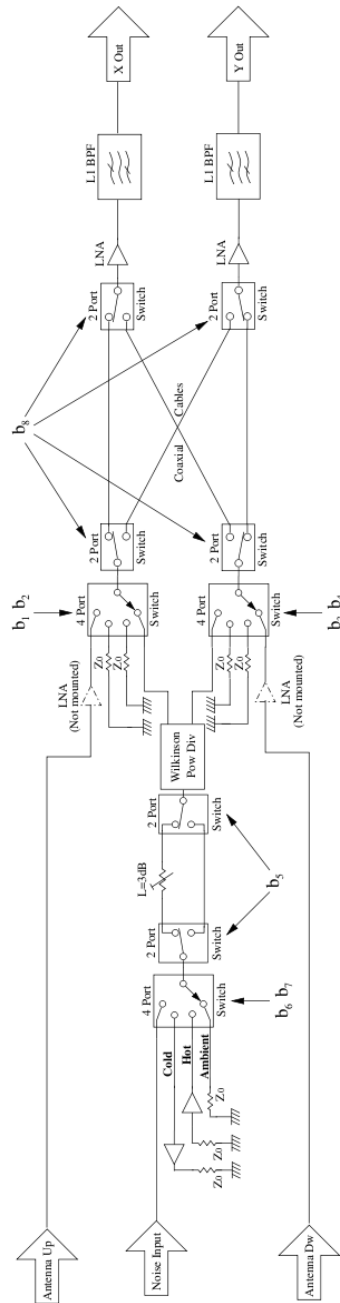
Figure 7.9: Block diagram of the RF front-end and calibration subsystem.
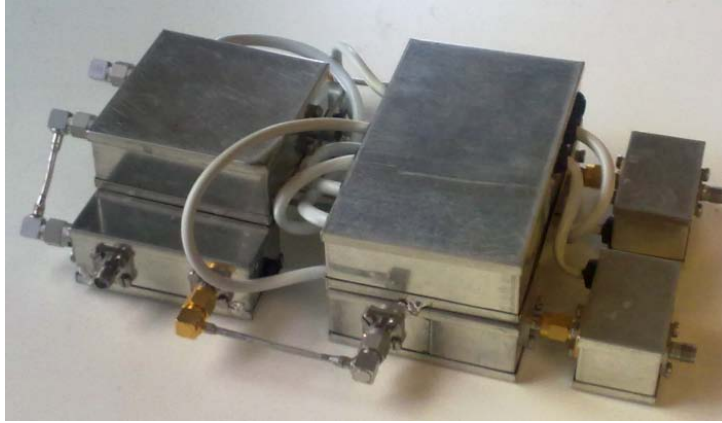
Figure 7.10: In-sight view of the modular implementation of the RF front-end and calibration subsystem.

Apart from the modular design, isolation was also guaranteed by enhancing the ground plane fences around the signal tracks placing a second line of via-holes, as well as with an improved routing. The system was integrated within an IP64 water-proof qualified commercial box (Fig. 7.11).

The final main figures of merit of the system are:

- Isolation: all the measured isolations are below -38 dB.

- Gain: each receiving chain has an overall 18-20 dB gain from the antenna input.

- Noise Figure: The NF is estimated to be 4-5 dB at most. It has been estimated by measuring the insertion losses of the first stage (4-port and 2-port switches) which are -1.8 dB, estimating the losses before the LNA in the second stage to be -1 dB and considering the LNA NF of 1.15 dB.

In the Table 7.2, the main relevant measured S-parameters of the system are shown (note that the measurement noise floor is at -45 dB due to the network analyzer sensitivity). The port numbering can be seen in Fig. 7.11 and the configuration naming is:

- A: Antenna input selected, thru paths.

- As: Antenna input selected, crossed paths.

- External thru: External correlated injection input selected, thru paths.

- External cross: External correlated injection input selected, crossed paths.

- U: Uncorrelated noise sources selected (internal matched loads).

Figure 7.11: External view of the RF front-end and calibration subsystem.

Table 7.2: Measured S-parameters of the "Calibration Box".

	A	As	External thru	External cross	U
S_{31}	18.5dB/-134°	-42dB	-19 dB	-	-20.5 dB
S_{42}	20.2dB/-121°	-36.2 dB	-20 dB	-	-18.5 dB
S_{32}	-33dB	18.3 dB/-148°	-	-21.7 dB	-
S_{41}	≤-45dB	20.2 dB/-128°	-	-18 dB	-
S_{35}	≤-45dB	≤-45 dB	12.7 dB/-120°	13.7 dB/-121°	-
S_{45}	≤-45dB	≤-45 dB	14.6 dB/-132°	14.4/-127°	-
S_{11}	-8.8dB	-9.2 dB	-	-	-
S_{22}	-9.7dB	-9.0 dB	-	-	-
S_{33}	-9.8dB	-9.7 dB	-	-	-
S_{44}	-14.3 dB	-14.7 dB	-	-	-
S_{55}	-	-	-15.9 dB	-15.6	-

7.3 Study of the sea surface roughness within the PIT-PoC Experiment

7.3.1 Experimental setup

During the PIT-PoC experiment, an L-band radiometer was deployed jointly with a GNSS-R real time receiver to study the effects of sea surface roughness over both instruments' measurements as well as the relationship among them.

Figure 7.12 depicts the measurement setup at the Zeelandbrug bridge with the radiometer deployed side-by-side to the GNSS-R antennas' mast. The RADAC waveguide X-band radar was mounted near the bridge's control tower.

7.3.1.1 Ground truth data

To validate the impact of the sea surface roughness on the radiometric and GNSS-R measurements, an independent data source is needed. The RADAC waveguide X-band radar significant wave height (SWH) measurements have been used in this study as sea surface roughness ground-truth. Again, more information about the RADAC instrument and its measurement setup can

Figure 7.12: Measurement setup at the Zeelandbrug bridge: There is the L-band radiometer in first term, and the GNSS-R antennas' mast behind it. The RADAC instrument was mounted near the bridge's control tower observed at the picture's background

be found in www.radac.nl.

7.3.1.2   L-band Radiometer

The radiometer that was used is the one designed for the ALBATROSS field experiment (see Chapter 4). This radiometer has a total power/direct detection architecture and works at 1.413 GHz with a bandwidth of 50 MHz and a RF gain of 63 dB. Dual polarization measurements are obtained by periodic switching of the RF front-end input between the outputs of the vertical and horizontal antenna arrays. Each antenna array has 7 elements hexagonally distributed, each element being a microstrip patch with dielectric air. The resulting beamwidth is 22°. A block diagram of the radiometer architecture is shown in Fig. 7.13.
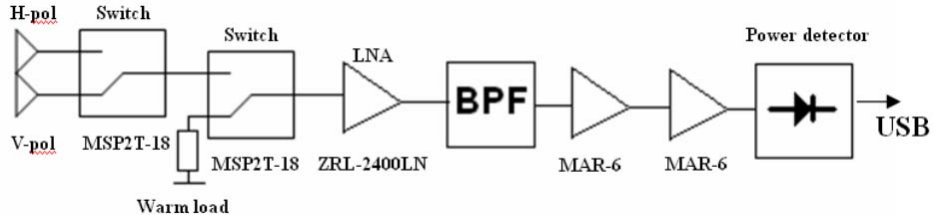
Figure 7.13: Schematic block diagram of the total power radiometer deployed at
the Zeelandbrug

Frequent calibration of the radiometer was performed during the experiment to overcome gain drifts. Considering the measured thermal stability of $0.34 \, \mathrm{K}/^\circ\mathrm{C}$, the periods were sky calibration every 20 minutes and internal hot load calibration every 5 minutes. The incidence angle for the measurements was set to $\theta = 35^\circ$. A basic integration time of 1 s was used.

7.3.1.3 GNSS-R receiver

GNSS-R measurements were acquired using the antenna, and the RF switching and conditioning HW manufactured by UPC for the PIT-PoC experiment. The signal was split and fed from the RF front-end of the PIR instrument to the GOLD-RTR instrument [48]. GOLD-RTR is a GNSS-R receiver developed by IEEC that computes waveforms in real time. The obtained waveforms are computed by correlation of the input UP (direct) and DW (reflected) signals with a set of local replicas of the GPS C/A code. More details about the GNSS-R instrumentation deployed and the bridge's measurement setup can be found in the main PIT-PoC experiment's documentation.

7.3.2 Measurements and results

The data corresponding to July 8th has been processed in this study. This day has been chosen as it is the most complete of the two experiment days in terms of collocated measurements of the three considered datasets: ground-truth data, L-band radiometric measurements, and GNSS-R measurements.

7.3.2.1 Ground-truth data

In this study, the significant wave height (SWH) product from the RADAC instrument has been used as a proxy for actual sea surface roughness. These measurements are delivered at a rate of one measurement per minute. In Fig. 7.14 the SWH measurements are shown. It can be observed that there was a weak sea surface roughness variation during the experiment. Actually, SWH had a mean of 12 cm and a standard deviation of 2.5 cm. These values indicate a very calm sea with respect to the L-band wavelength ($\approx$20 cm).
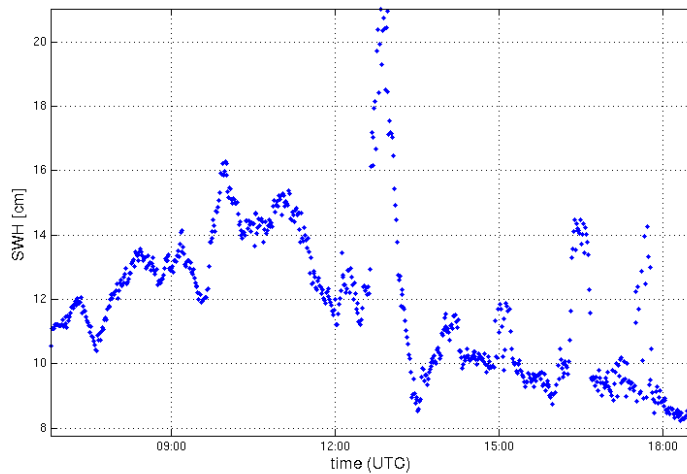
Figure 7.14: Significant wave height measurements delivered every minute by the RADAC instrument during the July 8th, 2010

7.3.2.2 Radiometric measurements

Dual polarization L-band radiometric measurements were acquired along the experiment. The first step to process this dataset has been to validate the radiometric sensitivity of the instrument. It has been done using the data acquired when sky-calibrating and computing its standard deviation. A value of $\Delta T = 0.18K$ is obtained, and a piece of data corresponding to sky mea-
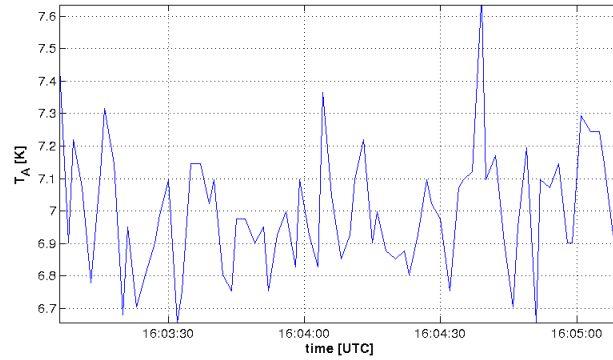
Figure 7.15: Piece of antenna temperature measured when pointing to sky for cold load calibration

surement is shown in Fig. 7.15. The instrument's stability is guaranteed by short-term calibration (Section 7.3.1.2).

Calibrated antenna temperatures for both polarizations are presented in Fig. 7.16. Only the data until 14:00 UTC has been considered since afternoon measurements were corrupted by the Sun glint (the radiometer was pointing North-West).

Some spikes are present in the measurements which are caused by boats passing and presence of seabirds within the antenna beam. Moreover, neglecting the spikes, measured antenna temperatures show instantaneous variations up to 2 K. However, these variations are larger than the predicted sea state influence using current models, since the expected brightness temperature sensitivity to SWH is around 1 K/m at most [27], and the sea conditions of the experiment day showed very small variations (Section 7.3.2.1). To assess that, antenna temperatures have been integrated up to 1 minute (i.e. the SWH measurements period), and have been plotted versus their corresponding SWH value. These results are shown in Fig. 7.17 where no correlation between antenna temperatures and SWH is observed.
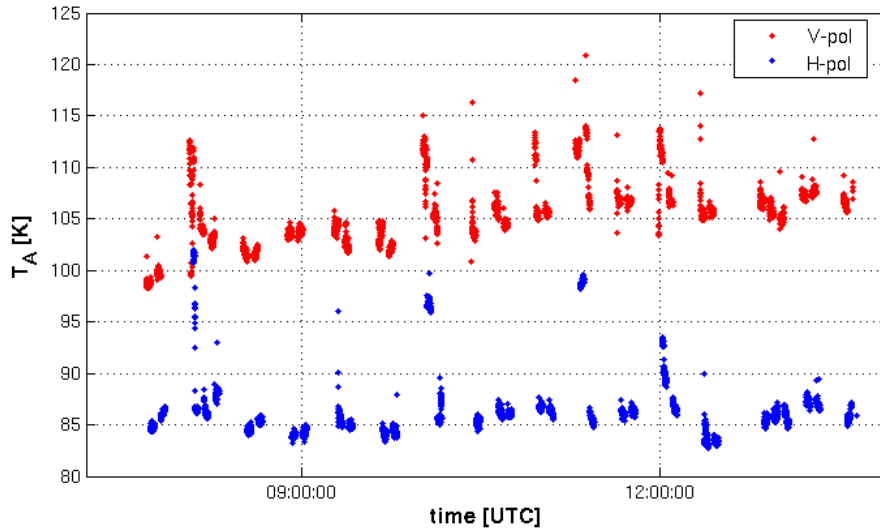
Figure 7.16: Calibrated antenna temperatures (1s integration time) measured during the July, 8th

7.3.2.3 GNSS-R measurements

The used GNSS-R measurements are the GOLD-RTR 64-lags waveforms incoherently integrated up to 1 s. These waveforms have been acquired and processed both for UP and DW signals, both acquired by the same GOLD-RTR RF link (LINK2) taking advantage of the switching sequence implemented for PIR calibration purposes. The resulting waveforms are plotted in Fig. 7.18 for a particular satellite pass.

The raw waveforms present a high variability even for the direct signal, which is due to the antenna pattern modulation that can be clearly appreciated when plotting the time evolution of the waveforms' maximum (Fig. 7.19).

To follow on processing the GNSS-R dataset, a correction of the antenna pattern has been applied. This has been done (first approach) by assuming that both antennas (UP and DW) have equal antenna patterns and that they are correctly pointed. By assuming this, a 5th order polynomial has been

(a) Horizontal polarization   (b) Vertical polarization
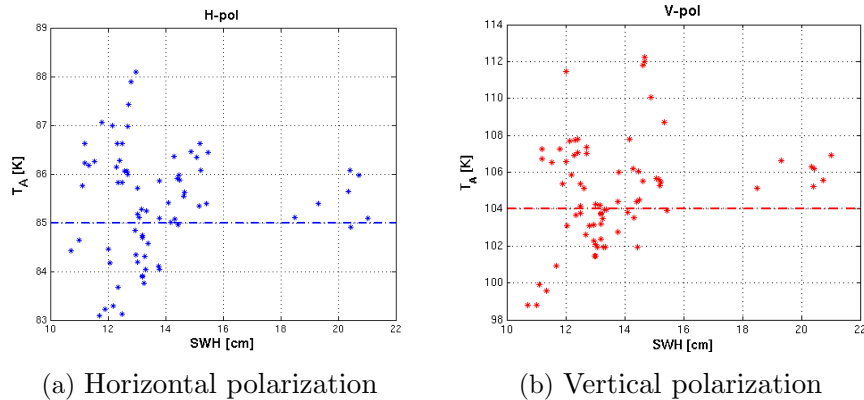
Figure 7.17: Calibrated antenna temperatures (incidence angle $\theta = 35°$) vs. significant wave height. The dashed line corresponds to the model output for a calm sea with SST=293 K and SSS=36 psu.

fitted to the time evolution of the UP waveforms' maximum, and it has been used to correct the DW waveforms. The result is shown in Figs. 7.21 and 7.20.

The time evolution of the DW waveforms' maximum presents a clear Speckle pattern (multiplicative noise) while the UP waveforms are mainly affected by additive noise (i.e. thermal) (Fig. 7.21). These effects are also visible in the stacked waveforms plots (Fig. 7.20).

To assess the impact of sea surface roughness, the shape of the waveform has been studied first. To do so, the DW waveforms (reflected signal) have been normalized by their maximum (Fig. 7.22), and the area below it has been computed after placing a threshold of 0.2 to minimize the impact of the noise floor (Fig. 7.23) (note that the Speckle-induced variability is canceled around the peak thanks to the normalization). The area of the normalized waveform is an observable (analogous to the volume of the normalized DDM volume [19]) that describes the power spreading of the received signal along the delay domain. It is well known that the larger sea surface roughness, the more power spreading will occur, so the normalized waveform's area can be

(a) Direct signal (UP)

(b) Reflected signal (DW)
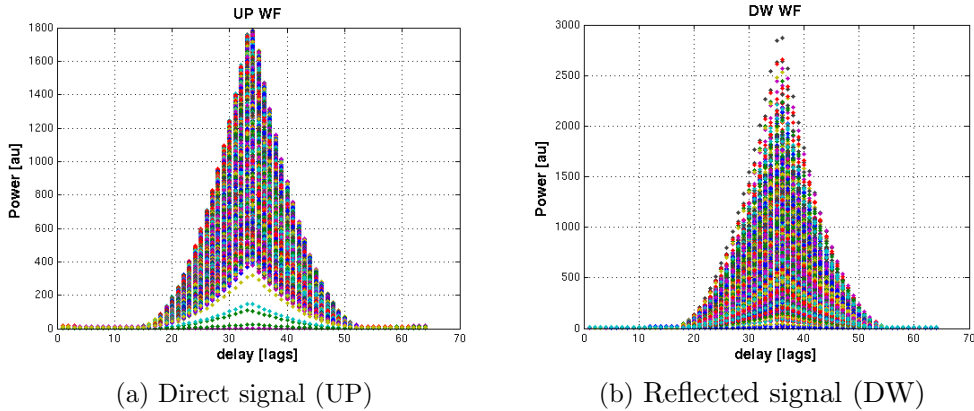
Figure 7.18: Raw waveforms measured by the GOLD-RTR instrument for a particular satellite pass (PRN26)
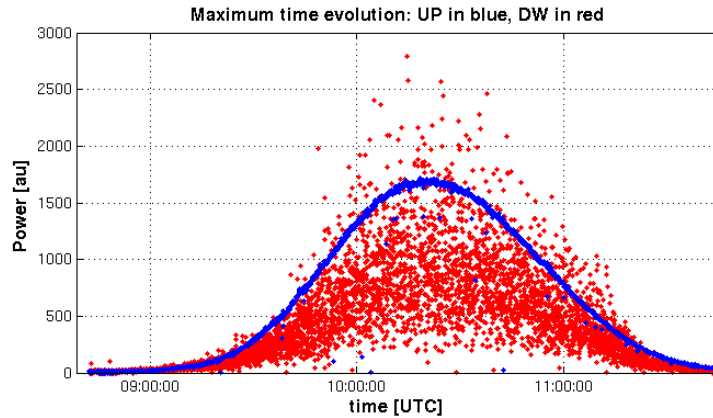
Figure 7.19: Time evolution of the waveforms' maximum (UP and DW waveforms) for a particular satellite pass (PRN26)

actually regarded as a sea surface roughness descriptor.

However, it is observed in Fig. 7.23 that the area of the normalized waveforms stick to a constant mean value for the acquired satellite passes along the experiment day (disregarding noise and error amplification effects due to the antenna pattern correction). Moreover, the mean area computed for the DW waveforms is very similar to that of the UP waveforms ($\mu_{UP} = 0.59$),

(a) Direct signal (UP)

(b) Reflected signal (DW)
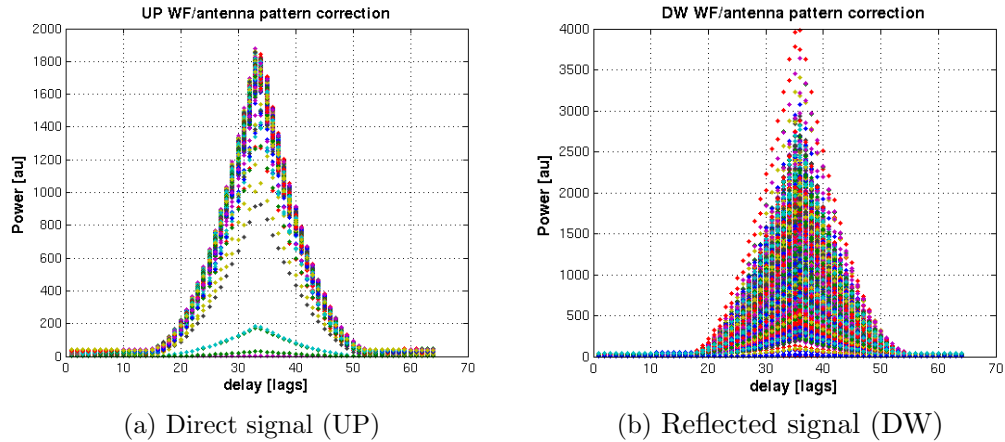
Figure 7.20: Raw waveforms measured by the GOLD-RTR instrument for a particular satellite pass (PRN26)
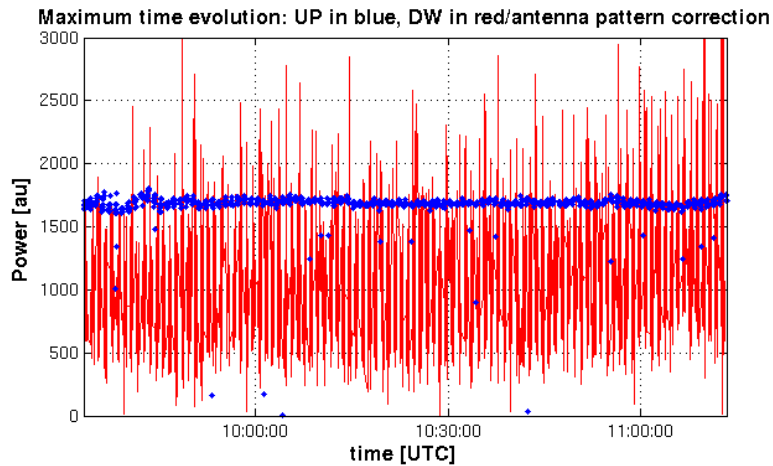
Figure 7.21: Time evolution of the waveforms' maximum (UP and DW waveforms) for a particular satellite pass (PRN26)

thus no significant power spreading is present and no sea surface roughness effects are affecting the waveform's shape. Nevertheless, taking into account the ground truth data (Section 7.3.2.1) that do not show significant sea surface roughness variations, and considering that the antenna footprint is smaller than the first chip iso-range region (very low height observations),
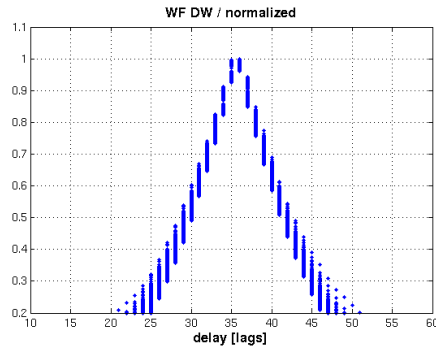
Figure 7.22: Stacked normalized 1s DW waveforms for a particular satellite pass (PRN26)
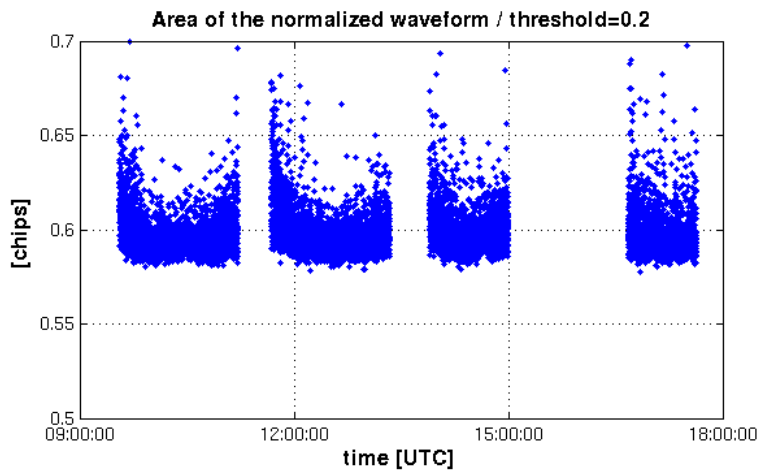
Figure 7.23: Time evolution of the normalized waveform area for the acquired satellite passes along the experiment day

this is a consistent result.

To follow on with the study of the sea surface roughness effects on GNSS-R data, the Speckle noise level has been monitored as another roughness descriptor. In order to minimize the fluctuations of the Speckle noise estimation, the Speckle noise level has been computed as the standard deviation of the individual 1 s incoherently averaged DW waveforms' maximum over its mean value (σ/μ) along 5 minutes intervals of measurements. This parame-

ter also accounts for the thermal noise, but the Speckle noise term is clearly dominant for this experiment case (low height observation). The Speckle noise level along the experiment day, considering all the satellite passes is shown in Fig. 7.24.

It is seen that the Speckle noise level has a random distribution around a clear mean $\sigma/\mu = 0.48$, which is lower than the expected for a Rayleigh distribution ($\sigma/\mu = \sqrt{2/\pi} = 0.799$) denoting the presence of a coherent component (resulting in a Rice pdf). The Speckle noise level is constant during the experiment day (the dispersion level is dependent of the length of the used data interval). This enforces the hypothesis that the very low sea surface roughness variations are not affecting the GNSS-R measurements.
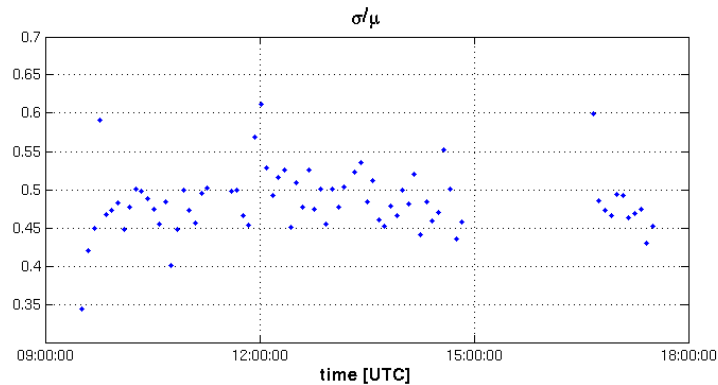
Figure 7.24: Time evolution of the Speckle noise level for the acquired satellite passes along the experiment day

7.4 Conclusions

The PIT-PoC experiment was sponsored by ESA and led by IEEC-ICE with collaborations of UPC and TU Delft. It was successfully undertaken to proof the centimetric resolution capabilities of the PARIS interferometric technique for altimetric applications. This experiment required the deployment of the appropriate instruments in the Zeeland Bridge, in the Netherlands, during two measuring days.

During the preparatory activities for the PIT-PoC experiment, the antennas and the RF front-end and calibration subsystem were designed and implemented according to the given requirements. Two symmetrical antennas were built in order to collect direct (RHCP) and reflected (LHCP) GPS L1 signals. These were designed to present a very low back-to-front ratio, and a high directivity along with low secondary lobes level in order to filter out all the possible undesired signals. Regarding the RF front-end and calibration subsystem, they were designed and implemented to provide the signals' paths swapping and signal injection capabilities required to perform the calibration techniques, as well as to have the lowest possible noise figure. Also a very low coupling among the two signal paths was achieved mainly by following a modular architecture, enclosing each stage in a separate box.

After the experiment, the data acquired by the GOLD-RTR (secondary GNSS-R receiver used in the experiment) and the L-band radiometric measurements were processed in order to perform a study on the sea surface roughness during the experiment. It was intended to serve for sea state effect correction purposes in line with the main objective of this PhD. Thesis. However, there were two main factors that prevented the study to pursue conclusive results. Firstly, the sea surface roughness conditions were very stable and low along the two measurement days. That implied a nearly specular reflection for the GNSS-R measurements, and a nearly negligible sea state induced ΔT_B for the radiometric data. Secondly, the urban environ-

ment where the experiment took place caused a high level of contamination on the radiometric measurements which presented a high level of variability, that could not be attributed to the sea state effect. Nevertheless, at least the study performed on the GNSS-R data showed consistent results with the low and stable sea surface roughness conditions (i.e. no waveform spreading).

Part III

Towards Spaceborne
Sea State Monitoring Using
GNSS-R Techniques

<div align="right" style="font-size:4em">**8**</div>

On the use of direct GNSS-R observables for sea state monitoring from space

8.1 Introduction

So far, for ground-based [66] and airborne [67] measurements, it has been empirically observed that the selected GNSS-R descriptors (normalized DDM volume and normalized waveform area, respectively) are practically independent of the observation geometry, so its effect can be neglected. However, in the way towards applying the proposed GNSS-R sea state descriptors to a spaceborne scenario, a deeper analysis of these descriptors dependence on the geometry must be performed. Even more, considering that in a spaceborne scenario the receiver dynamics are larger, the platform is at a higher altitude and, thus, the glistening zone becomes larger, and presents a significant Doppler spread across it. All these factors are very relevant at the time of determining the DDM shape, so they all are envisaged to have an impact on the observables/descriptors computed from the DDM and/or the waveform.

Previous studies such as [19], preliminary explored the performance for

sea state description of a particular GNSS-R observable (the normalized DDM volume) for a spaceborne receiver. However, that study did only consider a nadir reflection geometry. In this PhD. Thesis, a comprehensive simulation study of the observation geometry's impact on different GNSS-R observables has been performed for a spaceborne scenario (fixed receiver's speed and height). In this study the observation geometry has been programatically changed by modifying its three main parameters, which are: flying direction of the transmitter and the receiver, and the incidence angle of the reflection. Moreover, the observed surface has also been changed (wind speed and direction) to assess the magnitude of the geometry parameters' impact on the GNSS-R observables ability to describe sea state.

This chapter presents the results and main conclusions of this study, and it is organized as follows:

- Section 8.2 describes the setup of the simulation study. It presents the main parameters and assumptions that have been adopted.

- Section 8.3 compares the impact of the observation geometry on different GNSS-R observables.

- Section 8.4 assesses the performance of the normalized DDM volume to monitor the sea state from space.

8.2 Simulation setup

8.2.1 Considered observation geometries

When considering the different observation geometries that can take place in a GNSS-R space mission, a set of parameters have to be defined to properly describe them (Fig. 8.1). Apart from the receiver's platform height (h_{RX}) and speed (v_{RX}) that are determined by the mission's orbit; and apart from the the transmitter's platform height (h_{TX}) and speed (v_{TX}) that are determined by the GPS SV orbits; there are three main parameters that describe the scattering geometry: the local incidence angle of the reflection (θ_i) and the flying direction of the transmitter's and receiver's platforms (α_{TX} and α_{RX}, respectively). Moreover, the scattering surface has been parameterized in terms of the wind speed (WS) and the wind direction (ϕ).
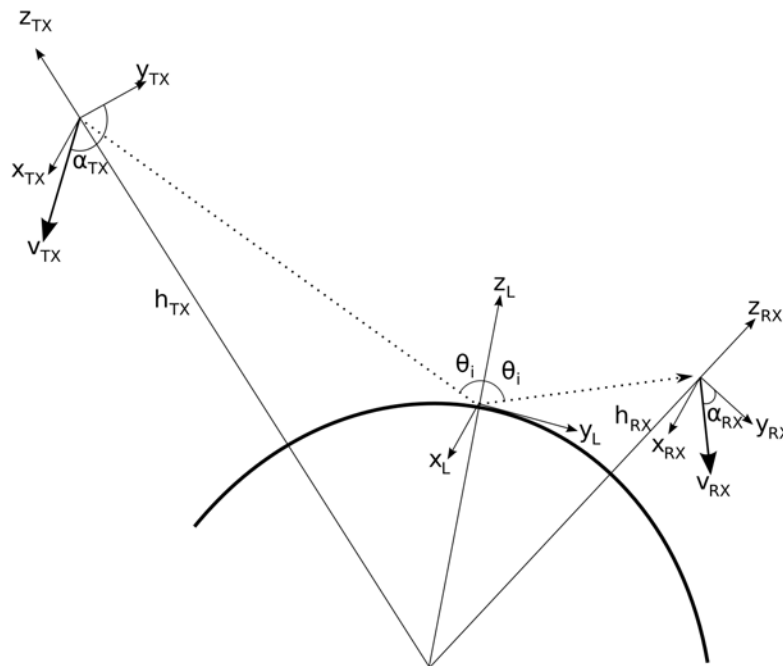
Figure 8.1: Definition of the observation geometry and its main parameters.

The considered values for the geometry's and surface's parameters are listed in Table 8.1. As it can be seen, the direction angles α_{TX}, α_{RX}, and ϕ have been quantized in 40° steps, fine enough to track the smooth evolution of the GNSS-R observables, but also coarse enough to reduce the simulation's number of iterations. With respect to WS, it spans from 3 m/s (low) to 21 m/s (moderate-high). According to these parameters' range and quantization, the total number of combinations is 56000 different scenarios that have been simulated.

8.2.2 Considered Delay-Doppler Mapping conditions

A DDM has been simulated for each of the resulting combinations of the five parameters previously mentioned. The used tool has been the PAU/PARIS End-to-end Performance Simulator [59] which requires very low computation time with respect to "classical" DDM simulation approaches (3 s per 250 x 250 points DDM, versus 2 h for the double integration over the surface, using the same PC) since it implements a numerically optimized version of the improved algorithm proposed in [63]. The simulation set has been computed with the Delay-Doppler (DD) domain quantized in 0.1 C/A chips in

Table 8.1: Considered values for the observation geometry's and surface's parameters.

	Range	Step
GPS SV height (h_{TX})	20192 km	-
GPS SV speed (v_{TX})	3.9 km/s	-
GPS SV flying direction (α_{TX})	[0,360]°	40°
Platform height (h_{RX})	500 km	-
Platform speed (v_{RX})	7 km/s	-
Platform flying direction (α_{RX})	[0,360]°	40°
Local incidence angle (θ_i)	[0,35]°	5°
Wind Speed (WS)	[3,21] m/s	3 m/s
Wind Direction (ϕ)	[0,360]°	40°

delay and 50 Hz in Doppler shift, which is fine enough for scatterometric applications since they are based on the shape of either the DDM or the waveform. Figure 8.2 shows a DDM from the obtained dataset. It is observed that the selected quantization of the Delay-Doppler domain allows to perfectly retrieve the received power distribution (i.e. DDM shape), as expected.

As a first approximation, and to clearly isolate the effect of the observation geometry, noise has been neglected and an isotropic antenna pattern has been assumed. The impact of noise is further taken into account in Section 8.4.2.

Taking into account the total number of DDMs to be simulated according to the different defined scenarios (56000 DDMs), a total computation time of 55 hours was required to perform the whole simulation process (versus nearly 13 years if the double integration method over the physical surface was to be used). Results were stored in a total of 28 GB data space.
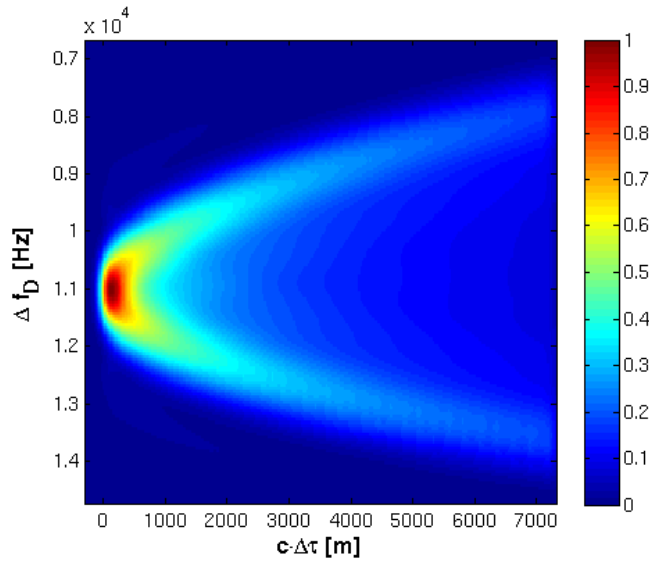
Figure 8.2: Sample of the simulated DDMs. Parameters of this run were: $\alpha_{TX} = 80°$, $\alpha_{RX} = 80°$, $\theta_i = 35°$, $WS = 9$ m/s, and $\phi = 160°$.

8.3 Comparison of the observation geometry's impact on direct GNSS-R observables

The first step of the simulation dataset analysis process has been to compute a set of 4 different GNSS-R observables from each one of the simulation's DDMs. This set has been chosen so as to be composed of 2 full-DDM based and 2 waveform's ($\Delta f_D = 0$) observables: the normalized DDM volume (V_{DDM}, see Chapter 4), the *taxicab* distance (d_{taxi}, recently proposed and defined in [58]), the normalized waveform area (A_{WF}, see Chapter 5), and the length of the waveform's tail (τ_{tail}, see Chapter 4).

To explore the observation geometry impact on the measurements, each of these 4 observables has been plotted versus the WS, including all the considered values for the other 4 scenario's parameters (namely flying direction of the transmitter's and receiver's platforms, the local incidence angle, and the wind direction). The resulting plots are presented in Fig. 8.3.

The 4 selected GNSS-R observables are clearly affected by the observation geometry and this effect appears to be proportional to the WS (i.e. sea surface roughness). Qualitatively, it can be affirmed that, when the sea is calm, sea surface roughness retrievals can be performed with a low error regardless of the observation geometry. However, for rough sea surfaces a correction of the geometry effect is mandatory.

A saturation effect is also observed in Fig. 8.3: The higher the WS is, the lower the sensitivity becomes. The combination of these two phenomena (i.e. geometry impact increasing and sensitivity decreasing with sea surface roughness), makes the sea surface roughness retrieval a true challenge for WS values over 10-12 m/s.

(a)   (b)

(c)   (d)

Figure 8.3: Impact of the observation geometry on: a) normalized DDM volume; b) *taxicab* distance; c) normalized waveform area; and d) length of the waveform's tail. Red lines correspond to logarithmic function fit to the values of the observables computed for each of the considered scenarios (blue dots).

The dependence of all these observables on the WS can be well described by logarithmic functions. The obtained fitting functions have been plotted along with the simulated values in Fig. 8.3, and their corresponding expressions are given in Table 8.2.

In order to compare the performance of these observables to describe the sea state parameterized by the WS, in terms of sensitivity and error, a quality metric Q^{-1} has been defined as:

$$Q^{-1} = \frac{RMSE}{\alpha},\tag{8.1}$$

where α is the multiplicative factor that is applied to the logarithm function (see Table 8.2) and, thus, representative of the observables sensitivity to WS. The closer Q^{-1} is to zero, the better.

As it can be seen, there is a clear difference in terms of performance among the observables derived from the full-DDM, and those derived from the waveform. While the first group presents determination coefficients (R^2) higher than 0.9, for the second group they are below 0.75. Moreover, the Q^{-1} factor is below 0.2 for the full-DDM observables, and over 0.37 for the waveform-based ones.

This significant performance difference is related to the observable's ability to describe the received scattered power distribution in the delay-Doppler (DD) domain. Since the observation geometry effect is basically to determine the iso-delay and iso-Doppler lines layout throughout the glistening zone, its

Table 8.2: Impact of the observation geometry on the considered GNSS-R observables.

Fit	R^2	$RMSE$	Q^{-1}
$V_{DDM} = 6771 \cdot ln(WS) + 3175$	0.93	1170	0.17
$d_{taxi} = 14210 \cdot ln(WS) + 15520$	0.91	2880	0.20
$A_{WF} = 0.71 \cdot ln(WS) + 1.48$	0.74	0.26	0.37
$\tau_{tail} = 0.49 \cdot ln(WS) + 1.13$	0.61	0.25	0.51

impact is reflected on the DDM shape. As the surface roughness increases, the scattered power distribution spreads over the DD domain. Thus, the full-DDM based observables will be more sensitive to this power spreading, and less to observation geometry because they account for the all the power contributions (i.e. they are computed as integrals over the DD domain). Although, both V_{DDM} and d_{taxi} perform similarly, the adoption of V_{DDM} appears to be preferable because its computation only requires one 2D integral, instead of the three that are needed to compute d_{taxi}.

On the other hand, there is also a significant performance difference among the two waveform based observables A_{WF} and τ_{tail}. This is due to the fact that the first one is computed as an integral of the waveform, so it is considering all the waveform's points, and the second one only takes into account two of the waveforms' points (the maximum and the one where the waveforms decays down to a 1/e factor).

The main conclusions of this comparison analysis can be summed up into the two following statements:

- Sea state monitoring from space using direct GNSS-R observables requires the use of the complete DDM to minimize the observation geometry impact on the measurements. For computation resources optimization, the use of V_{DDM} is preferable.

- Even though full-DDM based observables are used, a correction of the observation geometry impact is needed over moderate sea-surface roughness (WS values over 10-12 m/s).

8.4 Performance assessment of the normalized DDM volume

As it has been presented in Section 8.3, the normalized DDM volume is the best performing and less computation demanding direct full-DDM based GNSS-R observable for spaceborne scenarios. However, the variations of the observation geometry do cause an impact on V_{DDM} (see Fig. 8.3a) that has to be accounted for in order to perform useful sea state retrievals. In this Section, the impact of each of the scenario parameters considered in the simulation is particularly addressed and a correction is proposed, when possible.

8.4.1 Impact of the scenario

8.4.1.1 Transmitter's flying direction effect

The V_{DDM} has been observed (example shown in Fig. 8.4) to be totally independent of the transmitter's flying direction (α_{TX}). This is explained by the fact that the iso-delay and iso-Doppler lines layout is mainly determined by the receiver's platform flying speed and direction.

Figure 8.4: Impact of α_{TX} on V_{DDM} ($\alpha_{RX} = 0°$, $\theta_i = 0°$, and $\phi = 0°$).

8.4.1.2 Local incidence angle effect

The local incidence angle has a minor impact on V_{DDM} as it can be seen in Fig. 8.5a, and its effect is totally separable (i.e. independent) of WS and ϕ. In Fig. 8.5b, V_{DDM} is shown as a 2D function of the local incidence angle and the receiver's platform flying direction. The resulting function can be well fitted ($R^2 = 0.98$ and $RMSE = 48$ chips·Hz) by a simple equation, that can be used to correct the effect of the measurements' θ_i:

$$V_{DDM}|_{\theta_i\ corrected} = V_{DDM} -$$
$$\left[\left(-1.1\theta_i^2 - 0.7\theta_i \right) + 228.8 \left(cos(2\alpha_{rx}) - 1 \right) \right] - 220 \qquad (8.2)$$

The improvement after applying the proposed correction, can be observed in Fig. 8.6. A new logarithmic fit has been performed to the corrected V_{DDM}

(a)   (b)
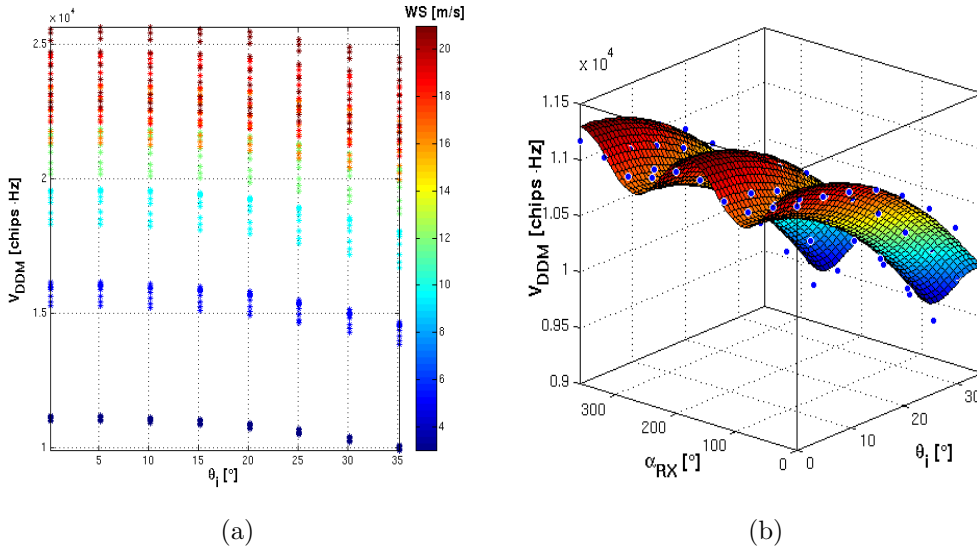
Figure 8.5: Impact of the local incidence angle: a) V_{DDM} as a function of θ_i, and b) V_{DDM} as a function of θ_i and α_{RX} ($WS = 3$ m/s; $\phi = 0°$) along with the fitted surface.

(Table. 8.3). By correcting the impact of θ_i, the $RMSE$ has been reduced, and the quality factor Q^{-1} has been improved from 0.17 to 0.14. In fact, there has not been a large improvement (recall that θ_i causes a minor impact), but the required correction can be easily performed since it can be analytically computed. For the sake of clarity, in Fig.8.7 the effect of the local incidence angle correction is also presented.

Table 8.3: Impact of the observation geometry on the considered normalized DDM volume after correction of the local incidence angle effect.

Fit	R^2	$RMSE$	Q^{-1}
$V_{DDM} = 6771 \cdot ln(WS) + 3654$	0.95	967	0.14
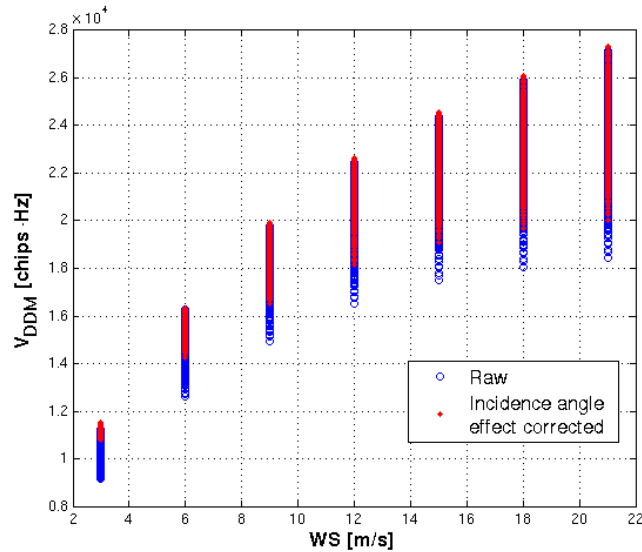
Figure 8.6: V_{DDM} as a function of WS (all considered observation scenarios) after correcting the impact of the local incidence angle.

8.4.1.3 Receiver's flying direction and wind direction effects

Once the local incidence angle impact has been corrected for, and taking into account that V_{DDM} is independent of α_{TX}, the effects of the receiver's flying direction and wind speed direction have to be properly considered in order to improve the final sea state (WS) retrievals. In Fig. 8.7c and Fig. 8.7d the dependence of V_{DDM} on these two scenario parameters is shown for two cases when one of these parameters is fixed.
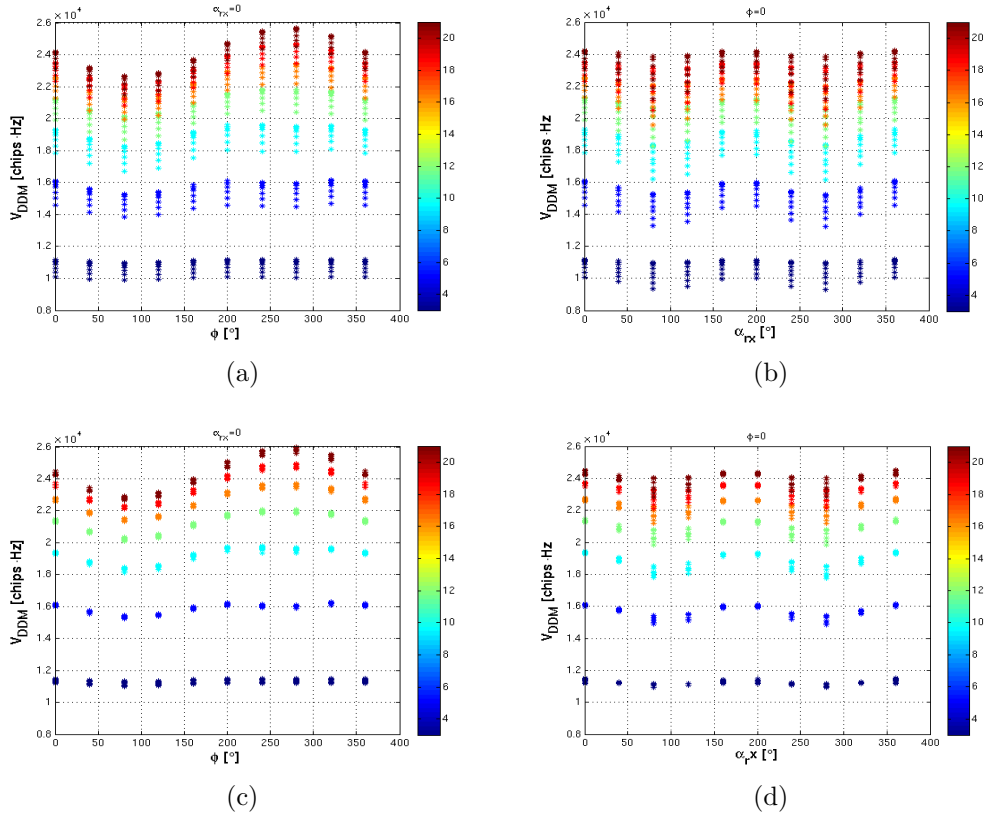
Figure 8.7: a) V_{DDM} vs. wind direction for a $\alpha_{RX} = 0°$; b) V_{DDM} vs. receiver's flying direction for $\phi = 0°$. c) and d) correspond respectively to a) and b) after applying the proposed local incidence angle correction (Eq. 8.2).

The first issue that can be observed in these figures is that the dependence of V_{DDM} on α_{RX} and ϕ is also dependent on WS. Moreover, in Fig. 8.8 V_{DDM} has been plotted as a 2D function of α_{RX} and ϕ for $WS = 21$ m/s, where it is seen that the effects of these two parameters are not independent, nor separable. Unlike the case of θ_i, it is not possible to apply a simple correction for the impact of these parameters. Nonetheless, wind direction is not a-priori known since it is a feature of the surface under observation.

From these statements, the best way to deal with the effect of α_{RX} might be to perform a comprehensive simulation during the mission preparation to generate a set of look-up tables $V_{DDM}(\alpha_{RX}, WS, \phi)$ that will serve to retrieve the desired WS value. In Fig. 8.9, the V_{DDM} has been plotted again as a function of WS, after θ_i correction, and assuming a known $\alpha_{RX} = 0°$ (other α_{RX} values result in similar plots).
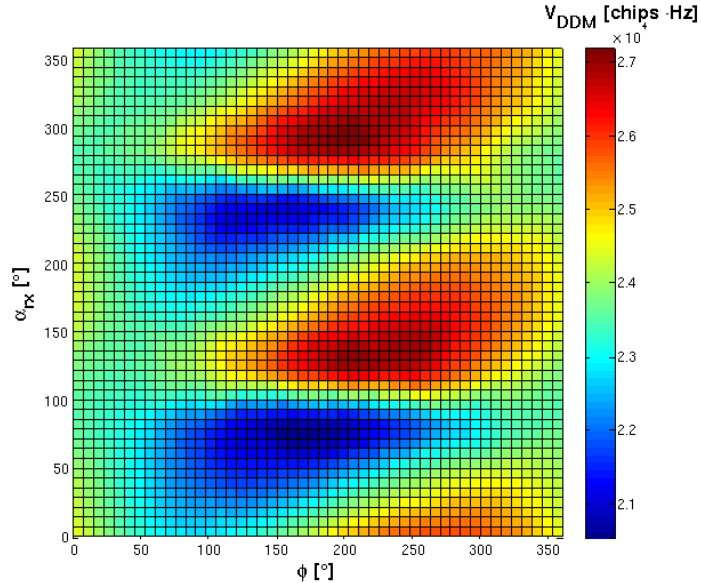
Figure 8.8
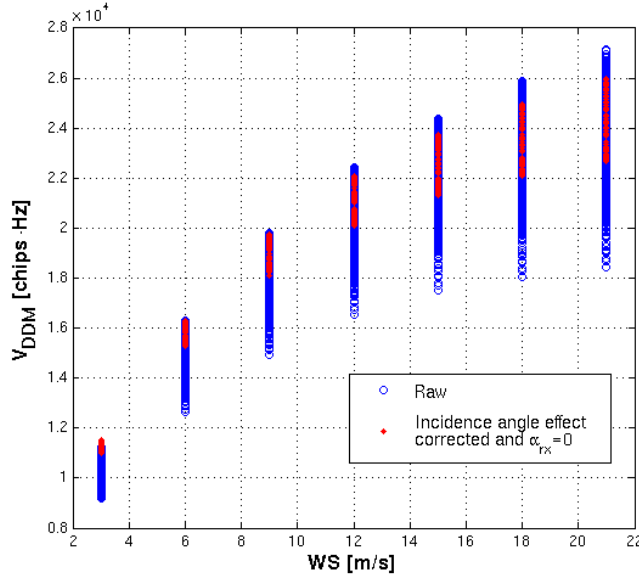
Figure 8.9: V_{DDM} as a function of WS after correcting the impact of the local incidence angle, assuming a known receiver's flying direction $\alpha_{RX} = 0°$. Results are similar for other α_{RX} values.

The resulting fitted logarithm function is given in Table 8.4. By considering the observation's geometry, the final performance of V_{DDM} as a sea state descriptor has been nearly doubled in terms of quality (Q^{-1} has decreased from 0.17 to 0.10). However, there still exists an ambiguity among wind speed and direction which cannot be resolved if extra information is not provided (i.e. a multi-look approach to solve for an equation system, or the use of auxiliary wind direction data).

Table 8.4: Impact of the wind direction on the considered normalized DDM volume. The incidence angle effect has been corrected and a known receiver's flying direction is assumed.

Fit	R^2	$RMSE$	Q^{-1}
$V_{DDM} = 6880 \cdot ln(WS) + 3572$	0.98	714	0.10

For a single V_{DDM} measurement, and without auxiliary information, the achievable absolute performance is limited to ± 3 m/s at intermediate WS values around 10 m/s, due to the ambiguity introduced by the wind direction effect.

8.4.2 Impact of noise on the normalized DDM volume performance

The impact of noise on the normalized DDM volume performance has been evaluated by means of simulating a "worst case" scenario. To do so, thermal complex noise has been added to the 1 ms DDM for a particular observation geometry ($\alpha_{TX} = 0°$, $\alpha_{RX} = 0°$ and $\theta_i = 0°$). The selected SNR for these DDMs has been the one observed from the UK-DMC measurements [68] which is around 0 dB (see Fig. 8.10b). To derive the final V_{DDM} products, these complex DDM have been incoherently integrated up to 1 s (Fig. 8.10c):

$$DDM_{noisy,\ 1\ ms} = \left| \sqrt{DDM_{ideal}} + \frac{\sqrt{DDM|_{peak}}}{\sqrt{2}\sigma_{noise}} \left(n_i + jn_q\right) \right|^2 ,$$

$$DDM_{noisy,\ 1\ s} = \frac{1}{1000} \sum_{N=0}^{1000} \left(DDM_{noisy,\ 1\ ms} - \left\langle n^2 \right\rangle\right) , \qquad (8.3)$$

where the term $< n^2 >$ is the average noise power which is subtracted to the noisy DDM every millisecond to compensate for the large offset that is introduced at the integration process (also known as the noise floor). This term is computed by averaging the DDM regions where there is no signal (i.e. DD points that do not have a physical correspondence in the scattering surface) [19].

This is a "worst case" scenario due to two main reasons: first, the noise has been considered to be thermal (constant SNR across the DD domain)

while real noise is a combination of thermal and Speckle noise which is proportional to the received power for each DD point; and second, the UK-DMC antenna has a relatively low directivity around 12 dB (i.e. lower signal's SNR) with respect to planned GNSS-R missions such as PARIS-IoD will have 6-8 dB larger directivity.

(a)

(b)

(c)
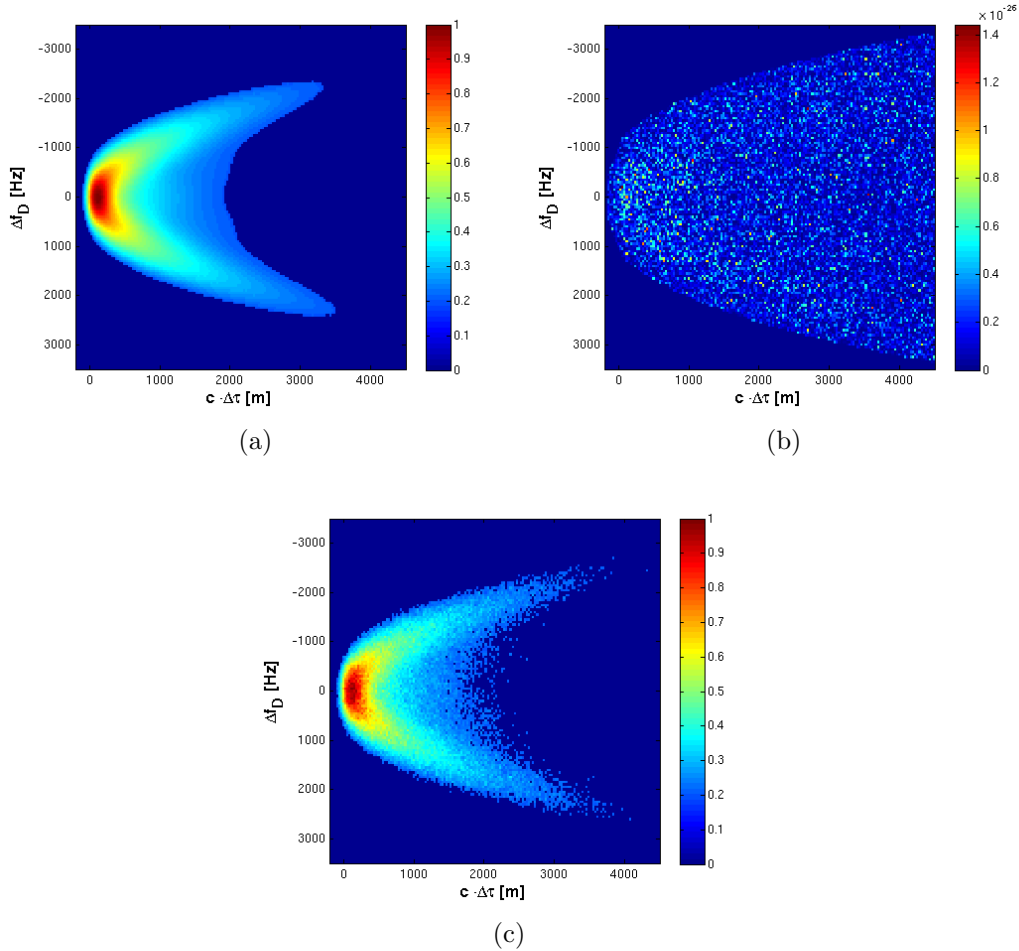
Figure 8.10: a) Ideal DDM without noise after normalization and applying the 20% threshold, b) DDM after 1 ms coherent integration ($SNR = 0$ dB), and c) DDM after incoherently averaging 1000 samples (i.e. 1 s incoherent integration time) after normalization and applying the 20% threshold.
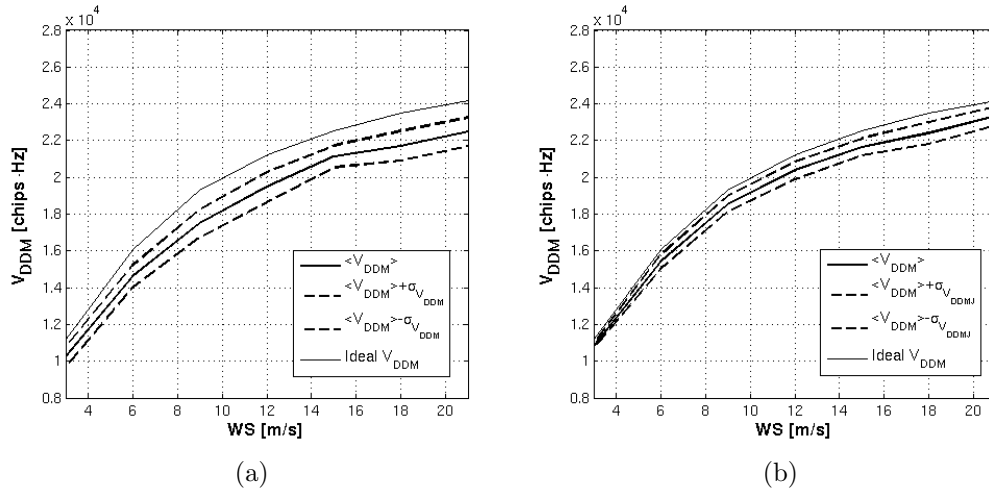
Figure 8.11: a) $SNR = 0$ dB, and b) $SNR = 5$ dB.

The V_{DDM} has been computed from the noisy DDM as the mean of 50 realizations. In Fig. 8.11a the mean of the normalized volumes of the noisy DDMs is plotted along with the ideal V_{DDM} as a function of WS. The $\pm\sigma_{V_{DDM}}$ values have also been plotted as a reference. The impact of noise on the V_{DDM} can be observed in two effects: a dispersion around the mean with a given standard deviation $\sigma_{V_{DDM}}$; and an offset on the mean value with respect to the ideal V_{DDM}.

The dispersion of the normalized noisy DDM volume, is relatively low (when WS is 21 m/s, $\sigma_{V_{DDM}} \approx 500$ chips·Hz for $< V_{DDM} >= 22500$ chips·Hz). However, the offset for that WS value is around 1800 chips·Hz. Even though, the overall impact of noise is still within, and of the same magnitude order of, the V_{DDM} dispersion caused by wind direction (a dispersion of ± 3700 chips·Hz for $WS = 21$ m/s, see red dots in Fig. 8.9).

The observed offset is caused by the residual error resulting from the noise floor estimation, which is over-estimated when computed as $< n^2 >$. A better estimation (to be defined) of the aforementioned noise floor would reduce that offset. Moreover, the low $\sigma_{V_{DDM}}$, even for the simulated low

$SNR = 0$ dB, is explained by the fact that the V_{DDM} itself is an integral observable, so it is actually performing an average of the noisy DDM in the DD domain, which further reduces the noise impact in terms of standard deviation.

Finally, another simulation set has been obtained with an $SNR = 5$ dB for the 1 ms DDM (Fig. 8.11b), which is an intermediate value among the UK-DMC antenna/receiver system, and the one for planned GNSS-R missions such as PARIS-IoD. It is seen a decrease of both the resulting offset and $\sigma_{V_{DDM}}$ (500 chips·Hz and 280 chips·Hz respectively, for $WS = 21$ m/s).

The main conclusion that can be derived from this noisy DDM simulation study is that the parameter that affects the most the V_{DDM} performance is not the noise, but the wind direction when unknown. Even more, if a better estimation of the noise floor is used to reduce the residual offset that has been observed. In this line, future research should be performed in order to reduce the uncertainty by trying to determine the wind direction in a manner alike the work done in Chapter 6.

8.4.3 Relationship with brightness temperature variations induced by the sea-state

This study has mainly focused to the use of direct GNSS-R observables to monitor sea-state and, specifically for wind speed retrieval. It has been presented that the best performing observable is the normalized DDM volume, but its performance is significantly impacted by the uncertainty introduced by the unknown wind direction (ϕ causes a final error of ± 3 m/s for $WS = 10$ m/s and up to ± 12 m/s for $WS = 20$ m/s).

Once the performance of V_{DDM} as a sea surface roughness descriptor has been assessed, it has to be studied how the resulting uncertainty affects its use to correct the brightness temperature variations induced by the sea-state, as it was proposed in the research framework of this PhD. Thesis, and as it was explored in Chapters 4 and 5 for ground-based and airborne scenarios.

To do so, the results of sea surface roughness impact on SMOS measured brightness temperature presented in [69] are used. These results establish a relationship between ΔT_B and WS for three different incidence angles of $10°$, $32°$, and $55°$. In this study the results for $10°$ and $32°$ are used since the third one considered incidence angle is not usable for GNSS-R measurements, and actually way out of the swath in planned missions such as PARIS-IoD [64]. Considering the half of the first Stokes parameter $(I/2)$ as the parameter used for salinity retrieval, the measured $\Delta T_B(WS)$ relationships are plotted in Fig. 8.12. The dependence of $I/2\,\Delta T_B$ on WS can be reasonably described by a parabolic function such as:

$$\Delta T_B = a \cdot WS^2 + b, \qquad (8.4)$$

where a and b are functions of the incidence angle, and here are assumed to be constant $(a = 7.5,\ b = 0)$ since, as expected, $I/2$ behavior is practically independent of the incidence angle up to $32°$ (see Fig. 8.12).

At this point, analytical functions are available to relate V_{DDM} and ΔT_B

(a)   (b)
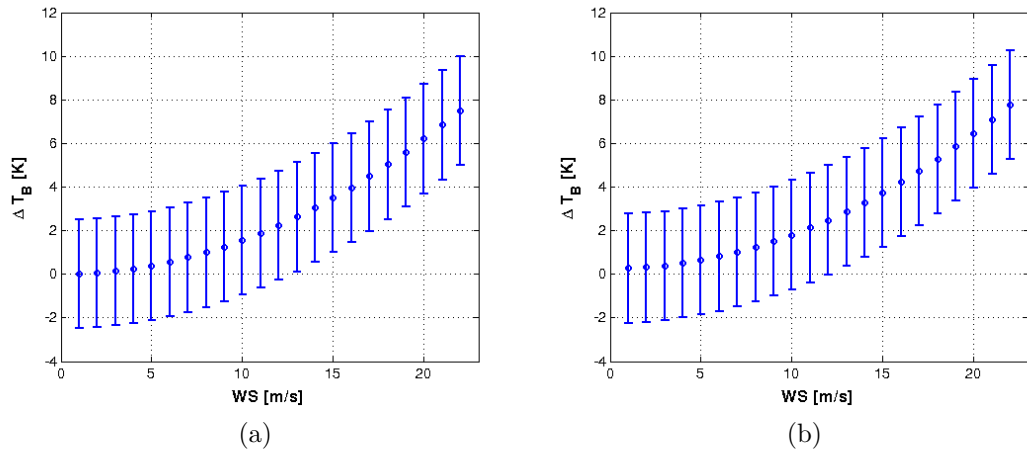
Figure 8.12: Parabolic fits to the $I/2\,\Delta T_B$ derived from [69], for: a) $\theta_i = 10°$, and b) $\theta_i = 32°$. It can be observed that $I/2$ is practically independent of θ_i up to $32°$.

to WS (Table 8.4 and Eqn. 8.4). Thus, V_{DDM} and ΔT_B can be related through WS as follows:

$$\Delta T_B = a \cdot e^{2(V_{DDM}-d)/c}, \tag{8.5}$$

where $c = 6880$, and $d = 3572$ are the logarithm parameters in Table 8.4. The resulting uncertainty of the ΔT_B estimated from V_{DDM} can then be obtained by derivation of Eqn. 8.5:

$$\sigma_{\Delta T_B} = 2 \cdot \frac{a}{c} \cdot e^{2(\sigma_{V_{DDM}}-d)/c}. \tag{8.6}$$

Figure 8.13 shows the ΔT_B estimation computed from V_{DDM}. Error bars are the derived uncertainties that account for the major V_{DDM} uncertainty source that is wind direction. To better assess the quality of the proposed estimation, the ΔT_B uncertainty has been plotted as a function of WS in Fig. 8.6. This $\sigma_{\Delta T_B}$ is below 1 K for wind speeds up to 20 m/s, that corresponds to a relative error in the estimation under 16%. Moreover, up to moderate WS around 12 m/s, $\sigma_{\Delta T_B}$ is under 0.25 K (10%).

The proposed estimation can be considered to be pretty good, and it has to be noticed that it would be performed with temporally and spatially collocated data. Indeed, further average would reduce the resulting error, as it is done for brightness temperature at the time of sea surface salinity retrieval. Figure 8.14 is displaying, then, an upper bound to the expected radiometric residual error. Nevertheless, the presented results are preliminary, and further work is required to test and improve the proposed sea surface roughness correction for spaceborne scenarios. However, the availability of L-band measurements from space provided by SMOS will certainly contribute to that.
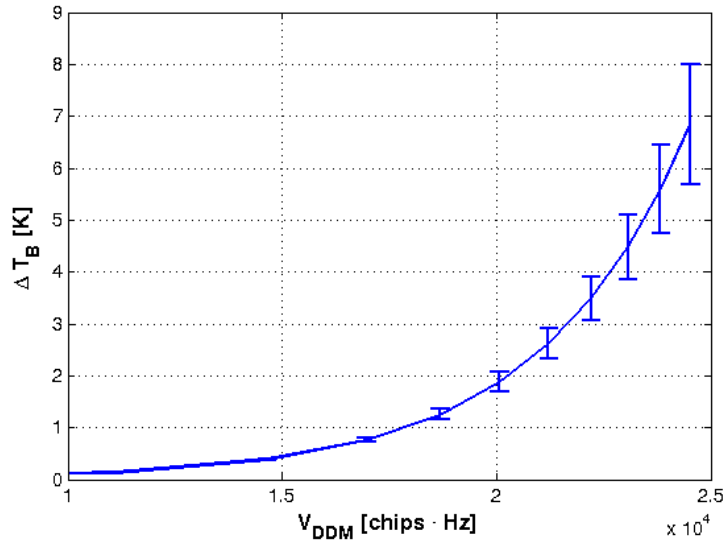
Figure 8.13: First Stokes parameter half ΔT_B estimated from V_{DDM} (Eqn. 8.5) with the associated 1-σ error bars.
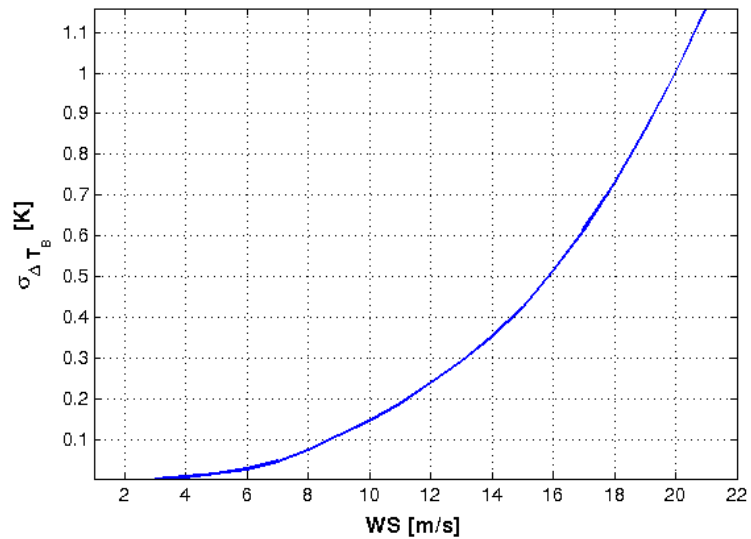
Figure 8.14: Uncertainty in the ΔT_B estimation caused by the V_{DDM} uncertainty due to wind direction (Eqn. 8.6).

8.5 Conclusions

A comprehensive simulation study has been performed to evaluate the impact of the observation geometry on GNSS-R observables, in order to assess the feasibility of using them to describe sea-state from space-borne missions. This study has required an extensive simulation process that required the computation of 56000 DDM for different values of the five main significant scenario's parameters: transmitter's and receiver's flying directions, reflection's local incidence angle, and wind speed and direction. This has been made possible by the use of the PAU/PARIS End to End Performance Simulator that implements an advanced and optimized DDM simulation algorithm, which has reduced the unrealistic 13 years required computation time for "classical" double integration methods, to just 55 h, using a regular PC.

First, four different GNSS-R observables have been compared: 2 computed from the full DDM (normalized DDM volume and *taxicab* distance), and 2 from the waveform (normalized waveform's area and length of the waveform's tail). It has been observed that the full-DDM based observables are more robust to the observation geometry than the waveform-based ones, since they are less sensitive to the DDM shape changes caused by the geometry variations. Thus, the use of the complete DDM is required when using direct observables for scatterometric applications from space. Even though, the dispersion caused by the observation geometry changes in the computed observables, leads to a mandatory need for a proper correction for these effects. From the 4 GNSS-R considered observables, the best performing one appears to be the normalized DDM volume, V_{DDM}.

The second part of this study has been devoted to assess the impact of each of the scenario's parameters on the performance of V_{DDM} as a sea-state descriptor. The first conclusion is that the V_{DDM} is independent of the transmitter's flying direction. It has been possible to analytically correct the effect of local incidence angle of the reflection by using a simple equation, as

this effect shows to be independent from others. However, the effects of the other three parameters (flying direction of the receiver, wind direction and speed) are not separable, and they cannot be analytically corrected for. Even though, assuming that the receiver's flying direction is known, wind direction has still a significant impact on the V_{DDM} which leads to an error of ± 3 m/s for $WS = 10$ m/s. After studying the impact of the noise, it is actually the wind direction the most critical parameter that determines the performance of V_{DDM} as a sea-state descriptor. However, future research should be conducted to try to reduce this uncertainty by applying wind direction determination techniques in line with the work presented in Chapter 6.

The performance of the sea surface roughness impact on T_B correction using GNSS-R observables such as V_{DDM}, for a spaceborne scenario, has been assessed by using recent results derived from SMOS measured data. The obtained preliminary results indicate that the ΔT_B estimation has an uncertainty below 1 K (16% relative error) up to strong winds of 20 m/s. Indeed, this error can be further reduced by averaging.

This indicates that, even though V_{DDM} alone may not be used for accurate wind speed retrievals from space, it might be used to correct the ΔT_B caused by sea-state. This is in line with previous studies undertaken in the framework of this PhD. Thesis for ground-based and airborne experimental data, but requires further analysis both from simulation and experimental points of view. In this line, a space-qualified version of the PAU instrument (Fig. 8.15b) has been designed and manufactured by ADTelecom to fly onboard the INTA's MicroSat-1 (Fig. 8.15a). This payload will provide GNSS-R DDMs along with L-band radiometric measurements acquired in a TPR configuration, that will help pursuing the study of the estimation of the sea-state contribution to ocean L-band emissivity, from GNSS-R data.
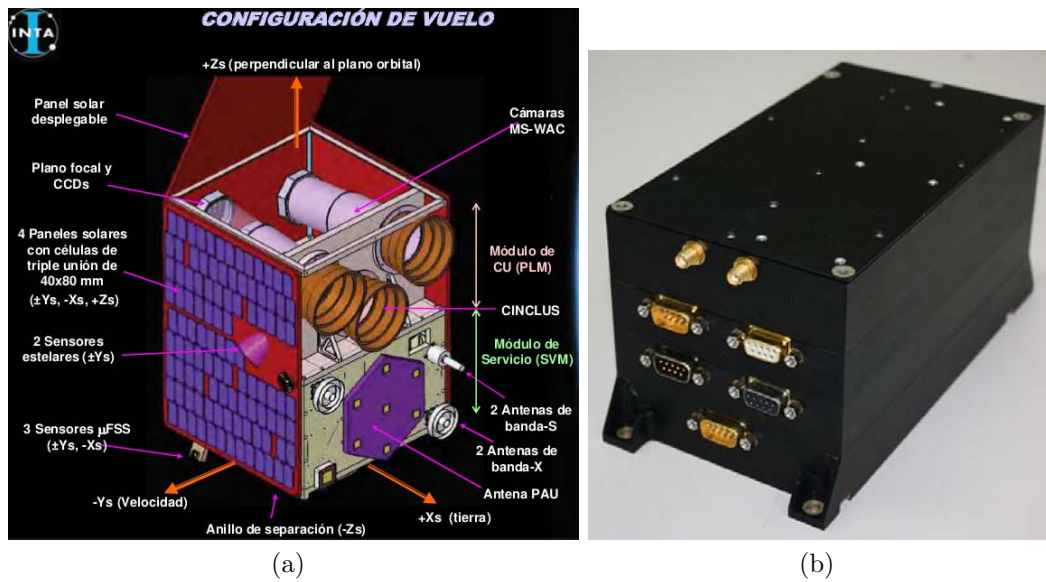
Figure 8.15: a) Art view of the INTA's MicroSat-1, and b) picture of the flight model of the space-qualified version of the PAU instrument.

9

Ocean surface imaging from DDM deconvolution

9.1 Introduction

In the past years, reflectometry of opportunity signals as Global Navigation Satellite System (GNSS-R) has stood as a technique with a great potential for remote sensing applications such as ocean monitoring. These techniques are mainly based on studying either the waveform or the Delay-Doppler Map (DDM). Two main approaches have been proposed to retrieve sea state from this kind of measurements:

1. Fitting real measurements to a model tuned with the desired parameter.

2. Directly linking some waveform or DDM parameter to the sea state descriptor by using previously developed empirical relationships.

In the literature these studies have been mainly conducted assuming a homogeneous sea surface roughness within the glistening zone so a sea state descriptor averaged over the observed surface is obtained for each measurement (i.e. DDM or waveform). However, in the general case, sea state cannot

be considered homogeneous at medium to large scales, especially for space-borne applications, since the glistening zone usually covers a surface on the order of hundreds of kilometers.

From another point of view, the autocorrelation properties of the PRN codes used in GNSS systems have also been successfully used in the literature to perform classical SAR processing. This approach, known as Space/Surface Bistatic SAR (SS-BSAR) [70, 71], is based on a ground-based or airborne receiver that collect the scattered GNSS signals. However, the power budget in SS-BSAR systems requires a long integration period (even up to 1000 s in the ground-based receiver case) to achieve a proper SNR [72]. This fact prevents classical SAR processing to be applied from spaceborne plattforms.

From these two approaches (GNSS-R and SS-BSAR) a third one can be derived, which is based on use the spaceborne GNSS-R measured DDMs to retrieve images from the scattering coefficient distribution over the glistening zone. When computing the DDM, the time-domain correlation with the replica of the PRN code and the coherent integration for different Doppler shifts are equivalent to range and azimuthal compression in a bistatic SAR, respectively.

Each pixel in the physical space (xy) is mapped in the $(\Delta\tau, \Delta f_D)$ delay-Doppler (DD) domain. This fact can be exploited to treat the DDM as a kind of SAR image (actually a bistatic SAR), and map the sea surface scattering coefficient (σ^0) from the DDMs, after properly taking into account the scenario's geometry and the autocorrelation properties of the considered GNSS code. However, a mapping ambiguity among the physical space and the DD domain exists and will have to be properly taken into account. From the retrieved σ^0 maps, geophysical parameters such as mean square slopes (MSS) or WS can be retrieved by using models and knowledge of the measurement geometry.

As an example, two DDMs have been computed for a Low Earth Orbiting (LEO) GNSS-R receiver (simulation parameters listed in Table 9.1): the first

one (Fig. 9.1a) considers a sea surface driven by a homogeneous 4 m/s wind speed (WS); for the second DDM (Fig. 9.1b) a non-homogeneous wind speed distribution has been considered (Fig. 9.1d).

In Fig. 9.1c the difference of these two DDMs is shown. By comparing it with the corresponding WS distribution (Fig. 9.1d), it can be seen that in the regions with the same WS (white color), both DDMs do not present any difference. However, the scattering contribution of the regions where WS is higher or lower than 4 m/s cause significant differences (Fig. 9.1c) that can
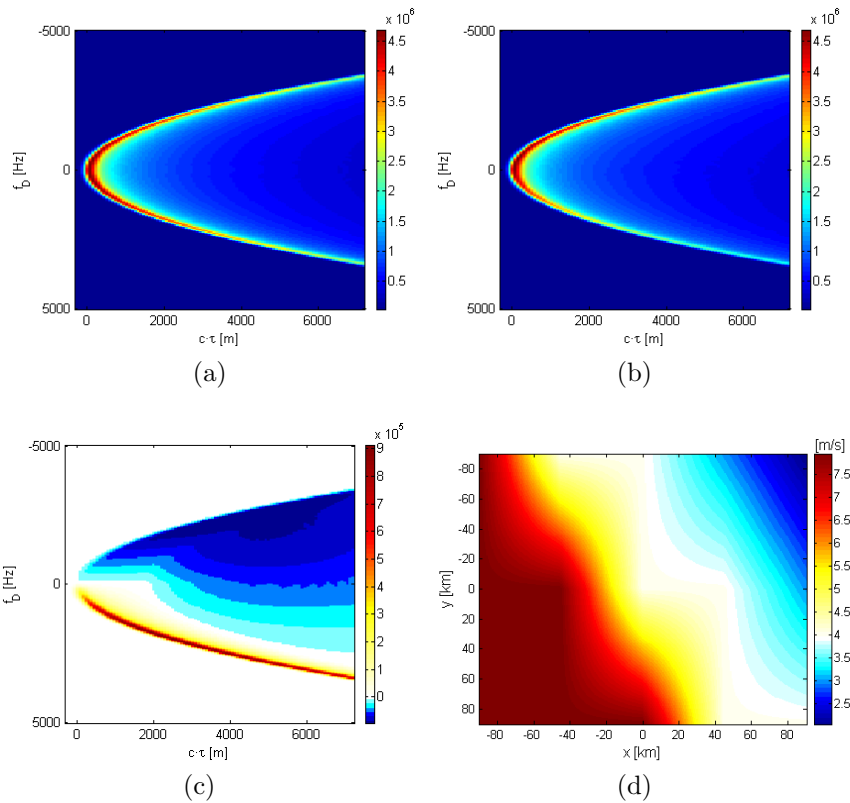
Figure 9.1: Example of sea surface mapping using DDM (simulated results): a) DDM considering homogeneous WS; b) DDM considering a WS distribution over the surface; c) difference of Fig. 9.1a and Fig. 9.1b DDMs; and d) corresponding Wind Speed distribution.

be clearly identified in the resulting DDM.

In this Chapter a method to retrieve σ^0 maps from measured DDMs is proposed for the first time, to authors' knowledge. This method is based on the inversion of the algorithm developed in [63] to efficiently compute DDM as a 2D convolution. The content of this Chapter is organized as follows:

- Section 9.2 briefly exposes the required theoretical background.

- Section 9.3 presents the σ^0 retrieval method from the spaceborne measured DDMs.

- Section 9.4 provides a simulation example that assesses the potential of the proposed method.

- Section 9.5 explores a potential application of this method for oil slick in the ocean surface detection.

9.2 Theoretical background

A DDM can be generally expressed in power terms as follows:

$$\left\langle |Y(\Delta\tau, \Delta f_D)|^2 \right\rangle = \chi^2(\Delta\tau, \Delta f_D) * *\Sigma(\Delta\tau, \Delta f_D), \tag{9.1}$$

where χ is the Woodward ambiguity function of the PRN coarse/acquisition (C/A) code [14], $\Delta\tau = \tau - \tau(\vec{r})$ and $\Delta f_D = f_D - f_D(\vec{r})$ are the delay and the Doppler shifts of each surface's point with respect to the specular point, respectively, $\vec{r}$ is the position vector of each surface's point, and Σ is a function defined as:

$$\Sigma(\Delta\tau, \Delta f_D) \triangleq$$
$$\left[T_c^2 \frac{D^2(\vec{r}(\Delta\tau, \Delta f_D))\sigma^0(\vec{r}(\Delta\tau, \Delta f_D))}{4\pi R_0^2(\vec{r}(\Delta\tau, \Delta f_D))R^2(\vec{r}(\Delta\tau, \Delta f_D))} \times |J(\Delta\tau, \Delta f_D)| \right], \tag{9.2}$$

where T_c is the coherent integration time, D is the antenna radiation pattern, σ^0 is the scattering coefficient distribution over the observed surface, R is the distance from the transmitter to each surface's point, R_0 is the distance from each surface's point to the receiver, and J is the Jacobian function resulting from the domain transform from the xy physical surface domain to the delay-Doppler (DD) domain. Equation 9.1 presents the DDM as a blurred image of the surface's scattering coefficient distribution in the DD domain, similarly to imaging systems where the actual image is blurred by the system's response (point spread function or PSF [73]).

The expression in Eqn. 9.1 is the starting point for the retrieval of the scattering coefficient distribution over the surface. As it can be seen, all the terms appearing in Eqns. 9.1 and 9.2 are well defined or can be directly computed from the scenario geometry.

9.3 GNSS-R imaging of the ocean surface

9.3.1 DDM deconvolution

The proposed method to retrieve the scattering coefficient distribution from the measured DDM consists of solving equation Eqn. 9.1 for the desired term σ^0. To do so, the first step is to deconvolve the measured DDM to obtain an estimation of the $\Sigma(\Delta\tau, \Delta f_D)$ function. This deconvolution process is similar to many imaging systems in which the resulting image is affected by the instrument response that distorts the true image. In this case, the well-defined χ^2 function plays the role of the instrument response and will be used for the deconvolution of the measured DDM. Conceptually, using the Fourier transform ($\mathscr{F}[\cdot]$) properties:

$$\mathscr{F}\left[\widetilde{\Sigma}(\Delta\tau, \Delta f_D)\right] = \frac{\mathscr{F}\left[\langle|Y(\Delta\tau, \Delta f_D)|^2\rangle\big|_{measured}\right]}{\mathscr{F}\left[\chi^2(\Delta\tau, \Delta f_D)\right]}. \tag{9.3}$$

However, to prevent error amplification effects and instability of the method, the actual deconvolution process cannot be as simple as in Eqn. 9.3. A number of deconvolution methods are found in image processing literature that can be used to retrieve Σ . The selected one is a constrained least squares (CLS) method, which is described and used in Section 9.4.

9.3.2 Unambiguous retrieval of the scattering coefficient distribution

Once an estimation of the $\Sigma(\Delta\tau, \Delta f_D)$ function has been derived, Eqn. 9.2 can be inverted and solved for the desired $\widetilde{\sigma}^0$. The resulting expression for the retrieved scattering coefficient distribution can be written as:

$$\widetilde{\sigma}^0(\vec{r}(\Delta\tau, \Delta f_D)) = \frac{\widetilde{\Sigma}(\vec{r}(\Delta\tau, \Delta f_D))}{|J(\vec{r}(\Delta\tau, \Delta f_D))|} \frac{1}{T_c^2}$$
$$\times \frac{4\pi R_0^2(\vec{r}(\Delta\tau, \Delta f_D))R^2(\vec{r}(\Delta\tau, \Delta f_D))}{D^2(\vec{r}(\Delta\tau, \Delta f_D))}. \qquad (9.4)$$

At this point the ambiguity in mapping the physical space into the delay-Doppler domain comes out. It is well known that a delay-Doppler coordinate corresponds to two different points over the observed surface (Fig. 9.2). This fact is treated in [63] by considering the total DDM as a combination of the independent contribution of two different physical zones. It implies linearly combining these two contributions weighted by their particular Jacobian (J_1 and J_2).

Although other approaches may be implemented to account for this ambiguity, in this work an observation geometry similar to that of synthetic aperture radar (SAR) is proposed. In SAR systems, the receiving antenna is
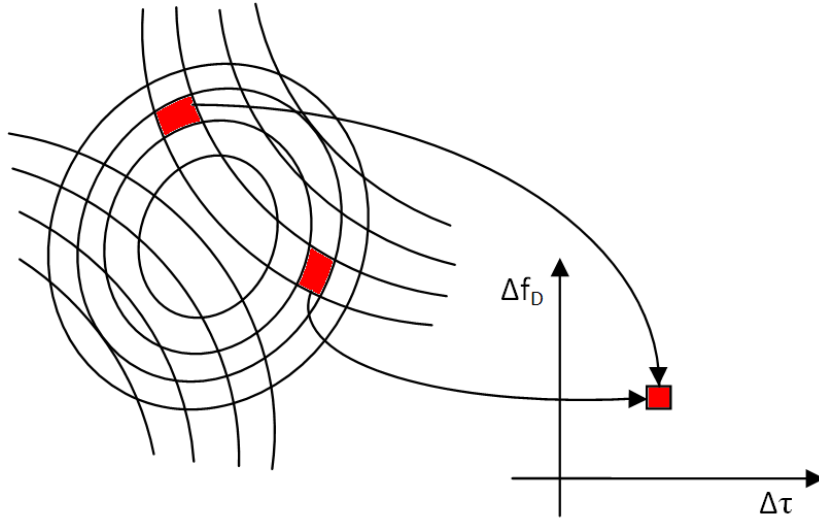
Figure 9.2: Each coordinate in the delay-Doppler domain is contributed by two points of the physical xy space.

pointed so that the observed area corresponds to only one of the two zones contributing to each delay-Doppler coordinate so the obtained measurement is no longer ambiguous [74]. The same approach can be applied to a GNSS-R system by tilting the antenna beam away from the specular reflection point (Fig. 9.3). As GNSS-R are bistatic systems, this tilt requires a beam-forming system to be implemented, which is already being considered in planned space missions such as [64].

This way, an unambiguous $\widetilde{\sigma}^0$ distribution in the delay-Doppler domain is obtained and the only remaining step is to transform it to the physical space by direct coordinates correspondence:

$$\widetilde{\sigma}^0(\vec{r}(\Delta\tau, \Delta f_D)) \to \widetilde{\sigma}^0(\vec{r}). \tag{9.5}$$
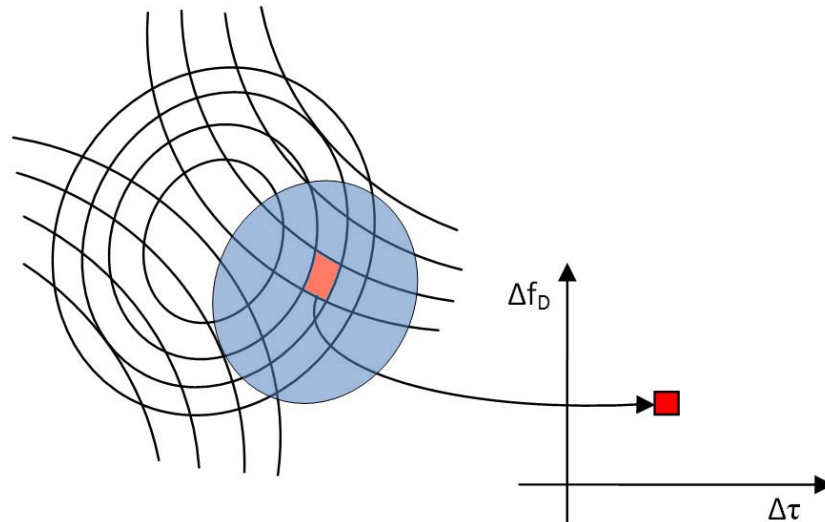
Figure 9.3: Mapping ambiguity can be avoided by spatial filtering taking advantage of a proper pointing of the antenna beam.

9.4 Method evaluation

A determined observation scenario has been simulated to validate the proposed method for scattering coefficient distribution retrieval. For the sake of clarity, and without loss of generality, the selected scenario has been kept simple enough to be as clear as possible. Transmitter and receiver velocity vectors are assumed to be parallel to achieve a simple layout for the iso-Doppler lines (Fig. 9.4a), and the hardware effects introduced by the receiver have been neglected [75]. The scenario key parameters are listed in Table 9.1.

The resulting iso-lines layout is shown in Fig. 9.4a, where the distance between lines is: 1 C/A code chip for the iso-range and 100 Hz for the iso-Doppler, corresponding to the 10 ms coherent integration time. Thus, each plots cell presents the dimensions of the considered WAF.

Once the scenario has been set, a reference DDM has been computed over a non-homogeneous sea surface (i.e. wind speed not constant over the surface) using the classical double-integration approach. To implement the spatial filtering of the desired space region, a generic antenna pattern has been simulated considering the 23 dB gain and 15° beam-width PARIS-IoD specifications for realism:

Table 9.1: Simulation parameters

Receiver height	700 km
Receiver velocity (V_{ty})	5000 m/s
Transmitter velocity (V_{ty})	3000 m/s
Elevation angle	90° (nadir reflection)
Observation surface x direction	[0 60] km
Observation surface y direction	[-60 60] km
Maximum considered delay ($\Delta\tau$)	10 chips (C/A code)
Maximum considered Doppler shift (Δf_D)	[-2500 2500] Hz
Coherent/incoherent integration times	10 ms / 1 s
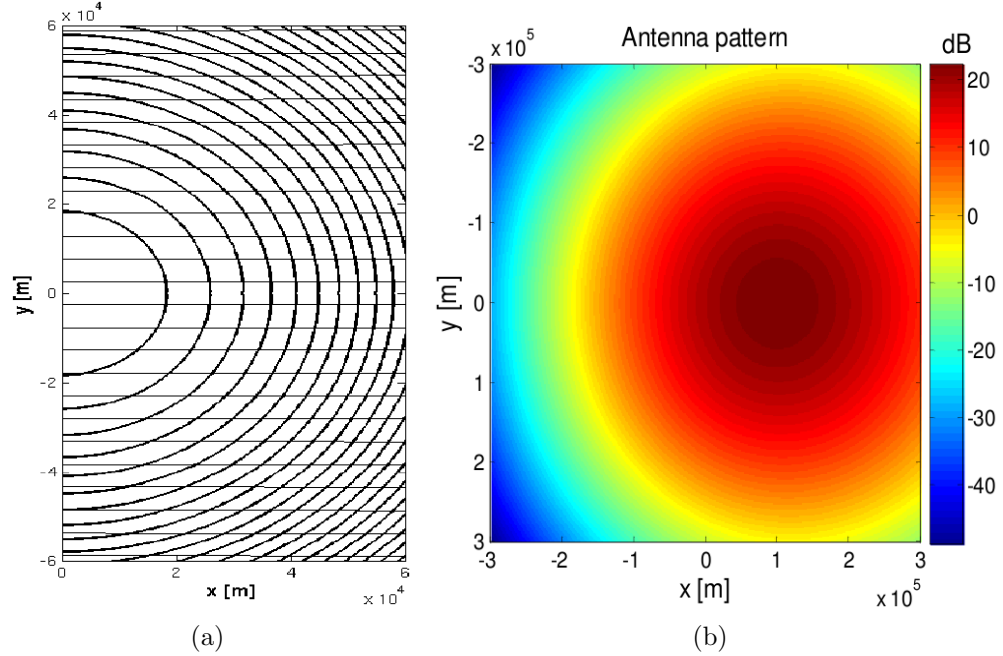
Figure 9.4: a) Resulting layout for the iso-range (1 chip separation) and iso-Doppler (100 Hz separation); and b) considered antenna pattern (PARIS IoD corresponding gain and beamwidth).

$$D(\theta)|\,[dB] = 23 - 12\left(\frac{\theta}{15°}\right)^2 \qquad (9.6)$$

where θ is the angle from the antenna boresight in degrees. The beam has been tilted along the x-axis direction to have the specular point in the -3 dB attenuation zone of the pattern (Fig. 9.4b). Then, a WS distribution has been defined (Fig. 9.5a) dividing the observation surface in four regions along the y-axis. The corresponding σ^0 distribution (Fig. 9.5b) has been computed by using the Zavorotny-Voronovich model [14]. Nevertheless, the presented method is independent of the model used to relate σ^0 to the surface properties. Note that the plots in Figs. 9.5a and 9.5b have a semi-circular shape because only the surface points corresponding to the considered delay-Doppler coordinates are shown (i.e. circular iso-range lines). Although only
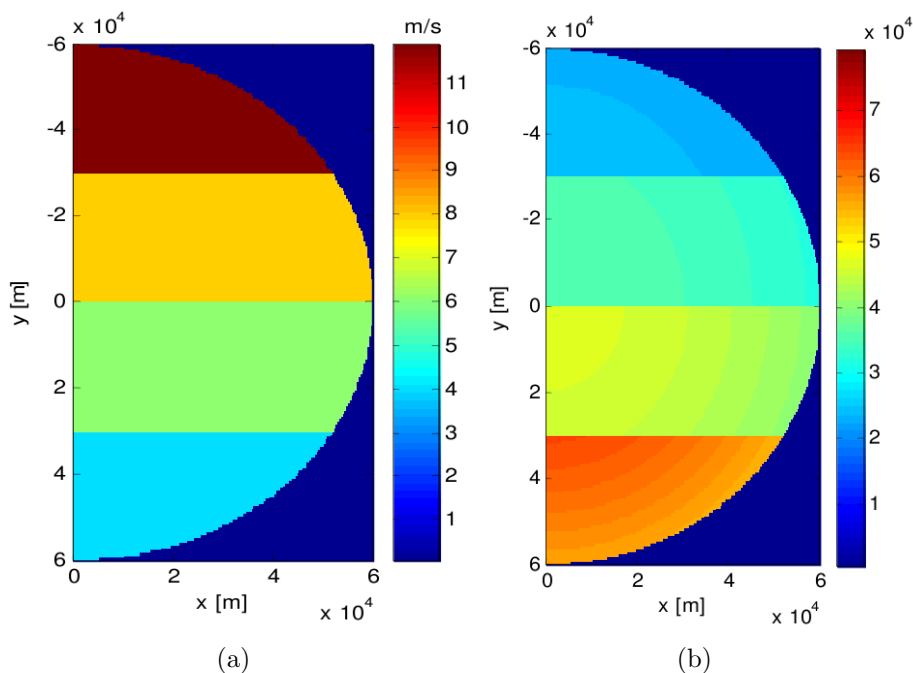
Figure 9.5: a) Defined wind speed distribution; and b) resulting scattering coefficient distribution.

the positive x-axis region is shown, WS and σ^0 have been defined symmetric with respect to the y-axis.

From this σ^0 distribution, a reference DDM_{xy} has been computed applying the classic double integration over the xy domain. To further validate the proposed method, also noise has been considered. This has been done by adding a Gaussian noise to the real and imaginary parts of the noise-free complex DDM. Gaussian noise amplitude is tuned to achieve a 17 dB peak-to-noise power ratio (similar to that observed in the space-borne measurements from the UK-DMC when using 1 s incoherent integration time [68]). The DDMs are then coherently integrated during 10 ms and then incoherently up to 1 s. The obtained DDM is shown in Fig. 9.6, along with a waveform (cut for a constant Doppler frequency) so as to be easily compared to the space-measured waveforms presented in [68].
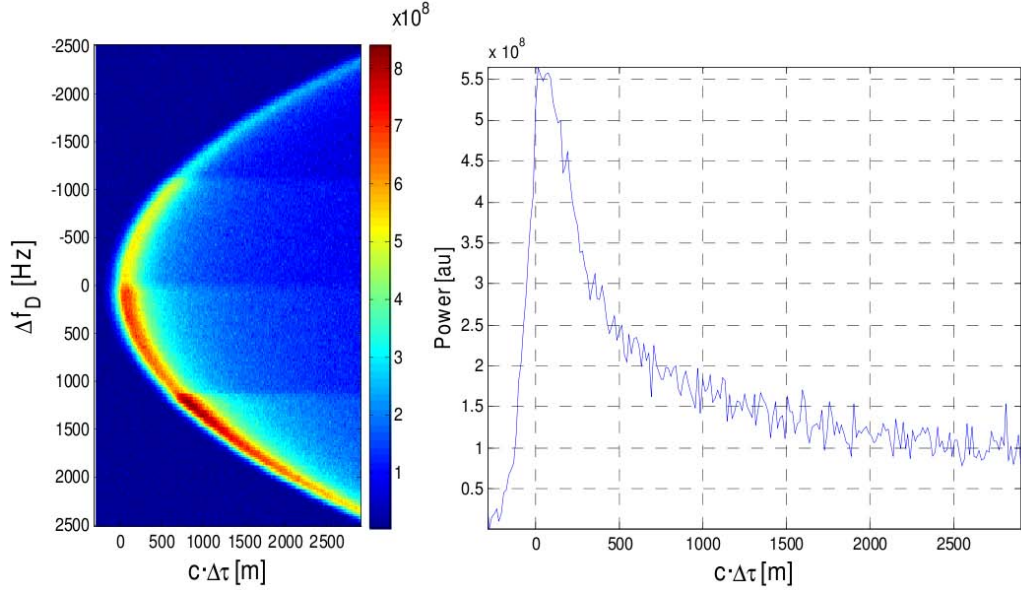
Figure 9.6: DDM_{xy} computed using the integration over the xy domain and considering the scattering coefficient distribution shown in Fig. 9.5b as well as a peak-to-noise ratio of 17 dB; and cut of DDM_{xy} for a constant Doppler frequency (waveform). The resulting waveform is similar in terms of noise to that measured from the UK-DMC satellite using an incoherent integration time of 1 s.

At this point, DDM_{xy} is considered to be the "measured" noisy DDM from which σ^0 is to be retrieved. As shown in Section 9.3, the first step to do so is to deconvolve DDM_{xy} from χ^2. In this work, a constrained least squares (CLS) filter has been chosen. This is a deconvolution method applied in the frequency domain:

$$\mathscr{F}\left[\widetilde{\Sigma}(\Delta\tau, \Delta f_D)\right] = K_{CLS} \cdot \mathscr{F}\left[DDM_{xy}\right] \tag{9.7}$$

with $\mathscr{F}[\cdot]$ being the Fourier transform, and K_{CLS} being the CLS filter defined as:

$$K_{CLS} = \frac{\mathscr{F}\left[\chi^2\right]^*}{\left|\mathscr{F}\left[\chi^2\right]\right|^2 + \gamma P} \tag{9.8}$$

where P is the Fourier transform of the smoothing criterion function, in this case, a second-order Laplacian operator [76], and the parameter γ can be adjusted to control the noise amplification and the resolution of the deconvolution process. For small values of the γ parameter, the filter tends to the simple inverse filter achieving the best resolution, but the largest noise amplification, while for large values of γ, noise impact is reduced, but a larger smoothing is introduced.

In this work, different γ values have been tested. Two results are shown in Fig. 9.7: the results for $\gamma = 0$ (inverse filter) and for $\gamma = 0.05$.

Both deconvolution results have been divided by the Jacobian function computed for the simulated scenario to obtain the $\widetilde{\sigma}^0(\vec{r}(\Delta\tau, \Delta f_D))$ distribution, after applying the other appropriate compensation terms such as the antenna pattern. These results are shown in Fig. 9.8. It can be seen in Fig. 9.8a that, for the inverse-filter case, the error amplification effects re-

(a) (b)
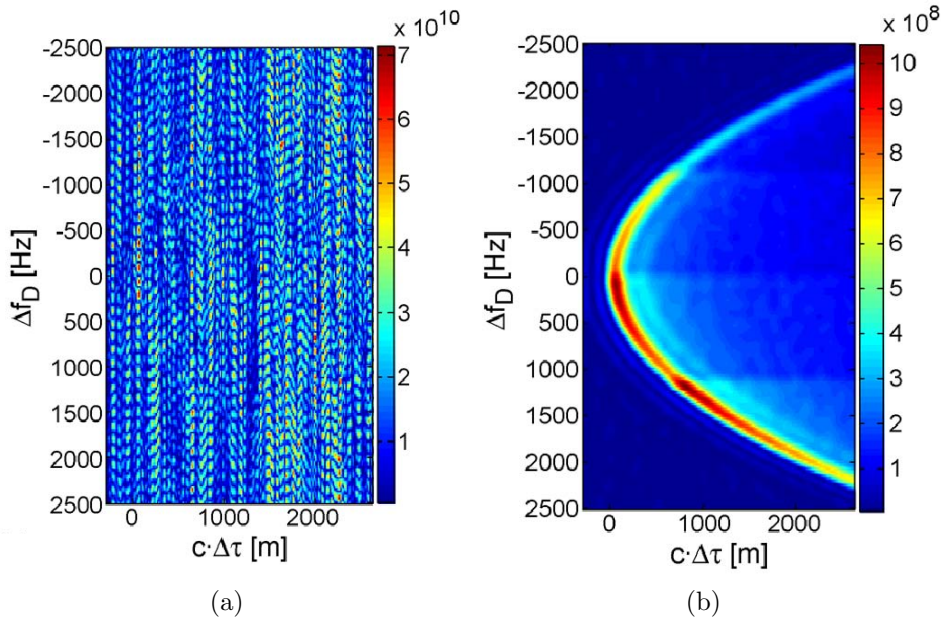
Figure 9.7: Deconvolution results for a) $\gamma = 0$ (inverse filter) and b) $\gamma = 0.05$.
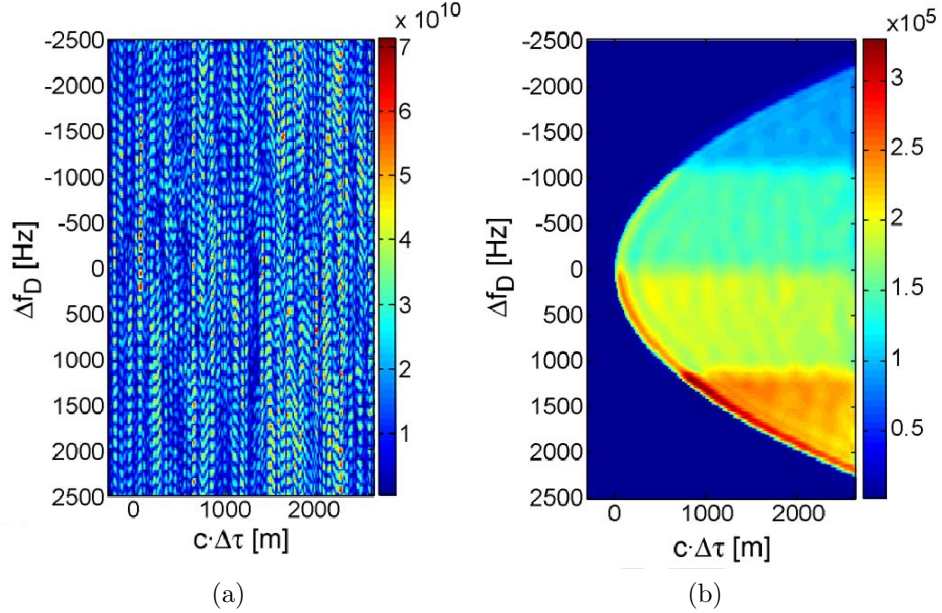
Figure 9.8: $\widetilde{\sigma}^0(\vec{r}(\Delta\tau, \Delta f_D))$ obtained using a) $\gamma = 0$ (inverse filter) and b) $\gamma = 0.05$.

sult in a completely blurred distribution. However, increasing the CLS filter parameter to $\gamma = 0.05$, a much clearer scattering coefficient distribution is obtained. This result is shown in Fig. 9.8b, where the four defined WS zones can be well differenced in the DD domain.

The last step of the proposed retrieval method is to use the DDxy-domain correspondence to map $\widetilde{\sigma}^0$ in the DD domain (Fig. 9.8b) to the physical xy surface domain. The final retrieved scattering coefficient distribution $\widetilde{\sigma}^0(\vec{r})$ is shown in Fig. 9.9a for the CLS filter parameter $\gamma = 0.05$ case.

The retrieved $\widetilde{\sigma}^0(\vec{r})$ distribution matches very well the one used as an input for the simulation (Fig. 9.5b). The four different WS zones are clearly delimited, and the retrieved scattering coefficient values are quantitatively close to the input ones (Fig. 9.9b) with an error smaller than 10%. However, a larger error is observed around the transition zones of the scattering distribution (ringing effects) and other deconvolution artifacts because of the sharp transition of the Jacobian function along the DDM border in the
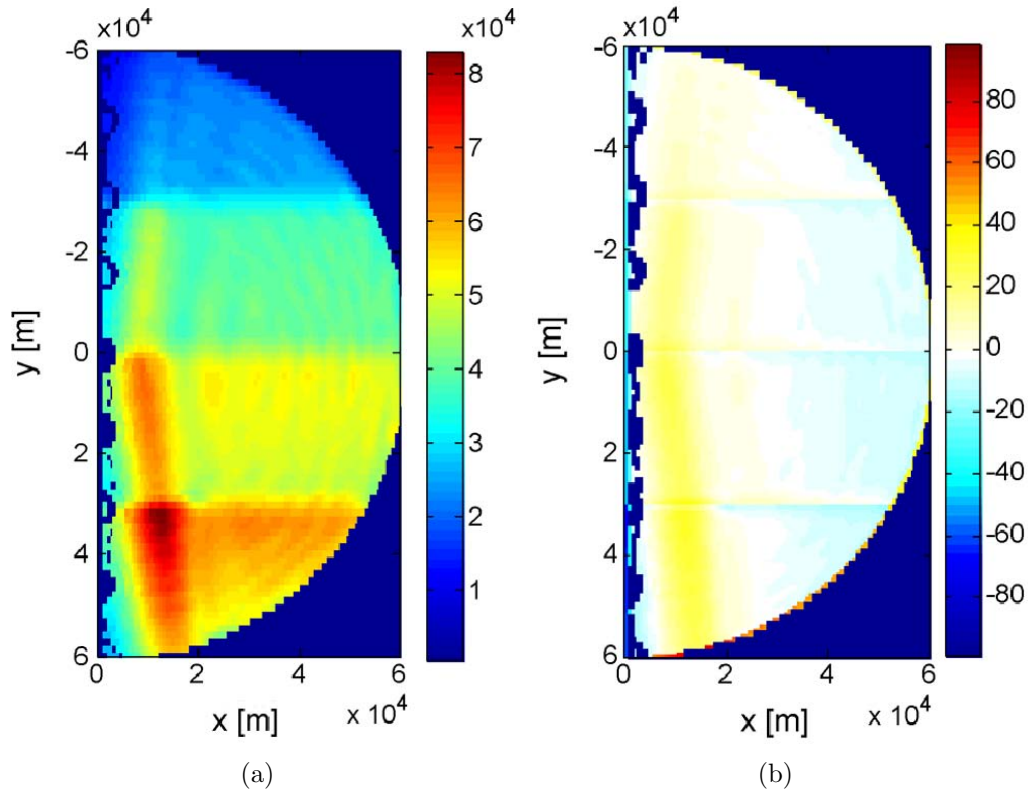
Figure 9.9: a) Retrieved scattering coefficient distribution mapped over the physical surface (xy domain) and b) corresponding error map (in percent) with respect to the original scattering coefficient distribution.

DD domain. These artifacts can be minimized by applying advanced image processing techniques. The deconvolution process will have to be optimized to deal best with noise; at the same time, those artifacts are minimized, achieving the minimum final error in the retrievals.

Moreover, one of the main error sources is the contamination introduced by the power contribution of the ambiguous zone which is not attenuated enough by the antenna pattern (simulations artificially suppressing this contribution result in a retrieval error below 4%-5%). Techniques to mitigate the contamination from the ambiguous zone will also have to be developed.

Finally, the final spatial resolution has been estimated for this particular scenario. As the input σ^0 has been defined with sharp transitions (along the y dimension of the surface) between the different WS zones, the spatial length of these transitions in the retrieved $\widetilde{\sigma}^0$ can be used as a first approximation of the achieved spatial resolution. This value has a mean of $\Delta y = 4$ km (from 10% to 90% of the rising edge). This value is approximately the length of the WAF projected over the y dimension of the surface (size of one cell in Fig. 9.4a).

However, since the performance of the proposed retrieval method is dependent on the measurement scenario, further work is required to explore the actual limits of the technique in terms of error and achievable spatial resolution as functions of the scenario, instrument and antenna errors, etc.

9.5 Application to oil slick detection

A potential application of the proposed GNSS-R technique is the detection of the scattering coefficient variations that oil slicks induce in the ocean surface. The presence of oil slicks on the sea surface translates into a change in the surface mean square slopes (MSS) [77]. In particular, for a given wind speed, the MSS presents lower values in an oil slick than for a clean sea, since the oil film damps the surface waves. According to that, the contaminated sea regions will appear in the restored images as isolated low wind areas. This MSS variations cause changes in the σ^0 distribution over the observed surface, so these regions may be detected by the proposed imaging method (as it is done in Synthetic Aperture Radar imaging), so they can be further classified as contaminated. This information should be relevant as an input to the oceanographic alarm systems for prevention, as well as for control objectives. The use of GNSS-R for oil slicks detection would provide an added value to other existing sensors (SAR, optical imagers, microwave radiometers, etc.) as it would provide L-band reflectivity information that should help to improve

the detection and classification algorithms by adding completeness to the oil slicks' spectral signature measurement.

In this section the σ^0 retrieval process, that would allow identifying the slick region of the ocean surface, is applied to a simulation case. Firstly, the ocean surface has been modeled in order to include the σ^0 variations induced by the oil slick presence and then, a measured DDM has been simulated including noise. This DDM has been used to retrieve the surface's σ^0 distribution.

9.5.1 Oil slick modeling

As in [78], the ocean surface has been modeled in a simple way by considering the relationship among the surface's MSS and the wind speed (WS) presented in [77]:

$$
\begin{aligned}
MSS_{cross-wind}|_{clean} &= 0.003 + 1.92 \cdot 10^{-3} U_{10}, \\
MSS_{up-wind}|_{clean} &= 3.16 \cdot 10^{-3} U_{10},
\end{aligned} \tag{9.9}
$$

where U_{10} is the WS at 10 m height from the surface. To model the effect of the oil slick presence, the MSS have been computed using the appropriate relationship with the WS also presented in [77]:

$$
\begin{aligned}
MSS_{cross-wind}|_{slick} &= 0.003 + 0.84 \cdot 10^{-3} U_{10}, \\
MSS_{up-wind}|_{slick} &= 0.005 + 0.78 \cdot 10^{-3} U_{10}.
\end{aligned} \tag{9.10}
$$

After applying the empirical modification proposed in [62], these MSS have been used as an input for the waveform model in [14] extended to the Doppler domain to compute the whole DDM.

9.5.2   Simulation results

To assess the feasibility of the GNSS-R imaging technique to detect oil slicks
in an ocean surface, a simulation example has been performed. All the simu-
lation parameters (Table 9.1) have been kept as in the simulation presented
in Section 9.4. However, in this work, it has been considered an ocean scat-
tering coefficient distribution corresponding to an homogeneous 12 m/s wind
speed with the presence of a 25x25 km oil spill (Fig. 9.10).

As it can be observed in Fig. 9.10, the slick region presents a higher scat-
tering coefficient as, due to oil damping of the surface waves, more power is
reflected in the forward direction from this region (although a uniform WS
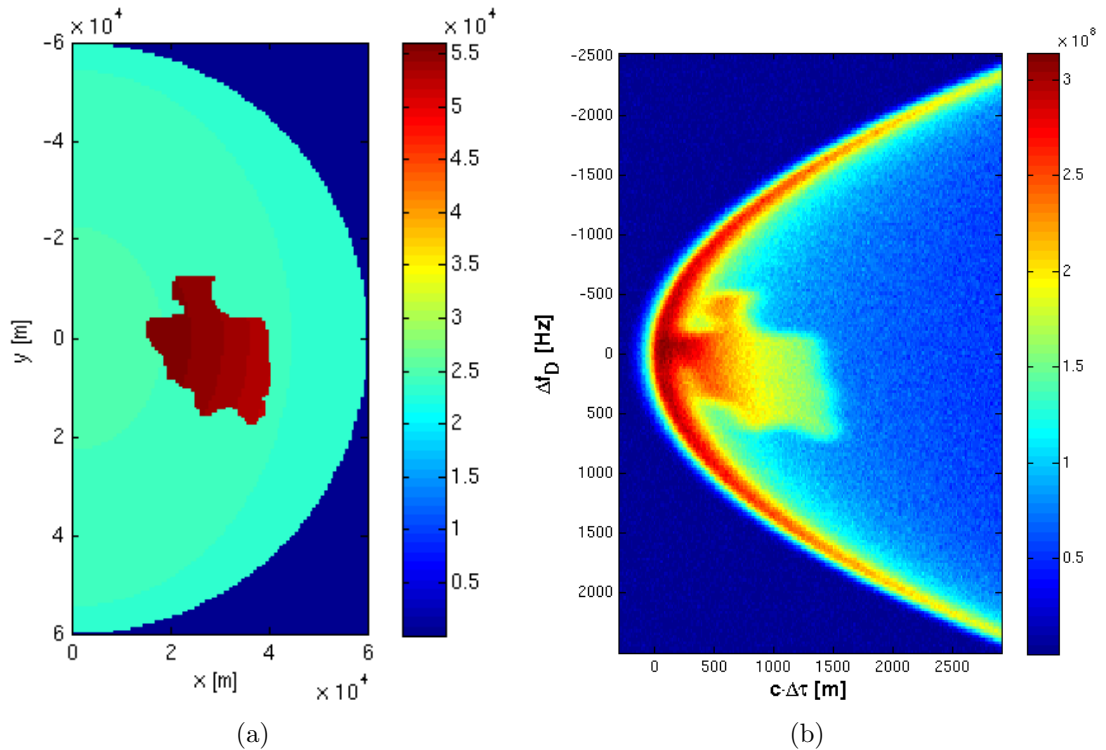
Figure 9.10: a) Scattering coefficient distribution of an homogeneous ocean surface
with the presence of an oil slick and, b) Simulated noisy DDM obtained by the
double-integration technique in the xy physical surface domain.

over the whole surface is considered). The simulated DDM for this observed surface is presented in Fig. 9.10. This simulation has been performed considering an antenna beam with a gain of 23 dBi and a beamwidth of 15°, which is steered 8° away from the specular point in the x direction to perform the required spatial filtering of one of the two ambiguous zones. Noise has been taken into account by adding to the DDM a Gaussian noise with a power similar to that observed in the UK-DMC measurements [68], accounting for the difference in the directivities between the UK-DMC's one, and the one considered in this work, and assuming a receiver with the same noise figure.

The final retrieved $\widetilde{\sigma}^0$ distribution is presented in Fig. 9.11 along with an error map with respect to the σ^0 distribution input to the simulation. The slick area is clearly distinguishable in the final $\widetilde{\sigma}^0$ retrieval and, in general, the resulting error is below 10%. However, the error increases up to 20% around the slick's border due to the deconvolution process. Deconvolution (ringing effect) is also responsible for the vertical strip observed in Fig. 9.11b, where the error also increases up to 20%.

Even though the slick area can be clearly delimited in the retrieved $\widetilde{\sigma}^0$, with only this information it is not possible to distinguish whether the observed $\widetilde{\sigma}^0$ feature is actually an oil slick, or simply a calmer region of the ocean surface with a lower WS. Nevertheless, $\widetilde{\sigma}^0$ information provided by GNSS-R measurements may help enhancing the existing detection procedures by improving the available spectral signature of the ocean surface.

To have a more complete picture of the proposed imaging technique capabilities to monitor oil slick, a realistic scenario has also been simulated. The EnviSat ASAR image (Fig. 9.12b) distributed by ESA of the Prestige vessel slick from November 17th, 2002 (Fig. 9.12a) has been used to generate the input ocean surface to perform another simulation of the imaging method presented in Section 9.3. The retrieved $\widetilde{\sigma}^0$ is presented in Fig. 9.12c were the oil slick can be distinguished, although the resolution is not as high as the one of the Envisat ASAR image (the WSM mode has a resolution of
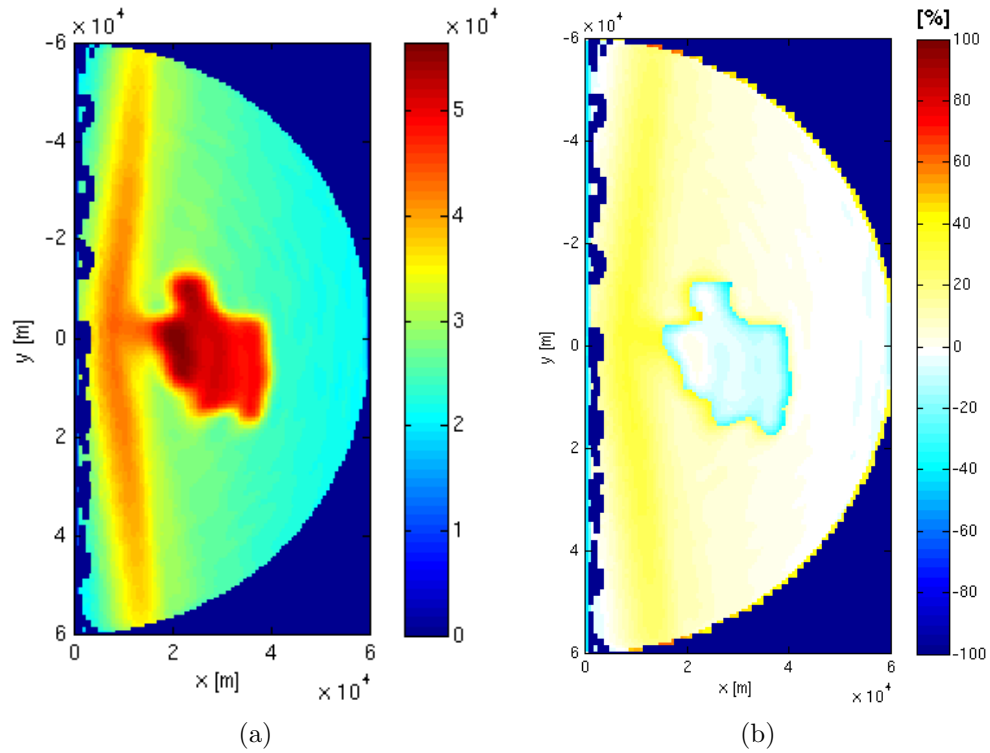
Figure 9.11: a) Retrieved $\widetilde{\sigma}^0$ distribution and, b) error map with respect to the σ^0 used for simulation of the measured DDM (Fig. 9.10).

150 m x 150 m). However, it has to be noticed that the signal bandwidth of the EnviSat ASAR signal is 16 MHz versus the 2.2 MHz of the GPS C/A code considered in the simulation, as well as its SNR is much higher than the one of the scattered GPS signal.

(a)   (b)

(c)
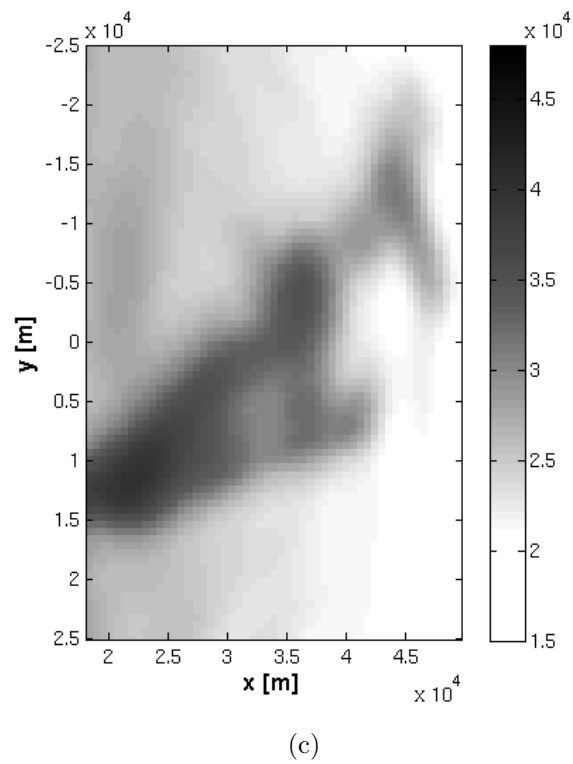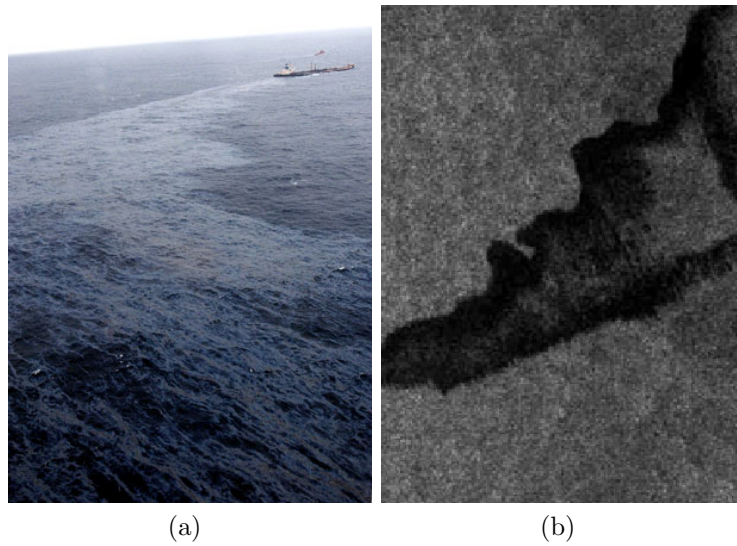
Figure 9.12: a) Picture of the Prestige vessel at the sinking time, b) EnviSat ASAR image of the caused oil slick (ESA), and c) Simulated oil slick GNSS-R retrieval.

To evaluate the resolution of the retrieved image, two representative cuts are presented in Fig. 9.13: one along the x-axis and the other along y-axis, which practically correspond to the SAR-defined range and azimuth domains for the measurement geometry. The selected cuts contain σ^0 features that approach the imaging detectability limit (i.e. detectable, but with a reduced amplitude). The resolution along each of these two directions is estimated by subtracting the half-amplitude width among the retrieved and original images (the final width is the sum of the original width and the impulse response width):

- Along the x-axis, σ^0 presents a 1.5 km width feature around 47.5 km. The retrieved width is 3.2 km, thus the resolution is estimated to be 3.2 km - 1.5 km = 1.7 km.

- Along the y-axis, σ^0 presents a 4 km width feature around 7 km. The retrieved width is 6.5 km, thus the resolution is estimated to be 6.5 km - 4 km = 2.5 km.

The estimated resolution values can be compared with the expected values that are found in bistatic SAR theory. In [79] the expected resolutions are derived for a geometry with parallel transmitter-receiver flights, side-looking receiver, and nadir-reflection (Eqs. 9.11 and 9.12).

The range resolution Δr is defined as a function of the light speed (c), the signal's bandwidth (B, 2.2 MHz of the C/A code for the present case), and the local incidence angle of each surface's point (θ_i):

$$\Delta r = \frac{c}{B sin(\theta_i)}. \tag{9.11}$$

Regarding the azimuth resolution Δa derived in [79] it is:

$$\Delta a = \frac{1}{T_c} \frac{\lambda h_{RX}}{V_{RX} cos(\theta_i)}, \tag{9.12}$$
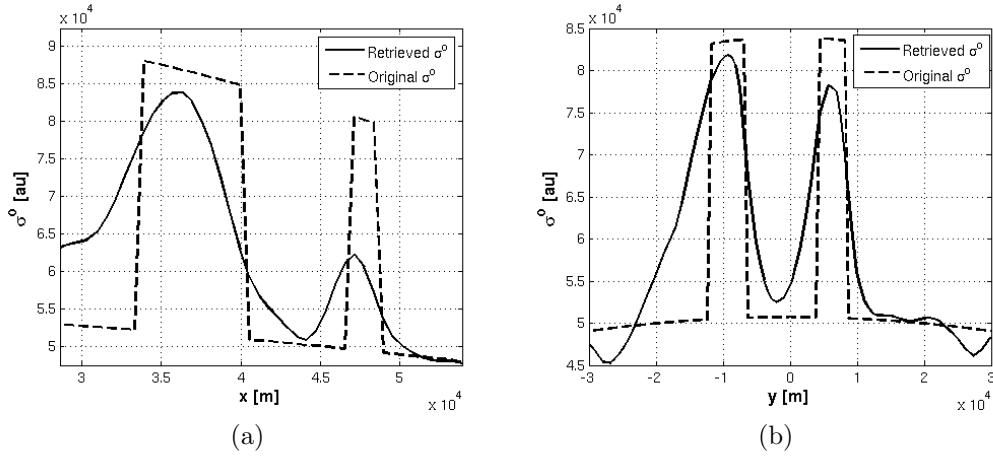
Figure 9.13: Cuts of the retrieved $\tilde{\sigma}^0$ along the: a) x-axis, and b) y-axis. The corresponding original σ^0 is also plotted as a reference.

where T_c is the coherent integration time, λ is the signal's wavelength, h_{RX} is the receiver's height, and V_{RX} is the receiver's speed. The evaluation of these expected resolutions over the simulated surface is plotted in Fig. 9.14. Note that they are plotted as a function of the distance to the specular point (r) since it determines the local incidence angle that drives both Eqs. 9.11 and 9.12. While Δa appears to be very constant over the observed surface, Δr significantly decreases with r.

The final expected resolutions for the cases presented in Fig. 9.13 are: $\Delta r = 2$ km, and $\Delta a = 2.7$ km. These values are very close to the actual ones previously observed from Fig. 9.13 (1.7 km and 2.5 km respectively).

It has to be noticed that the expected resolutions derived in [79] are the size of the C/A code WAF projected to each point of the physical xy surface domain (i.e. separation between the iso-lines). Thus, for the considered geometry, the iso-delay lines are circles that become closer with r, and the iso-Doppler lines are quasi-parallel and with a nearly constant separation (see Fig. 9.4a).

231

(a)   (b)
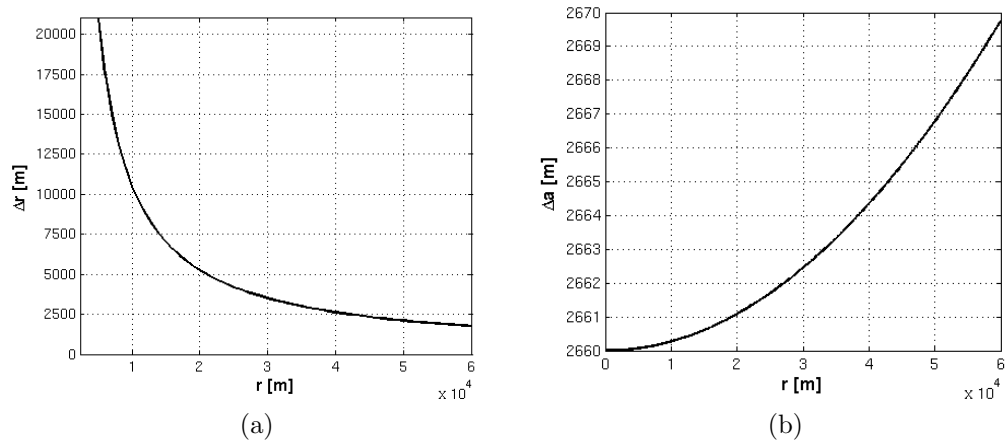
Figure 9.14: Evaluation over the observation surface of: a) theoretical range resolution, Δr, and b) theoretical azimuthal resolution, Δa. Both are plotted as a function of the distance to the specular point r.

9.6 Conclusions

An original method to retrieve the scattering coefficient, σ^0, distribution over the ocean surface from GNSS-R DDMs has been presented along with its numerical evaluation. This new concept is based on the treatment of the measured DDM as a SAR image exploiting the correspondence among the physical xy surface domain and the delay-Doppler one.

To do so, deconvolution of the DDM from the autocorrelation function of the GNSS PRN code has to be performed first. Secondly, the geometry is taken into account by using the Jacobian function computed for the given observation scenario. To solve for the ambiguity in the mapping from DD to the xy domain, a measurement setup that includes an antenna tilt away from the specular reflection point has been proposed.

This method has been firstly evaluated by means of a custom synthetic simulation scenario also considering noise, achieving an error below 10% in the scattering coefficient distribution retrieved (without considering deconvolution artifacts). For the noise case, a level close to the one present in the UK-DMC space-borne measurements has been introduced. However, the deconvolution process has been identified as the key step of the proposed method with a large impact on the retrieval error. Moreover, power contamination from the contribution of the ambiguous zone is also a major error source (accounting for about $\approx 50\%$ of the total error), despite being attenuated at least by 3 dB by the antenna pattern.

Although the feasibility of the proposed method has been shown with the present example, further work is required to optimize the deconvolution process as well as to reduce the aforementioned contaminations from the ambiguous zone by advanced processing techniques. Also the limits of the technique in terms of error and spatial resolution will have to be determined by a comprehensive study considering the scenario and instrument/antenna errors.

CHAPTER 9. OCEAN SURFACE IMAGING FROM DDM DECONVOLUTION

The proposed $\widetilde{\sigma}^0$ retrieval technique has been further applied to the oil slick detection problem. To do so, a simulation example has been conducted. A measured DDM has been simulated for a slick surface properly modeled using the different relationships between the MSS and the WS for the clean and slick regions. This simulation, performed by the "classical" double-integration approach (to have a DDM computation totally independent from the Jacobian method), has taken into account a realistic antenna pattern and noise level. From this DDM, the presented GNSS-R imaging technique has been used to retrieve the $\widetilde{\sigma}^0$ over the physical ocean surface.

The slick area can be clearly distinguished in the retrieved scattering coefficient distribution. The final error with respect to the input distribution is mostly below 10%. However, deconvolution artifacts and ringing cause an error increase up to 20% in some regions (mainly the slick border and the ambiguity-free line) that have to be masked. Although the application of this technique does not make possible the classification of a specific region as oil slick (it appears as a lower WS area), it may help to complete the available information from other sensors (radiometers, SAR, optical, etc.).

Finally, a realistic slick in the ocean surface has also been simulated by using a real image of the Prestige slick as the input for the proposed imaging technique. The retrieved $\widetilde{\sigma}^0$ shows clearly the shape of the slick, although it does not present a resolution as high of the one for a SAR system, which uses signals with larger badnwidths and higher SNR. However, since GNSS-R instruments can be smaller, and consume less power, it is expected that in the future GNSS-R satellites will fly, thus drastically reducing the revisit time, as compared to SAR systems.

10

Conclusions and future research lines

10.1 Conclusions

The present PhD. Thesis has been performed in the framework of the PAU project with two main objectives: 1) design and implement the GPS reflectometer instrument for the PAU project; and 2) perform experimental and theoretical studies in order to improve the understanding of GNSS-R ocean scatterometry, and the use of it for correction of L-band brightness temperature variations induced by sea surface roughness. Accordingly, the present manuscript has been divided in three parts. In Part I, the design and implementation of the griPAU instrument is presented along with the evaluation of its performance. Part II describes four different experimental campaigns, and presents and discusses the derived results. Finally, Part III explores theoretically spaceborne GNSS-R scatterometry by studying the expected performance of a hypothetical mission, and introduces a new technique for imaging of the ocean surface. The work performed in this PhD Thesis can be divided into two generic topics:

- GNSS-R ocean scatterometry; and

- its use for L-band brightness temperature correction.

Following, the main conclusions from each of these two topics are outlined.

10.1.1 GNSS-R ocean scatterometry

The main aim of the PAU project, when it comes to ocean scatterometry, was to prove that ocean surface roughness could be directly described by an observable derived from the DDM, without the use of electromagnetic/scattering models. The DDM is a representation of the scattered power distribution over the observed surface. Therefore, the rougher the sea is, the more spread the power in the DDM becomes. To measure this spreading effect, the volume of the normalized DDM was envisioned. In this PhD. Thesis, this hypothesis has been studied by processing experimental data of ground-based and airborne measurements, and by simulation of a spaceborne scenario.

For ground-based measurements, a low sensitivity to ocean surface roughness was obtained since the glistening zone extension is on the order of one chip in the delay domain, and there is not any spread in the Doppler domain. However, since the receiver is still, the ocean correlation time could be measured by studying the coherence time of the complex DDM peak after accounting for the polarity inversion caused by the navigation bit. The ocean correlation time was observed to range from the order of two hundred milliseconds, to some tens of milliseconds as a function of wind speed. The knowledge of this correlation time is a key point at the time of establishing a GNSS-R data processing strategy, since it is one of the factors that determine the maximum usable coherent integration time.

Data from airborne experiments was also processed for ocean scatterometry in this PhD. Thesis. However, the normalized DDM volume could not always be used due the lack of full-DDM measurements in some experiments. For those cases, the concept of quantifying the power spreading as a descriptor of the ocean surface roughness was reduced to the delay domain by defining a new GNSS-R observable: the normalized waveform area. For an

airborne scenario, it was observed that the normalized waveform area is a good descriptor of sea-state, and it showed to be very independent of other scenario parameters, such as the local incidence angle of the reflection (i.e. SV elevation) or the receiver flying direction. Moreover, when full-DDM measurements were available, an asymmetry along the Doppler domain was observed. That asymmetry was mainly caused by the wind direction and the receiver flying direction. Thus, it was modeled, and a metric of it was envisioned and successfully used for wind direction retrieval. Although models are needed to retrieve wind direction from the DDM asymmetry, sea surface roughness can be directly described by GNSS-R observables without using them. Then, calibration needs to be performed using ground-truth data and performing linear regressions.

With regard to an hypothetical spaceborne mission, an exhaustive simulation study was performed in order quantify the impact of all the scenario parameters on different GNSS-R direct observables proposed for ocean surface roughness determination. From those observables, the volume of normalized DDM is the one that appeared to be less affected by the measurement scenario. Anyhow, this impact was great enough to prevent directly performing sea surface roughness measurements for rough seas (i.e. $WS \geq 20$ m/s), without accounting for it. To do so, modeling is required to establish the observables behavior as a function of the different scenario parameters. Even though models are needed, using direct observables such as the volume of the normalized DDM still vantages the data fitting retrieval methods in terms of computational cost. Finally, it was found that the main uncertainty source is not the noise in the measurements, but the wind direction when it is unknown.

Last, but not least, a new technique to obtain images of the scattering coefficient distribution on the observed ocean surface was proposed. This technique is based on deconvolution of the DDM from the GNSS code ACF, and using Jacobians to transform back from the delay-Doppler domain to

the physical surface domain. The proposed technique was applied to oil slick detection, achieving a performance equivalent to that of a SAR system with similar specifications.

From all the work performed in ocean scatterometry by using direct GNSS-R observables, it can be concluded that it is a very suitable technique for airborne and spaceborne operational systems, although further work is still required to completely understand the second one. For this reason, the deployment of in-orbit demonstration missions is highly desirable. Nevertheless, the deployment of such a mission would also make possible to start implementing and testing the proposed imaging technique.

10.1.2   L-band brightness temperature correction for the sea-state effect using GNSS-R

Once it was assessed that direct GNSS-R observables such as the volume of the normalized DDM, or the area of the normalized waveform, are suitable to be used as sea-state descriptors, the information they provide was used for L-band brightness temperature correction. The increase in ocean surface roughness creates an increment in the measured brightness temperature, which has to be properly corrected in order to perform sea surface salinity retrievals. The estimation of this brightness temperature increase using GNSS-R data was experimentally validated for ground-based and airborne scenarios, and explored for a spaceborne mission through simulation.

During the ALBATROSS 2009 experiment, collocated radiometric and GNSS-R data were collected during a whole month. Along the experiment time, a high variability of sea-state was present (WS from 0 m/s to 12 m/s). Correlation was found between both datasets, and a study of brightness temperature sensitivity to V_{DDM} was performed for a wide incidence angle range. Obtained results were in well agreement with previous results available in the literature such as the study performed from the WISE experiment, where the brightness temperature variation was studied as a function of sea-

state descriptors like wind speed or significant wave height. However, salinity retrievals could not be performed due problems in the absolute calibration of the radiometric data caused by the land contribution corrupting the data when entering through the antennas secondary lobes.

Airborne measurements from the CoSMOS 2007 experiment provided by ESA were also processed with the aim of estimating the ΔT_B from GNSS-R data. In that case, data acquired by the EMIRAD radiometer in a nadir configuration was available along with GNSS-R waveforms computed by the GOLD-RTR instrument. Even though limited roughness conditions were present, the ΔT_B could be estimated from the area of the normalized waveform. The estimated ΔT_B was used to correct the measured brightness temperature prior to performing salinity retrievals. An improvement from 2.8 psu down to 0.51 psu (RMSE) was achieved by implementing the proposed correction derived from GNSS-R collocated data.

Finally, an hypothetic spaceborne mission was studied by using the ΔT_B measured by SMOS as a function of wind speed. To do so, the V_{DDM} was simulated for different scenarios and considering the noise effect, so as to derive its behavior as a function of WS, as well as to quantify the expected uncertainties. Both datasets (SMOS measurements and simulated GNSS-R data) were related using WS as the linking variable, and uncertainty propagation was used to derive the expected error in the ΔT_B estimation from V_{DDM}. The resulting radiometric residual error in the ΔT_B estimation, was obtained to be below 1 K (16% relative error) up to strong winds of 20 m/s, when considering instantaneous 1 s V_{DDM} measurements.

10.2 Future work lines

Taking into account the main conclusions of this PhD. Thesis, some future work lines can be pinpointed to follow on the research of using GNSS-R and L-band radiometry for ocean monitoring:

- Upgrade the griPAU instrument for airborne operation in order to proceed to its industrialization to become an operational system for measuring sea-state.

- Explore the use of new GNSS signals with larger bandwidth than the GPS C/A code, both for sea-state retrieval using direct GNSS-R observables, and for GNSS-R imaging.

- Improve the proposed GNSS-R imaging technique by applying enhanced deconvolution techniques.

- Extend the performed work to other incidence angles at the time of estimating the ΔT_B correction from GNSS-R data for airborne scenarios.

- Use available SMOS data to further study the estimation of the required ΔT_B correction from collocated GNSS-R simulated data (i.e. use the SMOS measurements geometry parameters to generate the expected GNSS-R observables).

- Study the data from the space-qualified version of the PAU instrument that will probably fly onboard the INTA's MicroSat-1, which will provide GNSS-R and L-band radiometric measurements.

Appendices

A

GNSS-R Delay-Doppler Maps over land: Results of the GRAJO field experiment

A.1 Introduction

ESAs SMOS mission [1] was recently launched in November 2nd, 2009 to provide global soil moisture and ocean salinity maps to improve climate and hydrological models. This mission needs an intensive calibration and validation (CAL/VAL) of the soil moisture products and thus, in-situ data collocated with the space-borne measurements is needed. In this framework, the long-term field experiment GPS and Radiometric Joint Observations (GRAJO) has been undertaken since November 2008 until the end of the Commissioning Phase [80].

The main purpose of the GRAJO field experiment is to jointly use L-band radiometry and Global Navigation Satellite System Reflectometry (GNSS-R) to study the effect of vegetation and soil surface roughness on soil moisture retrievals. This experiment was carried out at the REMEDHUS (Red de Medición de la Humedad del Suelo) site which is a soil moisture measure-

ment network that was selected as a secondary CAL/VAL site for SMOS. REMEDHUS covers a 40 km x 30 km area located at the Duero basin, Zamora, Spain, and has a continental and semiarid climate, with cold winters and warm summers (12°C annual mean temperature and 400 mm mean rainfall). The GRAJO experiment included two types of activities: 1) long-term observations: to study the evolution of the geophysical parameters and the farming over a full-year; 2) short-term experiment: to intensively test the effect of soil moisture and roughness on the brightness temperature measurements and GPS-reflectometry data by intentionally changing these soil parameters.

The GRAJO field experiment included LAURA, a ground-based L-band radiometer [27], and SMIGOL, an Interference Pattern Technique (IPT) GPS reflectometer [81]. During the intensive experiment carried out in July 2009, the griPAU instrument (see Chapter 3) was also deployed in the field (Fig. A.1). The griPAU instrument is a GNSS-R receiver that computes in real time the Delay-Doppler Map (DDM) equation [14]: one complex DDM every 1 ms that can then be averaged coherently and incoherently at user's wish. This instrument was already used in a field experiment over the ocean surface for sea-state determination and for sea surface salinity (SSS) retrieval purposes (see Chapter 4).

The DDM contains information about both the scattering geometry, and the scattering surface itself. Therefore, soil moisture is a key parameter to determine the scattering coefficient of the measured surface, and to less extent soil surface roughness, and vegetation.

In this Chapter, the results derived from the Delay-Doppler Maps measured over land by the griPAU instrument are presented and discussed. It is organized as follows:

- Section A.2 describes the experiment's measurement setup, and

- Section A.3 presents the obtained results, in terms of soil moisture retrieval, derived from the study of the chosen GNSS-R observable.

A.2 Measurement setup

In Fig. A.1a the griPAU instrument is shown when mounted on the scaffolding at the experiment site. The height of the antenna with respect to the ground was 3 m. The antenna was mounted in an automatic positioning system that was programmed to track the specular reflection point of the satellite under observations signal. The griPAU was configured to compute 1 s incoherently integrated 24 x 32 points DDMs with a resolution of 0.09 chips in delay and 200 Hz in Doppler. There were two 10 m x 4 m fields (North and East in A.1b) for observation with the L-band radiometer. The soil moisture was periodically monitored in a 1 m x 1 m grid in the morning and evening. This data will be used as ground truth in this work.

The main drawback of this experiment is that no information of the direct received power was collected. This fact does not allow retrieving absolute values for soil moisture, and different tracks can only be qualitatively compared.

(a)   (b)
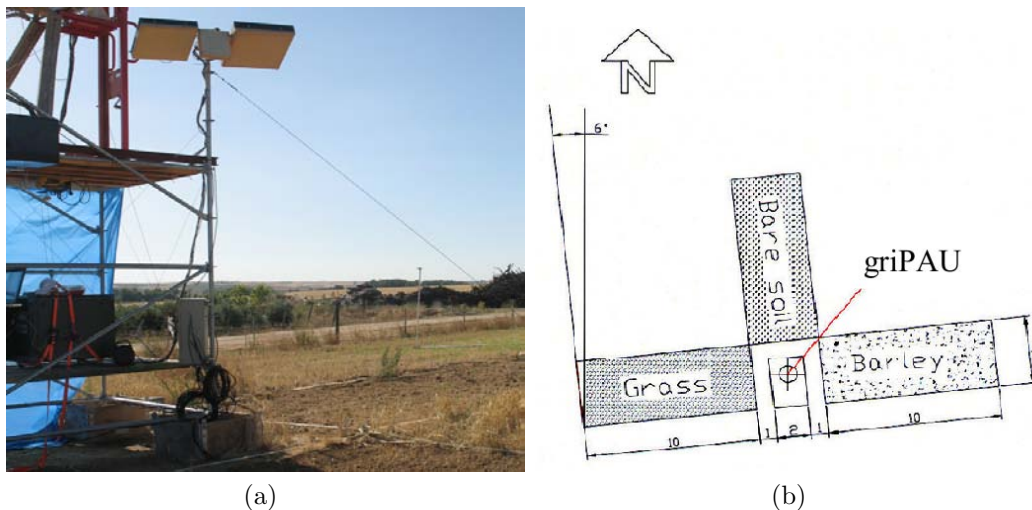
Figure A.1: a) ALBATROSS 2009 measurement setup: griPAU mounted with an L-band radiometer on an antenna positioner; and b) defined observation fields with monitored soil moisture.

A.3 Soil moisture retrieval

As a first approximation, the DDM peak value was studied thus, if constant satellite transmitted power is assumed, it should be proportional to soils reflectivity (i.e. soil moisture). As an example, two griPAU captures are shown in Fig. A.2: the first one shows the DDM peak over sea, and the second one over land.

When measuring the scattered signal over the ocean surface (Fig. A.2a), it is observed that the mean value of the DDMs peak is constant along the satellites track as the sea reflectivity is homogeneous over large areas. As expected, a heavy speckle noise is present.
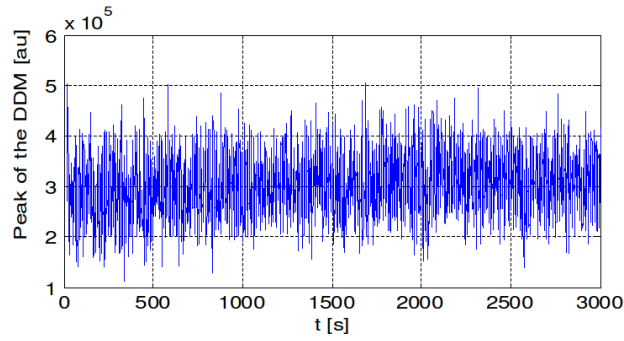
(a)
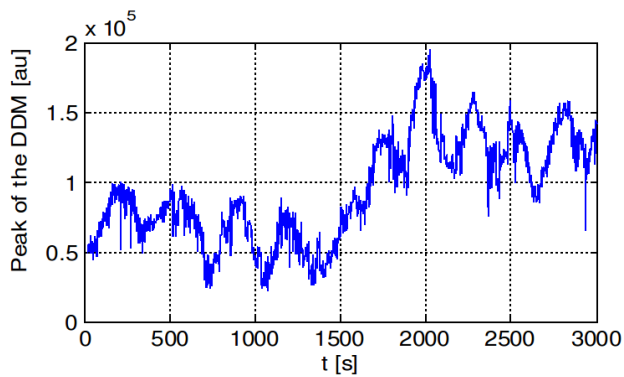
(b)

Figure A.2: Peak of the DDM over: a) the ocean surface; and b) land.

On the other hand, over land (Fig A.2b) the mean value is not constant along the satellite track as the soils reflectivity is not homogeneous, since it is a function of local soil moisture, etc. In addition to the mean value, a clear interference pattern (with a period of 250-300 s in the present case) is observed due to a secondary reflection. It has also to be noticed that the values for the DDM peak over the sea are higher than over land due to the higher reflectivity of the salty water with respect to the soil's.

Using the satellite elevation and azimuth information, the DDMs peak time series have been geometrically projected over the land surface for geolocation. Two satellite tracks that pass over the monitored fields are considered in this work. Both tracks are from the same day, and correspond to two different satellites. The first one was acquired at noon, and the second one in the afternoon just before the soil moisture measurement. In Fig. A.3 both tracks are plotted super-imposed to the interpolated soil moisture map measured that evening.
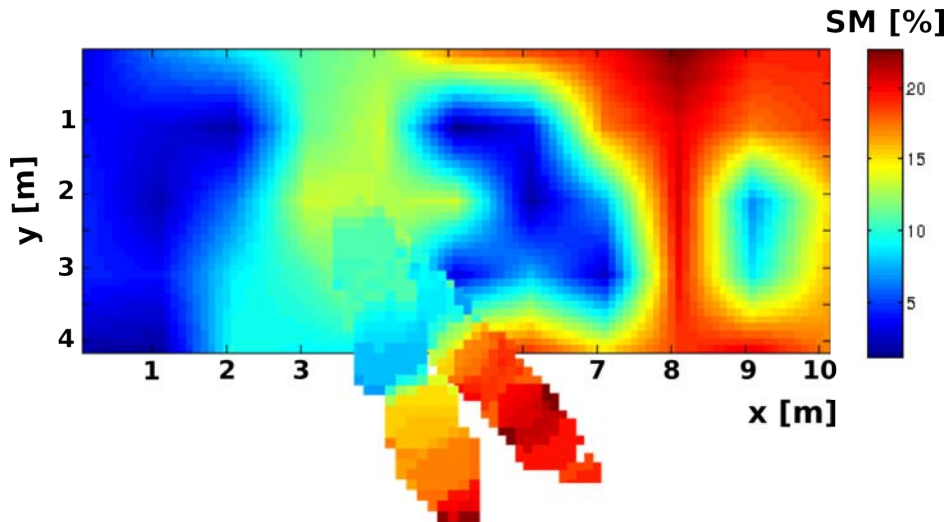
Figure A.3: Measured tracks (SV10 and SV14, arbitrary color scale) super-imposed on the ground-truth soil moisture map.

APPENDIX A. GNSS-R DELAY-DOPPLER MAPS OVER LAND: RESULTS OF THE GRAJO FIELD EXPERIMENT

As no information of the direct signals power was collected, the different tracks can not be quantitatively compared, neither directly linked to soil moisture. However, as it can be seen, the peak of the DDM matches well the soil moisture features of the field. Moreover, both tracks appear to be consistent among them.

To study in more depth the relationship between the peak of the DDM and the measured soil moisture, this work has focused on the track collected in the afternoon as it is the closest in time to the ground truth soil moisture map. In Fig. A.4, the satellite track and its collocated part of the ground truth map are shown. It is observed that the measured peak of the DDM matches the soil moisture features of the scene.
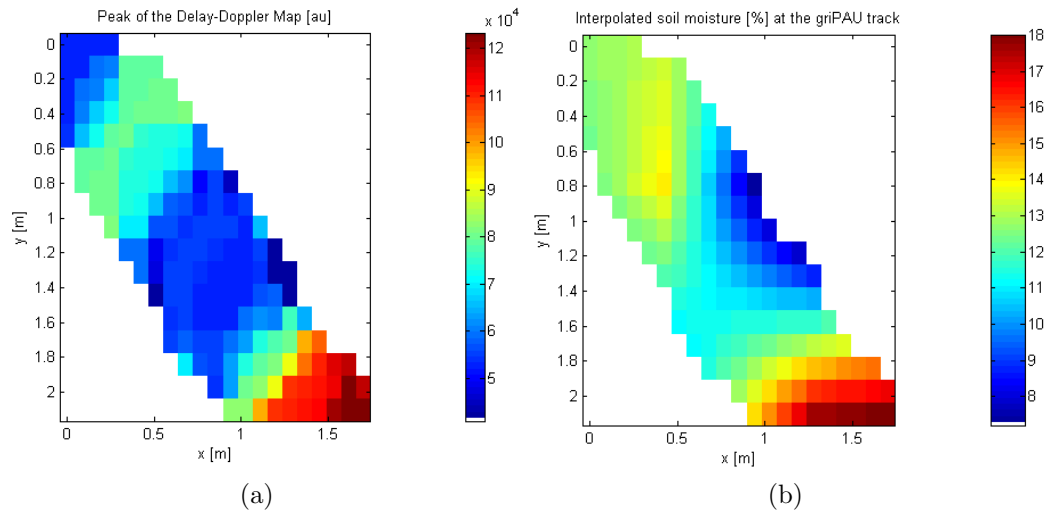
Figure A.4: a) Geolocated peak of the DDM during the satellite SV14 pass in arbitrary units [au]; and b) collocated points of the in-situ measured soil moisture map [%].

To better show this effect, the value of the DDM's peak has been plotted against the measured soil moisture for each collocated ground point in Fig. A.5. A high correlation level is observed (Pearson correlation coefficient $r = 0.83$), and the trend is linear confirming the assumption that the peak of the DDM is proportional to soil's reflectivity. Nevertheless, for soil moisture values lower than 10%, the trend saturates to a DDMs peak value around $5 \cdot 10^4$ au, which is the noise floor of the griPAU instrument (i.e. noise peak when no signal is received).
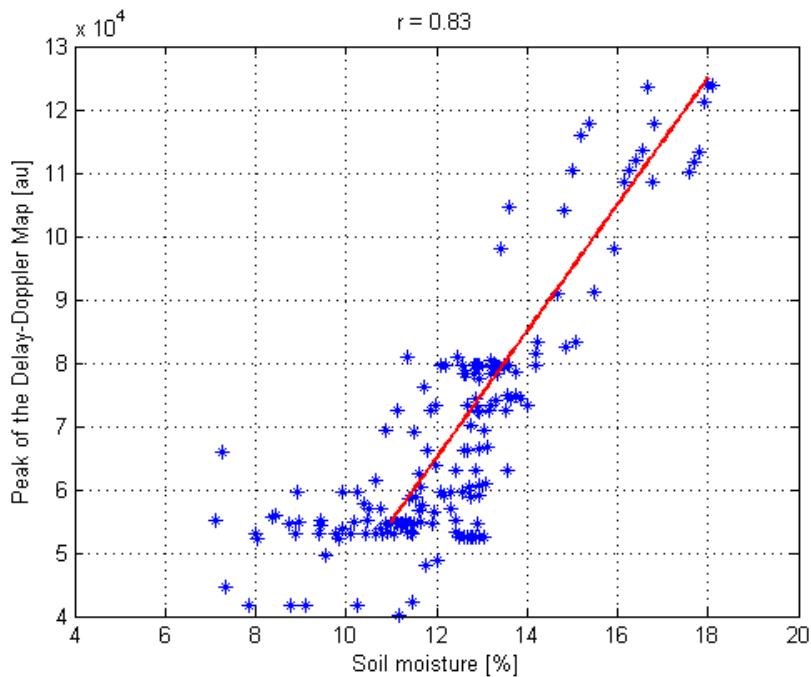
Figure A.5: Peak of the DDM in arbitrary units [au] vs. measured soil moisture [%] for each collocated ground point.

A.4 Conclusions

In the framework of the ESA's SMOS mission CAL/VAL activities, the GRAJO field experiment was undertaken from November, 2008 to May, 2010 to explore the impact of different soil parameters on the soil moisture retrieval when using L-band microwave radiometry. Moreover, that experiment served to explore the potentials of using combined L-band microwave radiometry and GNSS-R techniques at the time of retrieving soil moisture information.

The results from the GRAJO field experiment served to prove the potentials of GNSS-R derived data to retrieve surface's soil moisture. Since the scattering over land is quasi-specular (comes mostly from the first Fresnel zone) the peak of the DDM, which is proportional to the scattered power, exhibits a high correlation with in-situ soil moisture measurements. However, the lack of direct signal's power information prevented to quantitatively derive a generic relationship among the considered GNSS-R observable and the soil moisture.

Since the scattered signal comes from around the specular reflection direction, for ground based observations, soil moisture retrieval would benefit from consolidated simpler hardware approaches such as the Interferometric Pattern Technique [81], a technique that directly considers the power ratio of the received reflected signal over the direct one and allows to retrieve accurately additional parameters such as topography and vegetation height.

List of Publications

Journal Papers

E. Valencia, A. Camps, J.F. Marchan-Hernandez, X. Bosch-Lluis, N. Rodriguez-Alvarez, and I. Ramos-Perez, "Advanced architectures for real time Delay-Doppler Map GNSS-Reflectometer: the GPS Reflectometer Instrument for PAU (griPAU)," *Advances in Space Research*, vol. 46, pp. 196–207, Oct 2010.

E. Valencia, A. Camps, J.F. Marchan-Hernandez, N. Rodriguez-Alvarez, I. Ramos-Perez, and X. Bosch-Lluis, "Experimental determination of the sea correlation time using GNSS-R coherent data," *IEEE Geoscience and Remote Sensing Letters*, vol. 7 (4), pp. 675–679, Oct 2010.

E. Valencia, A. Camps, J. F. Marchan-Hernandez, H. Park, X. Bosch-Lluis, N. Rodriguez-Alvarez, and I. Ramos-Perez, "Ocean surface's scattering coefficient retrieval by Delay-Doppler Map inversion," *IEEE Geoscience and Remote Sensing Letters*, vol. 8, no. 4, pp. 750–754, Jul 2011.

E. Valencia, A. Camps, X. Bosch-Lluis, N. Rodriguez-Alvarez, I. Ramos-Perez, F. Eugenio, and J. Marcello, "On the Use of GNSS-R Data to Correct L-Band Brightness Temperatures for Sea-State Effects: Results of the ALBA-TROSS Field Experiments," *IEEE Transactions on Geoscience and Remote Sensing*, vol. 49, no. 9, pp. 3225–3235, Sep 2011.

E. Valencia, A. Camps, N. Rodriguez-Alvarez, I. Ramos-Perez, X. Bosch-Lluis, and H. Park, "Improving the accuracy of sea surface salinity retrieval using GNSSR data to correct the sea state effect," *Radio Science*, vol. 46, pp. RS0C02, Sep 2011.

LIST OF PUBLICATIONS

E. Valencia, A. Camps, H. Park, N. Rodriguez-Alvarez, and I. Ramos-Perez, "Using GNSS-R imaging of the ocean surface for oil slick detection," *Submitted to IEEE Journal of Selected Topics in Applied Earth Observations and Remote Sensing*, Mar 2012.

Contributions to conferences

E. Valencia, R. Acevo, X. Bosch-Lluis, A. Aguasca, N. Rodriguez-Alvarez, I. Ramos-Perez, J.F. Marchan-Hernandez, M. Glenat, F. Bou, and A. Camps, "Initial results of an airborne light-weight L-band radiometer," *Proceedings of the IEEE International Geoscience And Remote Sensing Symposium 2009*, vol. II, pp. 1176–1179, Jul 2008.

E. Valencia, J.F. Marchan-Hernandez, A. Camps, N. Rodriguez-Alvarez, J.M. Tarongi, M. Piles, I. Ramos-Perez, X. Bosch-Lluis, M. Vall-llossera, and P. Ferre, "Experimental relationship between the sea brightness temperature changes and the GNSS-R delay-Doppler maps: Preliminary results of the albatross field experiments ," *Proceedings of the IEEE International Geoscience And Remote Sensing Symposium 2009*, vol. III, pp. 741–744, Jul 2009.

E. Valencia, A. Camps, X. Bosch-Lluis, N. Rodriguez-Alvarez, I. Ramos-Perez, and J.F. Marchan-Hernandez, "Brightness temperature correction of the sea state effect using GNSS-R data," *Proceedings of the microwave and remote sensing of the environment, MICRORAD 2010*, Mar 2010.

E. Valencia, A. Camps, and M. Vall llossera et al., "GNSS-R Delay-Doppler Maps over land: Preliminary results of the GRAJO field experiment," *Proceedings of the IEEE International Geoscience And Remote Sensing Symposium 2010*, Jul 2010.

E. Valencia, A. Camps, H. Park, N. Rodriguez-Alvarez, X. Bosch-Lluis, and I. Ramos-Perez, "Oil slicks detection using GNSS-R," *Proceedings of the IEEE International Geoscience And Remote Sensing Symposium 2009*, pp. 4383–4386, Jul 2011.

E. Valencia, A. Camps, N. Rodriguez-Alvarez, H. Park, and I. Ramos-Perez, "Impact of the observation geometry on the GNSS-R direct descriptors for sea state monitoring," *Proceedings of the IEEE International Geoscience And Remote Sensing Symposium 2012*, Jul 2012.

Bibliography

[1] ESA, "SMOS: ESAs Water Mission," *Brochure BR-224*, Jun 2004.

[2] UNEP, "United Nation Environmental Programme - Climate," *Retrieved from http://www.grida.no/climate/vital/32.htm*, Nov 2008.

[3] W. Emery and R. Wert, "Temperature-Salinity Curves in the Pacific and their Application to Dynamic Height Computation," *IEEE Transactions on Geoscience and Remote Sensing*, vol. 6, pp. 613–617, 1976.

[4] S. Michel, B. Chapron, J. Tournadre, and N. Reul, "Global Analysis of Sea Surface Salinity variability from Satellite Data," *Oceans - Europe*, pp. 11–16, 1982.

[5] S. Levitus, T. Boyer, M. Conkright, T. OBrien, J. Antonov, and C. Stephens, "World Ocean Database," *National Oceanographic Data Center, NOAA/NESIDS 18*, 1998.

[6] J. Font, A. Camps, A. Borges, M. Marti andn Neira, J. Boutin, N. Reul, Y.H. Kerr, A. Hahne, and S. Mecklenburg, "SMOS: The Challenging Sea Surface Salinity Measurement From Space," *Proceedings of the IEEE*, vol. 98, no. 5, pp. 649–665, May 2010.

[7] "Soil Moisture and Ocean Salinity (SMOS) Consultative Meeting," *ESA-ESTEC, Noordwijk, Netherlands*, Apr 1995.

[8] J. Font, G.S.E. Lagerloef, D.M. Le Vine, A. Camps, and O.Z. Zanife, "The determination of surface salinity with the European SMOS space mission," *IEEE Transactions on Geoscience and Remote Sensing*, vol. 42, no. 10, pp. 2196–2205, Oct 2004.

[9] A. Camps, I. Corbella, M. Vall-llossera, F. Torres N. Duffo, R. Villarino, L. Enrique, F. Julbe, J. Font, A. Julia, C. Gabarro, J. Etchetto, J. Boutin, A. Weill, V. Caselles, E. Rubio, P. Wursteisen, and

BIBLIOGRAPHY

M. Martin-Neira, "L-band sea surface emissivity: Preliminary results of the WISE-2000 campaign and its application to salinity retrieval in the SMOS mission," *Radio Science*, vol. 38, no. 4, pp. 8071, 2003.

[10] D.M. Le Vine, G.S.E. Lagerloef, and S.E. Torrusio, "Aquarius and remote sensing of sea surface salinity from space," *Proceedings of the IEEE*, vol. 98, no. 5, pp. 688–703, May 2010.

[11] M. Martin-Neira, "A Passive Reflectometry and Interferometry System (PARIS): Application to ocean altimetry," *ESA Journal*, vol. 17, pp. 331–355, 1993.

[12] J.L. Garrison, A. Komjathy, V.U. Zavorotny, and S.J. Katzberg, "Wind speed measurement using forward scattered GPS signals," *IEEE Transactions on Geoscience and Remote Sensing*, vol. 40, no. 1, pp. 50–65, Jan 2002.

[13] H. You, J.L. Garrison, G. Heckler, and V.U. Zavorotny, "Stochastic voltage model and experimental measurement of ocean-scattered gps signal statistics," *IEEE Transactions on Geoscience and Remote Sensing*, vol. 42, no. 10, pp. 2160–2169, Oct 2004.

[14] V. U. Zavorotny and A.G. Voronovich, "Scattering of GPS signals from the ocean with wind remote sensing application," *IEEE Transactions on Geoscience and Remote Sensing*, vol. 38, pp. 951–964, Mar 2000.

[15] F. Soulat, M. Caparrini, O. Germain, P. Lopez-Dekker, M. Taani, and G. Ruffini, "Sea state monitoring using coastal GNSS-R," *Geophysical Research Letters*, vol. 31, no. 21, pp. 21303, Jun 2004.

[16] A. Rius, J. Aparicio, E. Cardellach, M. Martin-Neira, and B. Chapron, "Sea surface state measured using GPS reflected signals," *Geophysical Research Letters*, vol. 29, no. 23, pp. 2122, 2002.

[17] E. Cardellach, *Sea surface determination using GNSS reflected signals*, PhD. dissertation, Universitat Politècnica de Catalunya, Barcelona, 2001.

[18] J.F. Marchan-Hernandez, E. Valencia, N. Rodriguez-Alvarez, I. Ramos-Perez, X. Bosch-Lluis, A. Camps, F. Eugenio, and J. Marcello, "Sea-State Determination Using GNSS-R Data," *Geoscience and Remote Sensing Letters, IEEE*, vol. 7, no. 4, pp. 621–625, Oct 2010.

[19] J. F. Marchan-Hernandez, N. Rodriguez-Alvarez, A. Camps, X. Bosch-Lluis, I. Ramos-Perez, and E. Valencia, "Correction of the sea state impact in the L-band brightness temperature by means of Delay-Doppler Maps of Global Navigation Satellite Signals reflected over the sea surface," *IEEE Transactions on Geoscience and Remote Sensing*, vol. 46 (10), pp. 2914–2923, Oct 2008.

[20] A. Camps, "Passive Advanced Unit (PAU): A hybrid L-band radiometer, GNSS-Reflectometer and IR-radiometer for passive remote sensing of the ocean," *Project descriptions of the EURYI award winners 2004, Telecommunications Engineering*, 2004.

[21] A. Camps, X. Bosch-Lluis, I. Ramos-Perez, J.F. Marchan-Hernandez, B. Izquierdo, and N. Rodriguez-Alvarez, "New Instrument Concepts for Ocean Sensing: Analysis of the PAU-Radiometer," *IEEE Transactions on Geoscience and Remote Sensing*, vol. 45, no. 10, pp. 3180–3192, Oct 2007.

[22] F.T. Ulaby, R.K. Moore, and A.K. Fung, *Microwave Remote Sensing, Active and Passive, vol. I: Microwave Remote Sensing Fundamentals and Radiometry*, Addison-Wesley, 1982.

[23] L. Klein and C. Swift, "An improved model for the dielectric constant of sea water at microwave frequencies," *IEEE Transactions on Antennas and Propagation*, vol. 25 (1), pp. 104–111, Jan 1977.

[24] C. Koblinsky, P. Hildebrand, D. Le Vine, and F. Pellerano, "Sea Surface Salinity from Space: Science Goals and Measurement Approach," *Radio Science*, vol. 38, no. 4, 2003.

[25] C. Swift and R. Mcintosh, "Considerations for Microwave Remote Sensing of Ocean-Surface Salinity," *IEEE Transaction on Geoscience and Remote Sensing*, vol. 21, no. 4, pp. 480–491, 1983.

[26] R. Yueh, S.and West, W. Wilson, F. Li, E. Njoku, and Y. Rahmat-Samii, "Error Sources and Feasibility for Microwave Remote Sensing of Ocean Surface Salinity," *IEEE Transactions on Geoscience and Remote Sensing*, vol. 39, no. 5, pp. 1049–1060, 2001.

[27] A. Camps, J. Font, M. Vall-llossera, C. Gabarro, I. Corbella, N. Duffo, F. Torres, S. Blanch, A. Aguasca, R. Villarino, L. Enrique, J.J. Miranda, J.J. Arenas, A. Julia, J. Etcheto, V. Caselles, A. Weill, J. Boutin, S. Contardo, R. Niclos, R. Rivas, S.C. Reising, P. Wursteisen, M. Berger, and M. Martin-Neira, "The WISE 2000 and 2001 field experiments in support of the SMOS mission: sea surface L-band brightness temperature observations and their application to sea surface salinity retrieval," *IEEE Transactions on Geoscience and Remote Sensing*, vol. 42, no. 4, pp. 804–823, Apr 2004.

[28] C. Gabarró, J. Font, A. Camps, M. Vall-llossera, and A. Julià, " A New Empirical Model of Sea Surface Microwave Emissivity for Salinity Remote Sensing," *Geophysical research Letters*, vol. 31, pp. L01309, 2004.

[29] F. Soulat, *Sea Surface Remote Sensing with GNSS and Sunlinght Reflections*, PhD. dissertation, Universitat Politècnica de Catalunya, Barcelona, 2003.

[30] A. Camps, J.F. Marchan-Hernandez, E. Valencia, and et al., "PAU instrument aboard INTA MicroSat-1: A GNSS-R demonstration mission

for sea state correction in L-band radiometry," *Proceedings of the IEEE Geoscience and Remote Sensing Symposium 2011*, pp. 4126–4129, Jul 2011.

[31] S. Guimbard, *Interpretation et modelisation de mesures a distance de la surface marine dans le domaine micro-onde*, PhD. dissertation, Universite de Versailles, Saint Quentin en Yvelines, 2010.

[32] O. Nogués, A. Sumpsi, A. Camps, and A. Rius, "A 3 GPS-channels doppler-delay receiver for remote sensing applications," *Proceedings of the IEEE International Geoscience and Remote Sensing Symposium 2003*, vol. 7, pp. 4483–4485, 2003.

[33] J.F. Marchan-Hernandez, I. Ramos-Perez, X. Bosch-Lluis, A. Camps, N. Rodriguez-Alvarez, and D. Albiol, "PAU-GNSS/R, a real-time GPS-reflectometer for earth observation applications: architecture insights and preliminary results," *Proceedings IEEE International Geoscience and Remote Sensing Symposium 2007*, pp. 5113–5116, Jul 2007.

[34] E. Valencia, A. Camps, J.F. Marchan-Hernandez, N. Rodriguez-Alvarez, I. Ramos-Perez, and X. Bosch-Lluis, "Experimental determination of the sea correlation time using GNSS-R coherent data," *IEEE Geoscience and Remote Sensing Letters*, vol. 7 (4), pp. 675–679, Oct 2010.

[35] J.B. Tsui, *Fundamentals of Global Positioning Receivers*, Wiley Interscience, 2000.

[36] I. Ramos-Perez, X. Bosch-Lluis, A. Camps, J.F. Marchan-Hernandez, R. Prehn, and B. Izquierdo, "Design of a compact dual-polarization receiver for pseudo-correlation radiometers at L-band," *Proceedings of the IEEE International Geoscience and Remote Sensing Symposium 2006*, pp. 1172–1175, Aug 2006.

BIBLIOGRAPHY

[37] X. Bosch-Lluis, A. Camps, J.F. Marchan-Hernandez, I. Ramos-Perez, R. Prehn, B. Izquierdo, X. Banque, and J. Yeste, "FPGA-based Implementation of a Polarimetric Radiometer with Digital Beamforming," *Proceedings of the IEEE Geoscience and Remote Sensing Symposium 2006*, pp. 1176–1179, Aug 2006.

[38] R.D. Chapman, B.L. Gotwols, and R. E. Sterner II, "On the statistics of the phase of microwave backscatter from the ocean surface," *Journal of Geophysical Research*, vol. 99, pp. 16293–16301, 1994.

[39] E. Valencia, J.F. Marchan-Hernandez, A. Camps, N. Rodriguez-Alvarez, J.M. Tarongi, M. Piles, I. Ramos-Perez, X. Bosch-Lluis, M. Vall-llossera, and P. Ferre, "Experimental relationship between the sea brightness temperature changes and the GNSS-R delay-Doppler maps: Preliminary results of the albatross field experiments ," *Proceedings of the IEEE International Geoscience And Remote Sensing Symposium 2009*, vol. III, pp. 741–744, Jul 2009.

[40] A. Rius, E. Cardellach, and M. Martin-Neira, "Altimetric Analysis of the Sea-Surface GPS-Reflected Signals," *IEEE Transactions on Geoscience and Remote Sensing*, vol. 48, no. 4, pp. 2119–2127, Apr 2010.

[41] G. Hajj and C. Zuffada, "Theoretical description of a bistatic system for ocean altimetry using the GPS signal," *Radio Science*, vol. 38, no. 5, pp. 1–10, Oct 2003.

[42] J.T. Johnson and M. Zhang, "Theoretical study of the small slope approximation for ocean polarimetric thermal emission," *IEEE Transactions on Geoscience and Remote Sensing*, vol. 37, no. 5, pp. 2305–2316, sep 1999.

[43] S.J. Frasier and A. Camps, "Dual-beam interferometry for ocean surface current vector mapping," *IEEE Transactions on Geoscience and Remote Sensing*, vol. 39, no. 2, pp. 401–414, feb 2001.

[44] W.J. Plant nad E.A. Terray, R.A. Petitt Jr., and W.C. Keller, "The dependence of microwave backscatter from the sea on illuminiated area: Correlation times and lengths," *Journal of Geophysical Research*, vol. 99, pp. 9705–9723, 1994.

[45] S. Delwart, C. Bouzinac, P. Wursteisen, M. Berger, M. Drinkwater, M. Martin-Neira, and Y.H. Kerr, "SMOS Validation and the COSMOS Campaigns," *IEEE Transactions on Geoscience and Remote Sensing*, vol. 46, no. 3, pp. 695–704, Mar 2008.

[46] K. Rautiainen, J. Kainulainen, T. Auer, J. Pihlflyckt, J. Kettunen, and M.T. Hallikainen, "Helsinki University of Technology L-Band Airborne Synthetic Aperture Radiometer," *IEEE Transactions on Geoscience and Remote Sensing*, vol. 46, no. 3, pp. 717–726, Mar 2008.

[47] J. Rotbøll, S.S. Søbjærg, and N. Skou, "A novel L-band polarimetric radiometer featuring subharmonic sampling," *Radio Science*, vol. 38, no. 3, pp. 8046, Jan 2003.

[48] O. Nogues-Correig, E. Cardellach Gali, J. Sanz Campderros, and A. Rius, "A GPS-reflections receiver that computes Doppler/Delay Maps in real time," *IEEE Transactions on Geoscience and Remote Sensing*, vol. 45, no. 1, pp. 156–174, Jan 2007.

[49] M. Talone, R. Sabia, A. Camps, M. Vall-llossera, C. Gabarro, and J. Font, "Sea surface salinity retrievals from HUT-2D L-band radiometric measurements," *Remote Sensing of Environment*, vol. 114, no. 8, pp. 1756–1764, 2010.

[50] J. Kainulainen, K. Rautiainen, J. Lemmetyinen, M. Hallikainen, F. Martin-Porqueras, and M. Martin-Neira, "Sea surface salinity retrieval demonstration using datasets of synthetic aperture radiometer HUT-2D," *Proceedings of the IEEE International Geoscience and Remote Sensing Symposium 2009*, vol. 3, pp. 737–740, Jul 2009.

[51] H. You, J.L. Garrison, G. Heckler, and D. Smajlovic, "The autocorrelation of waveforms generated from ocean-scattered GPS signals," *IEEE Geoscience and Remote Sensing Letters*, vol. 3, no. 1, pp. 78–82, Jan 2006.

[52] E. Valencia, A. Camps, X. Bosch-Lluis, N. Rodriguez-Alvarez, I. Ramos-Perez, and J.F. Marchan-Hernandez, "Brightness temperature correction of the sea state effect using GNSS-R data," *Proceedings of the microwave and remote sensing of the environment, MICRORAD 2010*, Mar 2010.

[53] L. Leng, T. Zhang, L. Kleinman, and W. Zhu, "Ordinary least square regression, orthogonal regression, geometric mean regression and their applications in aerosol science," *Journal of Physics: Conference Series*, vol. 71, no. 1, pp. 12084, 2007.

[54] J.L. Garrison, "Anisotropy in reflected gps measurements of ocean winds," *Proceedings of the IEEE International Geoscience and Remote Sensing Symposium 2003*, vol. 7, pp. 4480–4482, 2003.

[55] C. Zuffada, T. Elfouhaily, and S. Lowe, "Sensitivity analysis of wind vector measurements from ocean reflected gps signals," *Remote Sensing of Environment*, vol. 88, no. 3, pp. 341–350, 2003.

[56] O. Germain, G. Ruffini, F. Soulat, M. Caparrini, B. Chapron, and P. Silvestrin, "The Eddy Experiment II: GNSS-R speculometry for directional sea-roughness retrieval from low aircraft," *Geophys. Res. Lett*, vol. 31, 2004.

[57] A. Komjathy, M. Armatys, D. Masters, P. Axelrad, V. Zavorotny, and S. Katzberg, "Retrieval of ocean surface wind speed and wind direction using reflected GPS signals," *Journal of Atmospheric and Oceanic Technology*, vol. 21, no. 3, pp. 515–526, 2004.

[58] N. Rodriguez-Alvarez, D.M. Akos, V.U. Zavorotny, J.A. Smith, A. Camps, and C.W. Fairall, "Airborne GNSS-R wind retrievals using delay-Doppler maps," *IEEE Transactions on Geoscience and Remote Sensing (In press)*, 2012.

[59] H. Park, J.F. Marchan-Hernandez, N. Rodriguez-Alvarez, E. Valencia, I. Ramos-Perez, X. Bosch-Lluis, and A. Camps, "End-to-end simulator for Global Navigation Satellite System Reflectometry space mission," *Proceedings of the IEEE International Geoscience And Remote Sensing Symposium 2010*, pp. 4294–4297, Jul 2010.

[60] A. Komjathy, V.U. Zavorotny, P. Axelrad, G.H. Born, and J.L. Garrison, "GPS signal scattering from sea surface: Wind speed retrieval using experimental data and theoretical model," *Remote Sensing of Environment*, vol. 73, no. 2, pp. 162–174, 2000.

[61] D.R. Thompson, T.M. Elfouhaily, and J.L. Garrison, "An improved geometrical optics model for bistatic GPS scattering from the ocean surface," *Geoscience and Remote Sensing, IEEE Transactions on*, vol. 43, no. 12, pp. 2810–2821, 2005.

[62] S.J. Katzberg, O. Torres, and G. Ganoe, "Calibration of reflected GPS for tropical storm wind speed retrievals," *Geophysical Research Letters*, vol. 33, pp. 18602, 2006.

[63] J.F. Marchan-Hernandez, A. Camps, N. Rodriguez-Alvarez, E. Valencia, X. Bosch-Lluis, and I. Ramos-Perez, "An efficient algorithm to the simulation of delay-doppler maps of reflected global navigation satellite system signals," *IEEE Transactions on Geoscience and Remote Sensing*, vol. 47, no. 8, pp. 2733–2740, Aug 2009.

[64] M. Martin-Neira, S. D'Addio, C. Buck, N. Floury, and R. Prieto-Cerdeira, "The PARIS Ocean Altimeter In-Orbit Demonstrator," *IEEE*

Transactions on Geoscience and Remote Sensing, vol. 49, no. 6, pp. 2209–2237, Jun 2011.

[65] A. Rius, O. Nogues-Correig, S. Ribo, E. Cardellach, S. Oliveras, E. Valencia, H. Park, J.M. Tarong, A. Camps, H. van der Marel, R. van Bree, Bas Altena, and M. Martn-Neira, "Altimetry with GNSS-R interferometry: first proof of concept experiment," *GPS Solutions*, June 2011.

[66] E. Valencia, A. Camps, X. Bosch-Lluis, N. Rodriguez-Alvarez, I. Ramos-Perez, F. Eugenio, and J. Marcello, "On the Use of GNSS-R Data to Correct L-Band Brightness Temperatures for Sea-State Effects: Results of the ALBATROSS Field Experiments," *IEEE Transactions on Geoscience and Remote Sensing*, vol. 49, no. 9, pp. 3225–3235, Sep 2011.

[67] E. Valencia, A. Camps, N. Rodriguez-Alvarez, I. Ramos-Perez, X. Bosch-Lluis, and H. Park, "Improving the accuracy of sea surface salinity retrieval using GNSSR data to correct the sea state effect," *Radio Science*, vol. 46, pp. RS0C02, Sep 2011.

[68] S. Gleason, S. Hodgart, Yiping Sun, C. Gommenginger, S. Mackin, M. Adjrad, and M. Unwin, "Detection and processing of bistatically reflected GPS signals from low Earth orbit for the purpose of ocean remote sensing," *IEEE Transactions on Geoscience and Remote Sensing*, vol. 43, no. 6, pp. 1229–1241, Jun 2005.

[69] S. Guimbard, J. Gourrion, M. Portabella, A. Turiel, C. Gabarró, and J. Font, "SMOS Semi-Empirical Ocean Forward Model Adjustment," *IEEE Transactions on Geoscience and Remote Sensing*, vol. 50, no. 5, pp. 1676, 2012.

[70] M. Cherniakov, K. Kubik, and N. David, "Bistatic synthetic aperture radar with non-cooperative LEOS based transmitter," *Proceedings of the IEEE International Geoscience and Remote Sensing Symposium 2000*, vol. 2, pp. 861–862, Jul 2000.

[71] M. Cherniakov, R. Saini, R. Zuo, and M. Antoniou, "Space-surface bistatic synthetic aperture radar with global navigation satellite system transmitter of opportunity-experimental results," *IET Radar Sonar Navigation*, vol. 1, no. 6, pp. 447–458, Dec 2007.

[72] X. He, T. Zeng, and M. Cherniakov, "Signal detectability in SS-BSAR with GNSS non-cooperative transmitter," *IEE Proceedings on Radar, Sonar and Navigation*, vol. 152, no. 3, pp. 124–132, Jun 2005.

[73] R.C. Gonzalez and R.E. Woods, *Digital image processing*, Prentice Hall, 2007.

[74] F.T. Ulaby, R.K. Moore, and A.K. Fung, *Microwave Remote Sensing, Active and Passive, vol. II, Radar Remote Sensing and Surface Scattering and Emission Theory*, Addison-Wesley, 1982.

[75] A. Camps, X. Bosch-Lluis, and Hyuk Park, "Impact of receiver's frequency response in GNSS reflectometers," *Proceedings of the IEEE International Geoscience and Remote Sensing Symposium 2010*, pp. 3817–3820, Jul 2010.

[76] N.P. Galatsanos and A.K. Katsaggelos, "Methods for choosing the regularization parameter and estimating the noise variance in image restoration and their relation," *IEEE Transactions on Image Processing*, vol. 1, no. 3, pp. 322–336, jul 1992.

[77] C. Cox and W. Munk, "Measurement of the Roughness of the Sea Surface from Photographs of the Sun's Glitter," *J. Opt. Soc. Am.*, vol. 44, no. 11, pp. 838–850, Nov 1954.

[78] E. Valencia, A. Camps, J. F. Marchan-Hernandez, H. Park, X. Bosch-Lluis, N. Rodriguez-Alvarez, and I. Ramos-Perez, "Ocean surface's scattering coefficient retrieval by Delay-Doppler Map inversion," *IEEE Geoscience and Remote Sensing Letters*, vol. 8, no. 4, pp. 750–754, Jul 2011.

[79] A. Moccia and A. Renga, "Spatial Resolution of Bistatic Synthetic Aperture Radar: Impact of Acquisition Geometry on Imaging Performance," *IEEE Transactions on Geoscience and Remote Sensing*, vol. 49, no. 10, pp. 3487–3503, Oct 2011.

[80] A. Monerris, N. Rodriguez-Alvarez, and M. Vall llossera et al., "The GPS And Radiometric Joint Observations Experiment at the REMED-HUS Site (Zamora-Salamanca Region, Spain)," *Proceedings of the IEEE International Geoscience And Remote Sensing Symposium 2009*, vol. III, pp. 286–289, Jul 2009.

[81] N. Rodriguez-Alvarez, A. Camps, M. Vall-llossera, X. Bosch-Lluis, A. Monerris, I. Ramos-Perez, E. Valencia, J.F. Marchan-Hernandez, J. Martinez-Fernandez, G. Baroncini-Turricchia, C. Perez-Gutierrez, and N. Sanchez, "Land Geophysical Parameters Retrieval Using the Interference Pattern GNSS-R Technique," *IEEE Transactions on Geoscience and Remote Sensing*, vol. 49, no. 1, pp. 71–84, Jan 2011.